Algorithmes de conception de lois de commande prédictives pour les systèmes de production d'énergie

van Quang Binh Ngo

▶ **To cite this version:**

van Quang Binh Ngo. Algorithmes de conception de lois de commande prédictives pour les systèmes de production d'énergie. Autre. Université Paris Saclay (COmUE), 2017. Français. NNT : 2017SACLC031 . tel-01560359

HAL Id: tel-01560359
https://theses.hal.science/tel-01560359

Submitted on 11 Jul 2017

HAL is a multi-disciplinary open access archive for the deposit and dissemination of scientific research documents, whether they are published or not. The documents may come from teaching and research institutions in France or abroad, or from public or private research centers.

L'archive ouverte pluridisciplinaire **HAL**, est destinée au dépôt et à la diffusion de documents scientifiques de niveau recherche, publiés ou non, émanant des établissements d'enseignement et de recherche français ou étrangers, des laboratoires publics ou privés.

NNT : 2017SACLC031

Thèse de doctorat
de
L'Université Paris-Saclay
Préparée à
CentraleSupélec

Ecole Doctorale N 580
Sciences et Technologies de l'Information et de la Communication
Spécialité de doctorat: Automatique

Par

Van Quang Binh NGO

Algorithmes de conception de lois de commande prédictives pour les systèmes de production d'énergie

Thèse présentée et soutenue à Gif-sur-Yvette, le 22 Juin 2017:

Composition du Jury:

M. Rachid AHMED	Professeur Université de Picardie Jules Verne	Président
M. Dimitri LEFEBVRE	Professeur Université du Havre	Rapporteur
M. Gonzalo ABAD BIAIN	Professeur Université de Mondragon	Rapporteur
M. Pierre LEFRANC	Maitre de conférences Université de Grenoble Alpes	Examinateur
M. Islam BOUSSAADA	Enseignant-Chercheur, HDR Laboratoire des Signaux et Systèmes	Examinateur
M. Pedro RODRIGUEZ-AYERBE	Professeur CentraleSupélec	Directeur de thèse
M. Sorin OLARU	Professeur CentraleSupélec	Co-encadrant
M. Niculescu SILVIU-IULIAN	Professeur Laboratoire des Signaux et Systèmes	Co-encadrant

Declaration

I hereby certify that this thesis is my own work based on the result of my original research and it has not been submitted for a degree to any other University and Institution.

I declare that this thesis is submitted in the form of a series of papers of which I am a joint author.

Acknowledgement

First of all, I would like to express my gratitude to my supervisor Prof. Pedro Rodriguez-Ayerbe for his guidance, confidence and consistent encouragement through my Phd study. To him and to my co-supervisors Prof. Sorin Olaru and Prof. Silviu-Iulian Niculescu I am grateful for their suggestion and invaluable supports during my work.

I would like to express my appreciation to my thesis committee members: Prof. Rachid Ahmed, Prof. Dimitri Lefebvre, Prof. Gonzalo Abad Biain, Dr. Pierre Lefranc and Asoc.Prof. Islam Boussaada for their discussions, suggestions, and feedbacks to improve my thesis.

I would like to thank Prof. Didier Dumur, the former Head of the Automatic Control Department for giving me the opportunity to do my Phd in the laboratory. I also thank all the people of our laboratory for making my stay here interesting and enjoyable.

I cannot forget to mention all my friends, especially Duong Tan Quang, Tu Lam Thanh, Nguyen Minh Tri, Nguyen Ngoc Anh, Tran Quang Hoa, Ngo Thoi Nhan, Ngo Khac Hoang, Nguyen Viet Dung, Nguyen Van Son, Nguyen Duy Minh, Tran Thi Thuong Hoai, Vo Anh Tuan, Mohammed-Tahar Laraba and Abid-Rahman Kodakkadan for their great friendship, help and support.

I would like to thank the Vietnam International Education Development of Ministry of Education and Training for giving me the opportunity to study abroad by granting me a scholarship. Also, thanks to the CentraleSupélec University for the support during all these years.

Finally, I express my respect and intense gratitude to my parents who were the source of inspiration and support all through my life. I am also thankful to my mother-in-law for helping me to take care of my daughter during my study time. I would like to express a deep sense of gratitude to the woman of my life Thanh Tam and my daughter Anh Thy, who always believed in me and encouraged me to overcome difficulties. This work is dedicated to them.

List of publication

Papers in Revision and Review

[1] Van Quang Binh Ngo, Pedro Rodriguez-Ayerbe, Sorin Olaru and Silviu-Iulian Niculescu, "Model Predictive Direct Power Control Based on Lyapunov Function for Doubly Fed Induction Generator Fed by a Three-level Neutral-Point Clamped Inverter", *International Journal of Electrical Power and Energy Systems*, 2017. (Manuscript submitted for review)

[2] Van Quang Binh Ngo, Pedro Rodriguez-Ayerbe and Sorin Olaru, "Improved Predictive Direct Power Control with dead-time compensation based on Lyapunov function for Grid connected Three-level Neutral-Point Clamped Inverter", *IET Power Electronics*, 2017. (Manuscript submitted for review)

Paper in Preparation

[3] Van Quang Binh Ngo, Pedro Rodriguez-Ayerbe and Sorin Olaru, "Modified Model Predictive Control for Grid connected Three-level Neutral-Point Clamped Inverter with reduced computational cost".

Papers published in Conference Proceedings

[4] Van Quang Binh Ngo, Pedro Rodriguez-Ayerbe and Sorin Olaru, "Model Predictive Control with Two-step horizon for Three-level Neutral-Point Clamped inverter", in *Proc. 20th International Conference on Process Control PC-2015*, June. 2015, pp. 215-220.

[5] Van Quang Binh Ngo, Pedro Rodriguez-Ayerbe, Sorin Olaru and Silviu-Iulian Niculescu, "Model Predictive Power Control based on Virtual Flux for Grid connected Three-level Neutral-Point Clamped Inverter", in *Proc. 18th European Conference on Power Electronics and Applications EPE-2016*, Sept. 2016, pp. 1-10.

[6] Van Quang Binh Ngo, Pedro Rodriguez-Ayerbe and Sorin Olaru, "Model Predictive Direct Power Control for Doubly fed induction generator based wind turbines with

Three-level Neutral-Point Clamped Inverter", in *Proc. 42nd Annual Conference on IEEE Industrial Electronics Society IECON-2016*, Oct. 2016, pp. 3476-3481.

Paper accepted for Presentation

[7] Van Quang Binh Ngo, Pedro Rodriguez-Ayerbe, Sorin Olaru and Silviu-Iulian Niculescu, "Model Predictive Direct Power Control of Doubly Fed Induction Generator with Dead-Time Compensation", in *The 20th World Congress of the International Federation of Automatic Control*, July. 2017, Toulouse, France.

Abstract

This thesis aims to elaborate new control strategies based on Model Predictive control for wind energy generation system. We addressed the topology of doubly fed induction generator (DFIG) based wind generation systems which is suitable for generation platform power in the range in 1.5-6 MW. Furthermore, from the technological point of view, the three-level neutral-point clamped (3L-NPC) inverter configuration is considered a good solution for high power due to its advantages: capability to reduce the harmonic distortion of the output voltage and current, and increase the capacity of the converter thanks to a decreased voltage applied to each power semiconductor.

In this thesis, we presented a detailed description of finite control set model predictive control (FCS-MPC) with two-step horizon for two control schemes: grid and DFIG connected 3L-NPC inverter. The principle of the proposed control scheme is to use system model to predict the behaviour of the system for every switching states of the inverter. Then, the optimal switching state that minimizes an appropriate predefined cost function is selected and applied directly to the inverter.

The study of issues such as delay compensation, computational burden and selection of weighting factor are also addressed in this thesis. In addition, the stability problem of FCS-MPC is solved by considering the control Lyapunov function in the design procedure. The latter study is focused on the compensation of dead-time effect of power converter.

Keywords: Doubly fed induction generator (DFIG), Three-level Neutral-Point Clamped Converter (3L-NPC), Finite control set model predictive control (FCS-MPC), Direct power control (DPC), Model predictive direct power control (MPDPC), Control Lyapunov function (CLF), Dead-time compensation, Two-step horizon, Computational burden.

Résumé

1 Aperçu des systèmes de génération à turbine éolienne

Pour satisfaire la forte demande d'électricité et réduire les émissions de gaz à effet de serre, les systèmes d'énergie renouvelable et surtout l'énergie éolienne ont suscité de l'intérêt ces dernières années. Selon le Conseil mondial de l'énergie éolienne (GWEC), la puissance éolienne a progressé de 2000 à 2015 avec environ 63 GW installés uniquement en 2015. En fait, la capacité d'énergie éolienne installée à l'échelle mondiale a atteint 432 GW (148 GW en Europe, a augmenté de 6.3 fois par rapport à l'année précédente) à la fin de 2015, ce qui indique que l'énergie éolienne a un rôle essentiel dans le système d'alimentation énergétique moderne [1]. À la fin de 2015, plus de 80 pays utilisent l'énergie éolienne sur une base commerciale et environ 26 pays disposent de plus de 1 GW d'énergie éolienne installée, dont 17 pays en Europe, 4 en Asie-Pacifique (Chine, Inde, Japon, Australie), 4 dans les Amériques (Brésil, Canada, États-Unis, Mexique) et 1 en Afrique (Afrique du Sud) [2]. L'objectif est de réaliser près de 2000 GW d'ici 2030, fournissant jusqu'à 19% de l'électricité mondiale [3]. En outre, l'éolienne reliée au réseau joue un rôle important pour le maintien et l'amélioration des performances électriques du système global.

En plus de la croissance rapide de la capacité totale installée, la taille et la capacité de l'éolienne individuelle augmentent également afin de réduire le prix par kWh généré et d'augmenter l'efficacité de la conversion de l'énergie éolienne. Récemment, la plupart des principaux fabricants d'éoliennes développent des grandes éoliennes dans la gamme de 1.5 à 6 MW [4], [5]. En fonction de la vitesse de rotation et du type d'électronique de puissance, le système d'éolienne (WTS) peut être classé en quatre groupes principaux comme suit :

- **Type 1** : Turbines éoliennes à vitesse fixe avec générateur d'induction de cage d'écureuil (SCIG).

- **Type 2** : Turbines éoliennes à vitesse variable partielle avec génératrice à rotor bobiné (WRIG).
- **Type 3** : Turbines éoliennes à vitesse variable avec convertisseur de puissance à échelle partielle et générateur asynchrone à double alimentation (GADA).
- **Type 4** : Turbines éoliennes à vitesse variable avec convertisseur de puissance à grande échelle et générateurs synchrones à aimants permanents (PMSG), SCIG ou WRIG.

La technologie initialement utilisée dans les éoliennes était basée sur un générateur d'induction de cage d'écureuil (SCIG) directement connecté au réseau. La plage de vitesse de fonctionnement du générateur dans ce cas est faible, c'est pour cette raison que cette configuration est souvent appelée une turbine éolienne à vitesse fixe. Les avantages de cette structure sont la construction simple et peu coûteuse. Cependant, le principal inconvénient de cette topologie est que le système ne délivre la puissance nominale au réseau qu'à une vitesse de vent donnée, ce qui entraîne une faible efficacité de conversion d'énergie à d'autres vents [5]. Un autre inconvénient de cette topologie est qu'un compensateur de puissance réactive tel qu'un banc de condensateur est nécessaire pour compenser la demande de puissance réactive par le générateur asynchrone, ce qui entraîne increment du coût.

La vitesse variable partielle consiste en une génératrice à rotor bobiné (WRIG) et un mécanisme de variation de la résistance du rotor. Le stator de la WRIG est directement connecté au réseau par le démarreur progressif, alors que l'enroulement rotorique est relié à une résistance externe du rotor à travers le convertisseur. L'amélioration par rapport à la configuration précédente est que la vitesse de rotation de l'éolienne peut être ajustée d'environ 10% de la vitesse synchrone du générateur, ce qui conduit à une efficacité accrue dans la conversion d'énergie. Cependant, la perte de puissance dissipée dans les résistances du rotor et la compensation externe requise reste un inconvénient important pour cette configuration.

Actuellement, la technologie s'est développée vers une vitesse variable. Les éoliennes à vitesse variable les plus courants peuvent être classées en deux types en fonction des types de générateurs et de la puissance nominale du convertisseur par rapport à la puissance totale du système. Le premier type consiste dans la configuration du générateur asynchrone à double alimentation (GADA) équipé d'un convertisseur de puissance à échelle partielle et le deuxième type consiste dans la configuration du convertisseur à grande échelle. Le

premier a suscité de l'intérêt ces dernières années. Dans cette configuration, les enroulements statoriques de GADA sont directement connectés au réseau électrique, tandis que les enroulements du rotor sont connectés au réseau électrique par un convertisseur en opposition (BTB). Ce convertisseur de puissance se compose de deux convertisseurs de puissance, un convertisseur côté rotor (RSC) et un convertisseur côté réseau (GSC), qui sont commandés indépendamment l'un de l'autre. Une bus de tension continue est placée entre deux convertisseurs pour le stockage d'énergie et pour faire la liason entre les deux convertisseurs. Ce concept représente une solution attrayante grâce aux caractéristiques importantes : permet au convertisseur électronique de puissance de traiter environ 30% de la puissance du générateur, il réduit le coût du convertisseur ainsi que les pertes de puissance. En outre, il est adapté à l'éolienne à vitesse variable qui donne la possibilité de produire la puissance maximale possible sur une large gamme de variation de la vitesse du vent. En utilisant cette configuration, il est possible d'autoriser le flux de puissance active et réactive bidirectionnel du côté du rotor au réseau [6–9]. En effet, la GADA permet un fonctionnement en génératrice super-synchrone où la puissance passe du rotor au réseau et sous-synchrone où la puissance passe du réseau au rotor. Par conséquent, le démarreur progressif et le compensateur de puissance réactive ne sont pas nécessaires. La topologie de génératrices éoliennes à vitesse variable en utilisant GADA est la plus grande part de marché des technologies dominantes dans les fabricants d'éoliennes avec une gamme de puissance de 1.5 à 6 MW et occupe environ 50% du marché de l'énergie éolienne [6], [8], [9]. Voici quelques exemples de solutions commerciales: Acciona AW 1.5-3 MW, Alstom ECO 1.67-3 MW et General Electric GE Energy 1.5-2.75 MW [6].

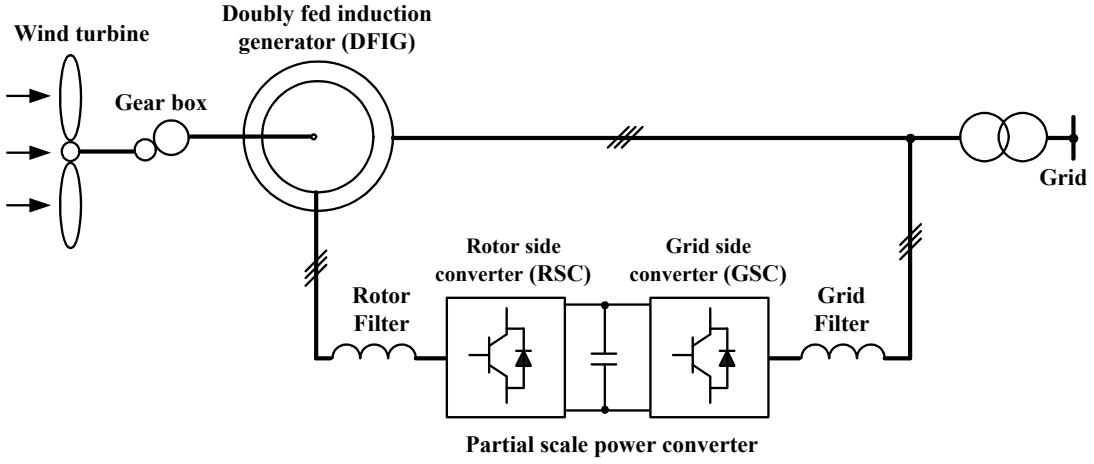

Figure 1: Turbines éoliennes à vitesse variable avec générateur asynchrone à double alimentation.

La turbine éolienne à vitesse variable avec la configuration du convertisseur de puissance à grande échelle est composée d'un générateurs synchrones à aimants permanents

(PMSG) ou d'un générateur d'induction de cage d'écureuil (SCIG) ou WRIG et d'un convertisseur en opposition. L'élimination de la bague collectrice, la pleine puissance et la régulation de vitesse ainsi qu'une meilleure capacité de support de réseau sont les principaux avantages par rapport à la configuration de GADA. Cependant, le principal inconvénient de ce concept est le convertisseur de puissance à grande échelle, qui conduit aux composants électroniques haute puissance ainsi que des pertes de puissance plus élevées dans le convertisseur. Par conséquent, cette topologie convient aux éoliennes de niveau MW de prochaine génération avec un niveau de tension moyen et une puissance élevée à partir de 7 MW tant que les algorithmes de contrôle sont conçus pour minimiser les pertes ci-dessus [4].

2 Etat de l'art de l'électronique de puissance pour les turbines éoliennes

L'électronique de puissance a rapidement changé au cours des dernières années en raison du développement de dispositifs semi-conducteurs. Leur intégration dans les systèmes de conversion joue un rôle important dans l'amélioration des performances et de la puissance des éoliennes. En tant qu'interface entre la GADA et le réseau dans le système, le convertisseur à deux niveaux est habituellement utilisé comme structure BTB pour le système d'éoliennes. Cependant, il devient difficile pour une topologie de convertisseur BTB à deux niveaux de réaliser des performances acceptables dans un système à éoliennes avec une puissance élevée. En effet, il est impossible d'augmenter la puissance en raison de la limite de tension imposée aux composants électroniques. Et la tension de sortie du convertisseur à deux niveaux a un dv/dt élevé, nécessitant un filtre de sortie volumineux pour limiter le gradient de tension et réduire le niveau des harmoniques [5], [10].

Avec les capacités pour atteindre un niveau de tension élevé, une puissance élevée et une petite tension de mode commun, les convertisseurs multiniveaux deviennent une solution préférée dans le système d'éoliennes. En général, trois topologies différentes ont été proposées: le convertisseur clampé par le neutre (NPC), le condensateur volant (FC) et cascade en pont H (CHB). Le convertisseur clampé par le neutre peut obtenir plus des niveaux de tension de sortie et moins de dv/dt par rapport à la topologie à deux niveaux, ce qui réduit la distorsion harmonique totale (THD) de la tension et du courant de sortie. En outre, la capacité du convertisseur peut être augmentée grâce à une tension réduite appliquée à chaque composant. L'équilibre de la tension du point neutre est un inconvénient principal, mais ce problème a été étudié et amélioré depuis plusieurs années. Par conséquent, le convertisseur BTB à trois niveaux et clampé par le neutre (3L-NPC) est considéré comme une bonne solution pour les systèmes de conversion de l'énergie éolienne grâce à ses avantages en termes de l'économie, de la complexité de la

commande et de la performance [10–13]. En effet, cette topologie est l'une des topologies multiniveaux les plus commercialisées disponibles sur le marché [8].

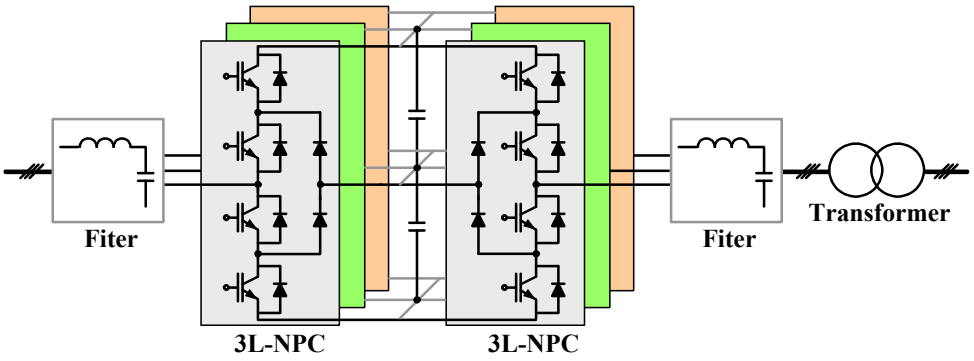

Figure 2: Le convertisseur BTB à trois niveaux et clampé par le neutre [5].

Similaire au convertisseur clampé par le neutre, le condensateur volant produisent également la tension de sortie avec réduction de dv/dt et THD. Les configurations de commutation redondantes qui offrent plus de possibilités pour commander la tension des condensateurs à liaison continue est le principal avantage de cette topologie. Cependant, il présente certaines limitations, y compris les suivantes : un grand nombre de condensateurs avec des circuits de pré-charge distincts, la complexité de la commande en charge du suivi des niveaux de tension pour tous les condensateurs et une fréquence de commutation plus élevée pour garder les condensateurs correctement équilibrés [12].

Le convertisseur en cascade en pont H peut atteindre des performances de sortie similaires au convertisseur clampé par le neutre. Le principal avantage de la topologie du convertisseur CHB est qu'il peut être facilement étendu pour des niveaux de tension plus élevées et de puissance supérieures. Néanmoins, en comparaison avec le transformateur standard utilisé pour le convertisseur NPC, le pont H en cascade a besoin d'un transformateur d'isolement de déphasage pour acquérir des alimentations courant continue isolées et, en conséquence, cette topologie est coûteuse et volumineuse.

3 Commande des convertisseurs électroniques de puissance pour le système de génération à turbine éolienne

L'architecture de commande de l'éolienne à vitesse variable se compose de trois parties principales: commande de l'éolienne, commande côté rotor et commande côté réseau. La commande de turbine éolienne fournit une référence de puissance active (P_{s_ref}) ou une référence de couple électromagnétique pour contrôler le GADA. Cette valeur de référence est calculée en fonction de la vitesse du vent mesurée en fonction de la table de recherche

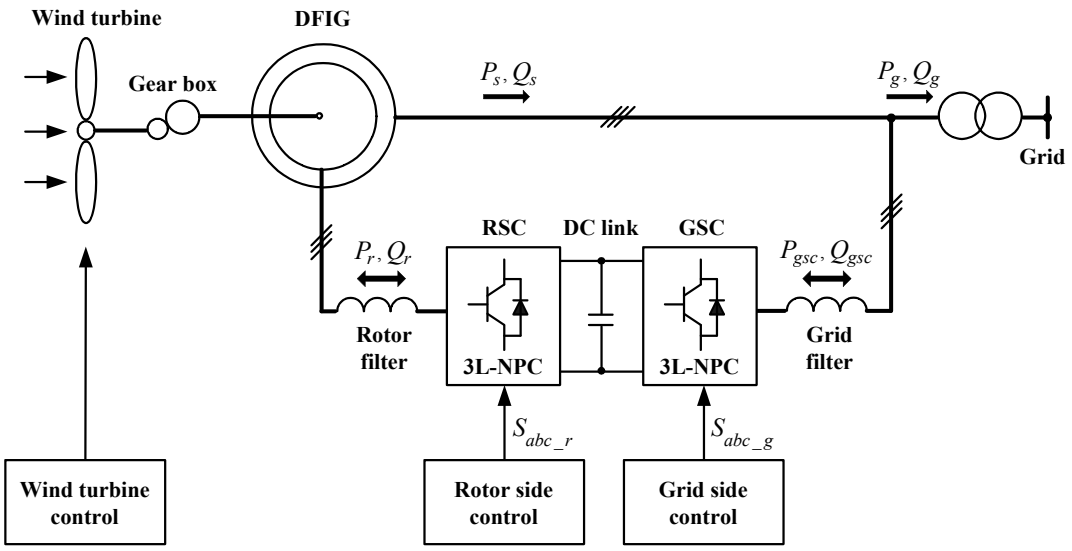

Figure 3: Le schema de commande pour les éolienne à base de GADA avec le convertisseur BTB 3L-NPC [5].

prédéterminée afin de déterminer la puissance optimale correspondant à la vitesse de rotation de l'éolienne. Une commande de suivi du point de puissance maximum (MPPT) est nécessaire afin de maximiser la puissance de sortie de l'éolienne en commandant l'angle d'inclinaison des pales de la turbine. Le convertisseur côté rotor (RSC) génère une tension triphasée avec une amplitude et une fréquence variables pour contrôler le couple du générateur ou la puissance active (P_s) et la puissance réactive (Q_s) échangés entre le stator et le réseau. Le convertisseur côté réseau (GSC) contrôle la puissance active (P_{gsc}) échangé bidirectionnellement entre le rotor de la machine et le réseau et peut également influencer le facteur de puissance. La puissance active peut être transférée entre le rotor et la tension du bus continu et le but de la commande est de calculer la puissance active échangée avec le réseau pour maintenir constante la tension du bus continu. Un fonctionnement à facteur de puissance unité est habituel pour GSC, mais il est également possible de contrôler le flux de puissance réactive (Q_{gsc}) entre le convertisseur et le réseau, indépendamment du RSC [9], [14], [15]. Le filtre du côté du rotor contribue à réduire la distorsion harmonique des courants et des tensions du générateur, tandis que le filtre du réseau permet d'obtenir des exigences harmoniques spécifiées par les norme du réseau.

Plusieurs méthodes ont été proposées pour contrôler le RSC et le GSC pour le système d'énergie éolienne. La commande de l'électronique de puissance et de la machine électrique peut être divisé en cinq groupes principaux: la commande linéaire, la commande à hystérésis, la commande de mode de glissement, la commande intelligente et la commande prédictive [16–18]. La plupart des méthodes de commande existantes utilisent la commande vectorielle classique basée sur l'orientation de la tension (contrôle orienté

tension-VOC) [15, 19–22] ou la commande orientée sur le champ (FOC) [9, 23, 24] qui garantissent la dynamique et la performance statique via des boucles de contrôle de courant interne avec un contrôleur linéaire proportionnel-intégral (PI). Cependant, il a une faible performance dynamique et ses performances dépendent des paramètres précis de la machine et de la qualité de la boucle de commande de courant, qui est fortement influencée par la tension du réseau. Ensuite, une technique de modulation complexe telle que la modulation de largeur d'impulsion (PWM) ou la modulation vectorielle (SVM) avec l'équilibrage des tensions des condensateurs du bus continu est nécessaire pour appliquer ces techniques aux convertisseurs 3L-NPC. Pour résoudre ce problème, plusieurs approches ont été proposées telles que SVM avec la sélection d'états de commutation redondante [25] et le PWM avec injection de tension homopolaire [26].

Récemment, une commande à hystérésis, surtout la commande directe du couple (DTC) [25, 27, 28] et la commande directe de la puissance (DPC) [14, 29, 30] ont été proposés pour améliorer les performances de l'asservisssement. Le DTC commande le couple et le flux de rotor de la machine, tandis que DPC commande les puissances active et réactive. Ces méthodes ont utilisé la commande à hystérésis et les états de commutation de l'onduleur, sélectionnés à partir d'une table de recherche (LUT) en fonction des erreurs entre la référence et les valeurs estimées (couple et flux dans DTC; puissances active et réactive dans DPC) et la position de la tension ou du flux virtuel. Donc, ces méthodes ne nécessitent pas les boucles de commande actuelles et la modulation vectorielle. En comparaison avec le contrôleur linéaire PI, ces méthodes ont une réponse dynamique rapide, aucune exigence de découplage entre la commande des composantes acitve et reactive, et conduit à une meilleure dynamique. Néanmoins, l'inconvénient de LUT est qu'il présente une grande ondulation de puissances active et réactive et la variation de la fréquence de commutation. Pour surmonter ce problème, une modulation vectorielle a été introduite dans la structure DPC [31], [32]. En outre, une fréquence d'échantillonnage élevée est utilisée pour DTC/DPC pour garantir des performances stables et dynamiques acceptables. Avec des techniques de contrôle linéaire et d'hystérésis, il n'est pas facile d'inclure les contraintes du système et les exigences techniques telles que le courant maximal, la distorsion harmonique totale, la tension en mode commun et la fréquence de commutation.

La commande de mode de glissement (SMC) [33–35] est une technique de contrôle avancée qui convient au système linéaire et non linéaire avec des incertitudes. La variable de contrôle est discontinue et suit une trajectoire prédéfinie. Avec cette méthode, elle présente une implémentation simple, des propriétés attractives de rejet de perturbation,

une forte robustesse et une réponse rapide même pendant les variations de paramètres du système et les perturbations externes par rapport à la technique de commande classique.

La logique floue [36], [37], les réseaux neuronaux artificiels [38–40] et neuro-flou [41] font partie de la classe de méthodes de commande intelligentes. Ces méthodes utilisent les fonctions d'appartenance du contrôleur de logique floue ou des réseaux neuronaux artificiels pour créer des signaux de commutation du convertisseur de puissance. Le principal avantage de ces méthodes est la capacité de fournir un signal de commande sans modèle de convertisseur exact, donc il est utile pour les caractéristiques du convertisseur de puissance de nature non linéaire. Cependant, la qualité de la performance dépend de l'expérience, de la connaissance précise de l'opération ou du comportement du système.

Au cours des dernières années, la commande prédictive est apparu comme une technique de commande majeure qui s'applique aux convertisseurs de puissance et aux entraînements électriques. La commande prédictive (MPC-model predictive control) utilise le modèle du système pour prédire le comportement futur du processus pour une variable de commande spécifique et ensuite obtenir une action optimale basée sur les critères d'optimisation prédéfinis. La famille de techniques de commande prédictive peut être divisée en cinq catégories: commande deadbeat, commande basée sur l'hystérésis, commande basée sur la trajectoire, commande prédictive à modèle et plusieurs autres stratégies de commande prédictive qui diffèrent par rapport à l'évaluation optimale de la prise de décision ou à la mise en œuvre de la stratégie sélectionnée .

Une commande prédictive deadbeat utilise un modèle du système pour calculer la variable de commande requise qui annule l'erreur entre la variable de commande et l'entrée de référence [42], [43]. Les signaux de commutation sont appliqués aux convertisseurs de puissance en utilisant le modulateur PWM/SVM. Cette stratégie de commande fournit une réponse dynamique rapide, mais les variations et les perturbations des paramètres du système peuvent détériorer les performances obtenues. En outre, il est difficile d'intégrer les non-linéarités et les contraintes du système.

Les techniques de MPC basées sur l'hystérésis et la trajectoire fonctionnent selon le principe de sélection des variables de commande dans les limites d'une zone d'hystérésis ou d'une trajectoire plus courte entre l'état initial et l'état souhaité [16, 42, 44]. Ainsi, ces méthodes n'exigent pas le bloc de modulation et appliquent les états de commutation directement au convertisseur.

De nos jours, la commande prédictive à modèle (MPC) est reconnu comme une stratégie de contrôle simple et puissante pour contrôler les convertisseurs de puissance

et les moteurs électriques grâce à ses avantages tels que simples à appliquer dans des systèmes multivariables et considèrent les non-linéarités et les contraintes dans le système à commande et présentent une rapide réponse dynamique. Le principe de fonctionnement de MPC est basé sur l'utilisation du modèle mathématique pour prédire le comportement du système, puis minimiser la fonction de coût prédéfinie pour atteindre les objectifs de commande spécifiés. Le MPC appliqué aux convertisseurs de puissance peut être classé en deux groupes principaux : Continuous Control Set MPC (CCS-MPC) et la commande prédictive à ensemble de commande fini (FCS-MPC). Dans CCS-MPC, les variables de commande sont continues, le problème d'optimisation peut être résolu en ligne en utilisant généralement une programmation quadratique (QP) [45–48] ou sous la forme d'une commande prédictive généralisée (GPC) [49] ou peut même être calculée hors ligne par une solution explicite avec des structures affines plus complexes (MPC explicite) [50], [51] pour réduire le nombre de calculs à effectuer. Dans le premier groupe, il faut un modulateur pour générer les états de commutation à partir de la sortie continue du contrôleur prédictif, conduisant à une fréquence fixe de commutation. Cependant, le principal inconvénient de CCS-MPC est que les non-linéarités prises dans le modèle conduisent à un problème d'optimisation complexe, difficile à résoudre en ligne à l'aide d'une plate-forme de matériel numérique classique.

D'autre part, avec FCS-MPC, le temps de calcul du problème d'optimisation est réduit en évaluant uniquement la fonction de coût avec un nombre fini d'états de commutation et en choisissant l'entrée de commande qui atteint la valeur de la fonction de coût la plus basse [16, 44, 52–54]. Le FCS-MPC est une technique de commande alternative attrayante en raison de ses avantages:

- Prend en compte la nature discrète du convertisseur de puissance.
- Fournit une réponse dynamique rapide et de bonnes performances en régime permanent.
- Est simple à appliquer dans les systèmes multivariables.
- L'optimisation est simplifiée grâce à un nombre fini d'états de commutation.
- Peut être appliqué à une large gamme d'applications de convertisseur de puissance et des applications d'entraînement.
- Les non-linéarités et les contraintes du système peuvent être incorporées directement dans le contrôleur.

- Le retard de calcul et le temps mort peut être compensé.
- Simple et facile à mettre en œuvre.

En général, le FCS-MPC peut être divisé en deux types: vecteur de commutation optimale MPC (OSV-MPC) et séquence de commutation optimale MPC (OSS-MPC). Avec le premier groupe, l'état de commutation optimale est directement appliqué au convertisseur sans modulateur, entraînant une fréquence variable de commutation. Cependant, la fréquence de commutation peut être contrôlée en imposant une restriction dans la fonction de coût. En revanche, la méthode OSS-MPC [55, 56] définit les séquences de commutation optimales (états de commutation et cycles de fonctionnement correspondants) à appliquer au convertisseur de puissance pendant la prochaine période d'échantillonnage. Ensuite, la séquence de commutation est traditionnellement implémentée sur la base d'une modulation vectorielle de tension, ce qui produit une fréquence fixe de commutation.

Récemment, certaines stratégies de commande novatrices de la commande prédictive ont été proposées pour améliorer les performances du contrôleur pour des topologies de convertisseur de puissance et des applications d'entraînement : commande direct de la puissance prédite (PDPC) [57, 58], MPC modulé (M2PC) [59–61], fréquence variable d'échantillonnage MPC (VSF-MPC) [62, 63], MPC commuté (SMPC) [64] et point de commutation variable MPC (VSP-MPC) [65–67].

Avec le FCS-MPC, tous les états de commutation doivent être évalués pour la fonction de coût pour obtenir la valeur optimale. Il est bien connu que le choix de longs horizons de prédiction, donne en général de meilleures performances en boucle fermée que le choix d'un horizon court. Malheureusement, la charge de calcul dans la résolution des problèmes d'optimisation augmente exponentiellement avec la longueur de l'horizon de prédiction. Donc, malgré les bonnes performances que le FCS-MPC offre, il reste encore des défis qui peuvent être repris par les points suivants :

- Nécessite une grande quantité de calculs, en particulier avec un nombre élevé d'états de commutation et de longs horizons de prédiction.
- Fonctionne avec une fréquence variable de commutation.
- La précision du modèle a un impact direct sur la qualité du contrôleur.
- L'un des principaux problèmes ouverts est que la stabilité du système n'a pas été prise en compte dans la procédure de conception.

4 La commande prédictive à ensemble de commande fini

Le but de la méthode de commande est de conduire une variable système $x(t)$ qui est déterminée par l'action de commande $S(t)$ (habituellement les signaux de commutation du convertisseur) le plus près possible d'une valeur de référence souhaitée $x^*(t)$. En raison d'un nombre fini d'états de commutation S_i, avec $i = 1, ..., n$, nous pouvons prédire toutes les variables possibles du système $(x^p(k+1))$ sur une période d'échantillonnage T_s en fonction du modèle du système et des valeurs mesurées. Ensuite, une fonction de coût g qui dépend de l'objectif de la commande peut être définie. Un exemple typique pour la fonction coût serait l'erreur absolue entre les valeurs prédites et leurs références $g = |x^*(k+1) - x^p(k+1)|$. L'évaluation de la fonction coût avec les n différents commandes possibles, entraînera n différents coûts. Enfin, l'état optimal de commutation qui minimise la fonction de coût est sélectionné et appliqué directement au convertisseur. En résumé, la conception FCS-MPC est réalisée selon les étapes suivantes :

- **Étape 1 : Mesures**

  Obtenir les signaux de retour requis pour le modèle prédictif ou le calcul de la référence.

- **Étape 2 : Calcul et extrapolation des références**

  Calculer la variable de référence en fonction de l'application spécifique, puis obtenir les valeurs futures de la référence en utilisant l'extrapolation.

- **Étape 3 : Construire des modèles en temps continu du système**

  La modélisation du système s'effectue en dérivant des équations qui décrivent le comportement dynamique des variables contrôlées généralement basées sur un modèle linéaire comme suit :

  $$\frac{dx}{dt} = Ax + Bu,$$

  Où x représente la variable à contrôler (tension, courant, flux, puissance) et u est l'entrée de contrôle (tension de réseau, état de commutation, tension continue).

- **Étape 4 : Construire des modèles à temps discret du système**

  Un modèle de temps discret du système est nécessaire pour prédire le comportement des variables évaluées par la fonction de coût. Afin de discrétiser le modèle de système, la méthode d'avant-première Euler est utilisée en raison de sa simplicité. Il donne également une précision acceptable qui est nécessaire pour de bonnes performances. Selon cette approche, nous avons la forme de temps discrète du système comme suit:

$$\frac{dx}{dt} \simeq \frac{x(k+1) - x(k)}{T_s},$$

  Où T_s est le temps d'échantillonnage, $x(k+1)$ et $x(k)$ sont la valeur de la variable d'état dans le prochain temps d'échantillonnage et à l'état actuel, respectivement.

- **Étape 5 : Prédiction des variables de commande**

  Prédire la valeur future des variables de commande basées sur les modèles à temps discret, les valeurs mesurées et tous les états possibles de commutation du convertisseur.

- **Étape 6 : Minimiser la fonction de coût**

  En dernière étape, toutes les valeurs des variables prédites $x_i^p(k+1)$ sont comparées avec leur références $x^*(k+1)$ à l'aide d'une fonction de coût g comme suit :

$$g = \left| x^*(k+1) - x_i^p(k+1) \right|, i = 1, ..., n.$$

  L'objectif de l'optimisation de la fonction coût est de sélectionner la valeur de coût g aussi près que possible de zéro. L'état optimal de commutation qui minimise la fonction de coût est choisi et ensuite appliqué au convertisseur au moment du prochain instant d'échantillonnage.

5 Objectifs

L'objectif de cette thèse est d'élaborer de nouvelles stratégies de commande basées sur une philosophie de commande prédictive à modèle pour les systèmes de production d'énergie éolienne. Il se concentre sur la topologie de GADA avec le convertisseur 3L-NPC pour un système d'éolienne qui convient à une plate-forme de génération avec une puissance comprise entre 1.5 et 6 MW. Malgré cette portée concentrée sur le côté de

l'application et de la modélisation, les développements méthodologiques seront génériques pour les stratégies prédictives définies par ensemble fini. Il est illustré comment mettre en œuvre FCS-MPC pour améliorer les performances en termes de qualité d'énergie, de réponse dynamique et d'efficacité des convertisseurs de puissance. Ainsi, les orientations de recherche de cette thèse tiennent compte des objectifs suivants :

- Développement de la stratégie FCS-MPC pour le convertisseur 3L-NPC.
- Compensation de la complexité computationnelle et développement de FCS-MPC avec horizon en deux étapes.
- Description détaillée du modèle de commande de puissance prédictive est présentée pour commander le réseau connectée au convertisseur 3L-NPC.
- Plusieurs approches sont introduites pour réduire le coût de calcul, la fréquence de commutation et la tension en mode commun.
- Aservissement des puissances actives et réactives pour la GADA connecté au convertisseur 3L-NPC, un modèle de commande de puissance directe prédictive est proposé.
- Une fonction Lyapunov est utilisée pendant la conception de la commande, ce qui inclut des considérations liées à la stabilité dans la décision basée sur l'optimisation pour le fonctionnement en boucle fermée du système.
- Pour compenser l'effet de temps mort et améliorer les performances en boucle fermée, la commande prédictive à modèle est modifiée pour prend en compte directement la compensation de temps mort.

En résumé, nos contributions sont d'élaborer une nouvelle stratégie de commande pour résoudre des défis de FCS-MPC :

- *Approche 1* : Pour réduire le nombre d'évaluations en temps réel, nous proposons dans une première étape de considérer d'appliquer le même vecteur de tension en deux pas, au lieu de différents vecteurs (Fig. 4).
- *Approche 2* : Afin d'éviter un saut en hauter de la tension de phase et réduire le nombre de commuatation, il est possible de limiter les éventuelles trasitions de commutation. Dans ce cas, nous proposons de considérer les combinations d'entrées ayant une seule variation de commutation à l'instant $k + 2$ (Fig. 5).

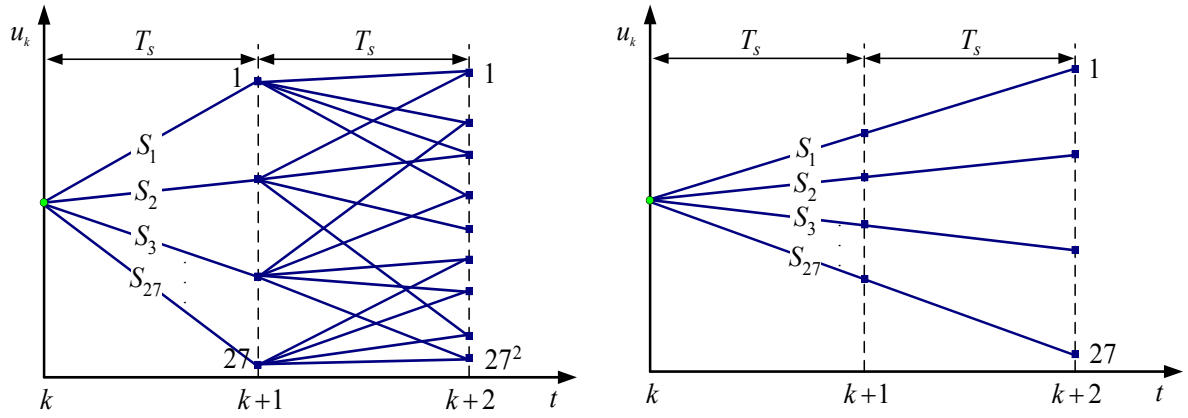

(a) Prévision standard en deux pas (b) Même vecteur de tension

Figure 4: Prévision variable de commande pour le convertisseur 3L-NPC avec un horizon en deux pas.

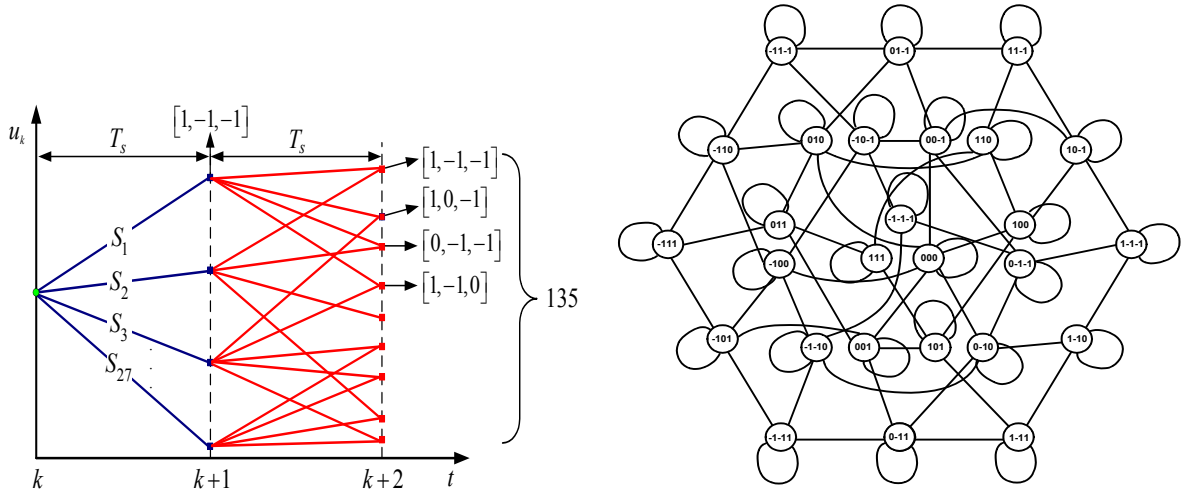

(a) Prévision variable de commande un deux pas (b) Commutation des transitions du convertisseur 3L-NPC

Figure 5: La méthode de commande proposée avec une variation de commutation.

- *Approche 3* : Nous proposons un schéma de commande basé sur le MPC qui intègre des informations liées à la stabilité dérivées d'une fonction de Lyapunov. Dans ce cas, nous imposons une méthode d'élagage pour les choix dans l'emsemble fini faisable de commandes basés sur la diminution de la fonction de Lyapunov comme illustré en Fig. 6.

$$V\left(\widetilde{i}_{gd},\widetilde{i}_{gq}\right)=\frac{1}{2}K_d\widetilde{i}_{gd}^2+\frac{1}{2}K_q\widetilde{i}_{gq}^2,\text{ avec dérivé }\dot{V}\left(\widetilde{i}_{gd},\widetilde{i}_{gq}\right)=K_d\widetilde{i}_{gd}\frac{d\widetilde{i}_{gd}}{dt}+K_q\widetilde{i}_{gq}\frac{d\widetilde{i}_{gq}}{dt}$$

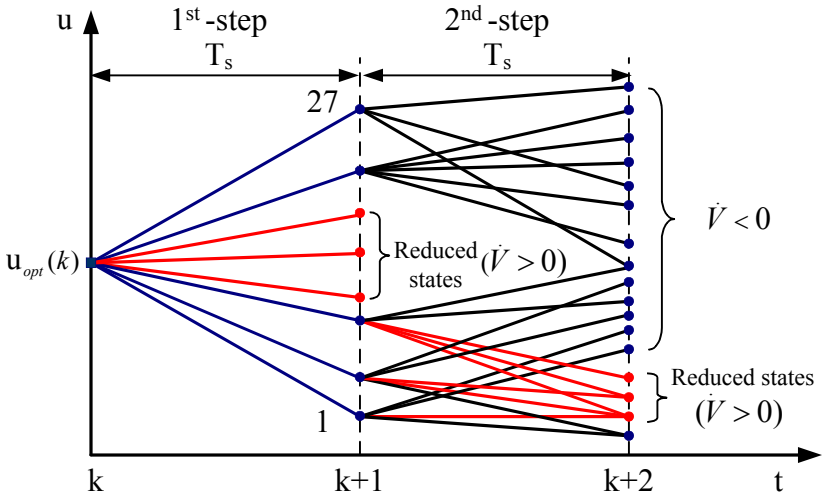

Figure 6: La commande prédictive à modèle utilisant la fonction de Lyapunov.

- *Approche 4* : Dans la commande de convertisseur, il est nécessaire d'insérer le temps mort dans les signaux de commutation pour éviter le court-circuit sur la source de tension continue de convertisseur. La tension pendant le temps mort et le délai de commutation est déterminé en fonction de l'état entre l'état de commutation précédent et l'état de commutation actuel et le signe du courant de phase comme indiqué dans la Fig. 7. Dans ce étude, nous concentrons sur la modélisation des erreurs causées par les retards de temps mort et de temps de commutation, puis nous proposons une nouvelle méthode de compensation pour améliorer le distortion de courant.

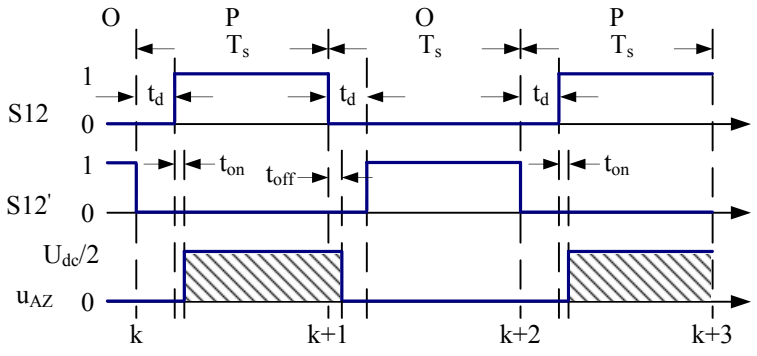

Figure 7: La tension réel de convertisseur u_{AZ} avec $i_{ag} > 0$.

6 Résumé de la thèse

L'introduction générale a presentée le système de génération éolienne, les objectifs et les contenus de la thèse. Le développement historique et l'état actuel de la commande des convertisseurs de puissance du système d'éoliennes ont également été résumés. Le reste de la thèse est organisé comme suit :

- **Chapitre 2: La commande prédictive à ensemble de commande fini pour l'onduleur 3L-NPC**

  Ce chapitre présente le développement du principe de la méthode FCS-MPC pour l'onduleur 3L-NPC avec une prédiction d'une et deux pas. Dans la première partie de ce chapitre, la topologie et le principe de fonctionnement du convertisseur 3L-NPC sont rappelés, puis le modèle mathématique du convertisseur 3L-NPC est établi. L'application de la stratégie FCS-MPC à l'onduleur 3L-NPC en fonction de la fonction coût est définie pour minimiser l'erreur entre les courants de référence et les valeurs prédites, équilibrer la tension de condensateur du bus continu et réduire la fréquence de commutation. Une approche de compensation pour le retard associé à la mise en œuvre numérique et la réduction du coût de calcul est présentée. En outre, pour vérifier la performance dynamique, une comparaison entre le contrôleur de courant linéaire avec la modulation vectorielle des tensions (PI-SVM) et FCS-MPC est fournie dans la dernière section de ce chapitre. La performance des stratégies proposées est évaluée en avec des simulations dans le domaine temporel.

- **Chapitre 3: Commande directe de la puissance basée sur la commande prédictive par modèle pour l'onduleur 3L-NPC connecté au réseau**

  La mise en œuvre et la commande d'un onduleur 3L-NPC connecté au réseau utilisant FCS-MPC est l'objectif principal de ce chapitre. Le modèle de prédiction de puissance est synthétisé en utilisant un modèle dynamique de l'onduleur 3L-NPC connecté au réseau en fonction de l'orientation du flux virtuel ou de la tension du réseau. Le principe du système de commande proposé est d'utiliser les valeurs prédites du flux virtuel, du courant du réseau et des tensions du condensateur de liaison pour toute configuration possible des vecteurs de tension. Les puissances actives et réactives peuvent être estimés en fonction du flux virtuel et du courant du réseau. Une fonction de coût est utilisée pour obtenir le profil prévu qui minimise l'erreur entre les puissances actives et réactives et leurs références, équilibre la tension du condensateur de liaison courant continu et réduit la fréquence de commutation. Certaines méthodes pour réduire le charge de calcul sont présentées dans

ce chapitre. En outre, les résultats de simulation basés sur Matlab/Simulink sont présentés et une comparaison avec la méthode classique de commande directe de la puissance avec contrôleur linéaire PI et la modulation vectorielle (DPC-SVM) est analysée.

- **Chapitre 4: Commande directe de la puissance basée sur la commande prédictive par modèle pour GADA alimenté par un onduleur 3L-NPC**

  Ce chapitre propose une stratégie de commande directe de la puissance basé sur la commande prédictive par modèle pour GADA alimenté par un onduleur 3L-NPC. Tout d'abord, le principe de fonctionnement de GADA est présenté, puis le modèle d'onduleur 3L-NPC connecté à GADA est établi. Deuxièmement, la fonction de coût associée aux objectifs de commande qui suivent les puissances actives et réactives, maintient la tension du condensateur du bus continu équilibrée et réduit la fréquence de commutation, la tension en mode commun est définie. Enfin, afin de valider l'efficacité de la méthode de contrôle proposée, les résultats de la simulation dans différentes conditions de variation de vitesse, de puissance et de paramètres du vent sont présentés et comparés avec une commande de puissance et une modulation vectorielle (DPC-SVM). Les résultats obtenus sont fournis pour confirmer et valider l'efficacité des stratégies de commande proposées.

- **Chapitre 5: Modèle de commande de puissance prédictive basée sur la fonction de Lyapunov pour le convertisseur 3L-NPC en opposition**

  Comme déjà résumé dans les chapitres 2, 3 et 4, la méthode FCS-MPC est une alternative intéressante pour commander les convertisseurs de puissance et les entraînements électriques. Cependant, la stabilité de cette stratégie reste un problème ouvert. Dans ce chapitre, afin de tenir compte des problèmes de stabilité, nous proposons un schéma de commande predictive pour asservir directement la puissance, ameliorer avec l'intégration des contraintes de stabilité d'une fonction de Lyapunov. En outre, la méthode proposée peut réduire la charge de calcul par rapport à la méthode conventionnelle FCS-MPC, permettant la mise en œuvre en temps réel avec des horizons de prédiction étendus. Afin de montrer l'efficacité de la stratégie de commande proposée, différents scénarios de long durée ont été réalisés en simulation. Les résultats de la simulation indiquent que la technique de contrôle proposée présente une bonne performance et une bonne robustesse par rapport aux variations des paramètres de la machine tout en réduisant considérablement le coût de calcul.

- **Chapitre 6: Modèle de commande de puissance prédictive avec compensation de temps mort pour le convertisseur 3L-NPC en opposition**

  Ce chapitre présente une nouvelle stratégie de compensation de commande prédictive de modèle pour convertisseur 3L-NPC afin de surmonter l'effet de temps mort des dispositifs de commutation. Le problème principal est le temps mort inclus pour éviter le court-circuit dans l'onduleur. Il est démontré qu'en prenant en compte les temps morts dans le modèle, il est possible de diminuer ses effets. Dans cette étude, nous nous concentrerons sur la modélisation des erreurs causées par les retards de temps mort et de commutation induits par le mécanisme de commutation physique. Avec cette approche, le modèle pour prédire la tension de sortie de l'onduleur et la tension du point neutre prend en compte le temps mort et le temps d'activation/désactivation du convertisseur pour compenser ses effets. Afin de démontrer la faisabilité et l'efficacité du schéma proposé, les résultats de la simulation seront fournis et comparés aux cas non compensés en utilisant Matlab et la boîte à outils SimPowerSytem.

- **Chapitre 7: Conclusions**

  Un résumé des contributions de cette thèse et les éventuelles extensions futures de la recherche sont présentés dans ce chapitre.

Contents

List of Figures

List of Tables

Acronyms and Symbols

Acronyms

3L-NPC	Three-level neutral-point clamped
BTB	Back-to-back
CCS-MPC	Continuous control set model predictive control
CHB	Cascaded H-bridge
CLF	Control Lyapunov function
CMV	Common-mode voltage
DC	Direct current
DFIG	Doubly fed induction generator
DPC	Direct power control
DPC-SVM	Direct power control with space vector modulation
DTC	Direct torque control
EMF	Electromotive force
FACTS	Flexible alternating current transmission systems
FC	Flying capacitor
FCS-MPC	Finite control set model predictive control
FFT	Fast Fourier Transform
FOC	Field oriented control
GPC	Generalized predictive control
GSC	Grid side converter
GWEC	Global wind energy council
IGBT	Insulated Gate Bipolar Transistor
ISS	Input to State Stability
LQR	Linear quadratic regulator
LUT	Lookup-table
M2PC	Modulated model predictive control

MAPE	Mean absolute percentage error
MPC	Model predictive control
MPDPC	Model predictive direct power control
MPDTC	Model predictive direct torque control
MPPC-VF	Model predictive power control based on virtual flux
MPPT	Maximum power point tracking
NPC	Neutral point clamped
OSS-MPC	Optimal switching sequence model predictive control
OSV-MPC	Optimal switching vector model predictive control
PC	Predictive control
PDPC	Predictive direct power control
PF	Power factor
PI	Proportional-Integral
PI-SVM	Proportional-integral controller with space vector modulation
PLL	Phase locked loop
PMSG	Permanent magnet synchronous generator
PWA	Piecewise affine
PWM	Pulse width modulation
QP	Quadratic program
RMS	Root mean square
RSC	Rotor side converter
SCIG	Squirrel-cage induction generator
SFO	Stator flux oriented
SMC	Sliding mode control
SMPC	Switched model predictive control
SO	Symmetric optimum
STATCOM	Static synchronous compensator
SVM	Space vector modulation
SVO	Stator voltage oriented
THD	Total harmonic distortion
VFOC	Virtual flux-oriented control
VOC	Voltage-oriented control
VSF-MPC	Variable sampling frequency model predictive control
VSP-MPC	Variable switching point model predictive control
WRIG	Wound rotor induction generator
WTS	Wind turbine system

Symbols

$[P]$, $[O]$, $[N]$	Switching states of three-level neutral-point clamped inverter
$\hat{U}_g$	Magnitude of the grid voltage
λ_{cm}	Weighting factor for common-mode voltage reduction
λ_{dc}	Weighting factor of the capacitor voltage balancing
λ_n	Weighting factor for switching frequency reduction
ω	Angular frequency of the grid
ω_s, ω_m, ω_r	Synchronous, rotor and slip angular frequencies of generator
ψ_g	Virtual flux of the grid
ψ_{inv}	Virtual flux of the inverter
ψ_r	Rotor flux linkage vector of generator $\psi_r = [\psi_{ra}, \psi_{rb}, \psi_{rc}]$
ψ_{ra}, ψ_{rb}, ψ_{rc}	Three-phase rotor fluxes of generator
ψ_s	Stator flux linkage vector of generator $\psi_s = [\psi_{sa}, \psi_{sb}, \psi_{sc}]$
ψ_{sa}, ψ_{sb}, ψ_{sc}	Three-phase stator fluxes of generator
θ	Synchronous angle in the stationary frame
θ_r	Angle between the rotor and stator flux of generator
θ_s, θ_m	Stator flux, rotor angles in the stationary frame of generator
ε_v	Stabilizing constraint
φ_g	Grid power factor angle
C	DC-link capacitor
e_a, e_b, e_c	Three-phase electromotive forces
f	Frequency of the grid
f_r	Rotor frequency of generator
f_{sp}	Sampling frequency of model predictive control
f_s	Stator frequency of generator
f_{svm}	Sampling frequency of space vector modulation
f_{sw}	Average switching frequency per semiconductor
g	Cost function
H_x, K_x	Coefficient of each inverter branch with the index $x \in \{a, b, c\}$
i_a, i_b, i_c	Three-phase load currents
i_{ag}, i_{bg}, i_{cg}	Three-phase grid currents
i_{dc1}	Neutral current of three-phase
i_{dc1a}, i_{dc1b}, i_{dc1c}	Neutral current of one phase
i_g	Grid current $i_g = [i_{ag}, i_{bg}, i_{cg}]$
I_g	RMS value of the grid phase current
i_r	Rotor current vector referred to the stator of generator $i_r = [i_{ra}, i_{rb}, i_{rc}]$

i_{ra}, i_{rb}, i_{rc}	Three-phase rotor currents referred to the stator of generator
i_s	Stator current vector of generator $i_s = [i_{sa}, i_{sb}, i_{sc}]$
i_{sa}, i_{sb}, i_{sc}	Three-phase stator currents of generator
J	Inertia of the mechanical axis
K	Ratio of the stator voltage to the rotor voltage of generator
K_d, K_q	Positive gains of Lyapunov function
L	Load inductance
L_f	Filter inductance
$L_{s\sigma}$, $L_{r\sigma}$	Stator, rotor leakage inductance
L_s, L_r, L_m	Stator, rotor self-inductance and mutual inductance
n_c	Number of switch changes in inverter
$n_{sw_{x1}}$, $n_{sw_{x2}}$	Number of switching changes in the gating signals of each upper switch
p	Number of pole pairs of generator
P_g	Grid active power
P_m	Mechanical input power to wind generator
P_r	Rotor active power of generator
P_s	Stator active power of generator
Q_g	Grid reactive power
Q_r	Rotor reactive power of generator
Q_s	Stator reactive power of generator
R	Load resistance
R_f	Filter resistance
R_r	Rotor resistance referred to the stator of generator
R_s	Stator resistance of generator
s	Slip of generator
S_x	State of each inverter branch with the index $x \in \{a, b, c\}$
t_d	Dead-time of the converter
T_{em}	Electromagnetic torque of generator
T_{load}	External torque applied to the mechanical axis
t_{off}	Turn-off time of switching device
t_{on}	Turn-on time of switching device
T_s	Controller sampling time
T_{sim}	Simulation time
u_1, u_2, u_3	Voltages between the midpoint of the branch and negative voltage

u_{ag}, u_{bg}, u_{cg}	Three-phase grid voltages
u_{AZ}, u_{BZ}, u_{CZ}	Phase to neutral voltages of inverter
u_{C1}, u_{C2}	DC-link capacitor voltages of inverter
u_{cm}	Common-mode voltage
U_{dc}	DC-link voltage
u_g	Grid voltage $u_g = [u_{ag}, u_{bg}, u_{cg}]$
U_g	RMS value of the grid phase voltage
u_{inv}	Inverter output voltage vector
u_{opt}	Optimal control sequence of three-level inverter
u_r	Rotor voltage vector of generator $u_r = [u_{ra}, u_{rb}, u_{rc}]$
u_{ra}, u_{rb}, u_{rc}	Three-phase rotor voltages referred the stator of generator
u_s	Stator voltage vector of generator $u_s = [u_{sa}, u_{sb}, u_{sc}]$
u_{sa}, u_{sb}, u_{sc}	Three-phase stator voltages of generator
u_z	Neutral-point voltage
V	Lyapunov function
V_f	Saturation voltage of IGBT
V_{fd}	Forward voltage of diode

Superscripts

$*$	Reference value
$\sim$	Error value
$\wedge$	Estimated value
dq	Synchronous reference frame
p	Predicted value
r, DQ	Rotor reference frame
s	Stator reference frame

Subscripts

α, β	α, β axis
d, q	d, q axis
D, Q	D, Q axis
s, r	Stator, rotor

Chapter 1

Introduction

1.1 Overview of wind turbine system

To satisfy the high demand for electricity and reduce greenhouse gas emissions, renewable energy systems and especially wind energy have attracted interest in recent years. According to the global wind energy council (GWEC), the wind power capacity has grown fast from 2000 to 2015 with around 63 GW installed only in 2015. Fig. 1.1 shows the annual global cumulative installed wind capacity from 2000 to 2015 [1]. In fact, the global installed wind power capacity reached 432 GW (148 GW in Europe, increased 6.3% more than in the previous year) at the end of 2015, indicating that the wind power is an essential role in the modern energy supply system [1]. By the end of 2015, more than 80 countries are using wind energy on a commercial basis and approximately 26 countries have more than 1 GW cumulative installed wind power capacity, including 17 countries in Europe, 4 in Asia-Pacific (China, India, Japan, Australia), 4 in the Americas (Brazil, Canada, United States, Mexico) and 1 in Africa (South Africa) [2]. The aim is to achieve nearly 2000 GW by 2030, supplying up to 19% of the global electricity [3]. Moreover, the wind turbine connected to the grid plays the important role for maintaining and improving the electrical performances of the overall system.

Besides the quick growth in the total installed capacity, the size and capacity of individual wind turbine are also increasing in order to reduce the price per generated kWh and increase the efficiency of wind energy conversion. Recently, most of the major wind turbine manufactures are developing large wind turbine in the 1.5-6 MW range [4],

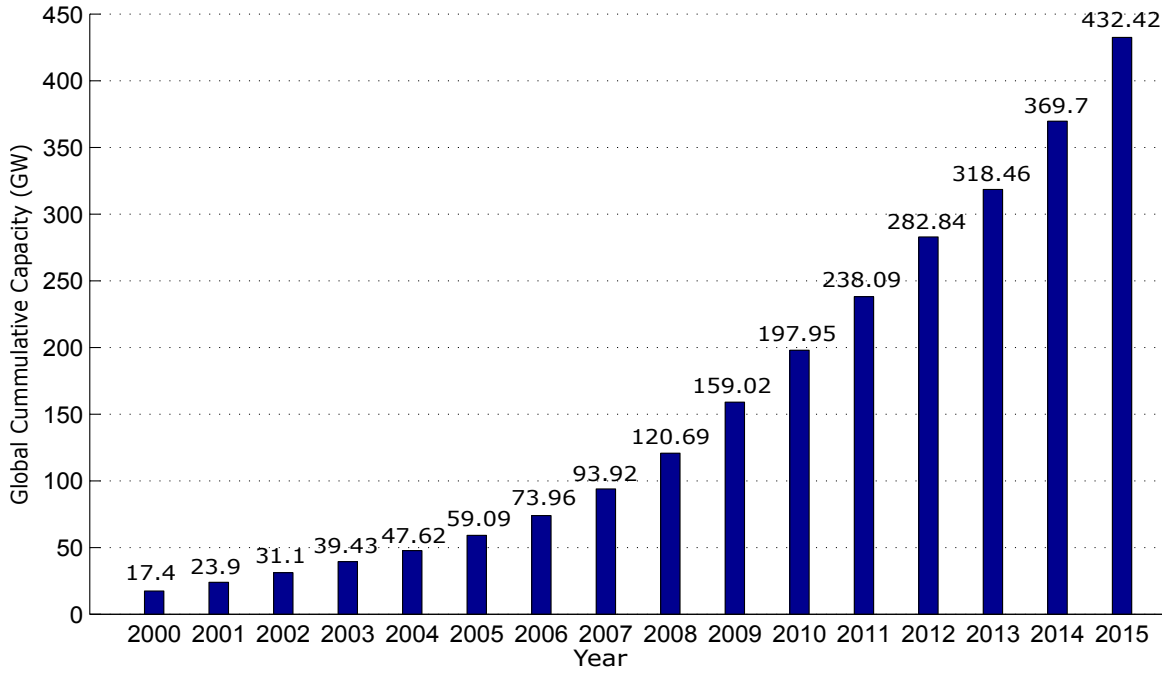

Figure 1.1: Annual global cumulative installed wind power capacity from 2000 to 2015
[source: Global Wind Energy Council (GWEC)].

[5]. Based on the rotational speed and the type of power electronics, wind turbine system (WTS) can be classified into four main groups as follows:

- **Type 1**: Fixed speed WTS with squirrel-cage induction generator (SCIG).
- **Type 2**: Partial variable speed WTS with wound rotor induction generator (WRIG).
- **Type 3**: Variable speed WTS with partial scale power converter and doubly fed induction generator (DFIG).
- **Type 4**: Variable speed WTS with full scale power converter and permanent magnet synchronous generator (PMSG), SCIG or WRIG.

The early technology used in wind turbines was based on squirrel-cage induction generator (SCIG) directly connected to the grid (Fig. 1.2). The speed range of the generator is small so that this configuration is often known as a fixed speed wind turbines. The advantages of this concept are the simple and cheap construction. However, the main disadvantage of this topology is the system delivers the rated power to the grid only at a given wind speed, leading to low energy conversion efficiency at other wind speed [5]. Another drawback of this topology is that a reactive power compensator such as capacitor

bank is required to compensate the reactive power demand by the asynchronous generator, leading to expensive cost.

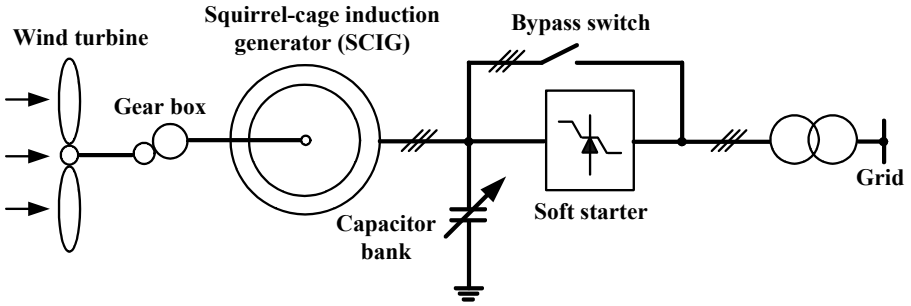

Figure 1.2: Fixed speed wind turbine with direct grid connection.

The partial variable speed consists of a wound rotor induction generator (WRIG) and a variable rotor resistance as shown in the Fig. 1.3. The stator of WRIG is directly connected to the grid by the soft starter, whereas the rotor winding is connected with external rotor resistance through the converter. The improvement of this concept is that rotational speed of the wind turbine can be adjusted about 10% of synchronous speed of generator, leading to an increased energy conversion efficiency. However the power loss dissipating in the rotor resistors and external compensation required remains a significant drawback for this concept.

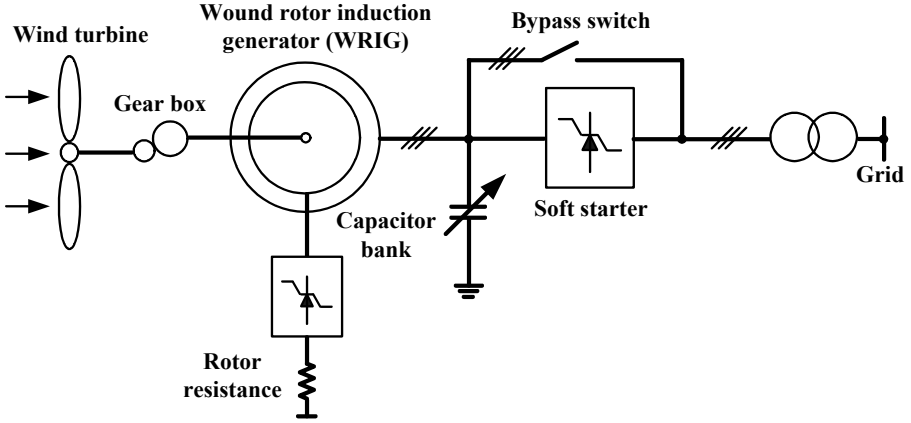

Figure 1.3: Partial variable speed wind turbine with variable rotor resistance.

Currently, the technology has developed toward variable speed. Variable speed wind turbines can be classified into two most common types based on the types of generators and power rating of the converter with respect to the total power of the system. The configuration of doubly fed induction generator (DFIG) equipped with partial scale power converter and the full scale power converter configuration. The first one (Fig. 1.4) has gain interest in recent years. In this configuration, the stator windings of DFIG are directly connected to the power grid, while the rotor windings are connected to the power grid via

a back-to-back (BTB) converter. The power converter consists of two power converters, the rotor side converter (RSC) and the grid side converter (GSC), which are controlled independently of each other. A DC-link voltage is placed between two converters for energy storage in order to reduce the variation of DC voltage. This concept represents an attractive solution thanks to the important features: allows the power electronic converter to deal with approximately 30% of the generator power, it reduces the converter cost as well as the power losses. Furthermore, it is suitable for variable speed wind turbine which gives the possibility to produce the maximum possible power on a wide range of variation of the wind speed. By using this configuration, it is possible to allow both bidirectional active and reactive power flow from rotor side to grid [6–9]. This capability allows DFIG to operate at both the super-synchronous mode where power flows from the rotor to the grid, and the sub-synchronous mode where the power flows from the grid to the rotor. Therefore, soft starter and reactive power compensator are not needed.

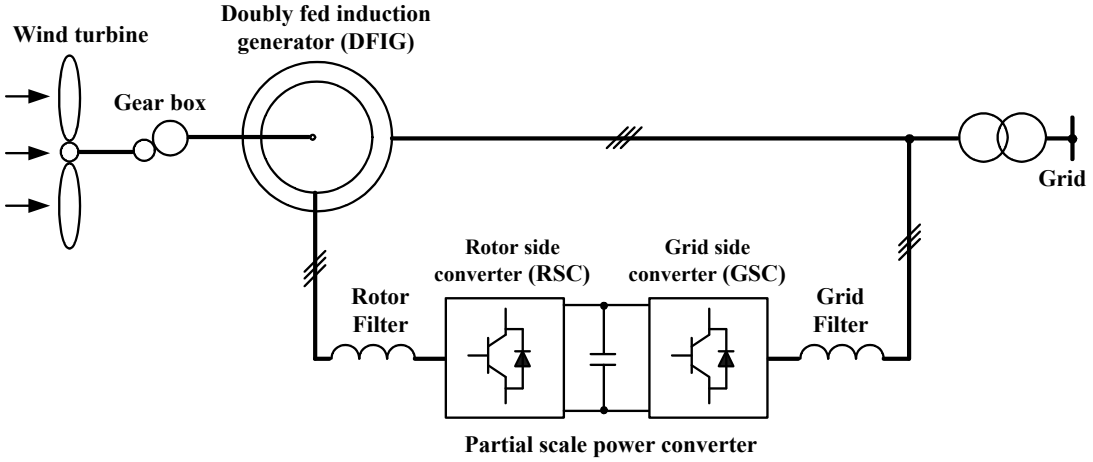

Figure 1.4: Variable speed wind turbine with doubly fed induction generator.

The variable speed wind turbine with full scale power converter configuration is composed of a permanent synchronous generator (PMSG) or squirrel-cage induction generator (SCIG) or WRIG and back-to-back converter as depicted in Fig. 1.5. The elimination of the slip rings, full power and speed controllability as well as better grid support ability are the main advantages compared with the DFIG configuration. However, the main drawback of this concept is the large scale power converter, which leads to have high power electronic component as well as the higher power losses in the converter. Therefore, this topology is suitable for next generation MW-level wind turbines with medium voltage level and high power range from 7 MW as long as the control algorithms are designed to minimize the above losses [4].

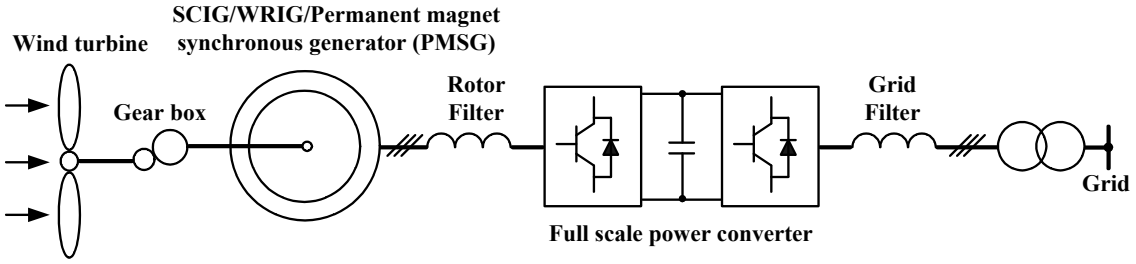

Figure 1.5: Variable speed wind turbine with full scale power converter.

The main features and drawbacks of all four types of wind turbine system configurations are summarized in Table 1.1. To demonstrate the popularity of each WTS configuration in the wind energy industry, the top 10 wind turbine manufacturers in 2014 and their priority technologies are illustrated in Fig. 1.6. The topology of variable wind speed using DFIG is the highest market share of the dominating technologies in wind turbine manufactures with power range in 1.5-6 MW and occupies about 50% of the wind energy market [6], [8], [9]. A few examples of commercial solutions are: Acciona AW 1.5-3 MW, Alstom ECO 1.67-3 MW and General Electric GE Energy 1.5-2.75 MW [6].

Table 1.1: Summary of the four types of wind turbine system configurations [68].

	Fixed speed	**Partial variable speed**	**Variable speed**	
Turbine type	Type 1	Type 2	Type 3	Type 4
Generator	SCIG	WRIG	DFIG	SCIG, PMSG
Speed Range	1%	10%	30%	100%
Power converter	Not Required	Diode+Chopper	BTB converter	BTB converter
Converter Capacity	0%	10%	30%	100%
Soft Starter	Required	Required	Not Required	Not Required
Reactive Power Compensation	Required (Capacitors)	Required (Capacitors)	Not Required	Not Required
Aerodynamic Power Control	Active Stall Stall, Pitch	Pitch	Pitch	Pitch
MPPT Operation	Not Possible	Limited	Achievable	Achievable
Current Market Penetration	Few or No Installations	Few or No Installations	Highest Share ($> 50\%$)	2^{nd} Highest Share
Example Commercial WT	Vestas V82 1.65 MW	Suzlon S88 2.1 MW	REpower 6M 6.0 MW	Enercon E-126 7.5 MW

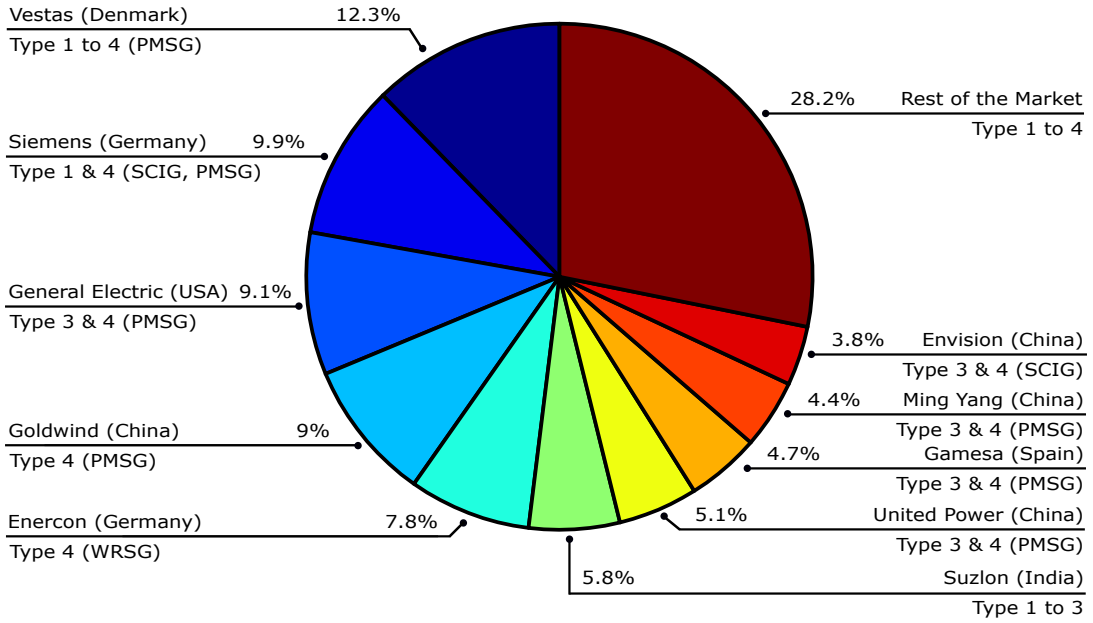

Figure 1.6: Top 10 wind turbine manufacturers in 2014 [17].

1.2 State of the art of power electronics for wind turbine system

Power electronics have changed rapidly in the recent years due to the development of semiconductor devices. Their integration in the conversion schemes is playing important role in the improvement of the performance and the power for wind turbines. Many possible technical solutions of wind turbine system have been proposed. As the interface between the DFIG and grid in the system, two-level converter is usually used as a BTB structure for the wind turbine system. However, it becomes difficult for a single two-level BTB converter topology to achieve acceptable performance in wind turbine system with high power. Indeed, it is impossible to increase power due to voltage limit imposed on electronic components. And the output voltage of the two-level converter has high dv/dt, requiring bulky output filter to limit the voltage gradient and reduce the harmonics level [5], [10].

With the abilities to achieve high voltage level, high power and smaller common mode voltage, the multilevel converters are becoming preferred solution in the wind turbine system. In general, three different topologies have been proposed: diode-clamped (neutral point clamped), capacitor-clamped (flying capacitor) and cascaded H-bridge (CHB). The diode-clamped (NPC) converter can achieve more voltage level output and less dv/dt compared to the two-level topology, reducing the total harmonic distortion (THD) of

output voltage and current. Furthermore, the capacity of the converter can be increased thanks to a decreased voltage applied to each component. The neutral point voltage deviation of the DC-link voltage is a main drawback, but this problem has been studied and improved for several years. Consequently, the three-level neutral-point clamped (3L-NPC) back-to-back converter (Fig. 1.7) is considered a good solution for the wind energy conversion systems thanks to its advantages in terms of economy, the complexity of control and performance [10–13]. Indeed, this topology is one of the most commercialized multilevel topologies available in the market [8].

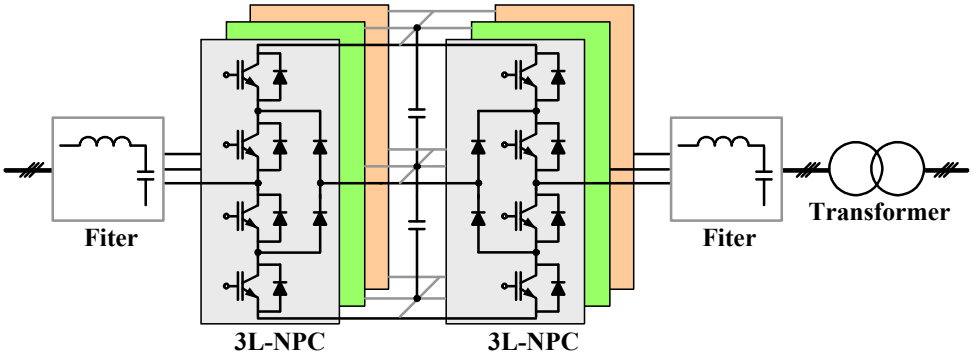

Figure 1.7: Three-level Neutral-Point Clamped back-to-back converter for wind turbine [5].

Similar to the diode-clamped converter, the flying capacitor (FC) converters (Fig. 1.8) are also producing the output voltage with reduce dv/dt and THD. The redundant switching configurations which provides more possibilities to control the voltage of DC-link capacitors is the main advantage of this topology. However, it has some limitations, including the following: a large number of DC capacitor with separate pre-charge circuits, the complexity of the control in charge with the tracking of the voltage levels for all of the capacitors and higher switching frequency to keep the capacitors properly balanced [12].

The cascaded H-bridge converter can achieve similar output performance than the diode-clamped converter, as shown in Fig. 1.9. The main advantage of the CHB converter topology is that it can be easily extended for higher voltage and higher power levels. Nevertheless, comparing with the standard transformer used for the NPC converter, the cascaded H-bridge needs a phase shifting isolation transformer to acquire isolated DC supplies, and in consequence this topology is expensive and voluminous.

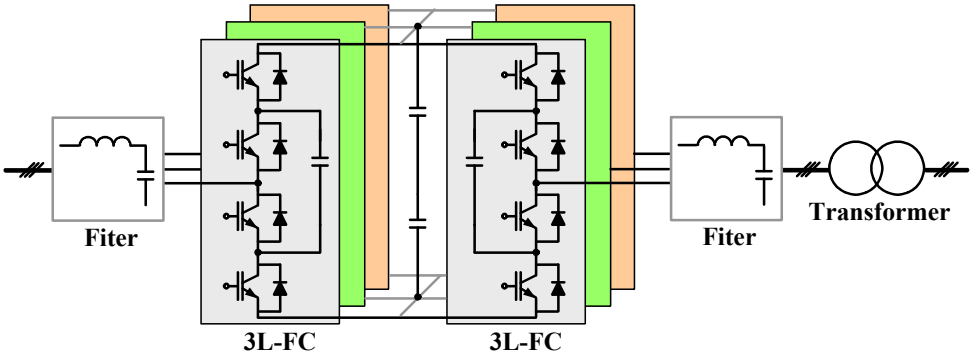

Figure 1.8: Three-level Flying capacitor back-to-back converter for wind turbine [5].

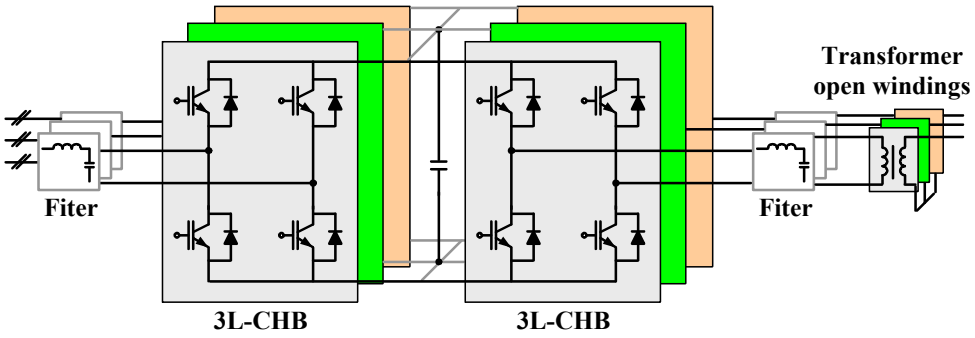

Figure 1.9: Three-level Cascaded H-bridge back-to-back converter for wind turbine [5].

1.3 Control of power electronic converters for wind turbine system

The general control architecture of the variable speed wind turbine consists of three principal parts: wind turbine control, rotor side control and grid side control (Fig. 1.10). Wind turbine control provides active power reference (P_{s_ref}) or electromagnetic torque reference for control the DFIG. This reference value is calculated based on the measured wind speed based on lookup-table which is predetermined in order to determine the optimum power corresponding to the rotational speed of wind turbine. A maximum power point tracking (MPPT) control is needed in order to maximize power output of the wind turbine by controlling the turbine pitch angle. The rotor side converter (RSC) generates a three-phase voltage with variable amplitude and frequency to control the generator torque or active power (P_s) and reactive power (Q_s) exchanged between the stator and grid. The grid side converter (GSC) controls the active power (P_{gsc}) exchanged bidirectionally between the rotor of the machine and the grid and can also influences the

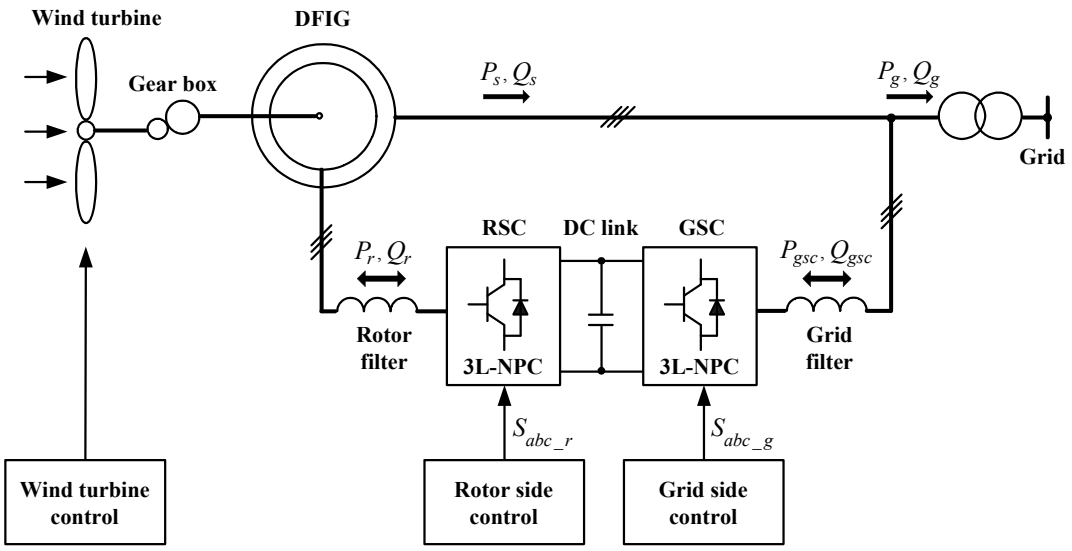

Figure 1.10: The control scheme for DFIG based wind turbines with 3L-NPC back-to-back converter [5].

power factor. The active power can be transferred between the rotor and the DC-link voltage and the control goal is to calculate the active power exchanged with the grid to keep the DC-link voltage constant. Close to unity power factor operation is usual for GSC, but it is also possible to control the reactive power (Q_{gsc}) flow between the converter and the grid, independently of the RSC [9], [14],[15]. In particular, when the low voltage ride through occurs, the grid side controller must remain the reactive power support to the grid in order to help the grid voltage recovery during and just after the clearance of grid faults. The filter on the rotor side helps to reduce harmonic distortion of the generator currents and voltages, whereas the grid filter helps to acquire harmonic requirements specified by the grid codes.

The overall control system of DFIG based wind turbine is illustrated in Fig. 1.11. RSC and GSC can be considered as two controllable voltage sources. The objective of the RSC is to supply voltages to the rotor side part of the DFIG such that the grid side active and reactive powers are maintained according to the power tracking and desired power factor. While for the GSC, it mainly controls the DC-link voltage but also provides limited reactive power similar to the operation of a static synchronous compensator (STATCOM), independently of the generator operation, allowing the performance of voltage support towards the grid. With a constant DC-link voltage the active power through the RSC will be the same as that through the GSC.

The DC-link voltage can be expressed in terms of the power from the RSC and the power leaving the GSC to the grid. The convention of P_r follows the rotor current

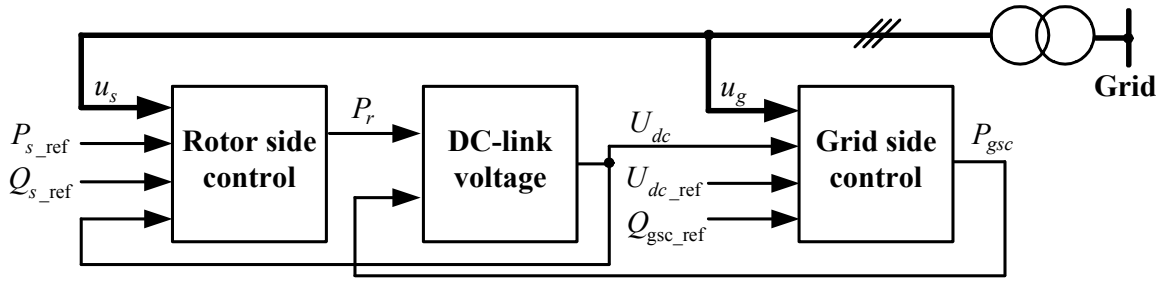

Figure 1.11: The block diagram of overall control system for DFIG.

convention, where injection to the rotor current is positive. The convention of P_{gsc} follows the GSC current convention, where from the GSC to the grid is positive. Thus, the dynamic equation of the DC-link voltage can be expressed as follows:

$$\frac{1}{2}C\frac{dU_{dc}^2}{dt} = -P_r - P_{gsc}. \tag{1.1}$$

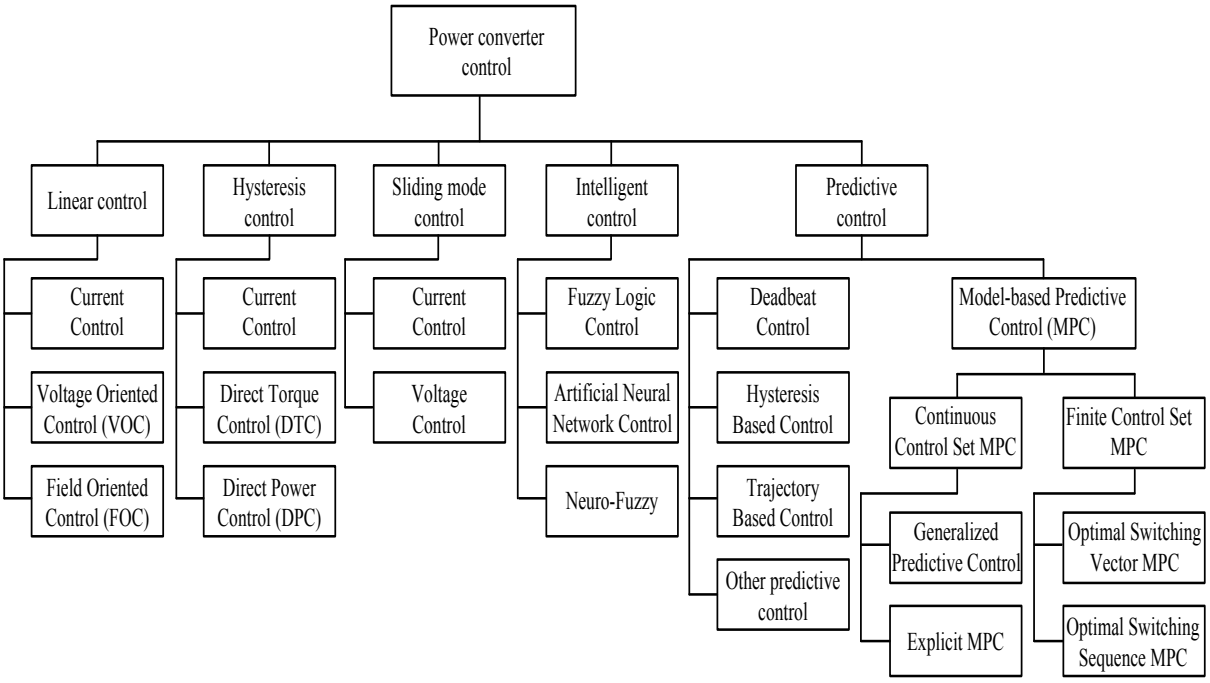

Figure 1.12: Classification of control techniques used in power converters.

Several methods have been proposed to control the RSC and GSC for wind energy system. The control in power electronics and electrical machine can be divided into five main groups: linear control, hysteresis control, sliding mode control, intelligent control and predictive control as shown in Fig. 1.12 [16–18]. Most of the existing control methods use the classical vector control based on the orientation of the voltage (voltage oriented

control-VOC) [15, 19–22] or the field oriented control (FOC) [9, 23, 24] which guarantee the dynamics and static performance via internal current control loops with linear proportional-integral (PI) controller. However, it has a low dynamic performance and its performances depend on the accurate machine parameters and the quality of the current control loop, which is strongly influenced by unbalanced grid voltage. Next, a complex modulation technique such as pulse width modulation (PWM) or space vector modulation (SVM) along with the DC-link capacitor voltage balancing is required to apply these techniques to 3L-NPC converters. To solve this issue, several approaches have been proposed such as SVM with the redundant switching states selection [25] and PWM with zero sequence voltage injection [26].

Recently, a hysteresis control especially direct torque control (DTC) [25, 27, 28] and direct power control (DPC) [14, 29, 30] have been proposed to improve the controller performance. The DTC controls the torque and rotor flux of the machine, while DPC controls the active and reactive powers. These methods used the hysteresis control and the inverter switching states, selected from a lookup-table (LUT) based on the errors between the reference and estimated values (torque and flux in DTC; active and reactive powers in DPC), and voltage or virtual flux position. Therefore, these methods do not require the current control loops and space vector modulation. Comparing with the linear PI controller, these methods have a fast dynamics response, no requirement for decoupling between control of the active and reactive components, and leads to a better dynamics. Nevertheless, the drawback of LUT is that it has large active and reactive power ripple and switching frequency variation. To overcome this problem, a space vector modulation was introduced to DPC structure [31], [32]. Furthermore, a high sampling frequency is used for DTC/DPC to guarantee acceptable steady-state and dynamic performances. With both linear control and hysteresis techniques, it is not easy to include the system constraints and technical requirements such as maximum current, total harmonic distortion, common-mode voltage and switching frequency.

Sliding mode control (SMC) [33–35] is an advanced control technique which is suitable for linear and non-linear system with uncertainties. The control variable is discontinuous and follows a predefined trajectory. With this method, it features simple implementation, attractive disturbance rejection properties, strong robustness and fast response even during the system parameters variations and external disturbances compared with the classical control technique.

The fuzzy logic [36], [37], artificial neural networks [38–40] and neuro-fuzzy [41] are part of the class of intelligent control methods. These methods use the membership

functions of the fuzzy logic controller or the artificial neural networks for create switching signals of the power converter. The main advantage of these methods is the ability to provide a control signal without an exact converter model, thus it is useful for the characteristics of the power converter which are nonlinear in nature. However, the quality of performance depends on the experience, accurate knowledge about the operation or behavior of the system.

In the recent years, the predictive control emerged as a major control technique which is applied for power converters and electrical drives. The predictive control (PC) uses the system model to predict the future behavior of the process for a specific control variable and then obtain the optimal actuation based on the predefined optimization criteria. The family of predictive control techniques can be divided into five categories: deadbeat control, hysteresis based control, trajectory based control, model predictive control and several other predictive control strategies which differ with respect to the optimal decision making evaluation or the implementation of the selected strategy.

A deadbeat predictive control uses a model of the system to calculate the required control variable that cancels the error between the control variable and the reference input [42], [43]. The switching signals are applied to the power converters by using the PWM/SVM modulator. This control strategy provides a fast dynamic response but the system parameter variations and perturbations can deteriorate the control performance. In addition, it is difficult to incorporate the nonlinearities and constraints of the system.

The hysteresis and trajectory based PC techniques work on the principle of selecting the controlled variables within the boundaries of a hysteresis area or shortest trajectory between the initial state and the desired state [16, 42, 44]. Thus, these methods don't require the modulation block and apply the switching states directly to the converter.

Nowadays, model predictive control (MPC) is recognized as a simple and powerful control strategy to control power converters and electrical drivers thanks to its advantages such as simple to apply in multivariable systems and consider nonlinearities and constraints in the control system, and present a fast dynamic response. The working principle of MPC is based on using the mathematical model to predict the system behavior and then minimize the cost function predefined to fulfill the control objectives. The MPC applied to power converters has been classified into two major groups: Continuous Control Set MPC (CCS-MPC) and Finite Control Set MPC (FCS-MPC). In Continuous Control Set MPC, the control variables are continuous, wherein the optimization problem can be solved online generally by using quadratic program (QP) [45–48] or taking the

form of a generalized predictive control (GPC) [49] or can even be precomputed offline by explicit solution with more complex affine structures (Explicit MPC) [50], [51] to reduce computational burden. In the first group, it needs a modulator to generate the switching states from the continuous output of the predictive controller, leading to a fixed switching frequency. However, the main drawback of CCS-MPC is that the nonlinearities taken in the model bring to a complex optimization problem, difficult to be solved on line using a conventional digital hardware platform.

On the other hand, with Finite Control Set MPC, the computational time of optimization problem is reduced by only evaluating the cost function with finite number of switching states and choosing the control input that achieve the lowest cost function [16, 44, 52–54]. The FCS-MPC is an attractive alternative control technique due to its advantages:

- Takes into account the discrete nature of the power converter.
- Provides a fast dynamic response and good steady state performance.
- Is simple to apply in multivariable systems.
- The optimization is simplified due to finite number of switching states.
- Can be applied to a wide range of power converter and drive applications.
- The nonlinearities and constraints of the system can be incorporated directly into the controller.
- Compensate the computational delay and dead-time.
- Simple concept and easy for the implementation.

In general, the FCS-MPC can be divided into two types: Optimal switching vector MPC (OSV-MPC) and Optimal switching sequence MPC (OSS-MPC). With the first group, the optimal switching state is directly applied to the converter without a modulator, leading to a variable switching frequency. However, the switching frequency can be controlled by imposing a restriction in the cost function. In contrast, the OSS-MPC [55, 56] defines the optimal switching sequences (switching states and corresponding duty cycles) to be applied in the power converter during the next sampling period. Next, the switching sequence is conventionally implemented based on a space vector modulation, thus it produces a fixed switching frequency.

Recently, some novel control strategies of predictive control has been proposed to improve the controller performance for power converter topologies and drive application: predictive direct power control (PDPC) [57, 58], modulated MPC (M2PC) [59–61], variable sampling frequency MPC (VSF-MPC) [62, 63], switched MPC (SMPC) [64] and variable switching point MPC(VSP-MPC) [65–67].

With the FCS-MPC, all switching states must be evaluated for the cost function to obtain the optimal value. It is well known that choosing long prediction horizons, in general, gives better closed-loop performance than choosing one-step horizon. Unfortunately, the computational burden of solving optimization problems increases exponentially with the length of the prediction horizon. Consequently, despite the good performance that the FCS-MPC offers, there still remain some challenges that can be resumed by the main points:

- Requires a large amount of calculations, especially with high number of switching states and long prediction horizons.
- Operates with the variable switching frequency.
- The accuracy of the model has a direct impact on the quality of the controller.
- One of the main open problems is that the stability of the system has not been considered in the design procedure.

1.4 Finite control set model predictive control

1.4.1 Operating principle

The aim of the finite-set control method is to drive a system variable $x(t)$ which is determined by the control action $S(t)$ (usually the gate signals of the converter) as close as possible to a desired reference value $x^*(t)$. Due to a finite number of switching states S_i, with $i = 1, ..., n$, we can predict all possible system variables ($x^p(k+1)$) over a sampling period T_s based on the system model and measured values. Then, a cost function g which depends on the objective of the control can be defined. A typical example for cost function would be the absolute error between the predicted values and their references $g = |x^*(k+1) - x^p(k+1)|$. The evaluation of the cost function with n predictions will

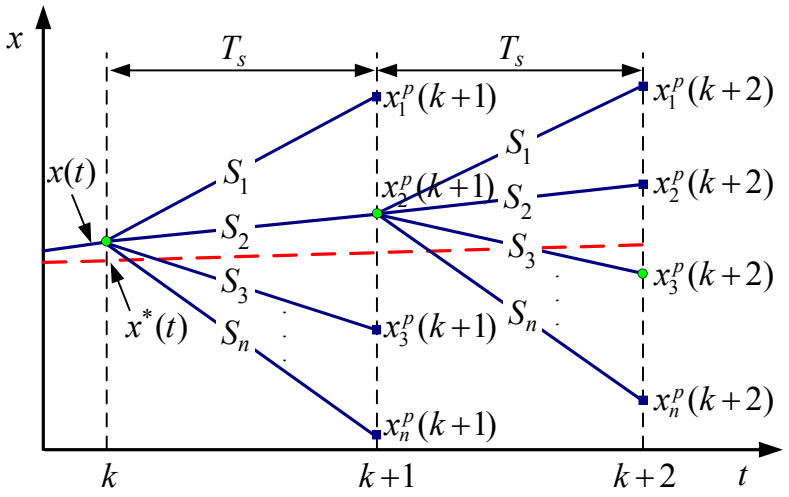

Figure 1.13: Operating principle of FCS-MPC [44].

lead to n different cost values. Finally, the optimal switching state that minimizes the cost function is selected and applied directly to the converter. The procedure of switching state selection has been illustrated in Fig. 1.13. The predicted value $x_2^p(k+1)$ is the closets to the reference $x^*(k+1)$, thus S_2 is selected and applied at instant $t = k$. Following the same way, S_3 is selected and applied in $t = k+1$.

1.4.2 Control strategy

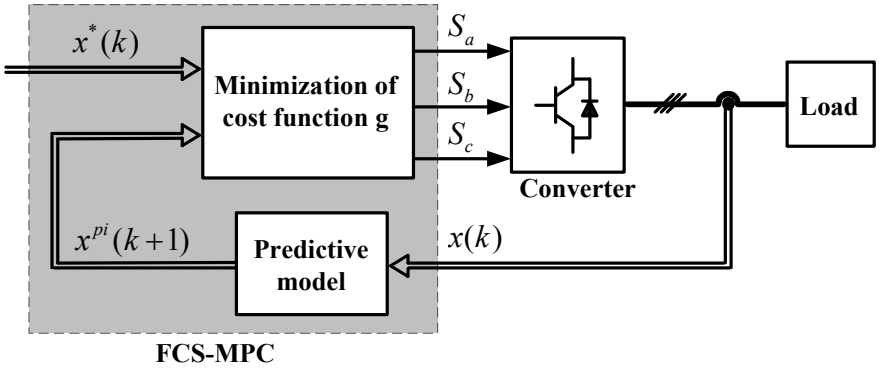

Figure 1.14: The control block diagram of FCS-MPC.

The block diagram of a general FCS-MPC control scheme is shown in Fig. 1.14 [16]. In summary, the FCS-MPC design is performed according to the following steps:

- **Step 1: Measurements**

  Obtain the required feedback signals for predictive model or reference calculation.

- **Step 2: Calculation and extrapolation of references**

  Calculate the reference control variable according to the specific application, then obtain the future values of the reference by using the extrapolation.

- **Step 3: Build a Continuous-Time models of the system**

  The modelling system is accomplished by deriving equations that describe the dynamic behaviour of the controlled variables generally based on a linear model as:

$$\frac{dx}{dt} = Ax + Bu, \tag{1.2}$$

  where x represents the variable to be controlled (voltage, current, flux, power) and u is control input (grid voltage, switching state, DC voltage).

- **Step 4: Build a Discrete-Time models of the system**

  A discrete-time model of the system is required to predict the behavior of the variables evaluated by the cost function. In order to discretize the system model, the first-order forward Euler method is used due to its simplicity. It also gives acceptable accuracy that is necessary for good performance. According to this approach, we have the discrete-time form of the system as follows:

$$\frac{dx}{dt} \simeq \frac{x(k+1) - x(k)}{T_s}, \tag{1.3}$$

  where T_s is the sampling time, $x(k+1)$ and $x(k)$ are the value of the controlled variable in the next sampling time and at the current state, respectively.

- **Step 5: Prediction of control variables**

  Predict the future value of the control variables based on the discrete-time models, measured values and all possible switching states of the converter.

- **Step 6: Minimize the cost function**

  As a final step, all values of predicted variables $x_i^p(k+1)$ are compared with their reference $x^*(k+1)$ using a cost function g as follows:

$$g = \left| x^*(k+1) - x_i^p(k+1) \right|, i = 1, ..., n. \tag{1.4}$$

  The goal of cost function optimization is to select the cost value g as close as possible to zero. The optimal switching state which minimizes the cost function is

chosen and then applied to the converter at the next sampling instant. Therefore, this method does not require a modulation block, which simplifies the system design.

1.5 Objectives

The aim of this thesis is to elaborate new control strategies based on model predictive control philosophy for wind energy generation systems. It focuses on the topology of DFIG with 3L-NPC back-to-back converter for wind turbine system which is suitable for generation platform with power in the range 1.5-6 MW. Despite this concentrated scope on the application and modelling side, the methodological developments will be generic for finite-control set predictive strategies. We will illustrate how to implement FCS-MPC to improve the performance in terms of power quality, dynamic response and efficiency of power converters. Thus, the research directions for this thesis consider the following objectives:

- Development of the FCS-MPC strategy for 3L-NPC converter.
- Compensation of the computational complexity, and development of FCS-MPC with two-step horizon.
- A detail description of the model predictive power control scheme is presented for control the grid connected to 3L-NPC inverter.
- Several approaches are introduced to reduce the computational cost, switching frequency and common-mode voltage.
- To control the active and reactive powers for DFIG connected to 3L-NPC inverter, a model predictive direct power control is proposed.
- A Lyapunov function is used during the control design thus including stability related considerations in the optimization-based decision for the closed-loop operation of the system.
- To compensate the dead-time effect and improve the closed-loop performance, a modified model predictive control takes into account directly the dead-time compensation.

1.6 Thesis Outline

The general introduction of the present chapter discussed wind turbine system background, objectives and contents of the thesis. Historical development and current status of the control for power converters of wind turbine system were also summarized. The remaining of the thesis is organized as follows:

- **Chapter 2: Finite control set model predictive control for 3L-NPC inverter**

  This chapter presents the development of the principle of FCS-MPC method for 3L-NPC inverter with one and two steps prediction. In the first part of this chapter, the topology and operating principle of 3L-NPC converter is recalled, then the mathematical model of 3L-NPC inverter is established. The application of FCS-MPC strategy to 3L-NPC inverter based on the cost function is defined to minimize the error between the reference currents and predicted values, balance the DC-link capacitor voltage and reduce the switching frequency. A compensation approach for the delay associated to the digital implementation and reduction of computational cost is presented. Moreover, to verify the dynamic performance, a comparison between the linear current controller with space vector modulation (PI-SVM) and FCS-MPC is provided in the last section of this chapter. The performance of the proposed strategies is evaluated based on time-domain simulation.

- **Chapter 3: Model predictive power control for grid connected 3L-NPC inverter**

  The implementation and control of a grid connected 3L-NPC inverter using FCS-MPC is the primary control objective in this chapter. Model predictive power control is synthesized using a dynamic model of the grid connected 3L-NPC inverter based on the orientation of virtual flux or grid voltage. The principle of the proposed control scheme is to use the predicted values of virtual flux, grid current and DC-link capacitor voltages for all possible configuration of voltage vectors. The active and reactive powers can be estimated based on the virtual flux and grid current. A cost function will be used to obtain the predicted profile which minimizes the error between the active, reactive powers and their references, balance the DC-link capacitor voltage and reduce the switching frequency. In order to reduce the computational burden, some methods are presented in this chapter. In addition, simulation results based on Matlab/Simulink are presented and a comparison with

classical direct power control method with linear PI controller and space vector modulation (DPC-SVM) is analyzed.

- **Chapter 4: Model predictive direct power control for DFIG fed by a 3L-NPC inverter**

  This chapter provides an overviews of model predictive direct power control for DFIG fed by a 3L-NPC inverter. Firstly, the principle operating of DFIG is presented, and then the model of DFIG connected 3L-NPC inverter is established. Secondly, the cost function associated with the control objectives that track the active and reactive powers, maintain the balanced DC-link capacitor voltage and reduce the switching frequency, common-mode voltage, is defined. Finally, in order to validate the effectiveness of the proposed control method, simulation results under different conditions of wind speed, powers and parameters variation are presented and compared with deadbeat power control and space vector modulation (DPC-SVM). The obtained results are provided to confirm and validate the efficiency of the proposed control strategies.

- **Chapter 5: Model predictive power control based on Lyapunov function for 3L-NPC back-to-back converter**

  As already summarized in Chapters 2, 3 and 4, FCS-MPC method is an interesting alternative to control the power converters and electrical drives. However, stability of this strategy still remains an open problem. In this chapter, in order to consider the stability issues, we will propose the Improved Model Predictive Direct Power Control scheme which incorporates stability constraints derived from a control Lyapunov function before the loop optimization. Furthermore, the proposed method can reduce the computational burden compared with the conventional FCS-MPC method, permitting the real time implementation with extended prediction horizons. In order to show the efficiency of the proposed control strategy, various scenarios have been carried out with extensive simulation. The simulation results indicate that the proposed control technique has a good performance and a robustness against machine parameters variations while reducing greatly the computational cost.

- **Chapter 6: Model predictive power control with dead-time compensation for 3L-NPC back-to-back converter**

  This chapter presents a new compensation strategy of model predictive control for 3L-NPC converter in order to overcome the dead-time effect of the switching

devices. The main issue is the dead-time included to avoid the short circuit in the inverter. It is shown that by taking into account the dead-time in the model, it is possible to compensate its effects. In this study, we will focus on the modelling of errors caused by dead-time and switching-time delays induced by the physical switching mechanism. With this approach, the model to predict the inverter output voltage and neutral-point voltage takes into account the dead-time and turn on/off time take of the converter to compensate its effects. In order to demonstrate the feasibility and effectiveness of the proposed scheme, simulation results will be provided and compared with uncompensated case by using Matlab and SimPower-Sytem toolbox.

- **Chapter 7: Conclusions**

  A summary of the contributions of this thesis and the possible future extensions of the research are presented in this chapter.

Chapter 2

Finite Control Set Model Predictive Control for 3L-NPC Inverter

Multilevel converters represent an attractive solution for high power applications due to the benefits in terms of high voltage capability and power quality. The main concept of the multilevel topologies is to synthesize their output voltage from several voltage levels in a staircase waveform. By increasing the number of levels in the converters, the output voltages approach sinusoidal forms with a reduced harmonic distortion. However, a high number of levels increases the control complexity and introduces voltage imbalance problem. One of the most popular multilevel converter topologies in industrial application is the three-level neutral-point clamped (3L-NPC) converter due to its advantages: higher grid power quality, reduced total harmonic distortion, lower switching frequency and high power operation.

This chapter presents the topological structure and mathematical model of 3L-NPC inverter. An overview of finite control set model predictive control for this topology is included. This chapter proposes an approach for control with respect to the current balance in the DC-link capacitor voltages and reduce switching frequency. A discrete-time model is used to predict the system variables to be controlled for each switching state of the inverter. The control goals are expressed as a cost function and its minimization is carried out by evaluating the cost function using every switching state and selecting the one which achieves the minimum. In addition, the real time implementation issues such as computational burden and delay compensation are also discussed in this chapter. The effectiveness of the proposed control method is verified by simulations with Matlab/Simulink.

2.1 Inverter configuration

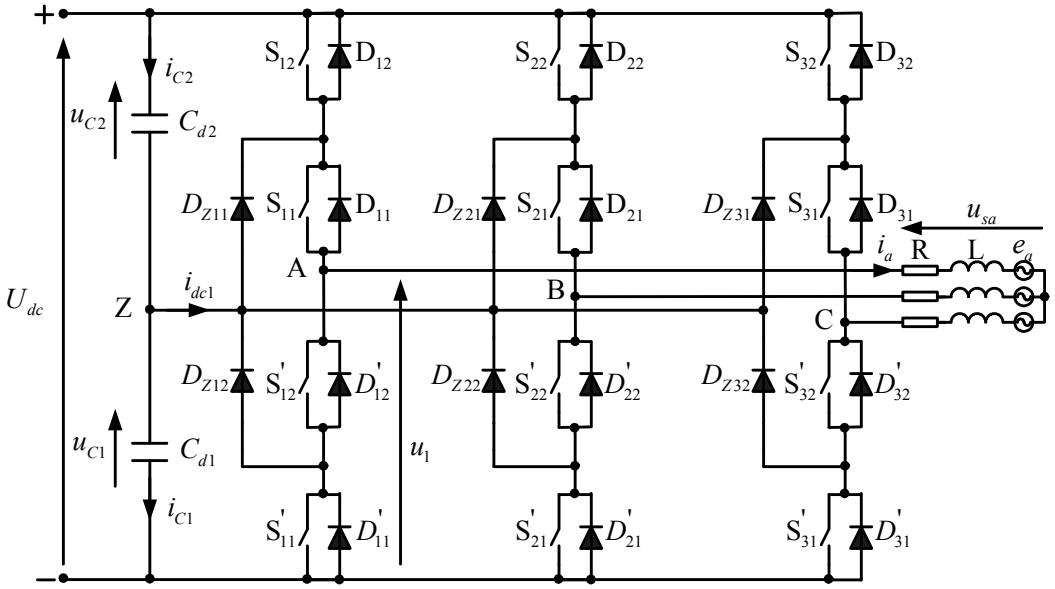

Figure 2.1: The configuration of three-level neutral-point clamped inverter.

Fig. 2.1 shows a simplified diagram of the three-level neutral point clamped inverter [16], [25]. Each inverter branch is composed of four switches with four anti-parallel diodes. On the DC side of the converter, the DC bus capacitor is divided into two parts, by providing a neutral point Z. The diodes connected to the neutral point Z, D_{Z11} and D_{Z12} are clamping diodes. The voltage across each of the DC capacitor is normally equal to the half of the total DC voltage U_{dc}. The operating status of 3L-NPC switches can be represented by three switching states [P], [O] and [N]. The switching state [P] or [1] signifies both S_{11} and S_{12} switches in branch A are positioned on "ONJ and the inverter terminal voltage U_{AZ} has the value $+U_{dc}/2$, while [N] or [-1] indicates two switches S_{11} and S_{12} are positioned on "OFF", leading to $U_{AZ} = -U_{dc}/2$. The switching state [O] or [0] means that the two internal switches S_{11} and S'_{12} are "ONJ and U_{AZ} is clamped to zero through the clamping diodes. Depending on the direction of load current i_a, one of the two clamping diodes is turned on. Fig. 2.2 shows the conductive devices according to the current direction and the switching state. To avoid short circuit, switch pairs (S_{x1}, S'_{x1}) and (S_{x2}, S'_{x2}) in each leg of the converter operate in a complementary mode. The principle switching states of 3L-NPC inverter can be summarized in the Table 2.1.

Fig. 2.3 shows an example of switching states in a fundamental period. The waveform for u_{AZ} has three voltage levels, $+U_{dc}/2$, 0, and $-U_{dc}/2$, based on which the inverter is referred to as a three-level inverter.

Table 2.1: Inverter output voltage with switching states.

Switching state	Switching gates's status				Inverter output
S_a	S_{11}	S_{12}	S'_{11}	S'_{12}	voltage u_{AZ}
P	ON	ON	OFF	OFF	$U_{dc}/2$
O	ON	OFF	OFF	ON	0
N	OFF	OFF	ON	ON	$-U_{dc}/2$

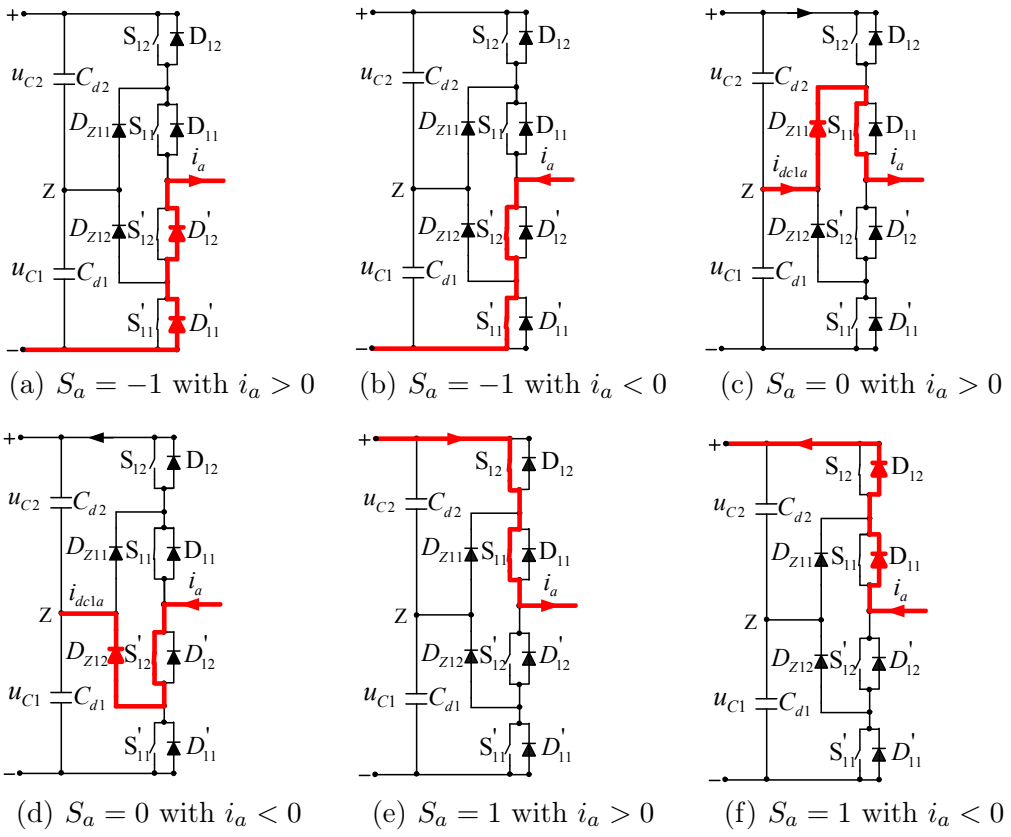

(a) $S_a = -1$ with $i_a > 0$ (b) $S_a = -1$ with $i_a < 0$ (c) $S_a = 0$ with $i_a > 0$

(d) $S_a = 0$ with $i_a < 0$ (e) $S_a = 1$ with $i_a > 0$ (f) $S_a = 1$ with $i_a < 0$

Figure 2.2: Switching states and current flow paths of phase a.

Taking into account three phases of the inverter, there are in total 27 possible combinations of switching states. For example, vector u_2 can be generated from three phase voltages: $u_{AZ} = U_{dc}/2$, $u_{BZ} = 0$ and $u_{CZ} = -U_{dc}/2$, resulting the inverter output voltage $u_2 = \frac{U_{dc}}{\sqrt{3}} e^{j\pi/6}$. In this way, we have a finite control set of 19 different voltage vectors in the complex plane as shown in Fig. 2.4. Based on their magnitude, the voltage vector can be divided into four groups:

- *Zero vectors* (from u_{25} to u_{27}) are represented by three switching states: [1 1 1], [0 0 0] and [-1 -1 -1]. The magnitude of these vectors is equal to 0.

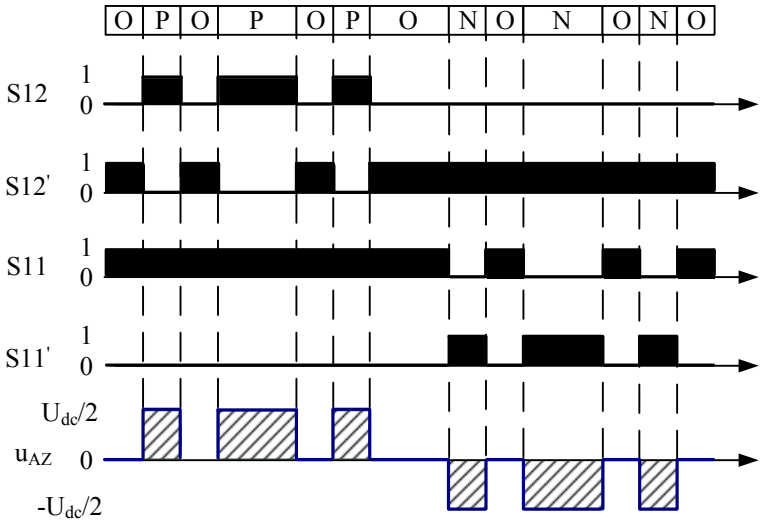

Figure 2.3: Switching states, gate signals and inverter output voltage u_{AZ}.

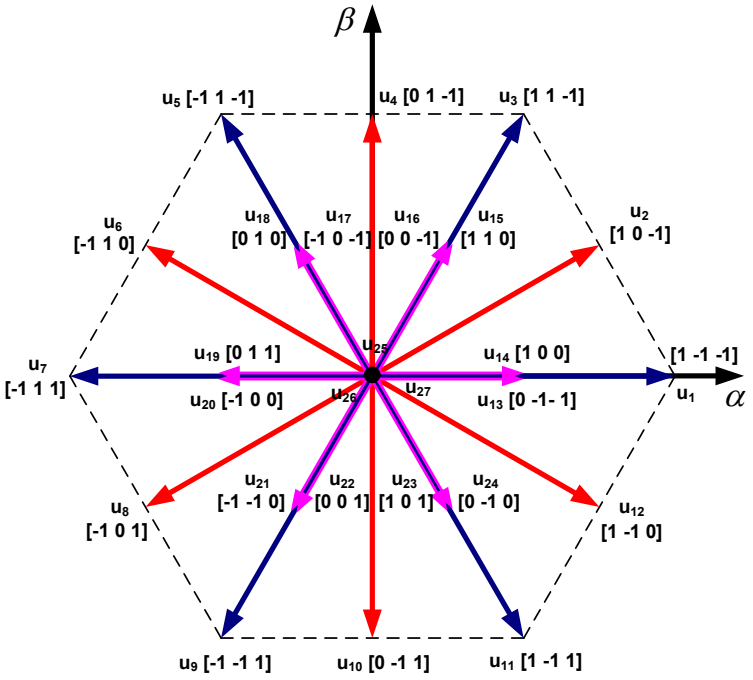

Figure 2.4: Space vector of three-level neutral-point clamped inverter.

- *Small vectors* (from u_{13} to u_{24}) have a magnitude of $U_{dc}/3$. Each vector in this category has two switching states: positive state [P] and negative state [N], respectively P and N-types small vector. The P-type small vector ([1 0 0]) makes neutral point voltage u_z increase, while the N-type small vector ([0 -1 -1]) causes u_z to decrease [25]. The deviation of neutral-point voltage u_Z causes a undesirable distortion at the converter, and increase the harmonic distortion of the voltage and current, leading to a decrease in power quality [25]. Consequently, a special attention has been

paid to maintain the neutral-point voltage and preserve acceptable performance of the output.

- *Medium vectors* (u_2, u_4, u_6, u_8, u_{10} and u_{12}), whose magnitude is $\sqrt{3}\ U_{dc}/3$.
- *Large vectors* (u_1, u_3, u_5, u_7 and u_9), all having a magnitude of $2U_{dc}/3$.

2.2 Mathematical model of 3L-NPC inverter

The inverter output voltage of 3L-NPC inverter can be expressed with phase to neutral voltages as:

$$u_s = \frac{2}{3}\left(u_{AZ} + a u_{BZ} + a^2 u_{CZ}\right), \tag{2.1}$$

with $a = e^{j2\pi/3} = -\frac{1}{2} + j\frac{\sqrt{3}}{2}$.

The phase to neutral voltages u_{AZ}, u_{BZ} and u_{CZ} of 3L-NPC inverter are calculated as a function of the DC-link voltage U_{dc} and switching states S_x:

$$u_{AZ} = S_a\frac{U_{dc}}{2};\ u_{BZ} = S_b\frac{U_{dc}}{2};\ u_{CZ} = S_c\frac{U_{dc}}{2}, \tag{2.2}$$

where S_x represents the state of a leg and has three possible values: $\{-1, 0, 1\}$ with the index $x \in \{a, b, c\}$.

In order to ensure proper operation of the inverter, the two voltages across the capacitors must be maintained equal to half of the total voltage:

$$u_{C1} = u_{C2} = U_{dc}/2. \tag{2.3}$$

To clarify the operation of the three-phase inverter, we took the first inverter branch (Table 2.2) as an example: u_1 is the voltage between the midpoint of the branch and negative voltage. From the analysis, we can express the voltage as follows:

$$u_1 = \sum_{i=1}^{2} S_{1i} u_{Ci} = S_{11} u_{C1} + S_{12} u_{C2}. \tag{2.4}$$

Table 2.2: Switching states of phase a.

Switching state	Switching gates's status				Inverter output	u_1	i_{dc1a}
S_a	S_{11}	S_{12}	S'_{11}	S'_{12}	voltage u_{AZ}		
P	ON	ON	OFF	OFF	$U_{dc}/2$	u_{C1}+u_{C2}	0
O	ON	OFF	OFF	ON	0	u_{C1}	i_a
N	OFF	OFF	ON	ON	$-U_{dc}/2$	0	0

From equation (2.4), we can express three-phase voltages set in matrix form as below:

$$\begin{bmatrix} u_1 \\ u_2 \\ u_3 \end{bmatrix} = \begin{bmatrix} S_{11} & S_{12} \\ S_{21} & S_{22} \\ S_{31} & S_{32} \end{bmatrix} \begin{bmatrix} u_{C1} \\ u_{C2} \end{bmatrix}. \tag{2.5}$$

Furthermore, the voltage on one phase of the load can be written in terms of voltage u_1 to u_3 inverter as follows:

$$\begin{aligned} u_{sa} &= \frac{1}{3}(2u_1 - u_2 - u_3), \\ u_{sb} &= \frac{1}{3}(-u_1 + 2u_2 - u_3), \\ u_{sc} &= \frac{1}{3}(-u_1 - u_2 + 2u_3). \end{aligned} \tag{2.6}$$

From equations (2.5) and (2.6), the load voltages are expressed in terms of DC-link capacitor voltages and switching states as:

$$\begin{bmatrix} u_{sa} \\ u_{sb} \\ u_{sc} \end{bmatrix} = \begin{bmatrix} S_{C11} & S_{C12} \\ S_{C21} & S_{C22} \\ S_{C31} & S_{C32} \end{bmatrix} \begin{bmatrix} u_{C1} \\ u_{C2} \end{bmatrix}, \tag{2.7}$$

where

$$
\begin{aligned}
S_{C11} &= \frac{1}{3}(2S_{11} - S_{21} - S_{31}), \\
S_{C12} &= \frac{1}{3}(2S_{12} - S_{22} - S_{32}), \\
S_{C21} &= \frac{1}{3}(-S_{11} + 2S_{21} - S_{31}), \\
S_{C22} &= \frac{1}{3}(-S_{12} + 2S_{22} - S_{32}), \\
S_{C31} &= \frac{1}{3}(-S_{11} - S_{21} + 2S_{31}), \\
S_{C32} &= \frac{1}{3}(-S_{12} - S_{22} + 2S_{32}).
\end{aligned} \tag{2.8}
$$

The equation of current i_a with RL load and electromotive force (EMF) e_a can be written as:

$$
\begin{aligned}
Ri_a + L\frac{di_a}{dt} + e_a &= u_{sa}, \\
\frac{di_a}{dt} &= -\frac{R}{L}i_a + \frac{1}{L}(u_{sa} - e_a).
\end{aligned} \tag{2.9}
$$

Based on equations (2.7), (2.8) and (2.9), the three-phase currents can be expressed by the dynamic equation:

$$
\frac{d}{dt}\begin{bmatrix} i_a \\ i_b \\ i_c \end{bmatrix} = \begin{bmatrix} -R/L & 0 & 0 & S_{C11}/L & S_{C12}/L \\ 0 & -R/L & 0 & S_{C21}/L & S_{C22}/L \\ 0 & 0 & -R/L & S_{C31}/L & S_{C32}/L \end{bmatrix} \begin{bmatrix} i_a \\ i_b \\ i_c \\ u_{C1} \\ u_{C2} \end{bmatrix} + \begin{bmatrix} -1/L & 0 & 0 \\ 0 & -1/L & 0 \\ 0 & 0 & -1/L \end{bmatrix} \begin{bmatrix} e_a \\ e_b \\ e_c \end{bmatrix}. \tag{2.10}
$$

On the other hand, the neutral current i_{dc1} can be obtained from three-phase load currents and the switching states as follows:

$$
\begin{aligned}
i_{dc1} &= i_{c2} - i_{c1} = (S_{11} - S_{12})i_a + (S_{21} - S_{22})i_b + (S_{31} - S_{32})i_c \\
&= H_a i_a + H_b i_c + H_c i_c,
\end{aligned} \tag{2.11}
$$

where the coefficient $H_x = 1$ when $S_{x1} = 1, S_{x2} = 0$ ($S_x = 0$), otherwise $H_x = 0$. Thus, it can be defined on the switching states of the inverter as:

$$H_x = 1 - |S_x| \,. \tag{2.12}$$

Assuming that the DC bus voltage U_{dc} is constant and $C_{d1} = C_{d2} = C$:

$$i_{c1} = C\frac{du_{C1}}{dt} = C\frac{d(U_{dc} - u_{C2})}{dt} = -C\frac{du_{C2}}{dt} = -i_{c2}. \tag{2.13}$$

By substituting equation (2.11) into equation (2.13), the DC-link capacitor voltages can be rewritten as:

$$\begin{aligned} \frac{du_{C1}}{dt} &= -\frac{1}{2C}(H_a i_a + H_b i_b + H_c i_c), \\ \frac{du_{C2}}{dt} &= \frac{1}{2C}(H_a i_a + H_b i_b + H_c i_c). \end{aligned} \tag{2.14}$$

The dynamics in (2.14) suggests that the DC-link capacitor voltages are also a function of switching signals. For this reason, we can maintain the balance of DC-link capacitor voltages by selecting appropriate switching state.

Consequently, we have the continuous-time dynamics of the system based on equation (2.10) and (2.14):

$$\frac{d}{dt}\begin{bmatrix} i_a \\ i_b \\ i_c \\ u_{C1} \\ u_{C2} \end{bmatrix} = \begin{bmatrix} -R/L & 0 & 0 & S_{C11}/L & S_{C12}/L \\ 0 & -R/L & 0 & S_{C21}/L & S_{C22}/L \\ 0 & 0 & -R/L & S_{C31}/L & S_{C32}/L \\ -K_a & -K_b & -K_c & 0 & 0 \\ K_a & K_b & K_c & 0 & 0 \end{bmatrix} \begin{bmatrix} i_a \\ i_b \\ i_c \\ u_{C1} \\ u_{C2} \end{bmatrix} + \begin{bmatrix} -1/L & 0 & 0 \\ 0 & -1/L & 0 \\ 0 & 0 & -1/L \\ 0 & 0 & 0 \\ 0 & 0 & 0 \end{bmatrix} \begin{bmatrix} e_a \\ e_b \\ e_c \end{bmatrix}, \tag{2.15}$$

where K_{abc} are given as

$$\begin{aligned} K_a &= \frac{1}{2C}H_a = \frac{1}{2C}\left(1 - |S_a|\right), \\ K_b &= \frac{1}{2C}H_b = \frac{1}{2C}\left(1 - |S_b|\right), \\ K_c &= \frac{1}{2C}H_c = \frac{1}{2C}\left(1 - |S_c|\right). \end{aligned} \tag{2.16}$$

2.3 The application of FCS-MPC to 3L-NPC inverter

The FCS-MPC controller is based on a prediction of the behavior of the inverter for finite number of possible voltage vector on each sampling interval. A cost function is used to evaluate the voltage vector for the next sampling interval based on the prediction model. The optimal switching state is selected and applied to the inverter during the next sampling period which minimizes the cost function. The schematic of FCS-MPC is shown in Fig. 2.5.

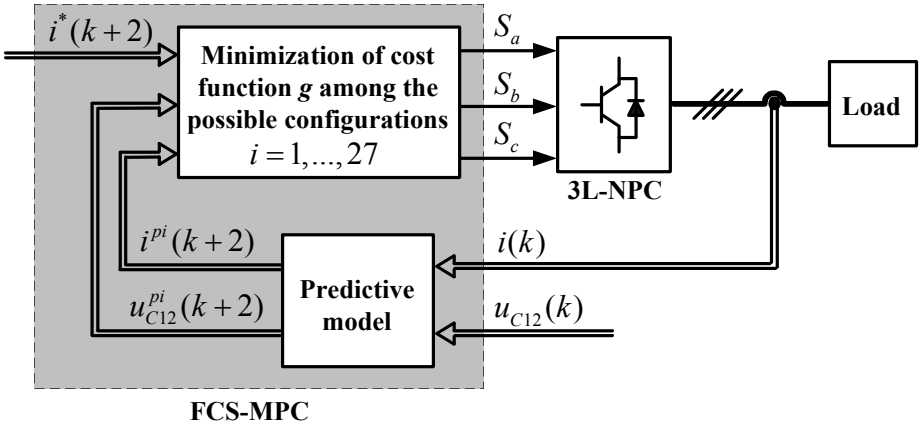

Figure 2.5: Predictive current control block diagram for 3L-NPC inverter.

The aim of the current control scheme is to minimize the error between the predicted current and the reference values, to maintain voltage balance of the capacitor and to reduce the switching frequency. In order to achieve these objectives, the cost function for 3L-NPC inverter will be constructed by weighting the ingredients suggested in previous studies [16, 44, 52]:

$$g = |i_\alpha^* - i_\alpha^p| + \left|i_\beta^* - i_\beta^p\right| + \lambda_{dc}\,|u_{C1}^p - u_{C2}^p| + \lambda_n n_c, \tag{2.17}$$

where i_α^p and i_β^p are the real and imaginary components of the predicted current which are obtained by using the system model; i_α^* and i_β^* are the real and imaginary components of the reference current; λ_{dc} and λ_n are the weighting factors of the capacitor voltage balancing and the reduction of commutation.

The first term in the cost function (2.17) accounts for the tracking error of the current. The second term in (2.17) weights the balance of DC-link capacitor voltage. The last term n_c is the number of switching change when the switching state $S(k)$ is applied compared

with previous state $S(k-1)$. It can be expressed as follows:

$$n_c = |S_a(k) - S_a(k-1)| + |S_b(k) - S_b(k-1)| + |S_c(k) - S_c(k-1)|. \tag{2.18}$$

The weighting factors λ_{dc}, λ_n can be adjusted to achieve an acceptable quality of the current, capacitor voltage balancing and reduction of switching frequency, which it is not a transparent task for the conventional control methods. The detail of the selection and influence of these parameters will present in next chapter.

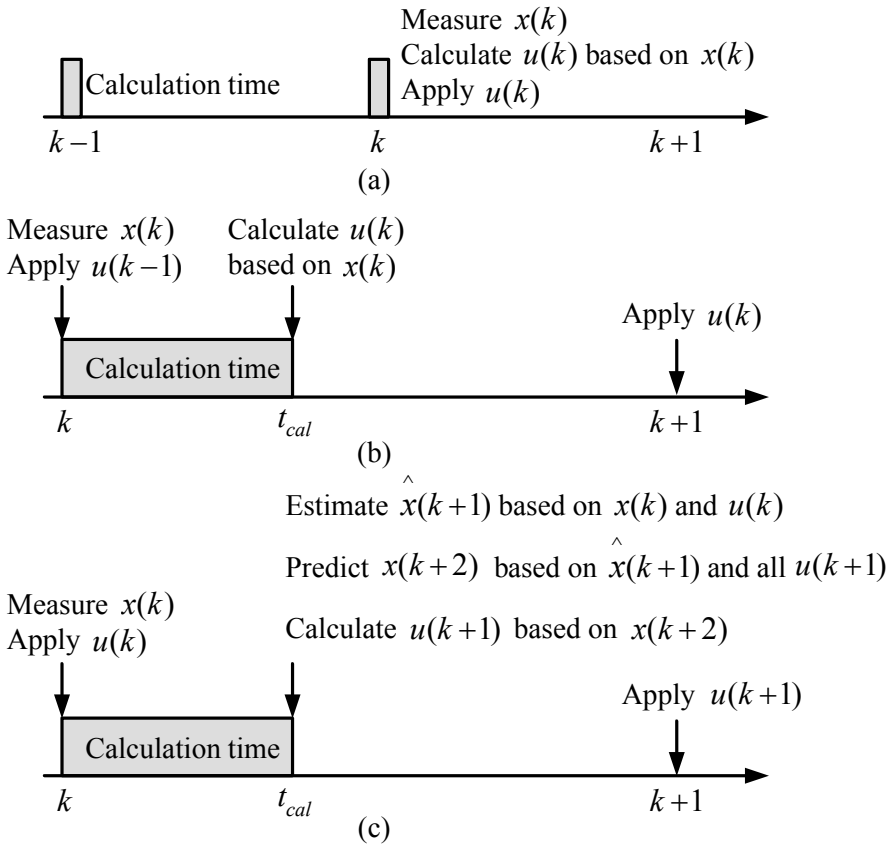

Figure 2.6: Operation of the predictive control [16] (a) Ideal case. (b) Real case without time delay compensation. (c) Real case with time delay compensation.

In the ideal case, the required time for the calculation can be ignored. The operation of predictive control is shown in Fig. 2.6(a). The states of the systems $x(k)$ are measured at the time k, the optimal switching state is calculated instantaneously. The switching state having the smallest error value at the time $k+1$ is chosen and applied at the time k. On the contrary, in real time implementation of the system, there will be a non-negligible time delay in the actuation caused by the computational time and the communication time required. Thus, the control variable $u(k)$ is available later after a sampling period

(Fig. 2.6(b)). At the beginning of sampling k, the state variables $x(k)$ are measured and the calculation of the new value for the control variable is started. The calculation is completed at the time $k+t_{cal}$. So, the updating of the control variable will be applied at $k+1$.

To account for computational delay, one popular compensation approach [16, 44, 52] is based on optimizing the cost function at $k+2$ and applying the optimal switching state at $k+1$. In order to implement this approach, it requires the state variable at $k+1$, hence, a simple solution is to estimate the values at $k+1$ using the previous optimal switching state at time k, measurement and the model of the system. Next, the future values at $k+2$ are predicted using the estimated values at $k+1$ and every switching state of the converter. Then, the optimal switching state that minimizes the cost function at $k+2$ is selected and applied to the converter at the time $k+1$. So this control scheme is considered as a modified one-step horizon as illustrated in Fig. 2.6(c).

A control action is a combination of switch state $S_p = [S_{pa}\ S_{pb}\ S_{pc}]^T$, represented as a set of p vector $S_p \in \{1, ..., 27\}$. Moreover, the switching input is restricted to belong to the set: $S_{px} \in \{-1, 0, 1\}$ with the index $x \in \{a, b, c\}$. Consequently, the optimal control action u_{opt} which will be applied to the converter at the time $k+1$ is obtained as the result of equation (2.19), in the case of modified one-step horizon:

$$\begin{aligned}
&\hat{i}(k+1) = f_1(u_k, i(k));\ i^p(k+2) = f_1(u_{k+1}, \hat{i}(k+1));\ u^p_{C1}(k+1) = f_2(u_k, i(k)),\\
&u^p_{C2}(k+1) = f_3(u_k, i(k));\ u^p_{C1}(k+2) = f_2(u_{k+1}, \hat{i}(k+1));\ u^p_{C2}(k+2) = f_3(u_{k+1}, \hat{i}(k+1)),\\
&g(u_{k+1}) = |i^*_\alpha(k+2) - i^p_\alpha(k+2)| + \left|i^*_\beta(k+2) - i^p_\beta(k+2)\right| +\\
&\qquad \lambda_{dc}\left|u^p_{C1}(k+2) - u^p_{C2}(k+2)\right| + \lambda_n n_c,\\
&u_{opt} = arg\left\{\min_{u_{k+1}\in\{-1,0,1\}^3} g(u_{k+1})\right\}.
\end{aligned} \tag{2.19}$$

With the aim to reduce the prediction error and improve the dynamic performance of the system, a long prediction horizon can be extended but increasing the complexity of the system and the computational cost. Fig. 2.7(a) shows a standard two-step prediction horizon [69]. With this proposition, there are 27 switching states which are used to predict the state variables at time $k+1$. On the same philosophy the future values are predicted at $k+2$ by using the already available predicted values at $k+1$ and 27 switching states at instant $k+1$. In this case, a discrete set of $27^2 = 729$ possible trajectories of the switching states has to be enumerated for the evaluation of the cost function. Consequently, such a strategy leads to large number of numerical operations and make difficult to implement

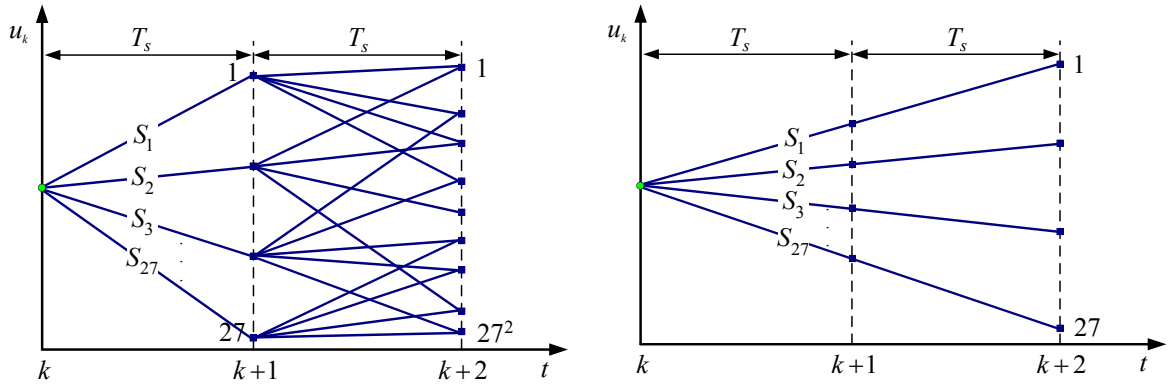

(a) Standard two-step prediction (b) Modified two-step prediction

Figure 2.7: Control variable prediction for the 3L-NPC inverter with two-step horizon.

the algorithm in practice at high sampling rate. To reduce the number of real time evaluation, we propose in a first stage to consider applying the same voltage vector in two-step horizon, instead of different vectors (Fig. 2.7(b)). Therefore, the computations required are limited with respect to the total of 729 trajectories but the impact of the switch is considered on a longer time scale. This represents practically a move-blocking strategy from the Model Predictive Control point of view and allows evaluating the impact of the control on a longer time windows. This leads to the following formula:

$$
\begin{aligned}
& i^p(k+1) = f_1(u_k, i(k));\ i^p(k+2) = f_1(u_{k+1}, i^p(k+1));\ u^p_{C1}(k+1) = f_2(u_k, i(k)), \\
& u^p_{C2}(k+1) = f_3(u_k, i(k));\ u^p_{C1}(k+2) = f_2(u_{k+1}, i^p(k+1));\ u^p_{C2}(k+2) = f_3(u_{k+1}, i^p(k+1)), \\
& g(u_k, u_{k+1}) = |i^*_\alpha(k+2) - i^p_\alpha(k+2)| + \left|i^*_\beta(k+2) - i^p_\beta(k+2)\right| + |i^*_\alpha(k+1) - i^p_\alpha(k+1)| + \\
& \qquad \left|i^*_\beta(k+1) - i^p_\beta(k+1)\right| + \lambda_{dc}\,|u^p_{C1}(k+2) - u^p_{C2}(k+2)| + \lambda_n n_c, \qquad (2.20) \\
& u_{opt} = \arg\left\{ \min_{u_k \in \{-1,0,1\}^3,\, u_{k+1} \in \{-1,0,1\}^3} g\left(u_k, u_{k+1}\right) \right\}, \\
& \qquad \text{subject to } u_k = u_{k+1}.
\end{aligned}
$$

As shown in Fig. 2.5, the cost function requires predicted load current $i^p(k+2)$ and capacitor voltages $u^p_{c1}(k+2)$, $u^p_{c2}(k+2)$ in discrete-time form. In this respect, the first-order forward Euler approximation will be used to obtain a discrete-time system representation. The differential state variable is approximated as follows:

$$
\frac{dx}{dt} = \frac{x(k+1) - x(k)}{T_s}, \qquad (2.21)
$$

where T_s is a sampling time.

Approaching equation (2.9) with equation (2.21), the load currents are represented in discrete-time as:

$$i^p(k+1) = \Big(1 - \frac{RT_s}{L}\Big)i(k) + \frac{T_s}{L}\Big(u_s(k) - \hat{e}(k)\Big), \tag{2.22}$$
$$i^p(k+2) = \Big(1 - \frac{RT_s}{L}\Big)i(k+1) + \frac{T_s}{L}\Big(u_s(k) - \hat{e}(k+1)\Big),$$

where $\hat{e}(k)$ represents the estimated back-EMF. To calculate back-EMF the equation (2.9) can be exploited:

$$\hat{e}(k-1) = u_s(k-1) - \frac{L}{T_s}i(k) - \Big(R - \frac{L}{T_s}\Big)i(k-1), \tag{2.23}$$

where $\hat{e}(k-1)$ is the estimated value of $\hat{e}(k)$ (a valid assumption as long as the variation of EMF is slow compared to the sampling frequency T_s).

Similarly, we have the discrete-time form for the capacitor voltages as follows:

$$u^p_{C1}(k+1) = u_{C1}(k) + \frac{T_s}{C}i_{c1}(k), \tag{2.24}$$
$$u^p_{C2}(k+1) = u_{C2}(k) + \frac{T_s}{C}i_{c2}(k),$$

where i_{c1}, i_{c2} depend on the switching states and the output currents, and can be calculated by using equation (2.11):

$$i_{c1}(k) = -\frac{1}{2}\Big(H_a i_a(k) + H_b i_b(k) + H_c i_c(k)\Big), \tag{2.25}$$
$$i_{c2}(k) = \frac{1}{2}\Big(H_a i_a(k) + H_b i_b(k) + H_c i_c(k)\Big).$$

The DC-link capacitor voltages for two-step prediction are obtained by shifting the variables into one future sample. Then, they can be described as:

$$u^p_{C1}(k+2) = u^p_{C1}(k+1) + \frac{T_s}{C}i^p_{c1}(k+1), \tag{2.26}$$
$$u^p_{C2}(k+2) = u^p_{C2}(k+1) + \frac{T_s}{C}i^p_{c2}(k+1),$$

where the current of DC-link capacitor can be estimated by using the equation (2.11):

$$i_{c1}^{p}(k+1) = -\frac{1}{2}\Big(H_a i_a^p(k+1) + H_b i_b^p(k+1) + H_c i_c^p(k+1)\Big), \tag{2.27}$$
$$i_{c2}^{p}(k+1) = -i_{c1}^{p}(k+1).$$

Finally, the cost function of FCS-MPC for the 3L-NPC inverter with one step prediction can be expressed as:

$$g = \Big|\, i_\alpha^*(k+1) - i_\alpha^p(k+1)\Big| + \Big|\, i_\beta^*(k+1) - i_\beta^p(k+1)\Big| + \lambda_{dc}\Big|\, u_{C1}^p(k+1) - u_{C2}^p(k+1)\Big| + \lambda_n n_c. \tag{2.28}$$

The expression of the cost function with two-step prediction can be written as follows:

$$\begin{aligned} g = &\Big|\, i_\alpha^*(k+2) - i_\alpha^p(k+2)\Big| + \Big|\, i_\beta^*(k+2) - i_\beta^p(k+2)\Big| + \Big|\, i_\alpha^*(k+1) - i_\alpha^p(k+1)\Big| + \\ &\Big|\, i_\beta^*(k+1) - i_\beta^p(k+1)\Big| + \lambda_{dc}\Big|\, u_{C1}^p(k+2) - u_{C2}^p(k+2)\Big| + \lambda_n n_c. \end{aligned} \tag{2.29}$$

The future reference currents $i^*(k+1)$, $i^*(k+2)$ can be estimated by extrapolation using Lagrange method based on the present and passed values. This process can be expressed as [16, 70]:

$$\begin{aligned} i^*(k+1) &= 3i^*(k) - 3i^*(k-1) + i^*(k-2), \\ i^*(k+2) &= 6i^*(k) - 8i^*(k-1) + 3i^*(k-2). \end{aligned} \tag{2.30}$$

Finally, the control results of proposed predictive control can be obtained from evaluation of the cost function by using a flowchart of the optimization process as shown in the Fig. 2.8. The following steps summarize the proposed control strategy:

1 Read the current reference, measure the load currents, DC-link voltage and extrapolate the reference.

2 Initialize the value of the optimal switching state j_{opt} and cost function g_{opt}.

3 Estimate back-EMF $\hat{e}(k-1)$ based on equation (2.23).

4 Predict the load currents and DC-link capacitor voltages for each switching state at instant $k+1$ and $k+2$ from equations (2.22) and (2.24).

5 Calculate the number of switching change n_c using (2.18).

6 Compute the cost function g for each prediction based on equation (2.29).

7 Select the optimal switching state that minimizes the cost function.

8 Apply the optimal switching state.

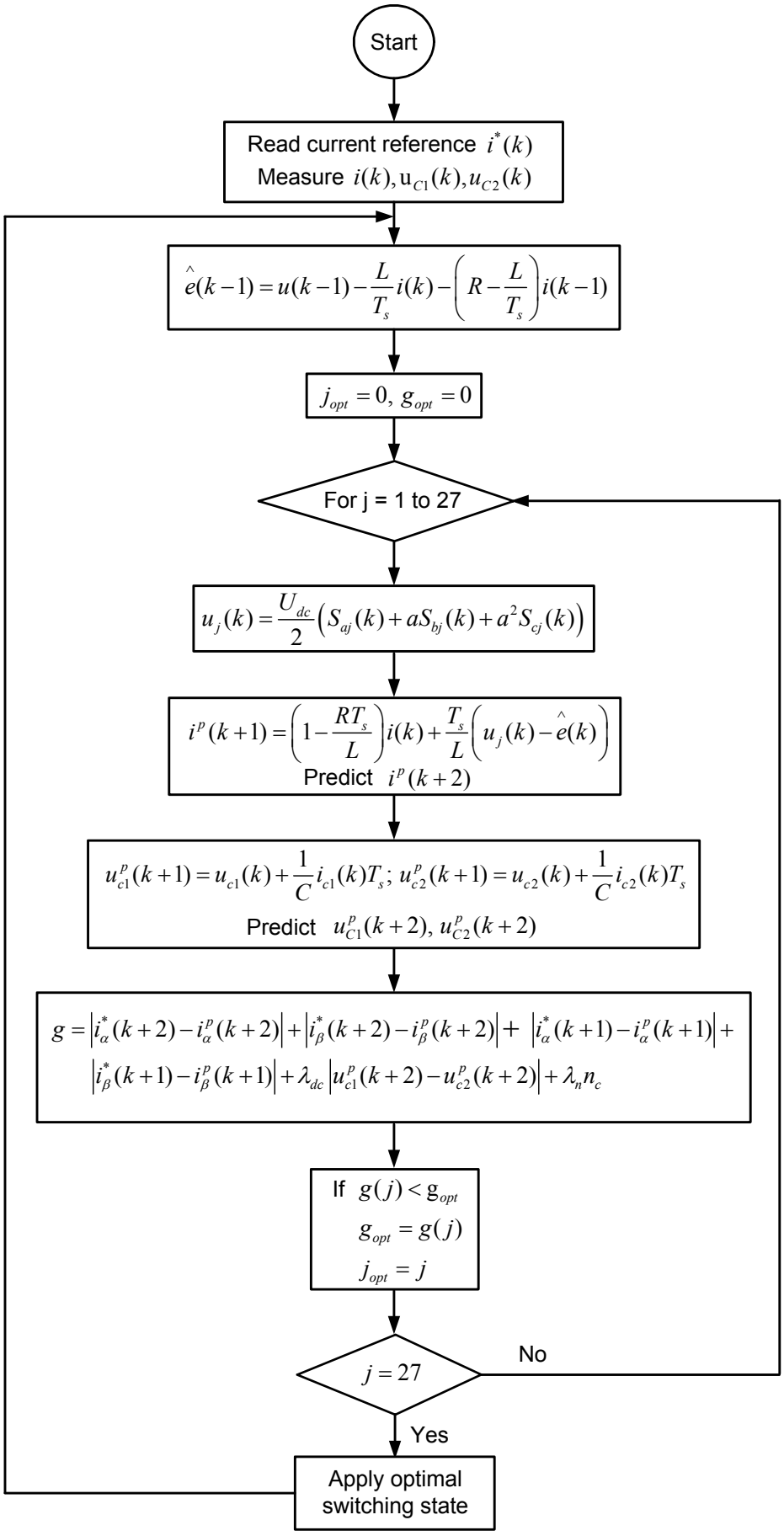

Figure 2.8: Flow diagram of the proposed FCS-MPC strategy.

2.4 Simulation results

In order to validate the effectiveness of this basic finite control set model predictive current control (FCS-MPC) strategy for 3L-NPC, the control scheme has been simulated using Matlab software with the parameters shown in Table 2.3. Moreover, to verify the dynamic performance, we perform a comparison between FCS-MPC and linear PI controllers [71] with space vector modulation which used converter redundant switching states to balance DC-link capacitor voltages [25] (PI-SVM) for different conditions of the references with the same parameters.

To evaluate the steady state performance, we use the mean absolute percentage error (MAPE) which can be express as follows:

$$MAPE = \frac{1}{n}\sum_{i=1}^{n}\left|\frac{y_i^* - y_i}{y_i^*}\right|, \tag{2.31}$$

where y_i^* is the reference vector and y_i is the vector measured.

On the other hand, with the aim to estimate the average switching frequency per semiconductor (f_{sw}) of FCS-MPC, the following expression proposed in [52] can serve as appropriate indicator:

$$f_{sw} = \sum_{x=a,b,c}\frac{f_{sw_{x1}} + f_{sw_{x2}}}{6} = \sum_{x=a,b,c}\frac{n_{sw_{x1}} + n_{sw_{x2}}}{6T_{sim}}, \tag{2.32}$$

where $n_{sw_{x1}}$, $n_{sw_{x2}}$ are the number of switching changes in the gating signals of each upper switch by measuring over a simulation time (T_{sim}).

Table 2.3: Parameters used for simulation.

Parameter	Value	Description
U_{dc}	540 [V]	DC-link voltage
C	1 [mF]	DC-link capacitor
R	10 [Ω]	Load resistance
L	50 [mH]	Load inductance
f_{sp}	10 [kHz]	Sampling frequency for FCS-MPC
f_{svm}	5 [kHz]	Sampling frequency for PI-SVM
f	50 [Hz]	Current reference frequency
E	100 [V]	Back-EMF peak amplitude
I_{ref}	10 [A]	Peak amplitude of reference current

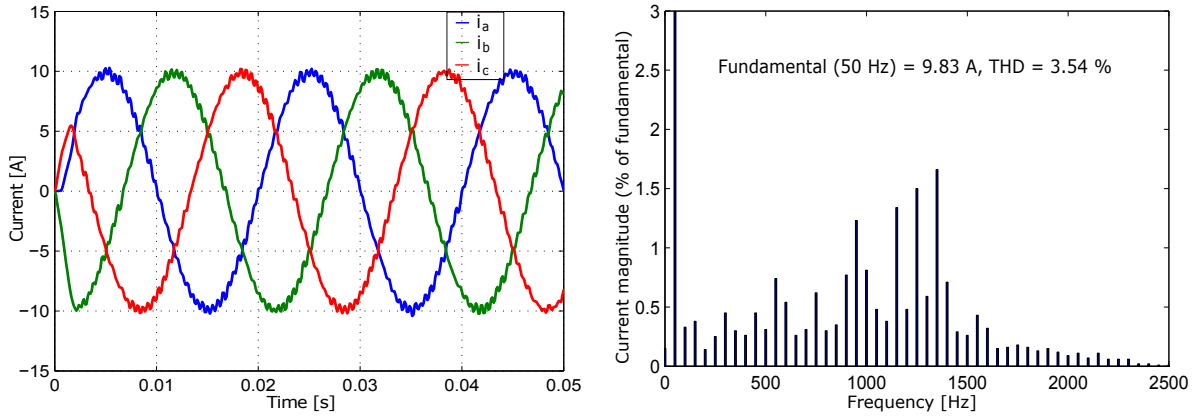

(a) The steady state (b) Fast Fourier Transform (FFT)

Figure 2.9: The steady state and FFT of three-phase current for PI-SVM.

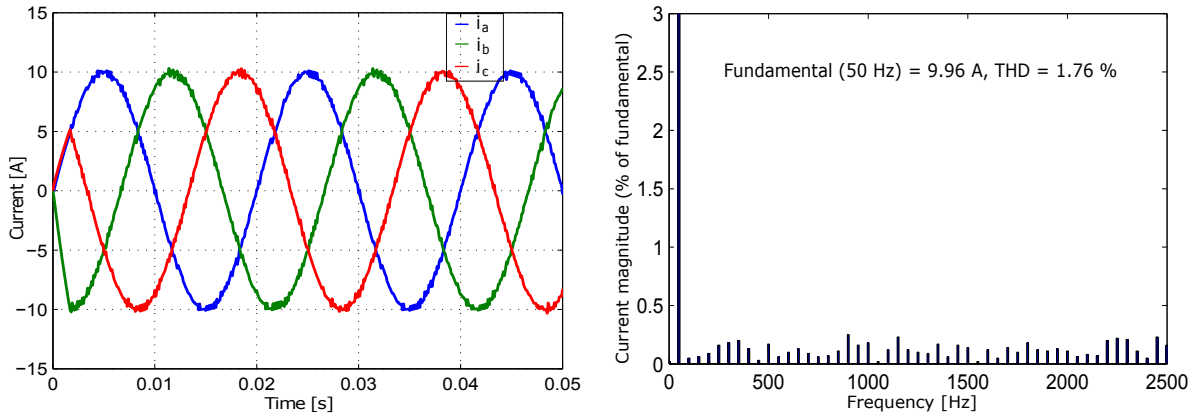

(a) The steady state (b) Fast Fourier Transform (FFT)

Figure 2.10: The steady state and FFT of three-phase current for FCS-MPC.

To generate the same average switching frequency per semiconductor, the sampling frequency of the FCS-MPC is considered $f_{sp} = 10$ kHz and the sampling frequency of the SVM is 5 kHz. For the SVM at 5 kHz, $f_{sw} = 2.5$ kHz and the expected value of f_{sw} for FCS-MPC is about 2.5 kHz. The DC-link voltage U_{dc} is set to 540 V. The transient responses of the PI-SVM and MPC from zero load current until the steady state and the total harmonic distortion (THD) are illustrated in Figs. 2.9 and 2.10. The current waveform of the FCS-MPC is smoother, and its THD is smaller. In order to observe the dynamics ability to track the current reference and the interaction between two components of the load current, the amplitude of the sinusoidal reference current presents a steps from 10 A to 5 A at $t = 0.065$ s as shown in Fig. 2.11. Figs. 2.11(c) and 2.11(d) indicate that the i_β is continued to track to its reference while the amplitude of reference current ($i_{a-ref} = i_{\alpha-ref}$) is decreased from 10 A to 5 A (Fig. 2.11(b)). The mean absolute percentage error of PI-SVM is 0.41 and 0.08 with FCS-MPC. From

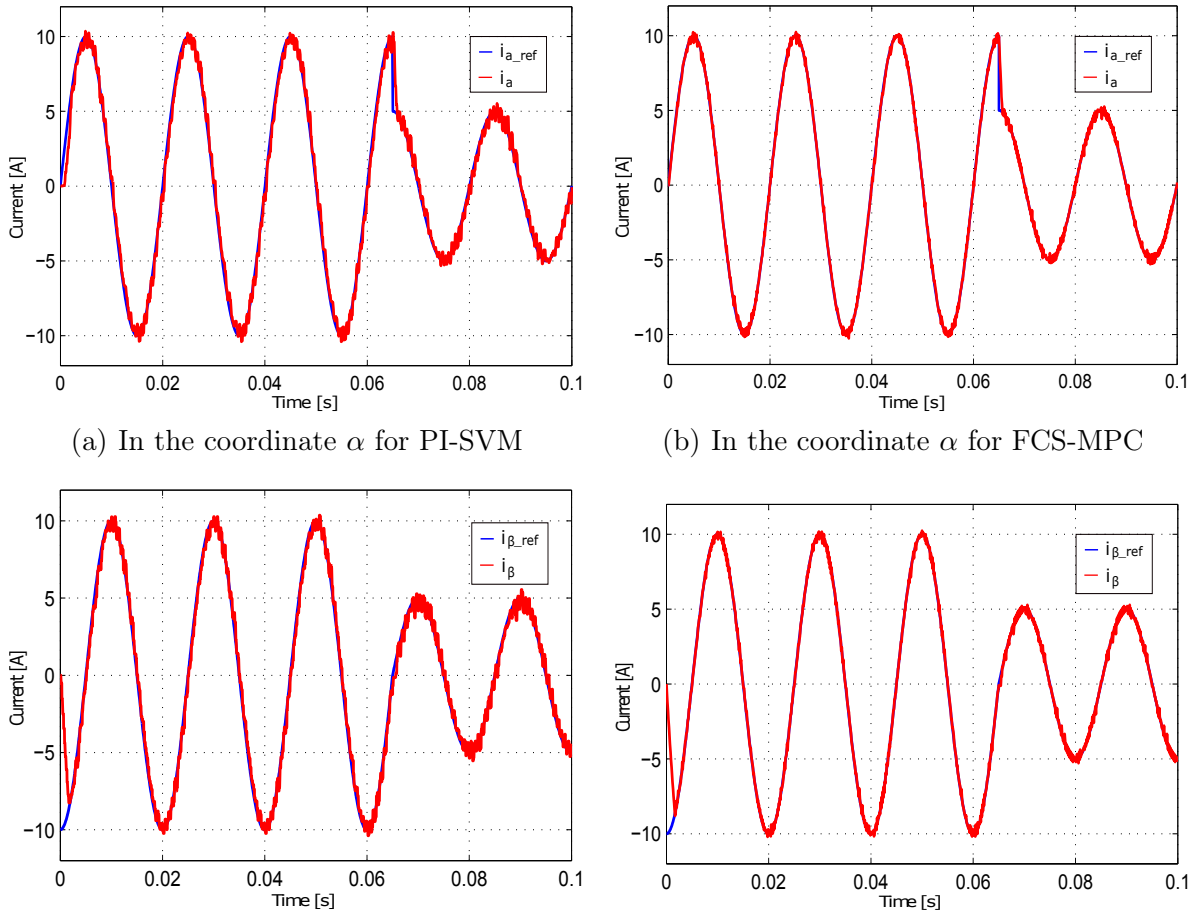

(a) In the coordinate α for PI-SVM

(b) In the coordinate α for FCS-MPC

(c) In the coordinate β for PI-SVM

(d) In the coordinate β for FCS-MPC

Figure 2.11: The load curent transient response for a reference step of 10A-5A.

the results presented, it is clear that the predictive method obtains an accurate current tracking ability with a low THD and low current ripple. Moreover, this simulation clearly demonstrated the ability of the proposed control algorithm to track reference currents with a fast dynamic response (the average computation time of the algorithm is 8 μs in a 3.3 GHz, i5-6600 CPU) and an inherent decoupling between two components: real and imaginary.

One of the important issues of 3L-NPC structure is the balancing voltage of the DC-link capacitor. Fig. 2.12 illustrates that the voltage of DC-link capacitor remains balanced with MAPE of DC-link capacitor voltages deviation for the proposed method 0.09% and for PI-SVM 0.71% in spite of the transition of the load current which causes the oscillation.

In an attempt to compare the FCS-MPC with one-step horizon with two-step proposed, we analyze the characteristic with the RL load with the weighting values $\lambda_{dc} = 0.45$

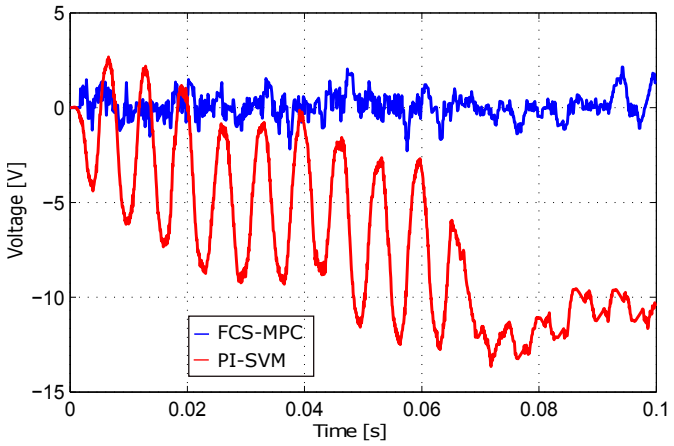

Figure 2.12: The difference between the DC-link capacitor voltage.

and $\lambda_n = 0.001$ in equation (2.17). The load current with one-step prediction, which is illustrated in Fig. 2.13, creates 1.2% THD. The average switching frequency f_{sw} is 1285 Hz. The load current with two-step prediction, which is shown in Fig. 2.14, creates 0.97% THD, and respectively 931 Hz. Thus, this method provides a new approach to control high power converter that require an operation with lower switching frequency. Furthermore, Figs. 2.15 and 2.16 show that the THD of the output voltage of proposed method (25.64%) is smaller than the THD obtained with MPC one-step prediction (28.14%), leading to improve the quality performance. In addition, the results of applying the proposed method with three-step ($u_k = u_{k+1} = u_{k+2}$) are not too much better than two-step horizon. The THD of the current and output voltage are 0.95% and 23.15% but increasing the computational cost due to estimation of the load current and DC-link capacitor voltages. Therefore, two-step horizon can be used to make a compromise between the performance and computational complexity.

Fig. 2.17 and Table 2.4 analyse the impact of the computational delay. Three cases are considered. In the first one any delay is considered, so the measurement at time instant k is used to compute the control signal at time instant k. In the second one, the computational delay exist but it is not compensate. In this case measurement at time instant k are used to compute the control signal at time instant k, but this control signal is effectively applied at time instant $k+1$. Finally in the third case, the computational delay is compensated. The measurements at time instant k are used to predict the state at $k+1$ that is used to compute the control signal of time instant $k+1$. Fig. 2.17 shows the cases for one step prediction without delay and with delay compensation, and two step prediction with delay compensation. As can be observed, compensate the delay

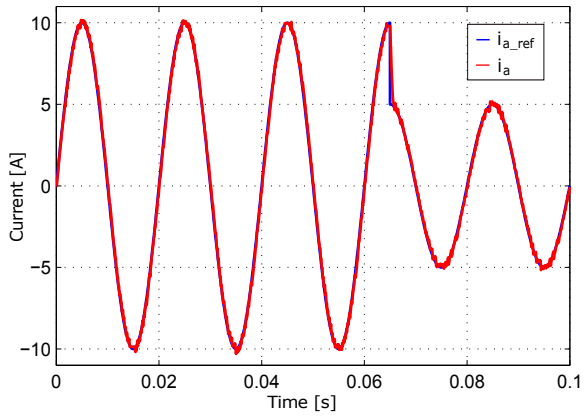

(a) The steady state and transient response

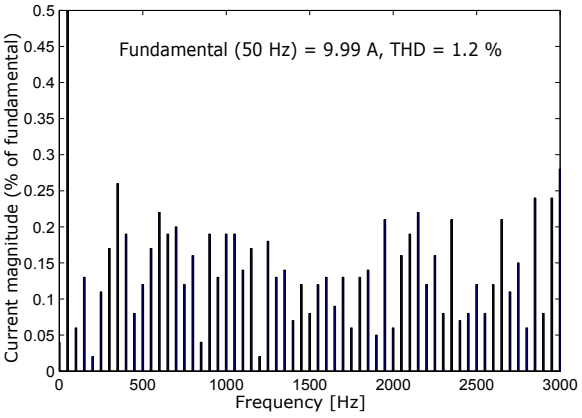

(b) Fast Fourier Transform

Figure 2.13: The transient response and FFT of current for FCS-MPC with one-step prediction.

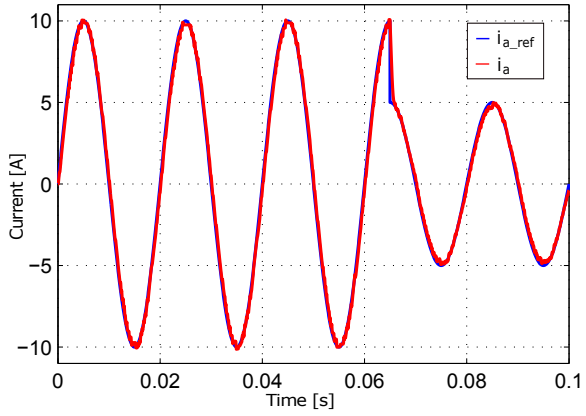

(a) The steady state and transient response

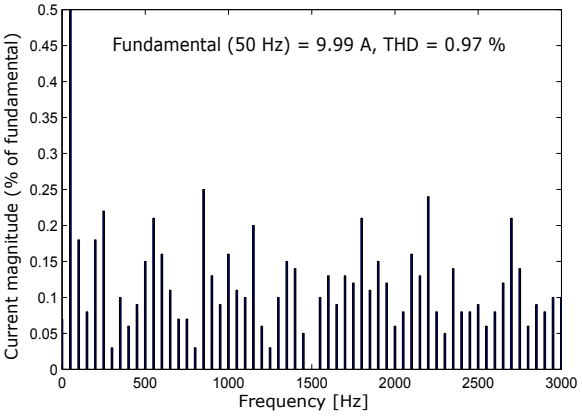

(b) Fast Fourier Transform

Figure 2.14: The transient response and FFT of current for two-step proposed method.

improves considerably the THD of currents. In Table 2.4 the results for one and two step prediction are summarized.

Table 2.4: Comparison of the performance of different methods.

FCS-MPC method	THD of current (%)	MAPE of current (%)	f_{sw} (Hz)
One-step prediction not considering the delay	1.2	0.12	1285
One-step prediction without delay compensation	2.89	0.34	1170
One-step prediction with delay compensation	1.75	0.19	1467
Two-step prediction not considering the delay	0.97	0.09	931
Two-step prediction with delay compensation	1.41	0.15	1245

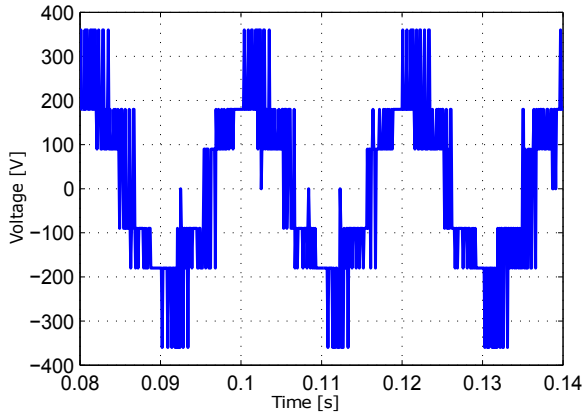

(a) The steady state

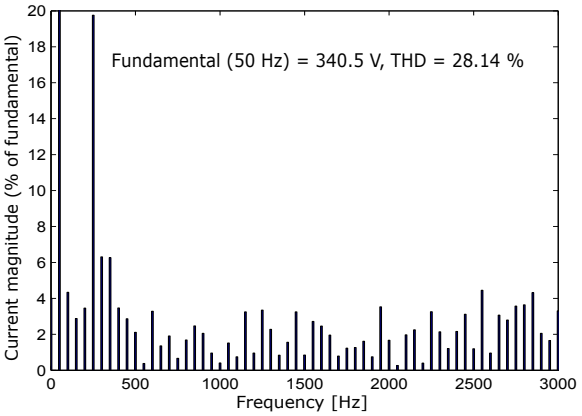

(b) Fast Fourier Transform

Figure 2.15: The steady state and FFT of inverter voltage for FCS-MPC with one-step prediction.

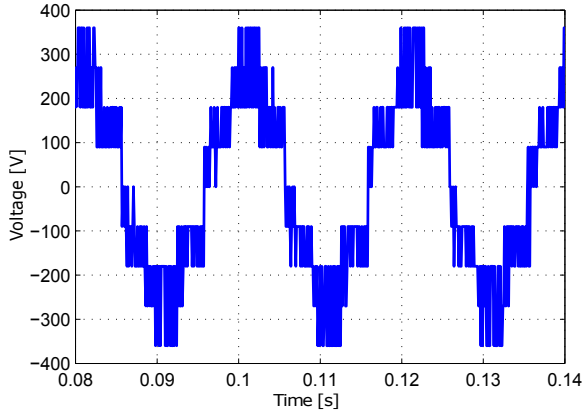

(a) The steady state

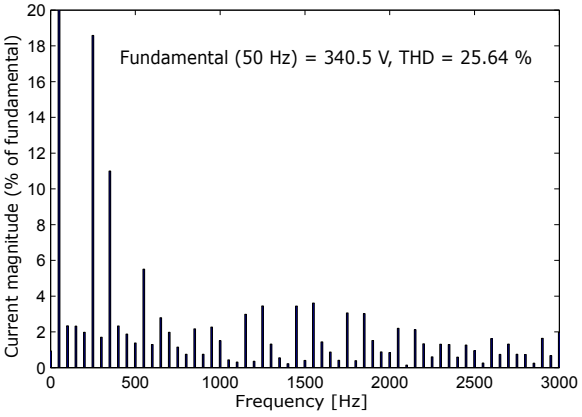

(b) Fast Fourier Transform

Figure 2.16: The steady state and FFT of inverter voltage for proposed method.

To confirm the robust performance of load variation, the operating condition discussed is repeated with unbalanced load ($R_a = 12\,\Omega, R_b = 10\,\Omega, R_c = 8\,\Omega$). The load currents effectively follow their references without overshoot as shown in the Fig. 2.18. This presented result demonstrates that the proposed controller is robust and can face the load parameter variations.

2.5 Conclusions

This chapter proposes an FCS-MPC strategy with one and two-steps prediction for 3L-NPC inverter. Firstly, the mathematical model of 3L-NPC inverter is established,

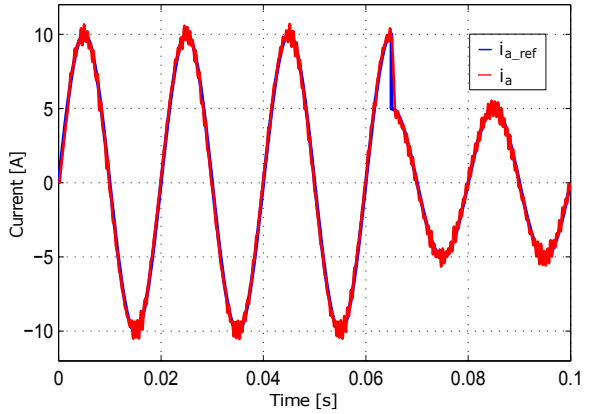

(a) Current response of one-step prediction without delay compensation

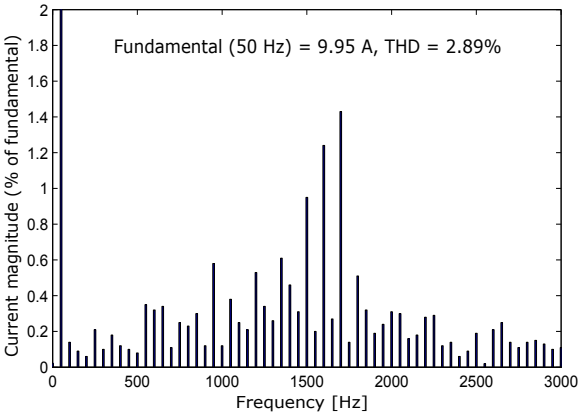

(b) Current spectrum of one-step prediction without delay compensation

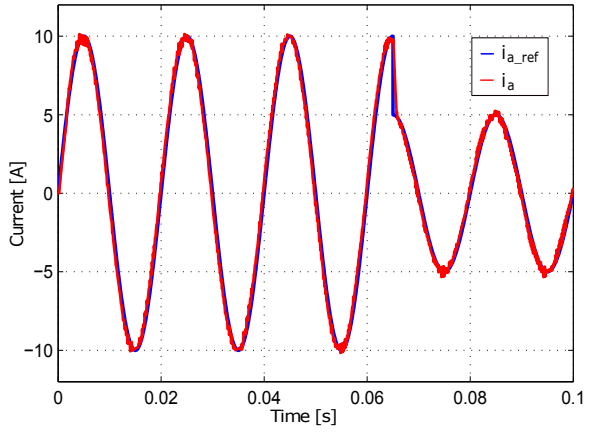

(c) Current response of one-step prediction with delay compensation

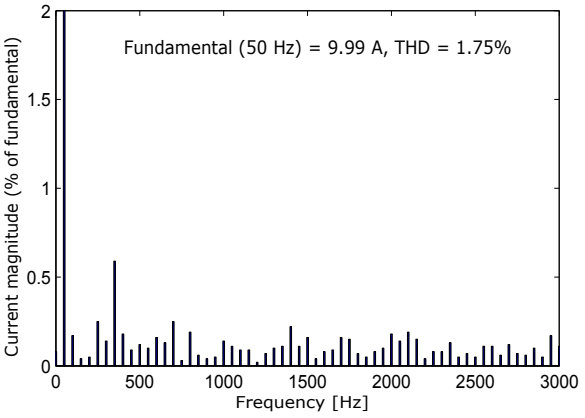

(d) Current spectrum of one-step prediction with delay compensation

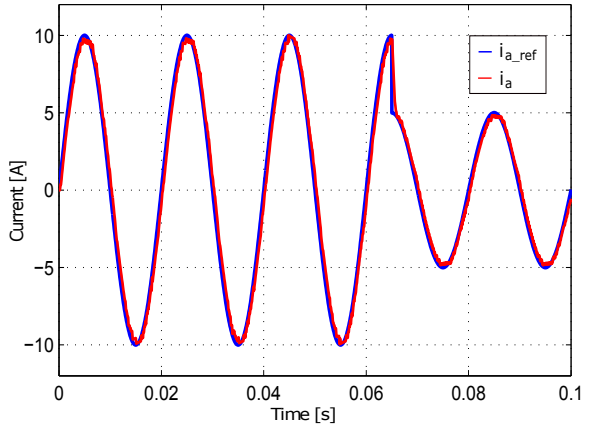

(e) Current response of two-step prediction with delay compensation

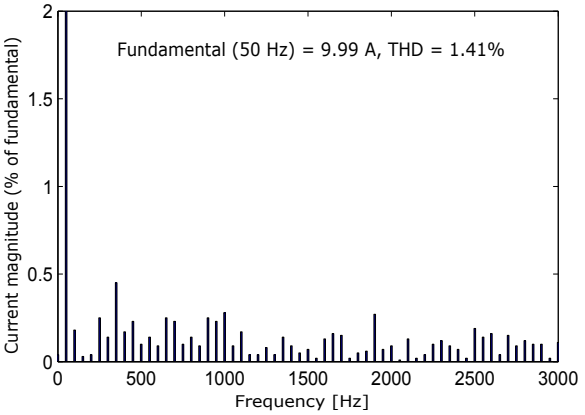

(f) Current spectrum of two-step prediction with delay compensation

Figure 2.17: The current response and current spectrum of one and two-step prediction with and without delay compensation.

and then the cost function, which contains the current error, the capacitor voltage balancing and the reduction of the switching frequency, is defined. Next, to give a better

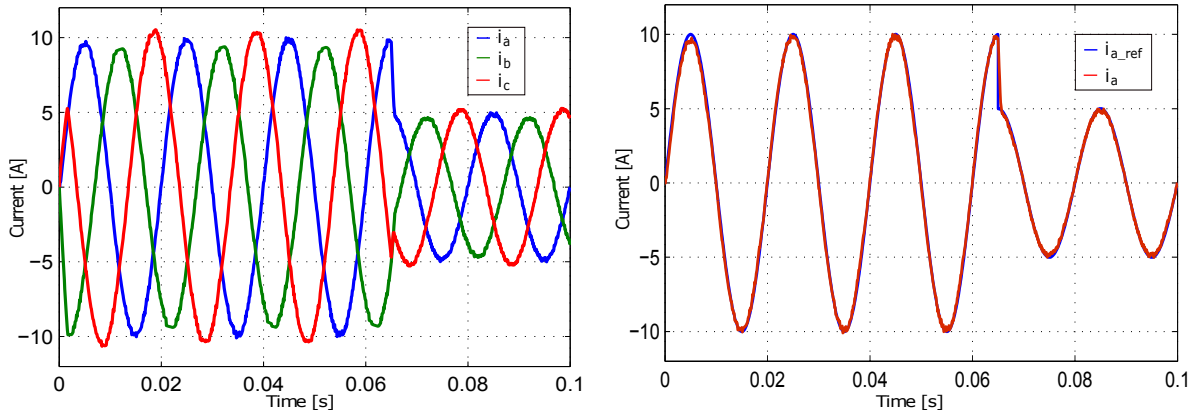

(a) The transient response of three-phase current

(b) The transient response in the current of phase a

Figure 2.18: The load current response of proposed method with unbalanced load.

performance a two-step horizon control has been considered in this chapter. In order to reduce the amount of calculations, the control is considered constant during the two step prediction. Furthermore, an approach to compensate the computational delay has been presented. Finally, in order to verify the performance of control scheme, there is a comparison between PI-SVM and FCS-MPC and then a comparative study between the two horizon is analyzed. The simulation results confirm that this control technique can successfully maintain their balanced capacitor voltages and reduce the switching frequency while achieving an acceptable quality of current and voltage. In addition, the presented results for one and two-step horizon demonstrate that the system performance is improved when two-step prediction is considered. The proposed controller can be adapted to track the references with the load variations. The linear PI current controllers and the modulation block are further eliminated, reducing system complexity. Therefore, the proposed method is an interesting alternative to a current control for the 3L-NPC converter.

Chapter 3

Model Predictive Power Control for Grid connected 3L-NPC Inverter

Grid connected power inverters play an important role in industrial applications such as new energy systems, high voltage direct current transmission and flexible AC transmission systems (FACTS), especially with the development of high power generators using wind power. The main objective of grid side converter (GSC) is to keep the DC-link voltage U_{dc} constant as well as to guarantee that the active power transfers bidirectionally between the rotor side converter (RSC) and the grid. Moreover, the THD of grid current must be below 5% to meet grid code requirements specified by IEEE standard 519. Due to the DC-link between the two converters, the reactive power exchanged by the GSC is also independent of the reactive power processed by the RSC. In normal operation, the GSC operates at unity power factor ($PF = 0$). However, in addition to the reactive power control of the RSC, the GSC is expected to provide additional reactive power support to the grid similar to the operation of a static synchronous compensator (STATCOM), which is significantly lower than the rating of the wind generator. The simplified block diagram of the grid side converter system is illustrated in Fig. 3.1. The pulses for the controlled switches (S_a, S_b, S_c) are generated in order to control the DC-link voltage and reactive power exchanged with the grid (Q_{gsc}). By controlling the DC-link voltage to a constant value, the active power (P_{gsc}) flows through the converter is ensured. The reference of the active power ($P_{gsc-ref}$) can be derived from the DC voltage controller according to the operating conditions.

To analyze the bidirectional power flow, the DC load can be modeled as a resistor R_{load} and a battery supply E. The active power transfers with the grid can be varied

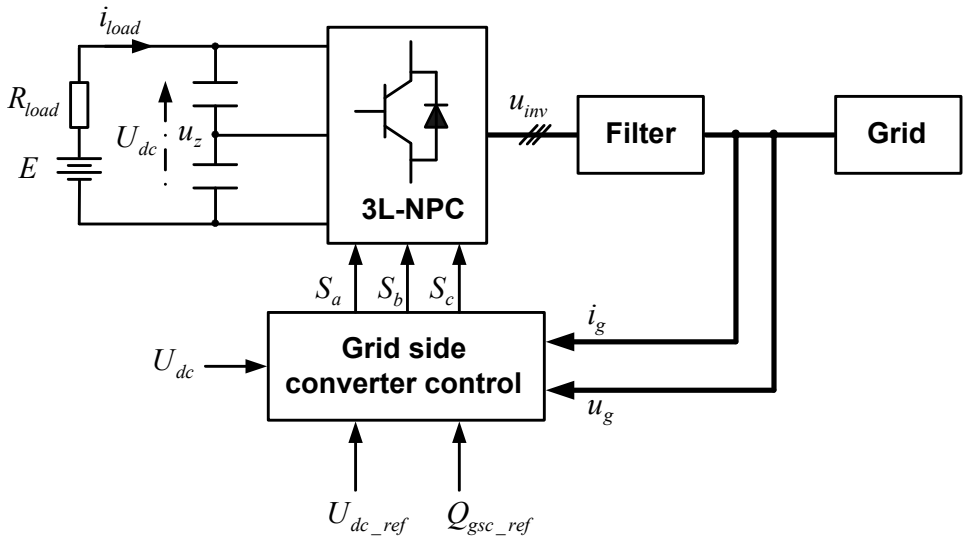

Figure 3.1: Block diagram of grid side converter control.

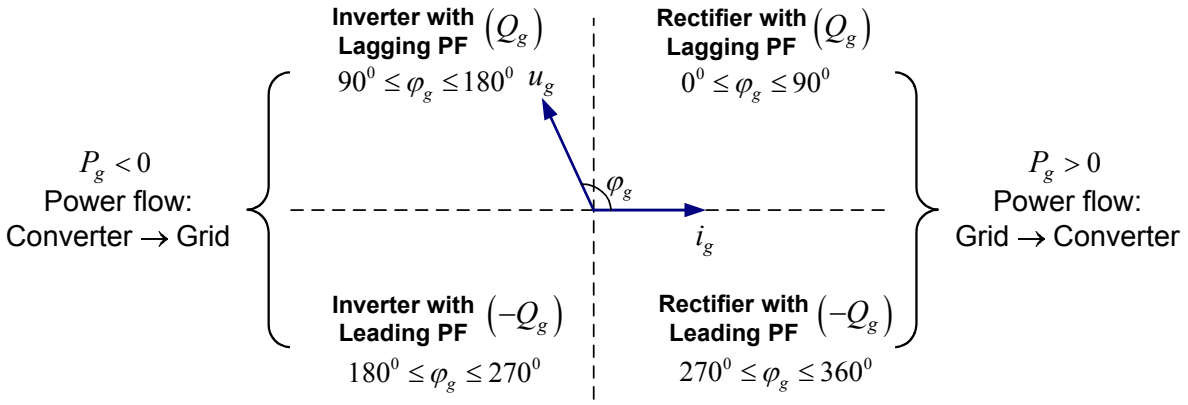

Figure 3.2: The phasor diagram of the grid side converter.

by changing the value of load current i_{load}. When the battery voltage $E > U_{dc}$, the i_{load} becomes positive and power flows from the inverter to the grid, whereas when $E < U_{dc}$ the inverter operates in a rectifying mode and power is absorbed from the grid.

The active and reactive powers exchanged with the grid can be calculated by:

$$P_g = 3U_g I_g \cos\varphi_g = 3U_g I_g PF;\ Q_g = 3U_g I_g \sin\varphi_g, \tag{3.1}$$

where U_g, I_g are the RMS value of the grid phase voltage and current; φ_g is the grid power factor angle. The grid power factor can be unity, lagging or leading based on the power factor angle as shown in Fig. 3.2.

The classical control technique for grid connected inverters is the voltage-oriented control (VOC) [19] or the virtual-flux-oriented control (VFOC) [23] which consit two control loops in the dq reference frame. The inner current loop controls the active and

reactive grid current components while the outer loop controls the DC-link voltage. These methods allow independently controlling the active and reactive powers by the mean of their current components. However, it operates with low dynamic response and its performances depend on the quality of the internal current controller, which is influenced by the accurate tuning of PI parameters and the completeness of current decoupling.

Recently, direct power control (DPC) [29] has been proposed to improve the controller performance. In this technique, the appropriate switching state is selected by a switching look-up table (LUT) based on the instantaneous error between the reference values and estimated values of the active and reactive powers as well as the position of voltage or virtual flux vector. Consequently, this method directly controls the active and reactive powers and no requirement of the current control loops and modulation block is needed. Nevertheless, the drawback of LUT is that it has large active and reactive power ripple and switching frequency variation. Furthermore, a high sampling frequency is required for LUT-DPC to guarantee acceptable steady-state and dynamic performances. With both linear control and hysteresis techniques, the system constraints and technical requirements such as maximum current, total harmonic distortion (THD) and switching frequency can not be considered at the design stage. To solve this problem, several techniques have been developed such as using DPC with SVM [32], sliding mode control [30], [33], proportional resonant [72] and generalized predictive control [49].

In the recent years, finite control set model predictive control (FCS-MPC) is considered as a simple (time-domain) and powerful control strategy for power electronics applications [16, 18, 44, 52, 73, 74]. The main advantage of FCS-MPC is that cascaded control loop structure is no needed and all the controlled variables are added as terms in the cost function. The objective of the cost function is to obtain the sequence of switching action that will minimize the cost function. Hence, no current loops are considered and the inverter switches are directly obtained from cost function minimization, which simplifies the system design.

The present chapter proposes the model predictive power control for grid connected to 3L-NPC inverter while maintaining the balance of the DC-link capacitor voltage and reducing the switching frequency. These objectives are accomplished through the cost function in a predictive control strategy. The main contribution of this chapter is methodological and it will be shown that the presented technique allows to improve the quality of the power regulation, reduce the computational time and the switching losses. A modified control horizon of two prediction steps is used for compensate the computational delay

and improve the dynamic performance of the system. In order to reduce the computational burden, two approaches are proposed in this chapter. To validate the effectiveness of the proposed control method, simulation results are presented and compared with the classical Direct Power Control methods with linear PI controllers and Space Vector Modulation (DPC-SVM).

3.1 Model Predictive Power Control based on Virtual Flux for Grid connected 3L-NPC Inverter

3.1.1 Mathematical model

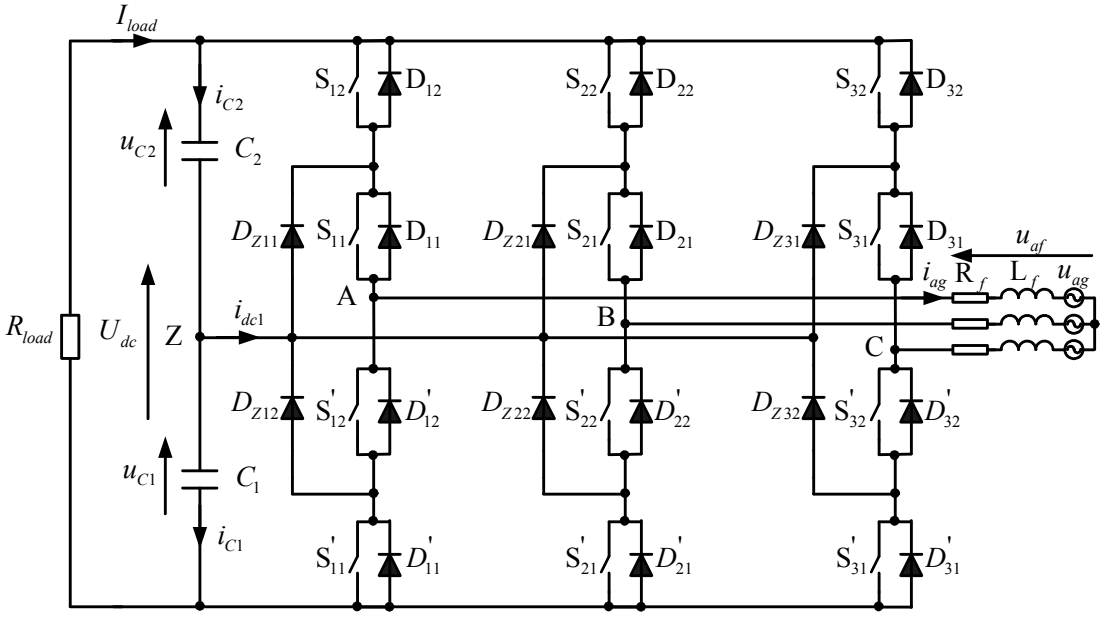

Figure 3.3: The configuration of the grid connected three-level neutral-point clamped inverter.

To analyze the operation of the system, the topological structure of the grid connected 3L-NPC inverter is represented in Fig 3.3. Based on equation (2.11), the neutral-point current i_{dc1} can be calculated from three-phase grid currents and the switching states as follows:

$$i_{dc1} = i_{c2} - i_{c1} = i_{dc1a} + i_{dc1b} + i_{dc1c} = (1 - |S_a|)i_{ag} + (1 - |S_b|)i_{bg} + (1 - |S_c|)i_{cg}. \quad (3.2)$$

Assuming that the DC bus voltage U_{dc} is constant and $C_1 = C_2 = C$, the neutral-point voltage (u_z) can be given by:

$$\frac{du_z}{dt} = -\frac{1}{2C}(i_{dc1}) = -\frac{1}{2C}\Big((1 - |\,S_a|)i_{ag} + (1 - |\,S_b|)i_{bg} + (1 - |\,S_c|)i_{cg}\Big). \tag{3.3}$$

By using the Clarke transformation which is presented in Appendix A, the dynamic of neutral-point voltage can be written as:

$$\frac{du_z}{dt} = \frac{1}{4C}\Big((2|\,S_a| - |\,S_b| - |\,S_c|)i_{g\alpha} + \sqrt{3}(|\,S_b| - |\,S_c|)i_{g\beta}\Big). \tag{3.4}$$

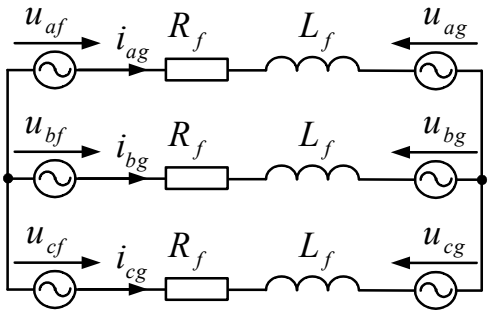

Figure 3.4: Simplified representation of the three-phase grid system.

In addition, the system configured by the grid side inverter, filter and grid voltage can be ideally by represented as shown in Fig. 3.4. So under steady state operation, the electric equation of the systems is given by:

$$u_{inv} = u_g + R_f i_g + L_f \frac{di_g}{dt}, \tag{3.5}$$

where u_g, i_g: are the grid voltage and current and R_f, L_f are the resistance and inductance filter.

The inverter output voltage u_{inv} can be estimated by the measured DC-link voltage and exploiting the knowledge of the current switching state. Based on equations (2.1) and (2.2), after the $\alpha\beta$ transformation this can be expressed as:

$$u_{inv} = \frac{U_{dc}}{6}\Big(2S_a - S_b - S_c + j\sqrt{3}(S_b - S_c)\Big). \tag{3.6}$$

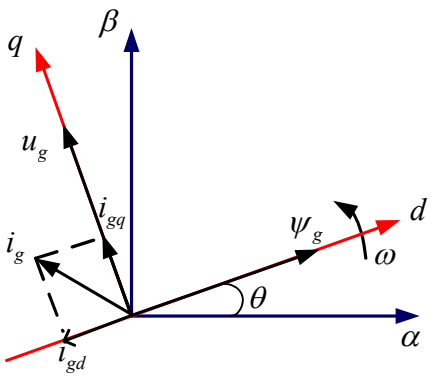

Figure 3.5: Reference coordinates and vectors.

On the other hand, from the Fig. 3.5, we can calculate the grid voltage from the virtual flux of the grid ψ_g as:

$$\begin{aligned} u_{g\alpha} &= \frac{d\psi_{g\alpha}}{dt} = -\left|\psi_g\right| \omega \sin \omega t = -\omega \psi_{g\beta}, \\ u_{g\beta} &= \frac{d\psi_{g\beta}}{dt} = \left|\psi_g\right| \omega \cos \omega t = \omega \psi_{g\alpha}, \end{aligned} \tag{3.7}$$

where ω is the angular frequency of the grid.

Based on equations (3.5) and (3.7) we can express the grid current as follows:

$$\begin{aligned} \frac{di_{g\alpha}}{dt} &= \frac{1}{L_f}\Big(u_{inv\alpha} + \omega \psi_{g\beta} - R_f i_{g\alpha}\Big), \\ \frac{di_{g\beta}}{dt} &= \frac{1}{L_f}\Big(u_{inv\beta} - \omega \psi_{g\alpha} - R_f i_{g\beta}\Big). \end{aligned} \tag{3.8}$$

The virtual grid flux ψ_g is subsequently defined as:

$$\psi_g = \int u_g \, \mathrm{d}t = \int \left(u_{inv} - R_f i_g\right) \mathrm{d}t - L_f i_g \tag{3.9}$$

Neglecting the resistance R_f, the virtual grid flux can be estimated by the virtual flux of the inverter ψ_{inv} as:

$$\psi_g = \psi_{inv} - L_f i_g, \tag{3.10}$$

where ψ_{inv} is derived from equations (3.6).

The active and reactive powers can be calculated as follows [29]:

$$\begin{aligned} P_g &= \frac{3}{2}\Big(u_{g\alpha}i_{g\alpha} + u_{g\beta}i_{g\beta}\Big) = \frac{3}{2}\omega\Big(\psi_{g\alpha}i_{g\beta} - \psi_{g\beta}i_{g\alpha}\Big), \\ Q_g &= \frac{3}{2}\Big(u_{g\beta}i_{g\alpha} - u_{g\alpha}i_{g\beta}\Big) = \frac{3}{2}\omega\Big(\psi_{g\alpha}i_{g\alpha} + \psi_{g\beta}i_{g\beta}\Big). \end{aligned} \tag{3.11}$$

Consequently, we have the continuous-time dynamics of the system in $\alpha\beta$ reference frame based on the equations (3.4), (3.6), (3.7) and (3.8):

$$\begin{aligned} \frac{di_{g\alpha}}{dt} &= \frac{1}{L_f}\Big(\frac{U_{dc}}{6}(2S_a - S_b - S_c) + \omega\psi_{g\beta} - R_f i_{g\alpha}\Big), \\ \frac{di_{g\beta}}{dt} &= \frac{1}{L_f}\Big(\frac{U_{dc}}{2\sqrt{3}}(S_b - S_c) - \omega\psi_{g\alpha} - R_f i_{g\beta}\Big), \\ \frac{d\psi_{g\alpha}}{dt} &= -\omega\psi_{g\beta}, \\ \frac{d\psi_{g\beta}}{dt} &= \omega\psi_{g\alpha}, \\ \frac{du_z}{dt} &= \frac{1}{4C}\Big(\big(2|\,S_a| - |\,S_b| - |\,S_c|\big)i_{g\alpha} + \sqrt{3}\big(|\,S_b|) - |\,S_c|\big)i_{g\beta}\Big). \end{aligned} \tag{3.12}$$

Or the continuous-time dynamics of the system can be expressed as:

$$\begin{aligned} \frac{dx}{dt} &= Ax + B_1 u + B_2(x)|\,u|, \\ y &= g(x), \end{aligned} \tag{3.13}$$

where $x = [i_{g\alpha}\ i_{g\beta}\ \psi_{g\alpha}\ \psi_{g\beta}\ u_z]^T$, $u = [S_a\ S_b\ S_c]^T$, $S_x \in \{-1, 0, 1\}$, $y = [P_g\ Q_g]^T$,

$$A = \begin{bmatrix} -R_f/L_f & 0 & 0 & \omega/L_f & 0 \\ 0 & -R_f/L_f & -\omega/L_f & 0 & 0 \\ 0 & 0 & 0 & -\omega & 0 \\ 0 & 0 & \omega & 0 & 0 \\ 0 & 0 & 0 & 0 & 0 \end{bmatrix}; B_1 = \frac{U_{dc}}{2L_f} \begin{bmatrix} 2/3 & -1/3 & -1/3 \\ 0 & 1/\sqrt{3} & -1/\sqrt{3} \\ 0 & 0 & 0 \\ 0 & 0 & 0 \\ 0 & 0 & 0 \end{bmatrix},$$

$$B_2(x) = \frac{1}{4C} \begin{bmatrix} 0 & 0 & 0 \\ 0 & 0 & 0 \\ 0 & 0 & 0 \\ 0 & 0 & 0 \\ 2i_{g\alpha} & -i_{g\alpha} + \sqrt{3}i_{g\beta} & -i_{g\alpha} - \sqrt{3}i_{g\beta} \end{bmatrix}; g(x) = \frac{3}{2}\omega \begin{bmatrix} \psi_{g\alpha} i_{g\beta} - \psi_{g\beta} i_{g\alpha} \\ \psi_{g\alpha} i_{g\alpha} + \psi_{g\beta} i_{g\beta} \end{bmatrix} \tag{3.14}$$

This bi-linear dynamics with the particularity that the control set is represented by a finite set of control moves.

3.1.2 Model predictive direct power control for 3L-NPC inverter

The aim of the predictive direct power control scheme is to:

- Minimize the error between the predicted active and reactive powers and their reference values.
- Maintain voltage balance of the DC-link capacitor.
- Reduce the switching frequency.

In order to translate these objectives in a convex cost formulation, we consider the following terms in the optimization problem for the grid connected 3L-NPC inverter with two-step prediction [12], [52], [61]:

$$\begin{aligned} g_{grid}(u_k, u_{k+1}) = &\left|P_g^*(k+1) - P_g^p(k+1)\right| + \left|P_g^*(k+2) - P_g^p(k+2)\right| \\ &+ \left|Q_g^*(k+1) - Q_g^p(k+1)\right| + \left|Q_g^*(k+2) - Q_g^p(k+2)\right| \\ &+ \lambda_{dc}\left|u_z^p(k+2)\right| + \lambda_n n_c, \end{aligned} \tag{3.15}$$

where P_g^p and Q_g^p are the predicted active and reactive powers; P_g^* and Q_g^* are the reference values for active and reactive powers; λ_{dc} and λ_n are the weighting factors of the capacitor voltage balancing and the reduction of commutation.

The weighting factors λ_{dc}, λ_n play the role of tuning parameters for the control law and can be adjusted to obtain an acceptable quality of the current, maintain the capacitor voltage balancing and reduce the switching frequency, which it is not easy for the conventional control methods. The detail of the selection process and influence of these parameters will present in next section.

In the cost function (3.15) n_c penalizes the number of switching change when the switching state $S(k)$ is applied compared with previous state $S(k-1)$. It can be expressed as follows:

$$n_c = |\,S_a(k) - S_a(k-1)\,| + |\,S_b(k) - S_b(k-1)\,| + |\,S_c(k) - S_c(k-1)\,|. \tag{3.16}$$

The equation (3.13) can be discretized considering T_s as a sampling period and k as the sampling time by using zero-order hold (ZOH) with no delay:

$$x(k+1) = A_d x(k) + B_{1d} u(k) + B_{2d}(x)\,|\,u(k)\,|, \tag{3.17}$$

where

$$A_d = e^{AT_s} \approx I + AT_s;\;\; B_{1d} = \int_0^{T_s} e^{A(T_s - d\tau)} B_1 d\tau \approx B_1 T_s;\;\; B_{2d}(x) \approx T_s B_2(x(k)), \tag{3.18}$$

and I is the 5x5 identity matrix.

According to equations (3.17) and (3.18), the grid current is represented in discrete-time at instant $k+1$ as follows:

$$\begin{aligned} i_{g\alpha}^p(k+1) &= \Big(1 - \frac{R_f T_s}{L_f}\Big) i_{g\alpha}(k) + \frac{T_s}{L_f}\omega\psi_{g\beta}(k) + \frac{T_s}{6L_f} U_{dc}\Big(2S_a(k) - S_b(k) - S_c(k)\Big), \\ i_{g\beta}^p(k+1) &= \Big(1 - \frac{R_f T_s}{L_f}\Big) i_{g\beta}(k) - \frac{T_s}{L_f}\omega\psi_{g\alpha}(k) + \frac{T_s}{6L_f} U_{dc}\Big(S_b(k) - S_c(k)\Big), \end{aligned} \tag{3.19}$$

where the virtual grid fluxes $\psi_{g\alpha}(k)$, $\psi_{g\beta}(k)$ are estimated from the equation (3.10).

Thus, the discrete-time forms for grid current can also be evaluated at instant $k+2$ as:

$$\begin{aligned} i^p_{g\alpha}(k+2) &= \Big(1-\frac{R_f T_s}{L_f}\Big) i^p_{g\alpha}(k+1) + \frac{T_s}{L_f}\omega\psi^p_{g\beta}(k+1) \\ &\quad + \frac{T_s}{6L_f}U_{dc}\Big(2S_a(k+1) - S_b(k+1) - S_c(k+1)\Big), \\ i^p_{g\beta}(k+2) &= \Big(1-\frac{R_f T_s}{L_f}\Big) i^p_{g\beta}(k+1) - \frac{T_s}{L_f}\omega\psi^p_{g\alpha}(k+1) + \frac{T_s}{6L_f}U_{dc}\Big(S_b(k+1) - S_c(k+1)\Big). \end{aligned} \tag{3.20}$$

In the same way, the virtual grid fluxes are expressed based on the equations (3.10) and (3.17) as:

$$\begin{aligned} \psi^p_{g\alpha}(k+1) &= \psi^p_{inv\alpha}(k+1) - L_f i^p_{g\alpha}(k+1), \\ \psi^p_{g\beta}(k+1) &= \psi^p_{inv\beta}(k+1) - L_f i^p_{g\beta}(k+1), \\ \psi^p_{g\alpha}(k+2) &= \psi^p_{g\alpha}(k+1) - T_s\omega\psi^p_{g\beta}(k+1), \\ \psi^p_{g\beta}(k+2) &= \psi^p_{g\beta}(k+1) + T_s\omega\psi^p_{g\alpha}(k+1). \end{aligned} \tag{3.21}$$

The evolution of neutral-point voltage for two-step prediction is obtained by using equations (3.17) and (3.12). Then its expression is given by:

$$\begin{aligned} u^p_z(k+1) &= u_z(k) + \frac{T_s}{4C}\big(2|\,S_a(k)| - |\,S_b(k)| - |\,S_c(k)|\big) i_{g\alpha}(k) \\ &\quad + \frac{\sqrt{3}T_s}{4C}\big(|\,S_b(k)| - |\,S_c(k)|\big) i_{g\beta}(k), \\ u^p_z(k+2) &= u^p_z(k+1) + \frac{\sqrt{3}T_s}{4C}\big(|\,S_b(k+1)| - |\,S_c(k+1)|\big) i^p_{g\beta}(k+1) \\ &\quad + \frac{T_s}{4C}\big(2|\,S_a(k+1)| - |\,S_b(k+1)| - |\,S_c(k+1)|\big) i^p_{g\alpha}(k+1). \end{aligned} \tag{3.22}$$

Since the active and reactive power references are DC quantities, to reduce the computational time and the oscillations in the powers when an abrupt change occurs in the reference, the extrapolation can be simplified as follows:

$$\begin{aligned} P^*_g(k+2) &= P^*_g(k+1) = P^*_g(k), \\ Q^*_g(k+2) &= Q^*_g(k+1) = Q^*_g(k). \end{aligned} \tag{3.23}$$

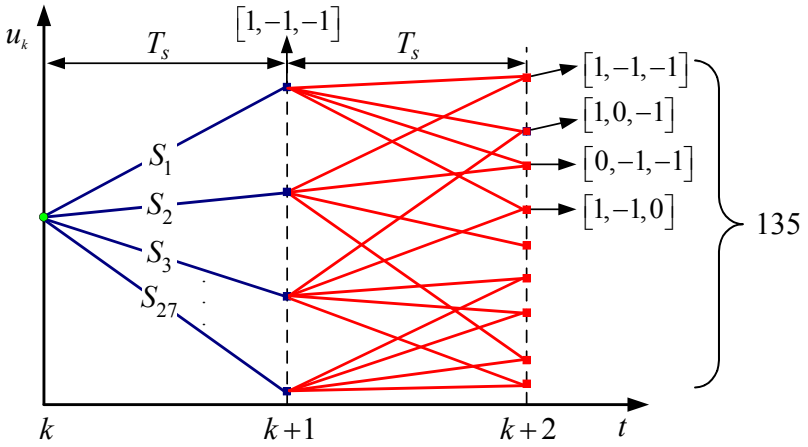

(a) Control variable prediction with two-step horizon

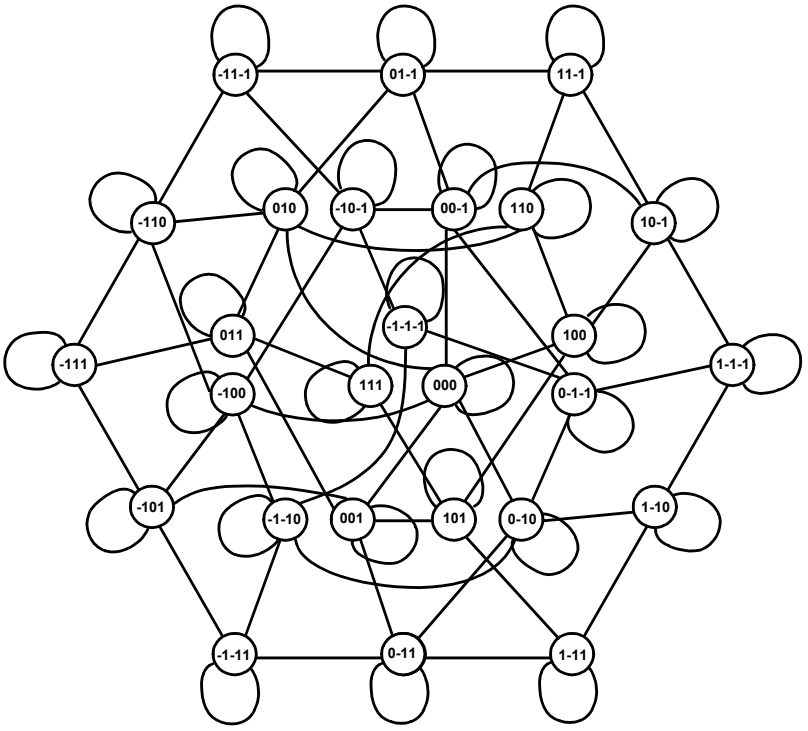

(b) Switching transitions of 3L-NPC inverter

Figure 3.6: The proposed control method with two-step horizon for reduce computational cost.

As previously mentioned, there are 27 voltage vectors which have to be evaluated within one step prediction. When two steps are considered for prediction, a discrete set of $27^2 = 729$ possible trajectories of the switching states has to be considered for the cost function, leading to a large number of cost computations which makes the real challenge to the actual digital system implementation. In order to avoid a high jump in phase voltage and reduce the number of commutations, it is possible to limit the possible switching transitions. In this section, we propose to consider the combinations of inputs

having only one switching variation at the instant $k+2$, as shown in Fig. 3.6. For example if $u(k+1) = [1,-1,-1]$, for $u(k+2)$ the set $\{[1,-1,-1],[1,0,-1],[0,-1,-1]$ and $[1,-1,0]\}$ is considered. This leads to 135 combinations. Thus, the computations required are limited with respect to the total of 729 trajectories. Therefore, the optimal control action u_{opt} is obtained as the result of equation (3.24):

$$u_{opt} = \arg\left\{ \min_{u_k \in \{-1,0,1\}^3, u_{k+1} \in \{-1,0,1\}^3} g_{grid}\left(u_k, u_{k+1}\right) \right\}. \tag{3.24}$$
$$\text{subject to } \|u_k - u_{k+1}\| < 1$$

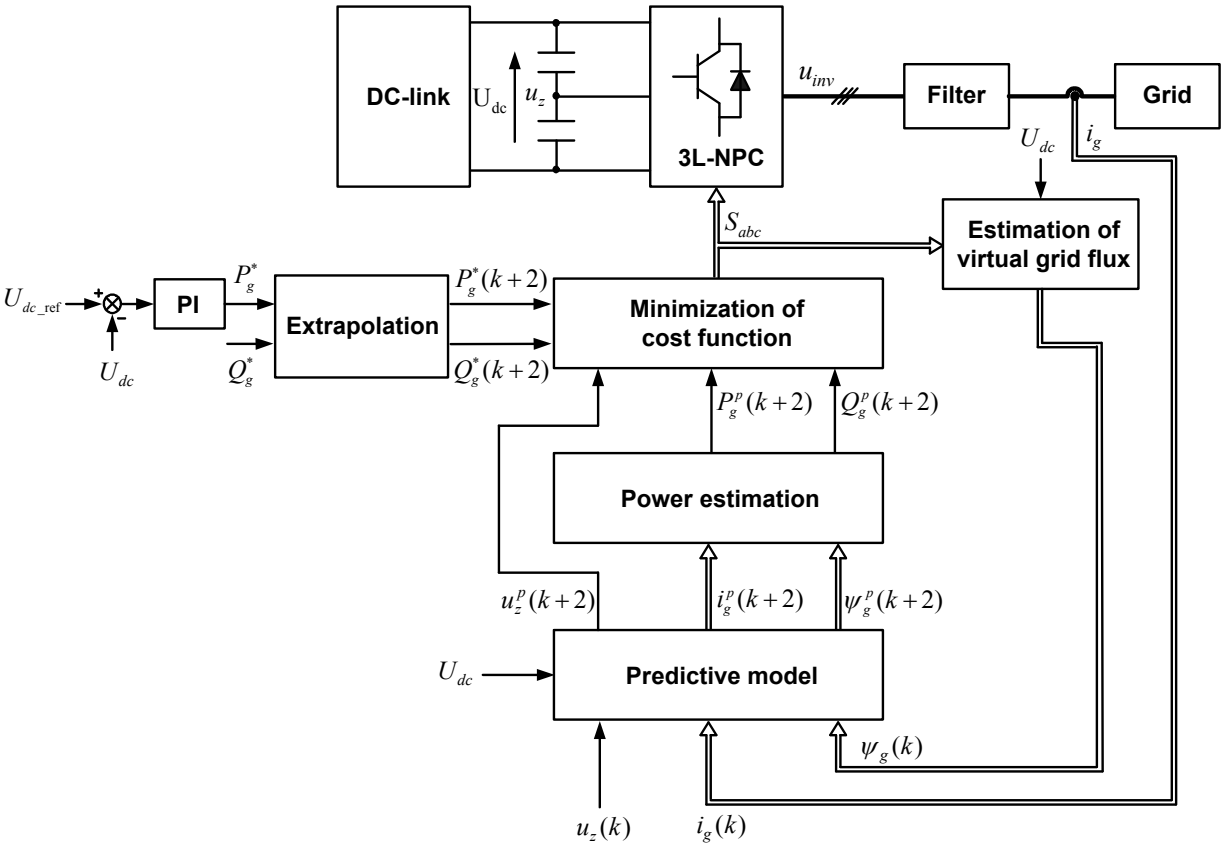

Figure 3.7: MPPC-VF control scheme for grid connected to 3L-NPC inverter.

Finally, the objective of proposed predictive control can be obtained by evaluation of the cost function for all trajectories (see algorithm 1). The overall control system is illustrated in the Fig. 3.7.

Algorithm 1: Algorithm of model predictive power control based on virtual flux for grid connected 3L-NPC inverter

Measure $i_g(k)$, $u_z(k)$ and U_{dc}; Read the reference values $U_{dc-ref}(k)$ and $Q_g^*(k)$;
Estimation of virtual grid flux $\psi_g(k)$ by using equations (3.6) and (3.10);
Extrapolation of references $P_g^*(k+2)$ and $Q_g^*(k+2)$ based on equation (3.23);
/* x_{opt}, g_{opt} are the optimal values of the switching states and cost function */
Initialize optimal values of the switching state x_{opt} and cost function g_{opt} ;
for $i = 1$ *to* 27 **do**
  Prediction of variables: $i_g^p(k+1)$, $\psi_g^p(k+1)$ and $u_z^p(k+1)$ from equations (3.19), (3.21) and (3.22);
  Predict switching transitions corresponding;
  /* m = length(switching transitions corresponding) */
  for $j = 1$ *to* m **do**
    Predict next state of variables: $i_g^p(k+2)$, $\psi_g^p(k+2)$ and $u_z^p(k+2)$ from equations (3.19), (3.21) and (3.22);
    Calculate the number of switching change n_c by using equation (3.16);
    Estimation of power: $P_g^p(k+2)$ and $Q_g^p(k+2)$ based on equation (3.11);
    Compute the cost function g_{grid} from (3.15);
    if $g_{grid} < g_{opt}$ **then**
      $g_{opt} = g_{grid}$; $x_{opt} = i$;
Store the present value of x_{opt} and apply optimal switching states: S_a, S_b, S_c;

3.1.3 DC-link voltage controller

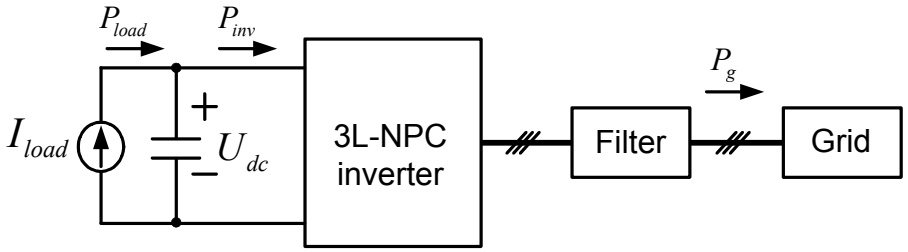

Figure 3.8: DC-link system.

The first objective of the controller is to keep constant the DC-bus voltage. In addition, it must control active power that the voltage source inverter exchanges with the grid (Fig. 3.8). We can have the relation that represents the transfer of power:

$$P_{load} - P_{inv} = \frac{1}{2} C_{dc} \frac{du_{dc}^2}{dt}, \tag{3.25}$$

where C_{dc} is the DC-bus equivalent capacitor: $C_{dc} = C_1/2 = C_2/2 = C/2$; P_{load}, P_{inv} are the load power and inverter output power.

According the equation (3.25), considering u_{dc}^2 the state variable and the output: $z = u_{dc}^2$, P_{inv}, P_{load} are considered as the control input and an external disturbance. Neglecting the losses in the inverter and filter, the active power in the inverter output power P_{inv} is equal the active power of the grid P_g. So, the dynamic system can be modeled by the Fig. 3.9. It can be written as follows:

$$\frac{1}{2}C_{dc}\frac{du_{dc}^2}{dt} = \frac{1}{2}C_{dc}\frac{dz}{dt} = P_{load} - P_g = -\left(P_g - P_{load}\right). \tag{3.26}$$

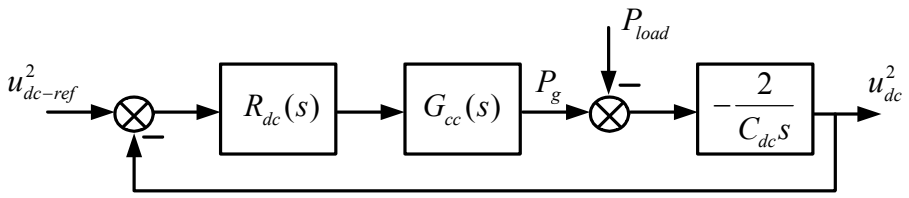

Figure 3.9: Block diagram of the DC-link voltage regulation loop.

$G_{cc}(s)$ is the transfer function of inner current controller dynamics with current control method or power controller dynamics with direct power control method. In this work, it is approximated by the first order transfer function with equivalent time constant T_c as [19]:

$$G_{cc}(s) = \frac{1}{1 + T_c s}, \tag{3.27}$$

where $T_c = 4T_\Sigma = 4\left(T_s + T_{PWM}\right)$ for power controllers designed by symmetric optimum (SO) criterion.

$R_{dc}(s)$ is the controller transfer function of DC-link voltage: $R_{dc}(s) = K_p\frac{1 + T_{dc1}s}{1 + T_{dc2}s}$. The open loop transfer function of the system can be derived:

$$G_{ol}(s) = K_p\frac{1 + T_{dc1}s}{1 + T_{dc2}s}\frac{1}{1 + T_c s}\frac{2}{C_{dc}s}, \tag{3.28}$$

T_{dc1} is chosen equal to T_c. Therefore, the closed loop transfer function can be expressed as:

$$G_{cl}(s) = \frac{2K_p}{2K_p + T_{dc2}C_{dc}s^2 + C_{dc}s} = \frac{\omega_n^2}{s^2 + 2\xi\omega_n s + \omega_n^2}, \tag{3.29}$$

where ω_n is the natural frequency and ξ is the damping ratio of the system.

DC-bus regulator is the outer control loop, so it is designed to have larger settling time than the current loop controllers in order to guarantee stable system response.

On the other hand, from equation (3.29) we can calculate the parameters of the controller as:

$$\begin{cases} T_{dc2} = \dfrac{1}{2\xi\omega_n} \\ K_p = \dfrac{\omega_n C_{dc}}{4\xi} \end{cases} \tag{3.30}$$

3.1.4 Simulation results

In order to validate the effectiveness of the proposed model predictive control strategy for grid connected 3L-NPC inverter under different conditions of power references, the whole control scheme were carried out using MATLAB/Simulink environment with the parameters as indicated in Table 3.1.

Table 3.1: Electrical and control parameters for simulation.

Parameter	Value	Description
U_{dc}	600 [V]	DC-link voltage
C	940 [μF]	DC-link capacitor
R_f	80 [$m\Omega$]	Filter resistance
L_f	10 [mH]	Filter inductance
f_{sp}	20 [kHz]	Sampling frequency
f	50 [Hz]	Frequency of the grid
U_{dm}	220 [V]	Rated phase grid voltage
P_{dm}	15 [kW]	Rated active power
I_{dm}	32 [A]	Rated current
λ_{dc}	100	Weighting factor of the voltage balancing
λ_n	150	Weighting factor of the switching frequency
ξ, ω_n	0.707, 313.78	Parameters for DC-link voltage controller

The performance of the proposed method for power control was tested by applying a step in the active power reference P_g^* without DC bus voltage control. The step change in P_g^* from 15 to -15 kW is applied at $t = 0.15$ s, with a unitary power factor reactive power set point set to zero $Q_g^* = 0$ (Fig. 3.25). Fig. 3.10(a) shows that the active power flow of the inverter system is bidirectional. When the active power is transferred from the grid to the DC-link ($P_g > 0$), the inverter operates in a rectifying mode, whereas when the power is delivered from the DC-link to the grid, the inverter is in an inverting mode ($P_g < 0$). The active power tracks the assigned reference with good performance

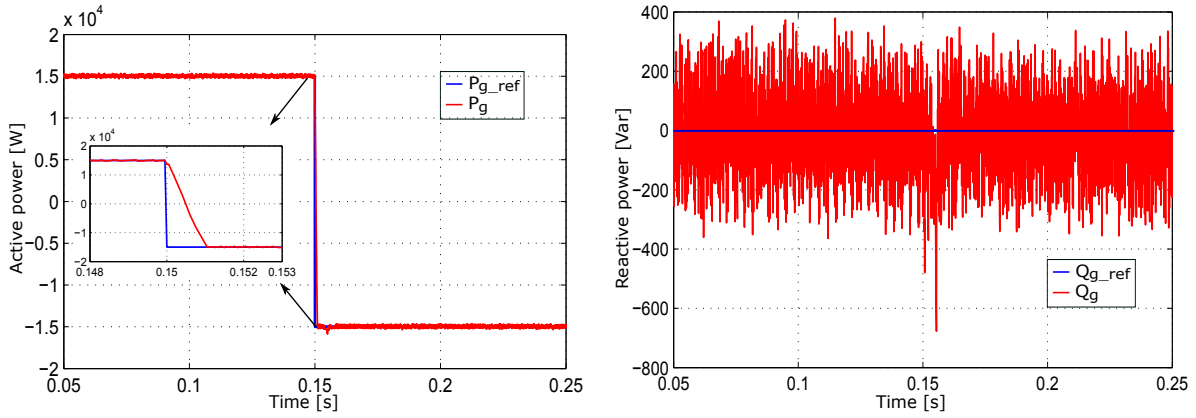

(a) Active power (b) Reactive power

Figure 3.10: The predictive power transient responses for a step in the active power reference from 15 to -15 kW.

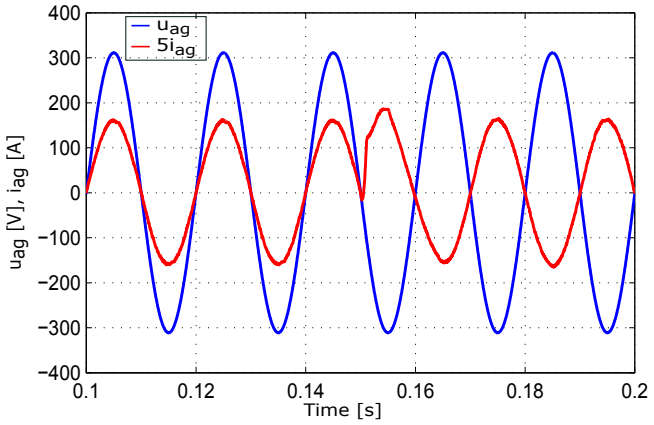

Figure 3.11: The single phase grid voltage with corresponding grid current.

in what it may concern during the transient and steady-state conditions. The phase shift between the voltage and current is also shown for this change in the power factor from 1 to -1 (Fig. 3.11).

With the purpose of verify the dynamic performances, we perform a comparison between MPPC-VF and Direct Power Control with linear PI controllers [19] and Space Vector Modulation [25] (DPC-SVM) for different conditions of references and the same parameters in Table 3.1. To generate the same average device switching frequency, the sampling frequency of the MPPC-VF is considered $f_{sp} = 20$ kHz and the sampling frequency of the DPC-SVM is 5 kHz. For the SVM at 5 kHz, $f_{sw} = 2.5$ kHz and the measured value of f_{sw} for MPPC-VF is about 2.5 kHz. In order to observe the dynamics ability to track the active and reactive power reference, several power steps has been applied to its references in the grid side. The active power reference presents a steps from

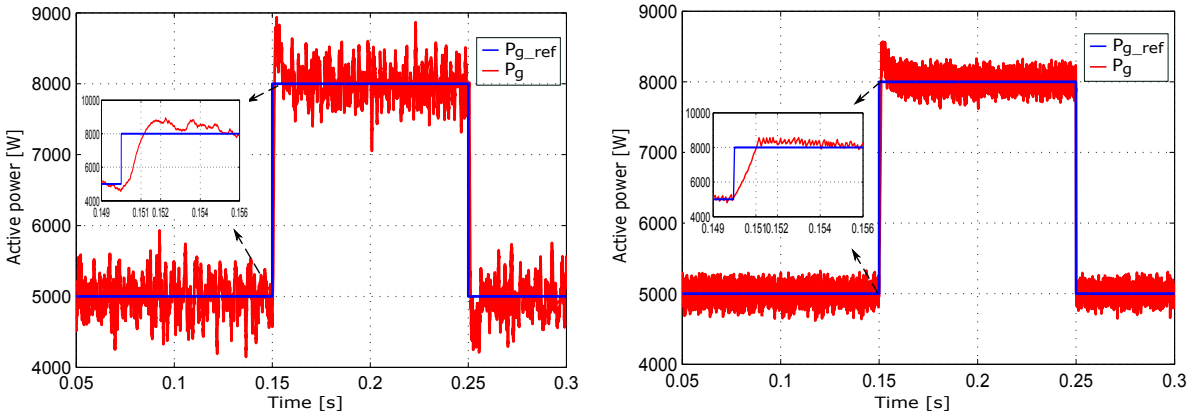

(a) DPC-SVM (b) MPPC-VF

Figure 3.12: The dynamic response of active power.

Table 3.2: Comparison of transient performance for two controllers.

Reference step	$P_g^* = 5 \rightarrow 8\,(kW)$		$P_g^* = 8 \rightarrow 5\,(kW)$	
	DPC-SVM	MPPC-VF	DPC-SVM	MPPC-VF
Rise time (ms)	1.2	1	1.2	0.12
Settling time (ms)	5	2	7	0.17
Overshoot (%)	11.75	7.12	12.5	3.4

5 kW to 8 kW at instant $t = 0.15$ s, then steps from 8 kW to 5 kW at instant $t = 0.25$ s (Fig. 3.12), while the reactive power reference is changed from -2 kVar for leading power factor operation to 2 kVar for lagging power factor operation at instant $t = 0.2$ s (Fig. 3.25(b)). The results shown in Figs. 3.12(b) and 3.13(b) indicate that the active power is tracking the reference with fast dynamics as confirmed by the Table 3.2. Settling time is the time taken by using a band of 5% for the reference steps, and the rise time is defined as the time required for the current to increase from the 10% to the 90% of the reference step change. The transient active power from 5 kW to 8 kW reaches its steady state in 2 ms with the proposed method and 5 ms, respectively for DPC-SVM. The mean absolute percentage error of active and reactive power for DPC-SVM is 3.9% and 10.48%, whereas, for the proposed method they are 2.08%, and 5.61%, respectively. Consequently, the proposed method presents better performance compared to the DPC-SVM. Moreover, the average running time of the algorithm is 35 μs in a 3.3 GHz, i5-6600 CPU. This makes the proposed control a feasible option for high performance digital controller.

The steady state behavior of the inverter phase voltage is performed with the total harmonic distortion (THD) for the proposed method of 23.08% in comparison with a classical method distortion of 27.72%. The transient responses of the grid current, i_{ag}

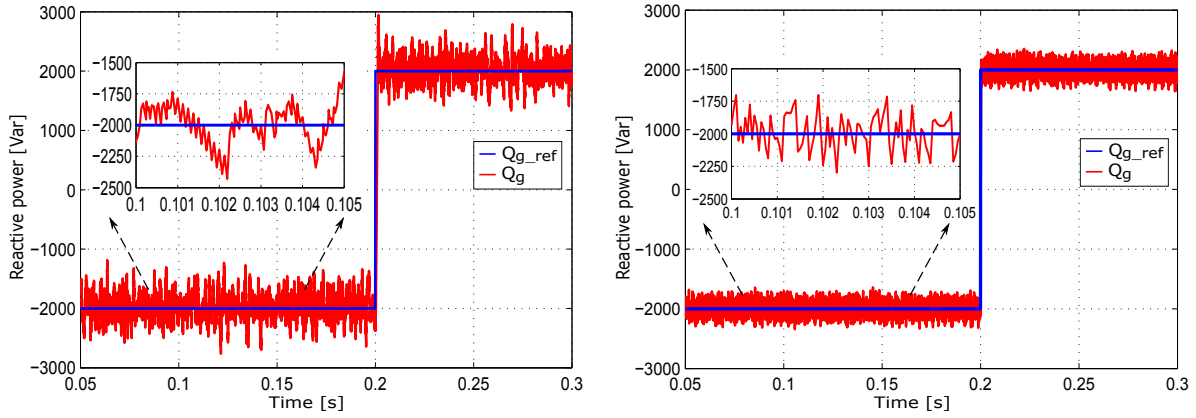

(a) DPC-SVM (b) MPPC-VF

Figure 3.13: The dynamic response of reactive power.

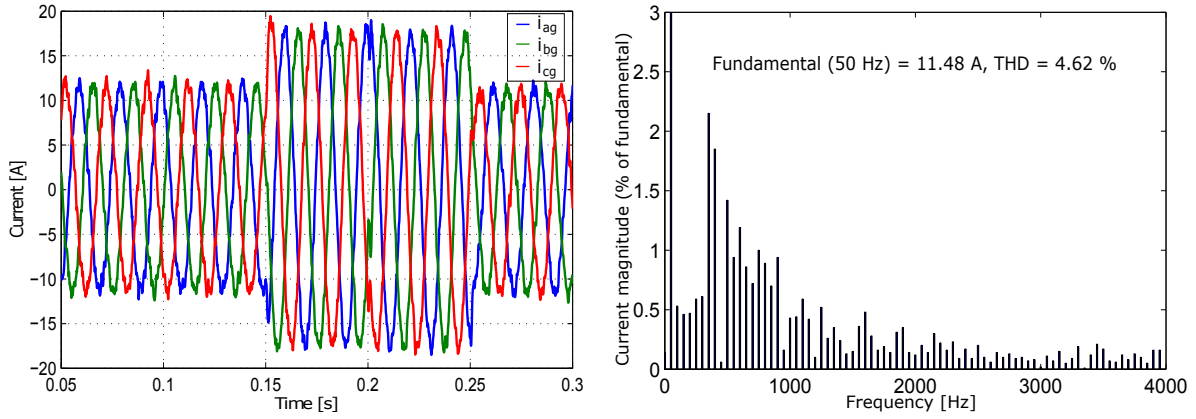

(a) The steady state and transient response of the grid current (b) Fast Fourier Transform of the grid current

Figure 3.14: The dynamic response and FFT of the grid current for DPC-SVM.

and its FFT are illustrated in Figs. 3.14 and 3.15, where the THD is found to be lower for the proposed method in contrast to the classical controller. The THD of grid current is under the 5% limit required by the IEEE 519 standards.

To investigate the robustness of the proposed method against load variation, a resistance load R_{load} is changed from 72 Ω to 45 Ω at the instant $t = 0.15$ s and from 45 Ω to 72 Ω at $t = 0.25$ s corresponding to the change of reference active power. The effect of DC side load on the operation of system is shown in Fig 3.18. As shown in this figure, with the proposed method the change in load doesn't affect too much to the transition of the DC-link voltage with lower overshoot (5.5 V) while linear PI control results in much higher value (8 V). One of the important issues of 3L-NPC structure is the balancing voltage of the DC-link capacitor. The voltage of DC-link capacitor will clearly remain

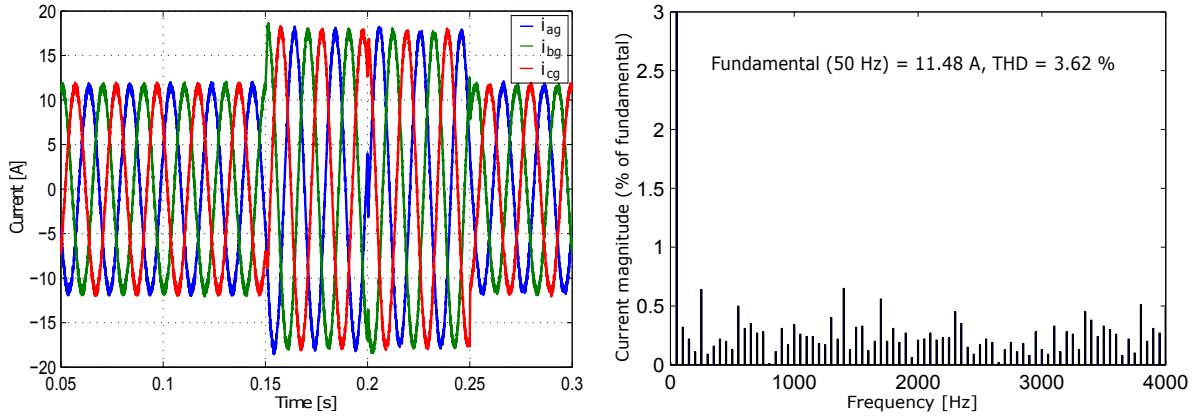

(a) The steady state and transient response of the grid current

(b) Fast Fourier Transform of the grid current

Figure 3.15: The dynamic response and FFT of the grid current for MPPC-VF.

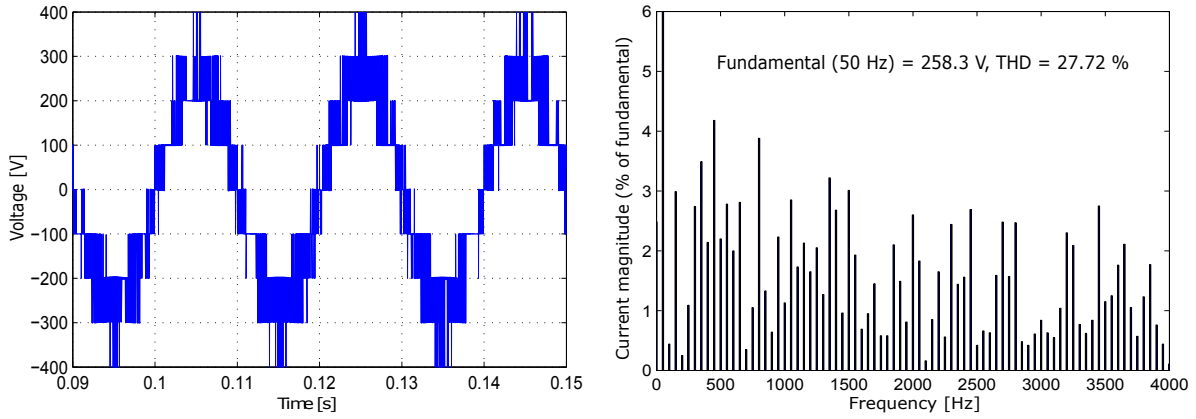

(a) The steady state of the inveter's output voltage

(b) Fast Fourier Transform of the output voltage

Figure 3.16: The steady state and FFT of the inverter's ouput voltage for DPC-SVM.

balanced with MAPE of DC-link capacitor voltages deviation for MPPC-VF 0.27% and for DPC-SVM 1.1% in spite of the transition of the power references (Fig. 3.19).

Since the performance of FCS-MPC depends largely on the sampling time, which is improved by selecting the smaller sampling period. To analyze the effect of sampling time on the quality of the current, the proposed control strategy is applied with four sampling times $20\,\mu s, 50\,\mu s$, $80\,\mu s$ and $100\,\mu s$. To evaluate the quality of the system, the THD of the grid current can be considered. Table 3.3 indicates that the quality of grid current is the best with sampling time $T_s = 20\,\mu s$ and the worst when the sampling time $100\,\mu s$ is considered. However, there is a limited sampling time due to the requirement of execution time such as computational time, measurement of signal and grid voltage orientation. In

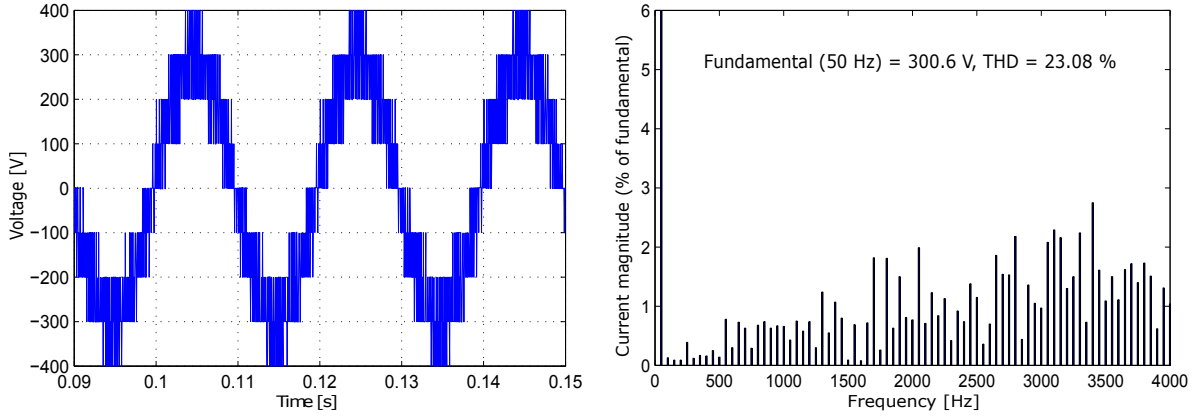

(a) The steady state of the inveter's output voltage

(b) Fast Fourier Transform of the output voltage

Figure 3.17: The steady state and FFT of the inverter's output voltage for proposed method.

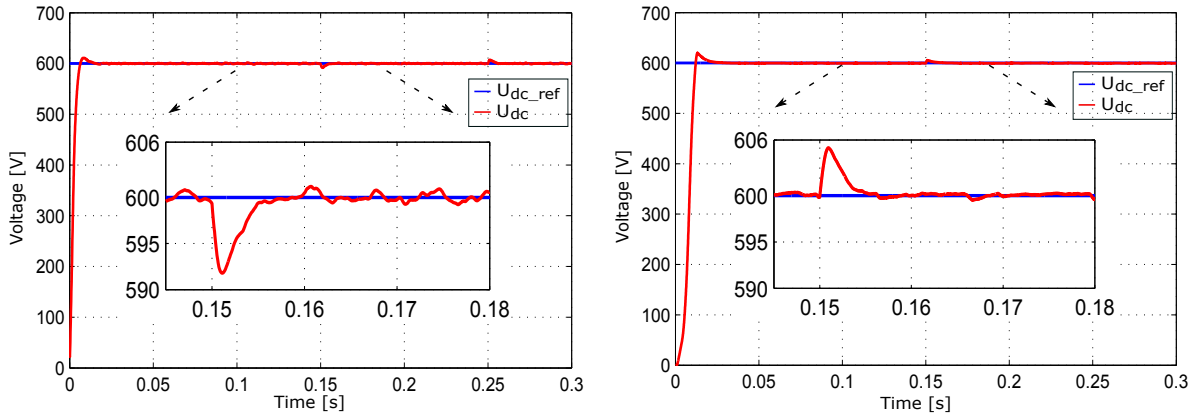

(a) DPC-SVM

(b) MPPC-VF

Figure 3.18: The DC-link voltage response with load change at $t = 0.15$ s and 0.25 s.

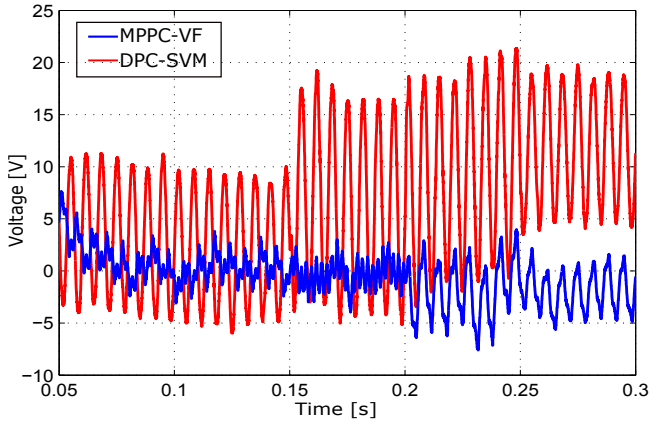

Figure 3.19: Performance of the neutral-point voltage u_z.

Table 3.3: Comparison of THD with different sampling time.

Sampling time (T_s)	Total harmonic distortion of i_{ag} (%)
20 (μs)	2.11
50 (μs)	3.62
80 (μs)	4.48
100 (μs)	4.66

addition, a smaller sampling period will result in a higher switching frequency which is not recommended for high power application. For this reason, the sampling time in the $50 - 100\,\mu s$ range can be selected for FCS-MPC method.

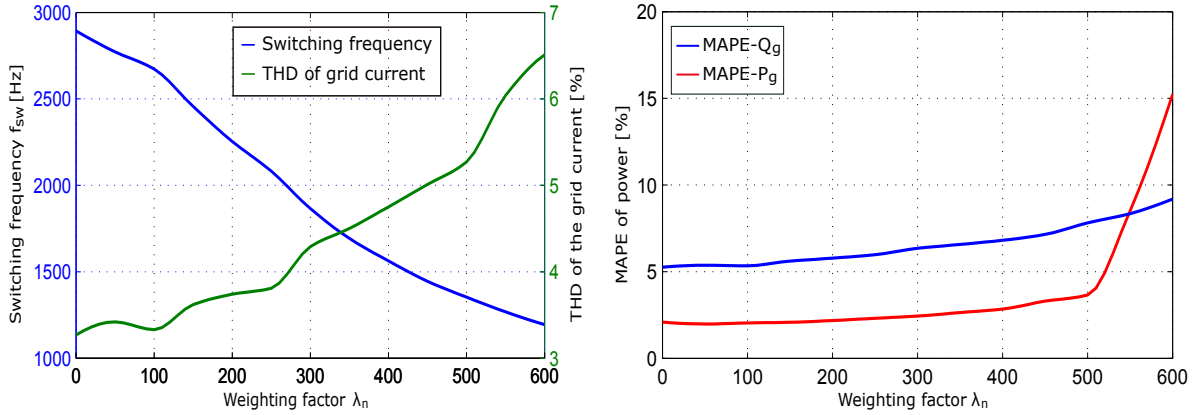

(a) (b)

Figure 3.20: Weighting factor influence on: (a) The THD of the grid current and average switching frequency. (b) The power errors.

The issue in FCS-MPC is the selection of weighting factor in the cost function, but this problem can be solved by using the guidelines proposed in [42]. A high value of λ_{dc} will assure the balance of DC-link capacitor voltages but increase the tracking power errors and THD of the grid current. A good suggestion for select λ_{dc} so that the neutral-point voltage deviation of the DC-link voltage is around 3% of nominal DC-link voltage as indicated in Fig. 3.19. On the other hand, by increasing the weighting factor λ_n, we can reduce the switching frequency, leads to reduce the switching losses. The THD of grid current and power tracking errors also increase due to the additional weighting term λ_n. By running a simulation and gradually increasing the value of λ_n, a satisfactory weighting factor can be obtained by evaluating the performance such as the THD of the grid current, MAPE of power errors. As the weighting factor λ_n increases from 0 to 600, the average switching frequency f_{sw} reduces from 2893 to 1194 Hz with a increase in power errors (Fig. 3.20(b)) and the THD of the grid current from 3.27% to 6.51% (Fig. 3.20(a)). For this reason, the weighting factors λ_{dc} and λ_n can be selected at 100 and 150

to achieve an acceptable quality of current, capacitor voltage balancing and reduction of switching frequency.

3.2 Modified Model Predictive Control with reduced computational cost

3.2.1 Mathematical model based on voltage orientation

By using rotational transformation, the dynamics can be described in dq reference frame based on the equation (3.5) as:

$$u_{inv\_d} = R_f i_{gd} + L_f \frac{di_{gd}}{dt} + u_{gd} - \omega L_f i_{gq}, \tag{3.31}$$
$$u_{inv\_q} = R_f i_{gq} + L_f \frac{di_{gq}}{dt} + u_{gq} + \omega L_f i_{gd},$$

where ω is the angular frequency of the grid.

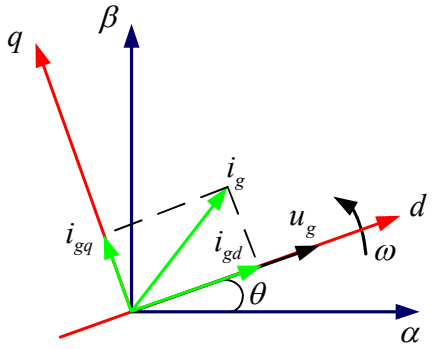

Figure 3.21: Vector presentation in stationary ($\alpha\beta$) and synchronously rotating (dq) reference frames.

Since the system is oriented with grid voltage (Fig. 3.21), the components of grid voltage can be expressed:

$$u_{gq} = 0; \; u_{gd} = \hat{U}_g, \tag{3.32}$$

where $\hat{U}_g$ is the magnitude of the grid voltage which is obtained by the phase locked loop (PLL).

Consequently, we have the continuous-time dynamics of the system based on grid voltage orientation from the equations (3.3), (3.31) and (3.32) as follows:

$$\begin{aligned}
\frac{di_{gd}}{dt} &= -\frac{R_f}{L_f} i_{gd} + \frac{1}{L_f}(u_{inv_d} - \hat{U}_g) + \omega i_{gq}, \\
\frac{di_{gq}}{dt} &= -\frac{R_f}{L_f} i_{gq} + \frac{1}{L_f} u_{inv_q} - \omega i_{gd}, \\
\frac{du_z}{dt} &= \frac{1}{4C}\Big(\big(2|\,S_a| - |\,S_b| - |\,S_c|\big) i_{g\alpha} + \sqrt{3}\big(|\,S_b|\big) - |\,S_c|\big) i_{g\beta} \Big),
\end{aligned} \tag{3.33}$$

where the grid current in dq reference frame can be calculated from the grid current in $\alpha\beta$ reference frame by using rotational transformation:

$$\begin{aligned}
i_{gd} &= i_{g\alpha}\cos\theta + i_{g\beta}\sin\theta, \\
i_{gq} &= i_{g\beta}\cos\theta - i_{g\alpha}\sin\theta.
\end{aligned} \tag{3.34}$$

Similarly, the inverter output voltage in dq reference frame can be estimated based on equations (2.1) and (2.2) as:

$$\begin{aligned}
u_{inv_d} &= \frac{U_{dc}}{6}\left((2S_a - S_b - S_c)\cos\theta + \sqrt{3}\,(S_b - S_c)\sin\theta \right), \\
u_{inv_q} &= \frac{U_{dc}}{6}\left(\sqrt{3}\,(S_b - S_c)\cos\theta - (2S_a - S_b - S_c)\sin\theta \right).
\end{aligned} \tag{3.35}$$

From the output control point of view, the active and reactive powers exchanged with the grid can be calculated as follows [29]:

$$\begin{aligned}
P_g &= \frac{3}{2}\left(u_{gd} i_{gd} + u_{gq} i_{gq}\right) = \frac{3}{2}\hat{U}_g i_{gd}, \\
Q_g &= \frac{3}{2}\left(u_{gq} i_{gd} - u_{gd} i_{gq}\right) = -\frac{3}{2}\hat{U}_g i_{gq}.
\end{aligned} \tag{3.36}$$

The above equation clearly shows that the active and reactive powers are decoupled and can be controlled via the components of grid current.

3.2.2 Proposed Model Predictive Control with reduced computational cost

In order to fulfill the control objectives, the cost function of the conventional FCS

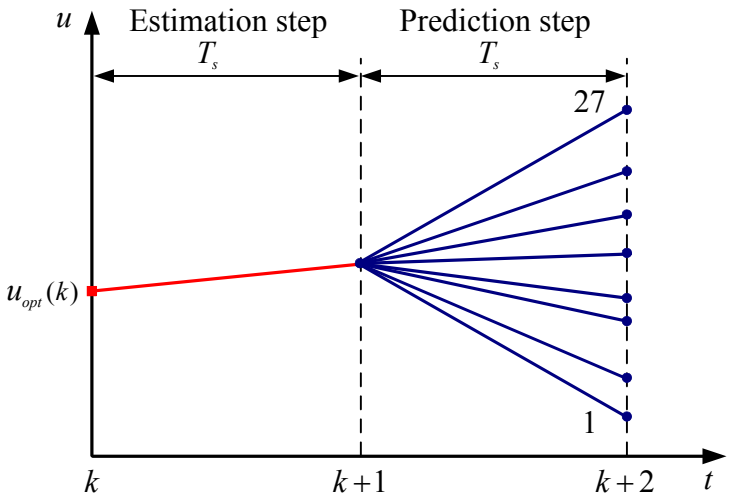

Figure 3.22: Control variable of one-step horizon for FCS-MPC with delay compensation.

model predictive current control for the grid connected 3L-NPC inverter with one-step prediction with delay compensation will use the following ingredients on the same rationale of the previous studies on the subject [12, 52, 75]:

$$g_{grid} = \left|i^*_{gd}(k+2) - i^p_{gd}(k+2)\right| + \left|i^*_{gq}(k+2) - i^p_{gq}(k+2)\right| + \lambda_{dc}\left|u^p_z(k+2)\right| + \lambda_n n_c. \tag{3.37}$$

The time delay produced by computation time is dealt with on the same principles as in the previous chapter. In short, to take into account the computational delay, the control scheme with one-step horizon which is illustrated in Fig. 3.22 will be used. In this case, the optimal control input u_{opt} is the one which minimizes the cost function:

$$\begin{aligned}
&\hat{i}_{gd}(k+1) = f_1(i_{gd}(k), i_{gq}(k), u_k);\ \hat{i}_{gq}(k+1) = f_2(i_{gq}(k), i_{gd}(k), u_k), \qquad (3.38)\\
&i^p_{gd}(k+2) = f_1(\hat{i}_{gd}(k+1), \hat{i}_{gq}(k+1), u_{k+1});\ i^p_{gq}(k+2) = f_2(\hat{i}_{gd}(k+1), \hat{i}_{gq}(k+1), u_{k+1}),\\
&\hat{u}_z(k+1) = f_3(i_g(k), u_z(k), u_k);\ u^p_z(k+2) = f_3(\hat{i}_g(k+1), \hat{u}_z(k+1), u_{k+1}),\\
&g_{grid} = \left|i^*_{gd}(k+2) - i^p_{gd}(k+2)\right| + \left|i^*_{gq}(k+2) - i^p_{gq}(k+2)\right| + \lambda_{dc}\left|u^p_z(k+2)\right| + \lambda_n n_c,\\
&u_{opt} = arg\left\{\min_{u_{k+1}\in\{-1,0,1\}^3} g_{grid}\right\}.
\end{aligned}$$

In order to reduce the computational time, a simplified FCS-MPC is presented in [76] but without delay compensation for power converters in standalone mode. To improve the dynamic performance and reduce the computational burden, in this section this idea is extended for the grid connected 3L-NPC inverter considering the delay compensation.

The main idea of the proposed method is to select inverter voltage (u_{inv_n}) at instant $k+1$ along with 27 voltage vector that is closer to the reference inverter voltage $u^*_{inv\_n}(k+1)$. The proposed control algorithm is described as follows:

- *Step I - Estimation of the current:* The components of grid current $\hat{i}_{gd}(k+1)$ and $\hat{i}_{gq}(k+1)$ at instant $k+1$ are estimated by using equation (3.40) with the previous optimal switching state (u_k) at instant k.
- *Step II - Calculation of the reference inverter voltage:* We can calculate the references of inverter output voltage $u^*_{inv\_d}(k+1)$ and $u^*_{inv\_q}(k+1)$ at instant $k+1$ based on the grid current reference at $k+2$ and estimation of the grid current $\hat{i}_{gd}(k+1)$ and $\hat{i}_{gq}(k+1)$ at $k+1$ by using the equation (3.41). Next, the neutral-point voltage can be evaluated at $k+1$ based on grid current $i_g(k)$ and switching state u_{k+1}.
- *Step III - Evaluation of the cost funtion and selection of the optimal switching state:* The optimal inverter output voltage will be applied to the inverter at instant $k+1$ by minimizing the modified following cost function g_{grid}:

$$
\begin{aligned}
\hat{i}_{gd}(k+1) &= f_1(i_{gd}(k), i_{gq}(k), u_k);\ \hat{i}_{gq}(k+1) = f_2(i_{gq}(k), i_{gd}(k), u_k), \qquad (3.39)\\
u^p_z(k+1) &= f_3(i_g(k), u_z(k), u_{k+1});\ u_{inv\_dn} = f_6(u_{inv\_n});\ u_{inv\_qn} = f_7(u_{inv\_n}),\\
u^*_{inv\_d}(k+1) &= f_4(i^*_{gd}(k+2), \hat{i}_{gd}(k+1), \hat{i}_{gq}(k+1)),\\
u^*_{inv\_q}(k+1) &= f_5(i^*_{gq}(k+2), \hat{i}_{gd}(k+1), \hat{i}_{gq}(k+1)),\\
g_{grid} &= \left|u^*_{inv\_d}(k+1) - u_{inv\_dn}\right| + \left|u^*_{inv\_q}(k+1) - u_{inv\_qn}\right| + \lambda_{dc}\left|u^p_z(k+1)\right| + \lambda_n n_c,\\
u_{opt} &= arg\left\{\min g_{grid}\right\},\ n = 1, ..., 27
\end{aligned}
$$

where $u^*_{inv\_d}(k+1)$ and $u^*_{inv\_q}(k+1)$ are the required reference inverter voltages at time $k+1$; u_{inv_dn} and u_{inv_qn} are the components of voltage which correspond to 27 switching states of 3L-NPC inverter.

Comparing (3.38) and (3.39), is becomes clear that the conventional FCS-MPC and the proposed method have a different composition of the cost function. With the conventional FCS-MPC, we have to evaluate 27 of the predicted currents in the cost function to obtain the optimal switching state. On the contrary, we only require 1 calculation of inverter voltage reference based on estimation of the grid current $\hat{i}_{gdq}(k+1)$ and reference current $i^*_g(k+2)$ for the proposed control system. Moreover, the selection procedure of choosing the control input is simple, no requirement of loop optimization. Therefore, the proposed method is more attractive from the computational point of view compared with

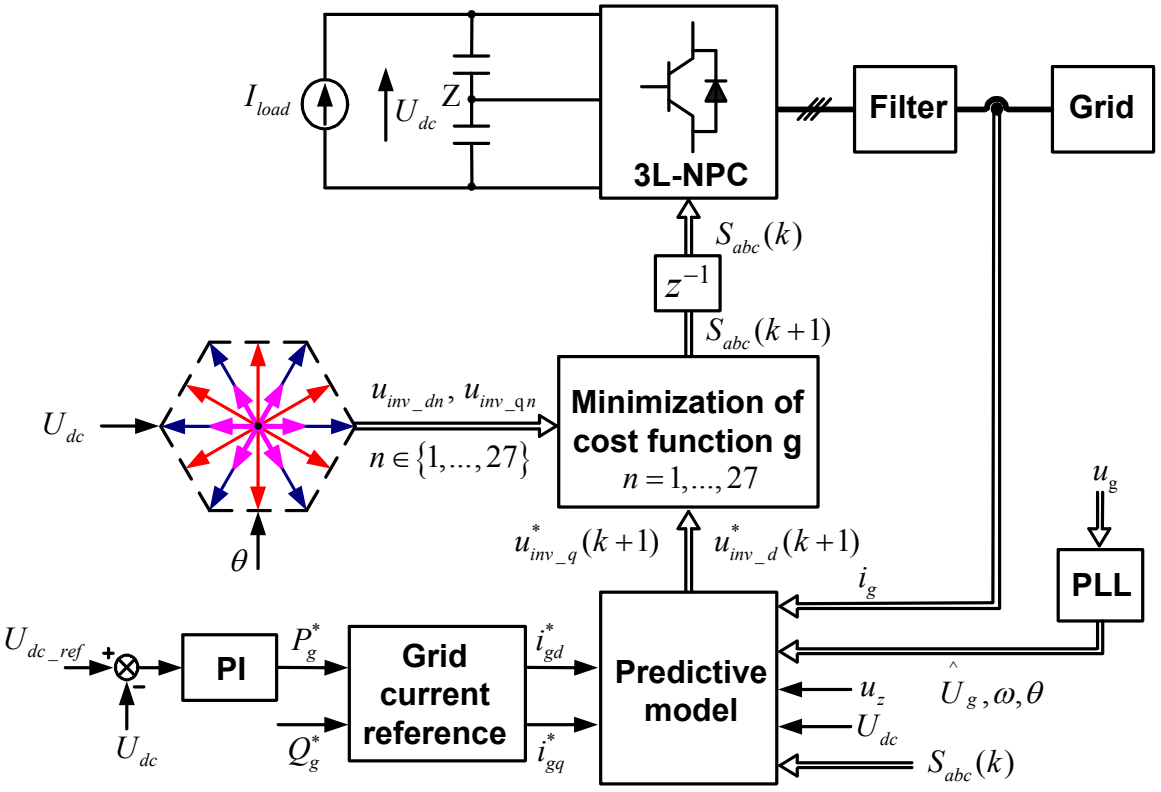

Figure 3.23: Block diagram of the proposed MMPC scheme.

the conventional FCS-MPC method, supporting the feasibility of the real time implementation. The overall system of the proposed control strategy is shown in Fig. 3.23.

According to equation (3.33) and assuming a sampling time of T_s, the grid current is estimated in discrete-time by using the first-order forward Euler approximation as follows:

$$\begin{aligned}
\hat{i}_{gd}(k+1) &= i_{gd}(k)\left(1-\frac{T_s R_f}{L_f}\right)+\frac{T_s}{L_f}\left(u_{inv_d}(k)-\hat{U}_g\right)+T_s\omega i_{gq}(k),\\
\hat{i}_{gq}(k+1) &= i_{gq}(k)\left(1-\frac{T_s R_f}{L_f}\right)+\frac{T_s}{L_f}u_{inv_q}(k)-T_s\omega i_{gd}(k),
\end{aligned} \tag{3.40}$$

where $u_{inv\_d}(k)$ and $u_{inv\_q}(k)$ can be obtained based on the previous control input u_k and U_{dc} by using equation (3.35).

The components of reference inverter output voltage are obtained by using the equation (3.33), replacing the predicted currents $i^p_{gd}(k+2)$, $i^p_{gq}(k+2)$ by theirs reference values

$i^*_{gd}(k+2)$ and $i^*_{gq}(k+2)$ as:

$$u^*_{inv\_d}(k+1) = \hat{i}_{gd}(k+1)\left(R_f - \frac{L_f}{T_s}\right) + \frac{L_f}{T_s} i^*_{gd}(k+2) + \hat{U}_g - \omega L_f \hat{i}_{gq}(k+1),$$
$$u^*_{inv\_q}(k+1) = \hat{i}_{gq}(k+1)\left(R_f - \frac{L_f}{T_s}\right) + \frac{L_f}{T_s} i^*_{gq}(k+2) + \omega L_f \hat{i}_{gd}(k+1), \tag{3.41}$$

where the grid current references are calculated from the active and reactive powers according to equation (3.36). In a simplified form these are given by:

$$i^*_{gd}(k+2) = i^*_{gd}(k) = \frac{2P^*_g}{3\hat{U}_g}, \tag{3.42}$$
$$i^*_{gq}(k+2) = i^*_{gq}(k) = -\frac{2Q^*_g}{3\hat{U}_g}.$$

The discrete-time model for neutral-point voltage can be obtained from (3.33) as follows:

$$u^p_z(k+1) = u_z(k) + \frac{T_s}{4C}\big(2|\,S_a(k+1)| - |\,S_b(k+1)| - |\,S_c(k+1)|\big) i_{g\alpha}(k) \tag{3.43}$$
$$+ \frac{\sqrt{3}T_s}{4C}\big(|\,S_b(k+1)| - |\,S_c(k+1)|\big) i_{g\beta}(k).$$

Finally, the aim of proposed predictive control can be achieved by evaluating the appropriate cost function for all considered switching states (see algorithm 2).

Algorithm 2: Algorithm of modified model predictive control with reduced computational cost

1. Measure $i_g(k)$, $u_z(k)$, $u_g(k)$, $S_{abc}(k)$ and U_{dc}; Read the reference values $U_{dc-ref}(k)$ and $Q^*_g(k)$;
2. Estimation of grid current $\hat{i}_{gd}(k+1)$ and $\hat{i}_{gq}(k+1)$ by using equation (3.40) ;
3. Calculate the reference of grid current $i^*_{gd}(k)$, $i^*_{gq}(k)$ from (3.42) and inverter output voltage $u^*_{inv\_d}(k+1), u^*_{inv\_q}(k+1)$ from (3.41) ;
4. Calculate the components of inverter output voltage: u_{inv_dn} and u_{inv_qn}, with $n = 1 - 27$ from equation (3.35) ;
5. Estimate the value: n_c for 27 voltage vector based on equation (3.16) ;
6. Predict the neutral-point voltage $u^p_z(k+1)$ for 27 voltage vector by using equation (3.43) ;
7. Compute the cost function g_{grid} from (3.39) ;
8. Select the optimal switching state x_{opt}: $[\sim, x_{opt}] = min(g)$;
9. Apply optimal switching states: S_a, S_b, S_c;

3.2.3 Simulation results

To verify the performance of the proposed control strategy in the present work, simulation studies were carried out in Matlab/Simulink environment and SimPowerSystems toolbox with the same parameters as the previous section. The parameters of the controller are given by $\lambda_{dc} = 20$ and $\lambda_n = 60$.

In order to illustrate the efficiency of control scheme, various scenarios with the step change in active and reactive power were carried out for an extensive simulation window (20 s). The reference of active power (P_{g-ref}) is derived from the DC-voltage control loop with linear PI controller. Fig. 3.24(a) shows that there are overshoots in transient response of active power mainly due to the effect of active power reference. As a side note we mention that, this issues can receive further improvements by using alternative design methods for DC-voltage control loop. However, this is not the main focus of this thesis and will not be developed here.

One of the main objectives of GSC is to provide a desired amount of reactive power which is demanded in the electrical grid. The results in Fig. 3.24 confirm that the proposed control strategy is able to operate with high dynamic performance and good tracking reference of the active and reactive powers. To further demonstrate the performance, a zoom of simulation results from 0.05 s to 0.3 s are presented in Figs. 3.25(a) and 3.25(b). The initial active power reference is 5 kW and reactive power reference is -2 kVar, corresponding to negative power factor ($PF = -0.93$). Thus, the grid voltage lags the current by 338^0 as shown in Fig. 3.26(b). At time $t = 0.15$ s, the reference of active power changes from 5 kW to 8 kW, then steps from 8 kW to 5 kW at instant $t = 0.25$ s. The reference P_{g-ref} and measured active power P_g are illustrated in Fig. 3.25(a). A step change in reactive power reference Q_{g-ref} from -2 kVar for leading power factor operation to 2 kVar for lagging power factor is applied at $t = 0.2$ s as shown in Fig. 3.25(b). Fig. 3.26(a) demonstrates the phase shift between the voltage and current for the different power factors. The results shown in Fig. 3.25 indicate that the proposed method achieves better performance than DPC-SVM, faster dynamic response with rise times of 1 ms and smaller overshoot. The mean absolute percentage error of active and reactive powers are 2.99%, and 7.81% respectively.

Figs. 3.27(c) and 3.27(d) are the transient responses and current spectrum of the grid current. Comparing the grid spectrum in Fig. 3.14(b) and Fig. 3.27(d), the proposed method achieves better performance. The current THD is 3.66% for the proposed method

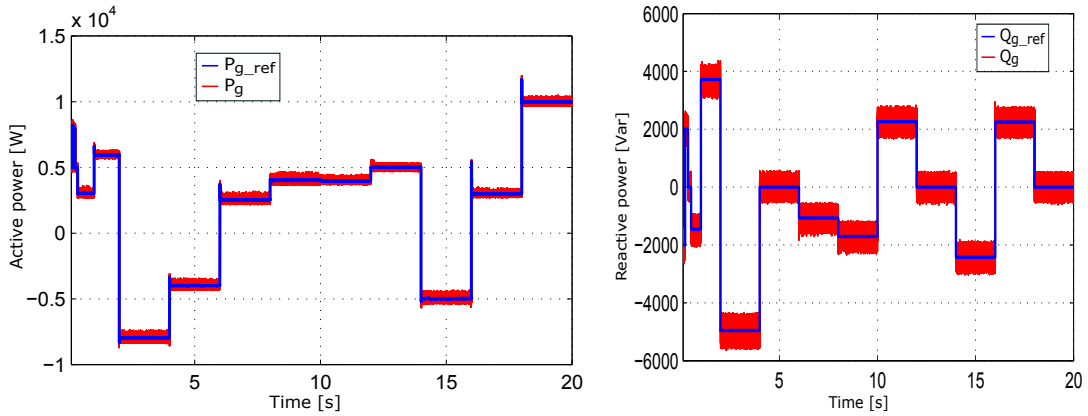

(a) The dynamic response of active power (b) The dynamic response of reactive power

Figure 3.24: The dynamic response of active and reactive powers for proposed method with long simulation time.

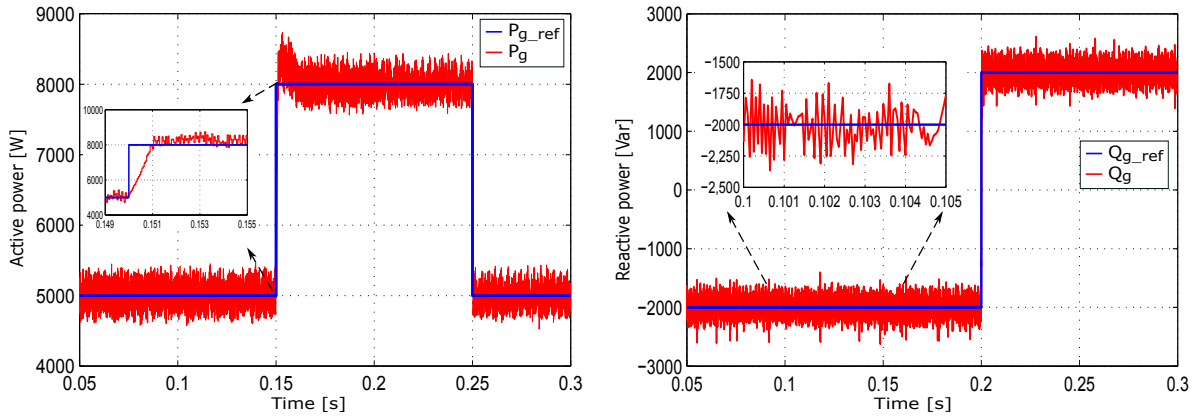

(a) The dynamic response of active power (b) The dynamic response of reactive power

Figure 3.25: Performance of control scheme with dynamic active and reactive power references.

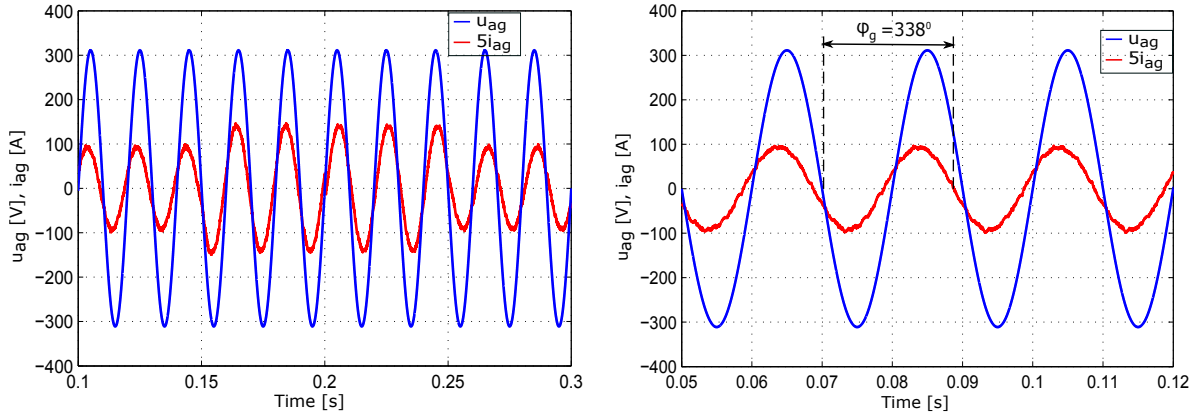

(a) The responses of the grid voltage and current (b) Steady state waveforms of the grid voltage and current

Figure 3.26: Transient waveforms of the grid voltage and current.

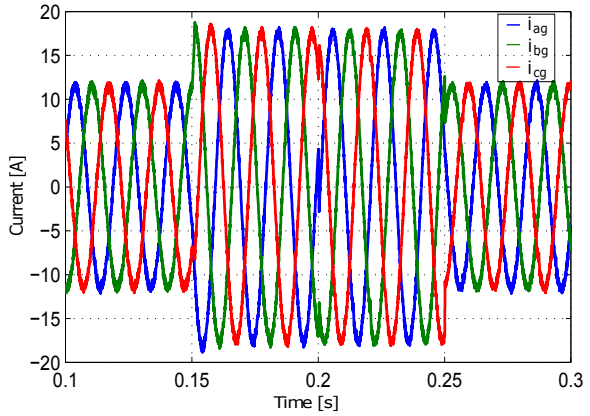

(a) Grid current response of the conventional FCS-MPC

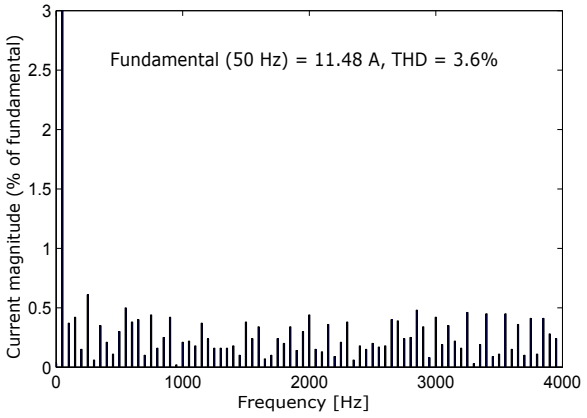

(b) Grid current spectrum of the conventional FCS-MPC

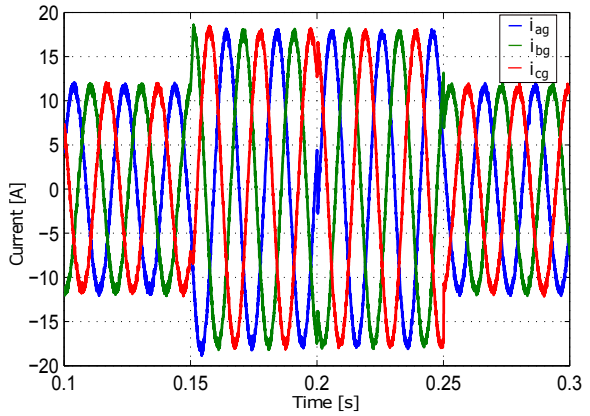

(c) Grid current response of the proposed method

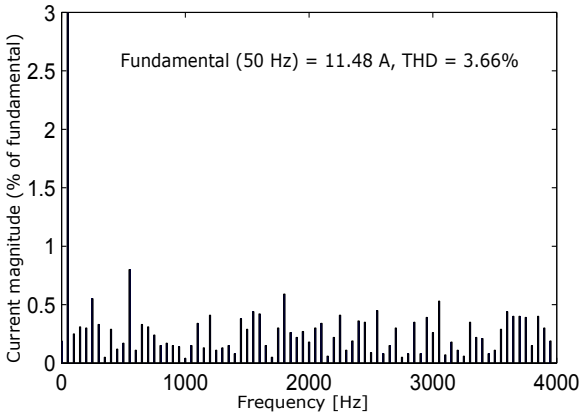

(d) Grid current spectrum of the proposed method

Figure 3.27: The dynamic response and harmonic spectrum of the grid current for the conventional FCS-MPC and proposed method.

which still meets the requirement of the IEEE 519 standard. In particular, comparing with the conventional FCS-MPC with one-step control horizon which used the cost function (3.38) the proposed method achieves the same performance of the current as illustrated in Fig. 3.27. The proposed method has a small increase in MAPE of active power and THD of the current from 2.94% to 2.99% and from 3.6% to 3.66%, respectively. However, the amount of calculations needed for the proposed method is reduced about 96% compared with the conventional FCS-MPC with one-step control horizon. In fact, the average computation time of the conventional FCS-MPC is about 25 μs, while the proposed method needs only 10 μs in a 3.3 GHz, i5-6600 CPU. This means that the proposed algorithm is faster than the conventional FCS-MPC, allowing a reliable and cost effective real time implementation.

To analyze the robustness of the controller against load changes, we can chose the

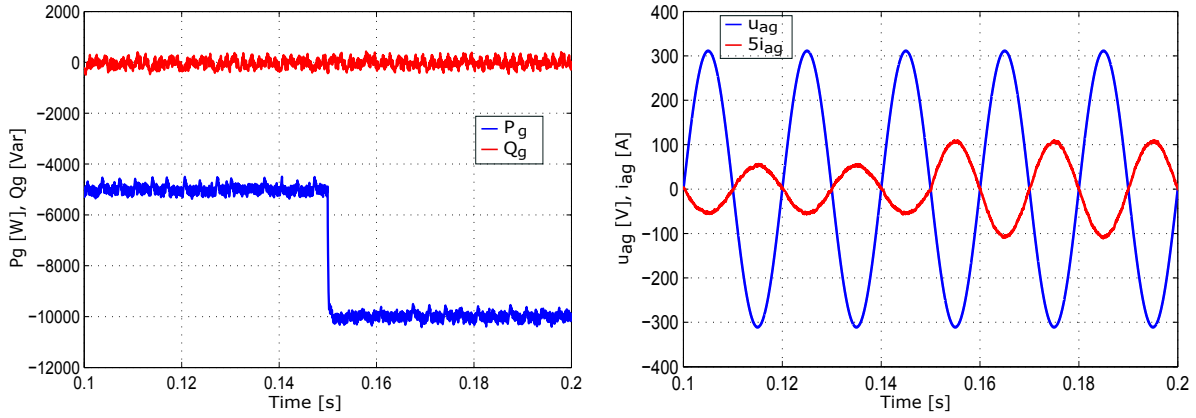

(a) Dynamic active and reactive power response (b) Phase current ($5i_{ag}$) and grid voltage (u_{ag})

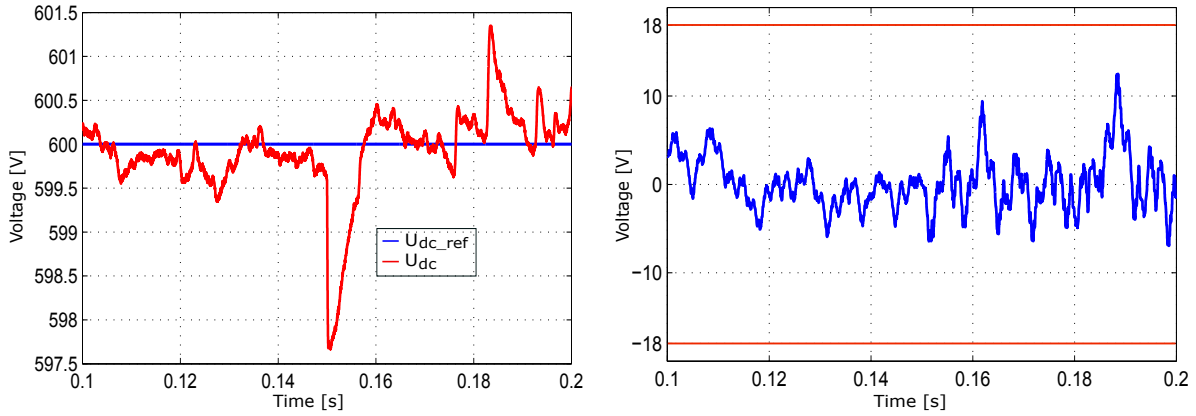

(c) DC-link voltage response (d) Neutral-point voltage response

Figure 3.28: Performance of the controller during load variation.

initial condition as the $U_{dc} = 600$ V, zero grid reactive power ($Q_g = 0$) and active power $P_g = -5$ kW, which is delivered to grid. At the instant $t = 0.15$ s, a resistance load R_{load} change of 50% is produced from 72 Ω to 36 Ω, leading to a change of active power to -10 kW as shown in Fig. 3.28(a). It can be seen from Fig. 3.28(c) that the proposed method is capable to keep the DC-voltage constant with a slight decrease at the transition. Moreover, the DC-link capacitor voltages are balanced within in a bound of 3% of nominal DC-link voltage as illustrated in Fig. 3.28(d).

3.3 Conclusions

In this chapter, two models predictive control for grid connected 3L-NPC inverter has been proposed to control the grid active and reactive powers. In the first control strategy, the proposed control operates in discrete-time to predict the state controlled

of virtual flux, grid current and neutral-point voltage for each switching configuration of the inverter. By using the cost function which includes the active and reactive powers, we can control directly the power exchanged with the grid. Two-step horizon is chosen to improve the performance. In order to reduce the computational burden, only combinations of inputs having one switching variation are considered. Moreover, this method does not require voltage measurement and coordinate transformation, leading to a simple implementation and fast dynamic response. The selection process of choosing the weighting factors are also presented in this chapter. In a second time, the control scheme based on grid voltage orientation with one-step prediction and delay compensation is proposed. The active and reactive powers can be controlled via the components of grid current. The main contribution of proposed method is the use of the cost function for reduce the amount of calculations. The reference of inverter voltage vector is employed to evaluate the modified cost function for selecting the optimal switching state. The simulation results indicate that proposed control strategy can successfully track the active and reactive powers, balance the DC-link capacitor voltages and reduce the switching frequency. The linear PI controllers for the internal current loops and the modulation block are further eliminated, leading to a simple practical implementation.

Chapter 4

Model Predictive Direct Power Control for DFIG fed by a 3L-NPC Inverter

Nowadays, doubly fed induction generator (DFIG) represents an attractive solution due to its advantages: for instance, only 30% of generator power passes through, reducing converter cost and power lost [5, 9] comparing with the full scale converter configuration. In wind energy, the comparison between the wind turbines using fixed speed and the DFIGs based wind turbines shows that the last category can operate with four-quadrant active and reactive power capabilities, leading to both bidirectional active and reactive power flow from the rotor side to grid through the rotor side converter (RSC) and grid side converter (GSC) (Fig. 4.1). Several control algorithms have been proposed to control DFIG based wind turbine system. The most popular control strategy is the well know field oriented control (FOC) based on the orientation of stator voltage (stator voltage oriented-SVO) [15] or the stator flux (stator flux oriented-SFO) [9], [24]. This method incorporates a cascaded structure with four PI regulators, two PIs in the outer loops for active and reactive powers of the stator and two PIs in the inner rotor currents loops. However, one drawback of this method is that its performance depends on accurate machine parameters such as stator and rotor resistance and mutual inductance. Another drawback of using PI controller is the necessity of tuning of the gains in the whole operating range of wind speed.

Recently, alternative approaches to field oriented control such as direct torque control (DTC) [27] or direct power control (DPC) [14] have been proposed to improve the controller performance. In these strategies, two hysteresis controllers are used to determine the inverter instantaneous switching state, which is selected from a lookup-table

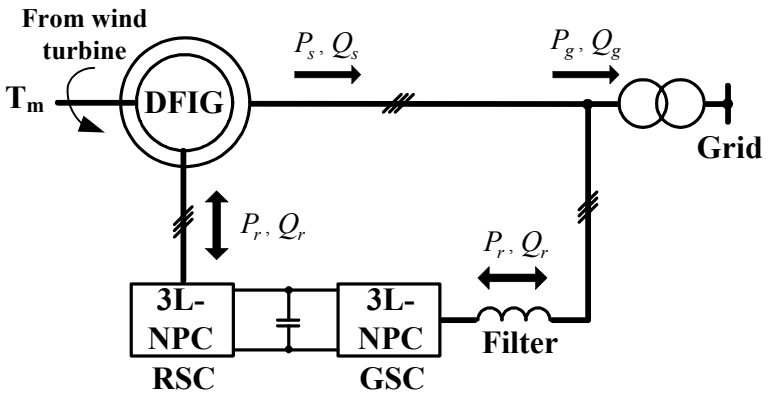

Figure 4.1: Schematic diagram of DFIG based wind generation systems [9].

(LUT) based on the errors between the reference and estimated values. Therefore, these techniques provide faster transient response in comparison with FOC without requiring current regulators nor coordinate transformations or specific modulations like PWM or SVM for pulse generation. However, the variable switching frequency and large power ripple are considered to be the main drawbacks of LUT. Moreover, in order to obtain an acceptable steady-state and high dynamic performances, a high sampling frequency is required for this method. With both linear control and hysteresis techniques, the system constraints and technical requirements such as voltage balancing, total harmonic distortion and switching frequency can not be considered at the design stage. To overcome this problem, several techniques have been developed such as using DPC with space vector modulation (SVM) [31], deadbeat power control [77], sliding mode control [35]. The common-mode voltage (CMV) generated by the voltage source inverter is known to cause the overvoltage stress on the winding insulation of the machines and premature failure of the bearings. Several studies have been presented to reduce the peak common-mode voltage by avoiding the zero vectors in pulse width modulation (PWM) [78, 79], applying model predictive control methods [80–82].

Over the last decade, model predictive control (MPC) proved to be an alternative control technique that was applied in machine drives and converters. Several approaches such as predictive current control [83], predictive direct torque control [84] and predictive direct power control [85] were applied to control the DFIG. The MPC for DFIG were presented in [46, 47, 50, 86]. These strategies use quadratic programming (QP) to solve online the control optimization problem or characterize the parametric solutions which can be precomputed offline, thus obtaining the explicit MPC solution as piecewise affine (PWA) control laws. Finite control set model predictive control has been recently discussed in the virtue of its advantages, such as easy inclusion of non linearities in the

model, delay compensation and additional constraints such as switching frequency and common-mode voltage.

The present chapter presents a model predictive direct power control (MPDPC) for DFIG connected to 3L-NPC inverter. The mathematical model of DFIG with two reference frames are introduced. A control goal is derived by optimization of an objective cost function that considers the tracking errors of the active and reactive powers, voltage balancing and reduction of switching frequency and common-mode voltage. The principle of the proposed control scheme is to use the dynamical model to calculate prediction of the future values of the stator flux, rotor current, DC-link capacitor voltages and CMV. The active and reactive powers can be estimated based on the stator flux and the rotor current. Consequently, this method can control directly the power of DFIG without using rotor current loop. In order to validate the effectiveness of the proposed control strategy, simulation tests are carried out using Matlab and Simulink with different modes of speed operation.

4.1 Introduction to the doubly fed induction generator for wind turbine

The doubly fed induction generator consists in a stator and a rotor each carrying three-phase windings which are spatially shifted by 120^0. The stator is supplied by three-phase voltage source of the grid (u_s) with frequency f_s, whereas the rotor is supplied by three-phase voltage source inverter (u_r) with frequency f_r. Thus, a stator flux is induced in the air gap and rotates at synchronous speed (n_s). This is given by the expression:

$$n_s = \frac{60 f_s}{p}(rpm), \tag{4.1}$$

where p is number of pole pairs of the machine.

The angular frequency of the induced rotor voltages and currents is given by [9]:

$$\omega_r = \omega_s - \omega_m, \tag{4.2}$$

where ω_s, ω_r are the angular frequency of the voltages and currents of stator windings and rotor windings (rad/s), ω_m is the angular frequency of the rotor and is related to

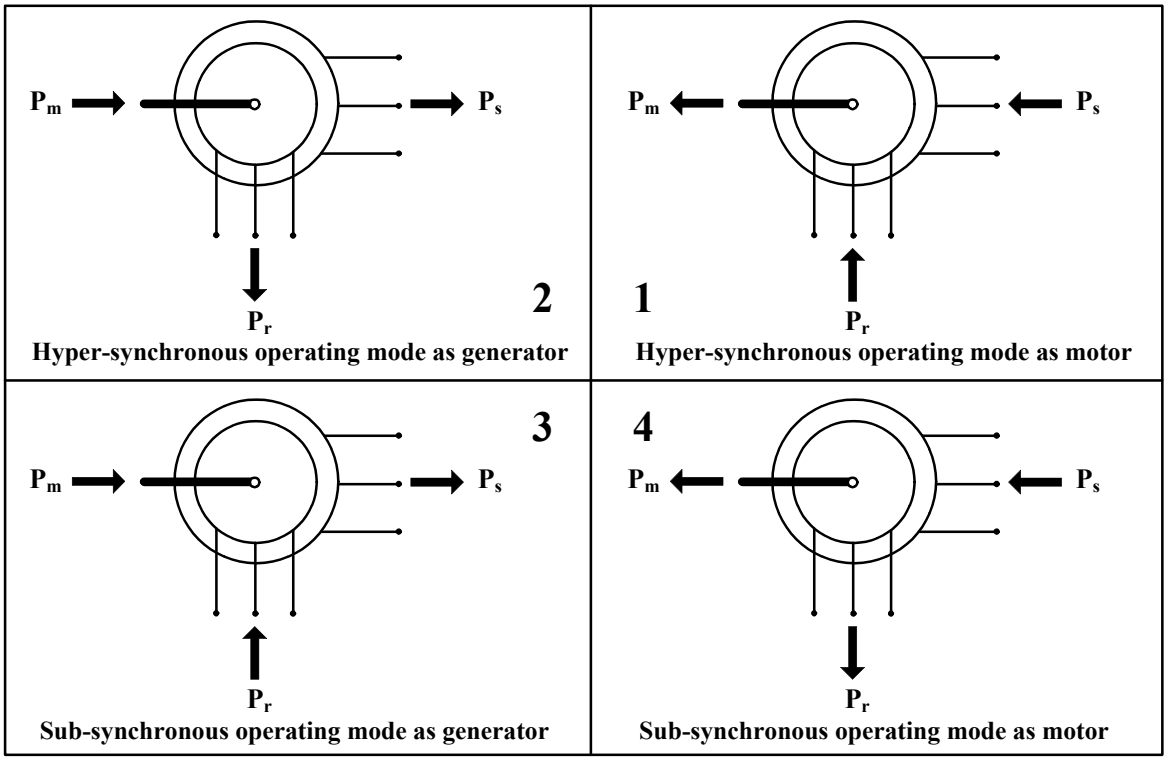

Figure 4.2: Four quadrant modes of operation of the DFIG.

mechanical rotational speed Ω_m as:

$$\omega_m = p\Omega_m(rad/s). \tag{4.3}$$

Hence, slip (s) is defined as difference between synchronous speed and rotor speed as:

$$s = \frac{\omega_s - \omega_m}{\omega_s}. \tag{4.4}$$

By combining equations (4.2) and (4.4), we can obtain the relationship between the slip, the stator, and the rotor angular frequency:

$$\begin{aligned} \omega_r &= s\omega_s, \\ f_r &= sf_s. \end{aligned} \tag{4.5}$$

The DFIG can operate under different conditions depending on the power and wind speed (Fig. 4.2) [9]. The stator output power P_s flows from the DFIG stator to the grid under operating mode as generator. The DFIG can operate below the synchronous speed ω_s (sub-synchronous mode) and above the synchronous speed (hyper-synchronous mode)

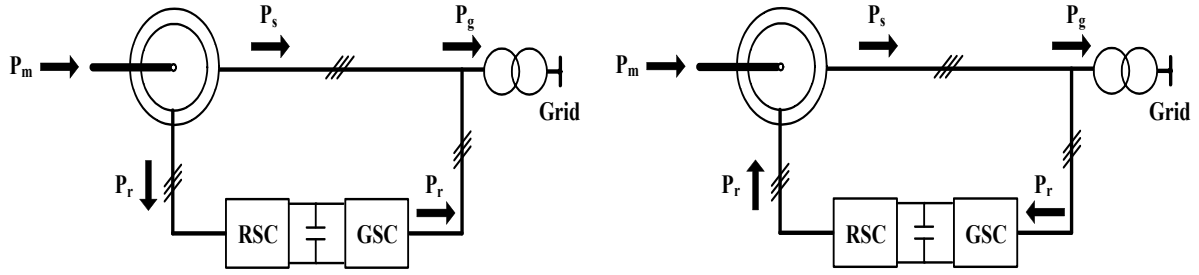

(a) Hyper-synchronous operating mode (b) Sub-synchronous operating mode

Figure 4.3: Active power flow representation of DFIG for hyper and sub-synchronous speed under generating mode.

which allow an operational speed range of about 30% around the synchronous speed. Fig. 4.3 shows that it is possible to exchange power through both the stator and rotor sides to the grid in operation modes 2 and 3. The rotor power P_r is negative for negative slip (hyper-synchronous speed) and positive for positive slip (sub-synchronous speed). For hyper-synchronous speed operation, P_r is transmitted to DC-link voltage and tends to rise the DC voltage. On the other hand, P_r is received from the DC-link voltage and tends to decrease the DC voltage for sub-synchronous speed operation. Consequently, neglecting the power losses in the converters, DFIG and filter, the power delivered to the grid P_g is the sum of the stator and rotor powers, given by:

$$|P_g| = \begin{cases} |P_s| + |P_r| & \text{for hyper-synchronous speed,} \\ |P_s| - |P_r| & \text{for sub-synchronous speed.} \end{cases} \tag{4.6}$$

4.2 Dynamic modelling of the DFIG

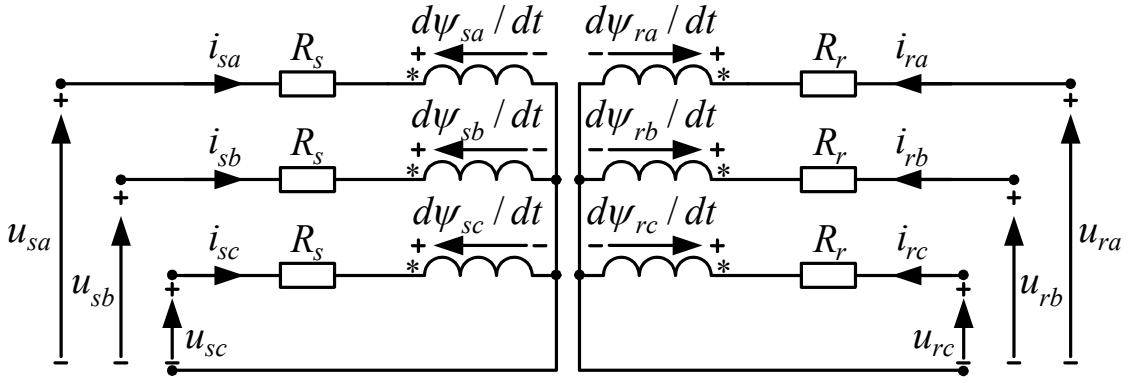

Figure 4.4: Equivalent circuit of the DFIG.

The doubly fed induction generator can be modelled by the equivalent circuit (see [9]). The stator voltage, current and flux of the DFIG can be described from Fig. 4.4 as follows:

$$u_{sa} = R_s i_{sa} + \frac{d\psi_{sa}}{dt}, \tag{4.7a}$$

$$u_{sb} = R_s i_{sb} + \frac{d\psi_{sb}}{dt}, \tag{4.7b}$$

$$u_{sc} = R_s i_{sc} + \frac{d\psi_{sc}}{dt}, \tag{4.7c}$$

where R_s is the stator resistance; i_{sa}, i_{sb}, i_{sc} are the stator currents of phases a, b and c; u_{sa}, u_{sb}, u_{sc} are the applied stator voltages; ψ_{sa}, ψ_{sb}, ψ_{sc} are the stator fluxes.

Similarly, the rotor side is described by:

$$u_{ra} = R_r i_{ra} + \frac{d\psi_{ra}}{dt}, \tag{4.8a}$$

$$u_{rb} = R_r i_{rb} + \frac{d\psi_{rb}}{dt}, \tag{4.8b}$$

$$u_{rc} = R_r i_{rc} + \frac{d\psi_{rc}}{dt}, \tag{4.8c}$$

where R_r is the rotor resistance referred to the stator; i_{ra}, i_{rb}, i_{rc} are the rotor current referred to the stator of phases a, b and c; u_{ra}, u_{rb}, u_{rc} are the rotor voltages referred the stator; ψ_{ra}, ψ_{rb}, ψ_{rc} are the rotor fluxes.

4.2.1 A dynamical model of DFIG in stator reference frame

By multiplying equations (4.7a) and (4.8a) by $\frac{2}{3}$, then multiplying equations (4.7b) and (4.8b) by $\frac{2}{3}a$ and also multiplying equations (4.7c) and (4.8c) by $\frac{2}{3}a^2$, we can obtain the voltage equation of the DFIG in vector form:

$$u_s^s = R_s i_s^s + \frac{d\psi_s^s}{dt}, \tag{4.9}$$

$$u_r^r = R_r i_r^r + \frac{d\psi_r^r}{dt}, \tag{4.10}$$

where u_s^s, i_s^s, ψ_s^s are the stator voltage, current and flux vector in stator coordinate $(\alpha\beta)$; u_r^r, i_r^r, ψ_r^r are the rotor voltage, current and flux vector in rotor coordinate (DQ).

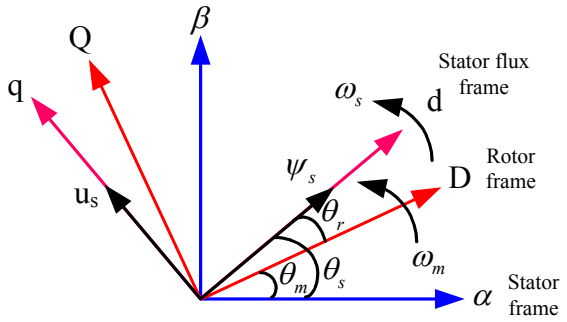

Figure 4.5: Vector representation in different reference frame.

The constant 2/3 is chosen to scale the space vectors according to the maximum amplitude of the three phase magnitudes. In this case, the superscripts s and r indicate that vector are referred to stator and rotor reference frames, respectively. (We point to the Appendix for further details on the developments and the explicit expression of the constant a).

On the other hand, the relationship between the flux and the current is given by:

$$\psi_s^s = L_s i_s^s + L_m i_r^s, \tag{4.11}$$

$$\psi_r^r = L_m i_s^r + L_r i_r^r, \tag{4.12}$$

where L_s and L_r are the stator and rotor inductances; L_m is the magnetizing inductance.

The stator leakage inductance $L_{\sigma s}$ and the rotor leakage inductance $L_{\sigma r}$ can be related as follows:

$$L_s = L_m + L_{\sigma s}, \tag{4.13}$$

$$L_r = L_m + L_{\sigma r}. \tag{4.14}$$

By using Park transformation (A.8), the stator and rotor fluxes can be rewritten as follows:

$$\psi_s^s = L_s i_s^s + L_m i_r^s = L_s i_s^s + L_m i_r^r e^{j\theta_m}, \tag{4.15}$$

$$\psi_r^r = L_m i_s^r + L_r i_r^r = L_r i_r^r + L_m i_s^s e^{-j\theta_m}, \tag{4.16}$$

where θ_m is the angle between the stator reference frame $\alpha\beta$ and the rotor reference frame DQ. Consequently, referring the corresponding vector to the stator reference frame by multiplying equations (4.10) and (4.16) by $e^{j\theta_m}$, the model of the DFIG is obtained in

the $\alpha\beta$ coordinate:

$$u_s^s = R_s i_s^s + \frac{d\psi_s^s}{dt}, \tag{4.17}$$
$$u_r^s = R_r i_r^s + \frac{d\psi_r^s}{dt} - j\omega_m \psi_r^s, \tag{4.18}$$
$$\psi_s^s = L_s i_s^s + L_m i_r^s, \tag{4.19}$$
$$\psi_r^s = L_r i_r^s + L_m i_s^s. \tag{4.20}$$

According the equations (4.17) and (4.18), the components of stator and rotor voltages can be expressed as:

$$\begin{aligned} u_{\alpha s} &= R_s i_{\alpha s} + \frac{d\psi_{\alpha s}}{dt}, \\ u_{\beta s} &= R_s i_{\beta s} + \frac{d\psi_{\beta s}}{dt}, \\ u_{\alpha r} &= R_r i_{\alpha r} + \frac{d\psi_{\alpha r}}{dt} + \omega_m \psi_{\beta r}, \\ u_{\beta r} &= R_r i_{\beta r} + \frac{d\psi_{\beta r}}{dt} - \omega_m \psi_{\alpha r}. \end{aligned} \tag{4.21}$$

And the stator and rotor fluxes are given by:

$$\begin{aligned} \psi_{\alpha s} &= L_s i_{\alpha s} + L_m i_{\alpha r}, \\ \psi_{\beta s} &= L_s i_{\beta s} + L_m i_{\beta r}, \\ \psi_{\alpha r} &= L_r i_{\alpha r} + L_m i_{\alpha s}, \\ \psi_{\beta r} &= L_r i_{\beta r} + L_m i_{\beta s}. \end{aligned} \tag{4.22}$$

Based on the equations (4.21) and (4.22), we have the equivalent model of the DFIG which chooses the currents as state space variables:

$$\begin{aligned} \frac{di_{\alpha s}}{dt} &= -\frac{R_s}{\sigma L_s} i_{\alpha s} + \frac{\omega_m L_m^2}{\sigma L_s L_r} i_{\beta s} + \frac{R_r L_m}{\sigma L_s L_r} i_{\alpha r} + \frac{\omega_m L_m}{\sigma L_s} i_{\beta r} + \frac{1}{\sigma L_s} u_{\alpha s} - \frac{L_m}{\sigma L_s L_r} u_{\alpha r}, \\ \frac{di_{\beta s}}{dt} &= -\frac{\omega_m L_m^2}{\sigma L_s L_r} i_{\alpha s} - \frac{R_s}{\sigma L_s} i_{\beta s} - \frac{\omega_m L_m}{\sigma L_s} i_{\alpha r} + \frac{R_r L_m}{\sigma L_s L_r} i_{\beta r} + \frac{1}{\sigma L_s} u_{\beta s} - \frac{L_m}{\sigma L_s L_r} u_{\beta r}, \\ \frac{di_{\alpha r}}{dt} &= \frac{R_s L_m}{\sigma L_s L_r} i_{\alpha s} - \frac{\omega_m L_m}{\sigma L_r} i_{\beta s} - \frac{R_r}{\sigma L_r} i_{\alpha r} - \frac{\omega_m}{\sigma} i_{\beta r} - \frac{L_m}{\sigma L_s L_r} u_{\alpha s} + \frac{1}{\sigma L_r} u_{\alpha r}, \\ \frac{di_{\beta r}}{dt} &= \frac{\omega_m L_m}{\sigma L_r} i_{\alpha s} + \frac{R_s L_m}{\sigma L_s L_r} i_{\beta s} + \frac{\omega_m}{\sigma} i_{\alpha r} - \frac{R_r}{\sigma L_r} i_{\beta r} - \frac{L_m}{\sigma L_s L_r} u_{\beta s} + \frac{1}{\sigma L_r} u_{\beta r}, \end{aligned} \tag{4.23}$$

with $\sigma = 1 - {L_m}^2 / L_s L_r$, the leakage coefficient.

By using Clarke transformation (A.5), the electric power on the stator side can be calculated as:

$$\begin{aligned} P_s &= u_{sa}i_{sa} + u_{sb}i_{sb} + u_{sc}i_{sc} = \frac{3}{2}\left(u_{\alpha s}i_{\alpha s} + u_{\beta s}i_{\beta s}\right), \\ Q_s &= \frac{1}{\sqrt{3}}\left(\left(u_{sb} - u_{sc}\right)i_{sa} + \left(u_{sc} - u_{sa}\right)i_{sb} + \left(u_{sa} - u_{sb}\right)i_{sc}\right) = \frac{3}{2}\left(u_{\beta s}i_{\alpha s} - u_{\alpha s}i_{\beta s}\right). \end{aligned} \quad (4.24)$$

Furthermore, neglecting the cooper power losses in the stator and rotor resistances, the active and reactive powers in stator and rotor can be expressed (see [9]) as follows:

$$\begin{aligned} P_s &= 3R_s|I_s|^2 + 3\mathrm{Re}\left\{j\omega_s L_m i_r i_s^*\right\} \approx 3\mathrm{Re}\left\{j\omega_s L_m\left(i_{\alpha r} + ji_{\beta r}\right)\left(i_{\alpha s} - ji_{\beta s}\right)\right\} \\ &\approx 3\omega_s L_m\left(i_{\alpha r}i_{\beta s} - i_{\alpha s}i_{\beta r}\right), \\ P_r &= 3R_r|I_r|^2 + 3\mathrm{Re}\left\{js\omega_s L_m i_s i_r^*\right\} \approx 3\mathrm{Re}\left\{js\omega_s L_m\left(i_{\alpha s} + ji_{\beta s}\right)\left(i_{\alpha r} - ji_{\beta r}\right)\right\} \\ &\approx 3s\omega_s L_m\left(i_{\alpha s}i_{\beta r} - i_{\alpha r}i_{\beta s}\right) \approx -sP_s, \end{aligned} \quad (4.25)$$

where the superscript * represents the complex conjugate of a space vector.

In the same way, the expression of the reactive powers of stator and rotor can be given by:

$$\begin{aligned} Q_s &= 3\omega_s L_s|I_s|^2 + 3\omega_s L_m\mathrm{Im}\left\{j\omega_s L_m i_r i_s^*\right\} \approx 3\omega_s L_m\mathrm{Re}\left\{i_r i_s^*\right\} \approx 3\omega_s L_m\left(i_{\alpha r}i_{\alpha s} + i_{\beta s}i_{\beta r}\right), \\ Q_r &= 3s\omega_s L_r|I_r|^2 + 3\mathrm{Im}\left\{js\omega_s L_m i_s i_r^*\right\} \approx 3s\omega_s L_m\mathrm{Re}\left\{i_s i_r^*\right\} \approx 3s\omega_s L_m\left(i_{\alpha r}i_{\alpha s} + i_{\beta s}i_{\beta r}\right) \approx sQ_s. \end{aligned} \quad (4.26)$$

The electromagnetic torque of the DFIG can be defined as [9]:

$$T_{em} = \frac{3}{2}pL_m\mathrm{Im}\left\{i_r^* i_s\right\}. \quad (4.27)$$

The mechanical equation of the system dynamics is represented by the following equation:

$$T_{em} - T_{load} = J\frac{d\Omega_m}{dt}. \quad (4.28)$$

where J is the inertia of the mechanical axis and T_{load} is the external torque applied to the mechanical axis.

4.2.2 The model of DFIG in dq coordinate based on stator fluxed orientation

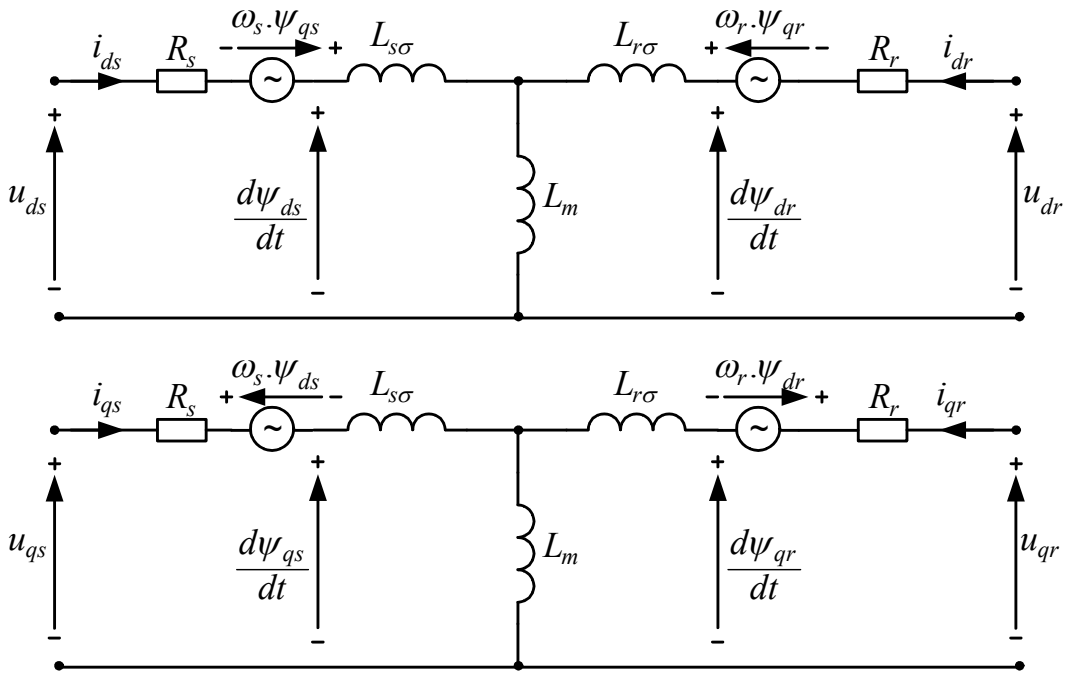

Figure 4.6: Steady state equivalent circuit of DFIG in dq reference frame.

Fig. 4.6 shows the generalized equivalent circuit of a DFIG in dq coordinate based on stator flux orientation. From the voltage equations (4.9) and (4.10), multiplying them by $e^{-j\theta_s}$ and $e^{-j\theta_r}$, respectively the stator and rotor voltages can be rewritten as:

$$u_s^{dq} = R_s i_s^{dq} + \frac{d\psi_s^{dq}}{dt} + j\omega_s \psi_s^{dq}, \tag{4.29}$$

$$u_r^{dq} = R_r i_r^{dq} + \frac{d\psi_r^{dq}}{dt} + j\omega_r \psi_r^{dq}, \tag{4.30}$$

where the superscripts dq indicates the stator flux reference frame.

From the equations (4.11) and (4.12) by using the same way, the flux expression can be obtained as:

$$\psi_s^{dq} = L_s i_s^{dq} + L_m i_r^{dq}, \tag{4.31}$$

$$\psi_r^{dq} = L_r i_r^{dq} + L_m i_s^{dq}. \tag{4.32}$$

From equation (4.31), the stator current is written as:

$$i_s^{dq} = \frac{1}{L_s}\left(\psi_s^{dq} - L_m i_r^{dq}\right). \tag{4.33}$$

By substituting equation (4.33) into equation (4.29), the stator flux dynamics is given by:

$$\frac{d\psi_s^{dq}}{dt} = \frac{1}{T_s}\left(-\left(1 + j\omega_s T_s\right)\psi_s^{dq} + L_m i_r^{dq} + T_s u_s^{dq}\right), \tag{4.34}$$

where $T_s = \frac{L_s}{R_s}$ is the time constant of the stator.

By substituting equation (4.33) into equation (4.32), the rotor flux can be rewritten as:

$$\psi_r^{dq} = \frac{L_m}{L_s}\psi_s^{dq} + \left(L_r - \frac{L_m^2}{L_s}\right) i_r^{dq}. \tag{4.35}$$

By substituting equations (4.34) and (4.35) into equation (4.30), the dynamics of the rotor current is represented as follows:

$$\frac{di_r^{dq}}{dt} = \frac{1}{\sigma L_r}\left(\psi_s^{dq}\left(\frac{L_m}{L_s T_s} + j\omega_m \frac{L_m}{L_s}\right) + u_r^{dq}\right) - \frac{1}{\sigma L_r}\left(i_r^{dq}\left(R_\sigma + j\omega_r \sigma L_r\right) + \frac{L_m}{L_s} u_s^{dq}\right), \tag{4.36}$$

where $R_\sigma = R_r + L_m^2/L_s T_s$.

Based on the equations (4.34) and (4.36), the dynamical model of DFIG can be expressed in matrix form as below:

$$\dot{x} = A(\omega_s, \omega_m, \omega_r)x + Bu, \tag{4.37}$$

where $x = \begin{bmatrix} \psi_{ds} \\ \psi_{qs} \\ i_{dr} \\ i_{qr} \end{bmatrix}$, $u = \begin{bmatrix} u_{ds} \\ u_{qs} \\ u_{dr} \\ u_{qr} \end{bmatrix}$,

$$A(\omega_s,\omega_m,\omega_r)=\begin{bmatrix} -\frac{1}{T_s} & \omega_s & \frac{L_m}{T_s} & 0 \\ -\omega_s & -\frac{1}{T_s} & 0 & \frac{L_m}{T_s} \\ \frac{L_m}{L_sT_s\sigma L_r} & -\frac{\omega_m L_m}{L_s\sigma L_r} & -\frac{R_\sigma}{\sigma L_r} & \omega_r \\ \frac{\omega_m L_m}{\sigma L_s L_r} & \frac{L_m}{L_sT_s\sigma L_r} & -\omega_r & -\frac{R_\sigma}{\sigma L_r} \end{bmatrix}, \tag{4.38}$$

$$B=\begin{bmatrix} 1 & 0 & 0 & 0 \\ 0 & 1 & 0 & 0 \\ -\frac{L_m}{\sigma L_s L_r} & 0 & \frac{1}{\sigma L_r} & 0 \\ 0 & -\frac{L_m}{\sigma L_s L_r} & 0 & \frac{1}{\sigma L_r} \end{bmatrix}.$$

The components of the equation (4.29) in dq reference frame can be rewritten as:

$$\begin{aligned} u_{ds} &= R_s i_{ds} + \frac{d\psi_{ds}}{dt} - \omega_s \psi_{qs}, \\ u_{qs} &= R_s i_{qs} + \frac{d\psi_{qs}}{dt} + \omega_s \psi_{ds}. \end{aligned} \tag{4.39}$$

Since the stator is connected to the grid, the stator flux is a function of the grid voltage in steady state (with the assumption $\frac{d\psi_s^{dq}}{dt}=0$). Neglecting the small drop in the stator resistance, under stator flux orientation (Fig. 4.5), the component of stator voltage can be simplified based on equation (4.39) as follows [24]:

$$u_{ds}=\psi_{qs}=0;\ \ u_{qs}=\hat{U}_g\approx\omega_s\psi_{ds}, \tag{4.40}$$

where $\hat{U}_g$ is the magnitude of the grid voltage.

The active power in the stator can be expressed as follows:

$$P_s=\frac{3}{2}\left(u_{ds}i_{ds}+u_{qs}i_{qs}\right)=\frac{3}{2}u_{qs}i_{qs}=\frac{3}{2}\psi_{ds}\omega_s i_{qs}=-\frac{3}{2}\psi_{ds}\frac{L_m}{L_s}\omega_s i_{qr}. \tag{4.41}$$

and the reactive power can be rewritten as:

$$Q_s=\frac{3}{2}\left(u_{qs}i_{ds}-u_{ds}i_{qs}\right)=\frac{3}{2}u_{qs}i_{ds}=\frac{3}{2}\omega_s\psi_{ds}\left(\frac{\psi_{ds}}{L_s}-\frac{L_m}{L_s}i_{dr}\right). \tag{4.42}$$

From equation (4.17), two stator flux components can be estimated by integration as:

$$\psi_{\alpha s} = \int (u_{\alpha s} - R_s i_{\alpha s})\, dt, \tag{4.43}$$
$$\psi_{\beta s} = \int (u_{\beta s} - R_s i_{\beta s})\, dt.$$

In order to avoid DC-offsets, a digital low pass filter with a low cutoff frequency can replace the pure integrator. The position of stator flux is estimated by using function as follows:

$$\theta_s = \arctan\left(\frac{\psi_{\beta s}}{\psi_{\alpha s}}\right). \tag{4.44}$$

4.3 Model Predictive Direct Power Control of DFIG

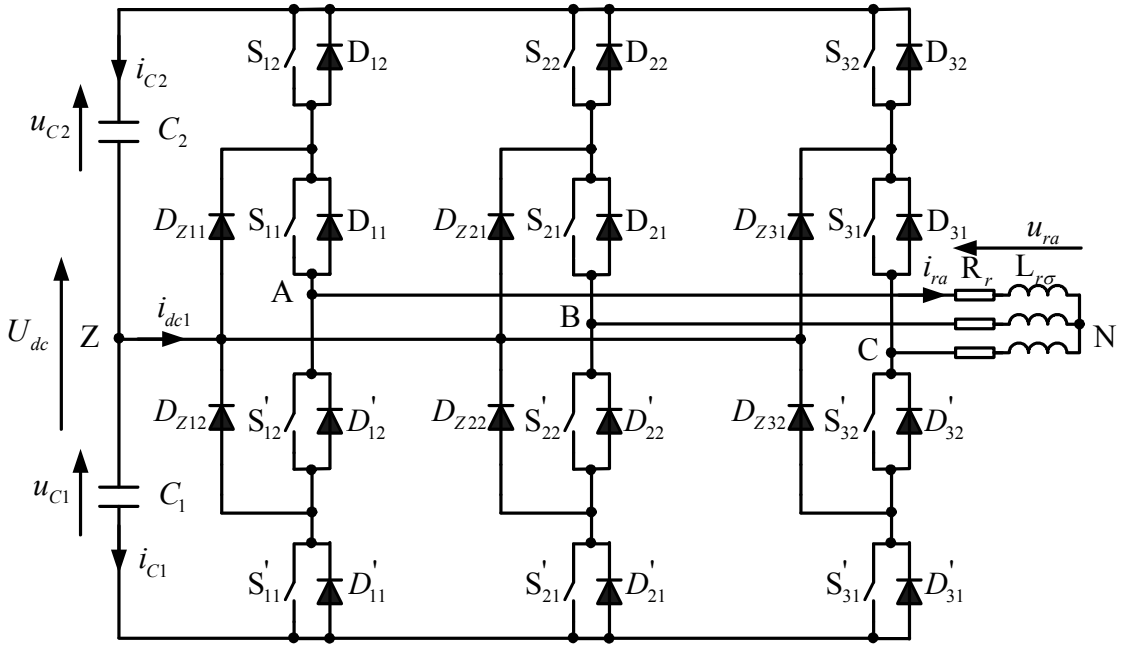

Figure 4.7: Simplified electrical circuit of 3L-NPC inverter connected the rotor of DFIG.

The configuration of the rotor of DFIG connected 3L-NPC inverter is illustrated in Fig. 4.7. The rotor voltage which will be injected into DFIG, is also the output voltage of 3L-NPC inverter. Thus, the inverter output voltage in rotor reference frame (DQ) u_{inv}^{DQ} can be calculated by using equation (2.1):

$$u_{inv}^{DQ} = \frac{2}{3}\left(u_{AZ} + a u_{BZ} + a^2 u_{CZ}\right). \tag{4.45}$$

Consequently, the rotor voltage referred to the stator in dq reference frame (u_r^{dq}) can be calculated by using rotational transformation as [9]:

$$u_r^{dq} = K u_{inv}^{DQ} e^{-j\theta_r}, \tag{4.46}$$

where K is the ratio of the stator voltage to the rotor voltage of the DFIG.

The rotor current referred to the stator in dq reference frame (i_r^{dq}) can be calculated based on the rotor current in rotor reference (i_r^{DQ}) by using rotational transformation:

$$i_r^{dq} = \frac{1}{K} i_r^{DQ} e^{-j\theta_r}. \tag{4.47}$$

Based on the configuration in Fig. 4.7, the dynamic of neutral-point voltage (Z) is obtained based on the rotor currents and the switching states of 3L-NPC inverter:

$$\frac{du_z}{dt} = \frac{1}{4C}\left(2\left|S_a\right| - \left|S_b\right| - \left|S_c\right|\right) i_{Dr} + \frac{\sqrt{3}}{4C}\left(\left|S_b\right| - \left|S_c\right|\right) i_{Qr}. \tag{4.48}$$

In an inverter driven system, the common-mode voltage (u_{cm}) is defined as the voltage between the rotor neutral (N) and the neutral-point voltage (Z). Thus, the common-mode voltage (CMV) can be expressed as follows [12]:

$$u_{cm} = \frac{u_{AZ} + u_{BZ} + u_{CZ}}{3}. \tag{4.49}$$

The inverter output voltage is synthesized from the DC-link voltage, and the neutral phase voltage and has 3 possible values: $\{-U_{dc}/2, 0, U_{dc}/2\}$. Consequently, the CMV constitutes 7 steps $\{-U_{dc}/2, -U_{dc}/3, -U_{dc}/6, 0, U_{dc}/6, U_{dc}/3, U_{dc}/2\}$ and changes from $-U_{dc}/2$ to $U_{dc}/2$, depending on the inverter switching states.

In summary, a model for DFIG with stator flux and rotor current will be used as state variable, and the stator active and reactive powers are considered as the output. The control input of the system is rotor voltage which is calculated based on the switching state S_x and DC-link voltage U_{dc}. The stator voltage is normally fixed by the grid, thus it is considered as disturbance.

The aim of model predictive direct power control (MPDPC) scheme is to select the inverter switching state that leads the active and reactive powers closest to their respective references, balances the DC-link capacitor voltages and reduces the switching frequency

and CMV. In order to facilitate a multi-objective optimization, we consider the following terms in the cost function for the DFIG connected 3L-NPC inverter with two-step prediction (see further choices in [52], [16], [87, 88]):

$$\begin{aligned} g_{rsc} = &|P_s^*(k+1) - P_s^p(k+1)| + |P_s^*(k+2) - P_s^p(k+2)| + |Q_s^*(k+1) - Q_s^p(k+1)| \\ &+ |Q_s^*(k+2) - Q_s^p(k+2)| + \lambda_{dc}\,|u_z^p(k+2)| + \lambda_{cm}\,|u_{cm}^p(k+2)| + \lambda_n n_c, \end{aligned} \tag{4.50}$$

where λ_{dc}, λ_n and λ_{cm} are the weighting factors of the capacitor voltage balancing, the reduction of commutation and common-mode voltage.

The continuous-time model can be converted to discrete-time by using forward Euler approximation and considering T_{sp} as a sampling period:

$$\begin{bmatrix} \psi_{ds}^p(k+1) \\ \psi_{qs}^p(k+1) \\ i_{dr}^p(k+1) \\ i_{qr}^p(k+1) \end{bmatrix} = A_d \begin{bmatrix} \psi_{ds}(k) \\ \psi_{qs}(k) \\ i_{dr}(k) \\ i_{qr}(k) \end{bmatrix} + B_d \begin{bmatrix} u_{ds}(k) \\ u_{qs}(k) \\ u_{dr}(k) \\ u_{qr}(k) \end{bmatrix}, \tag{4.51}$$

where

$$A_d = e^{AT_{sp}} \simeq I + AT_{sp}, \quad B_d = \int_0^{T_{sp}} e^{A(T_{sp}-d\tau)} B d\tau \simeq BT_{sp}, \tag{4.52}$$

and $u_{ds} = \psi_{qs} = 0$.

In the same way, the neutral-point voltage is represented in discrete-time by using the first-order forward Euler approximation as:

$$\begin{aligned} u_z^p(k+1) = &\, u_z(k) + \frac{T_{sp}}{4C}\left(2\,|S_a(k)| - |S_b(k)| - |S_c(k)|\right) i_{Dr}(k) \\ &+ \frac{\sqrt{3}T_{sp}}{4C}\left(|S_b(k)| - |S_c(k)|\right) i_{Qr}(k), \\ u_z^p(k+2) = &\, u_z^p(k+1) + \frac{T_{sp}}{4C}\left(2\,|S_a(k+1)| - |S_b(k+1)| - |S_c(k+1)|\right) i_{Dr}^p(k+1) \\ &+ \frac{\sqrt{3}T_{sp}}{4C}\left(|S_b(k+1)| - |S_c(k+1)|\right) i_{Qr}^p(k+1). \end{aligned} \tag{4.53}$$

The active and reactive powers of the stator depend on the stator flux ψ_{ds} and rotor current i_{dr}, i_{qr} predictions according to equations (4.41) and (4.42):

$$P_s^p(k+1) = -\frac{3}{2}\psi_{ds}^p(k+1)\frac{L_m}{L_s}\omega_s i_{qr}^p(k+1), \tag{4.54}$$
$$Q_s^p(k+1) = \frac{3}{2}\frac{\omega_s\psi_{ds}^p(k+1)}{L_s}\left(\psi_{ds}^p(k+1) - L_m i_{dr}^p(k+1)\right).$$

In the real-time implementation of the control scheme, the calculation time of the control law will induce sample time delay in the actuation. Several studies regarding the delay compensation are available in the litterature, and this particular aspect will not be further detailed in the present chapter. We mentioned only that a simple solution to compensate the computational delay is to compute at time instant k the cost function corresponding to time instant $k+1$ using an estimation of the state at time $k+1$ and then the optimal switching state is applied at time $k+1$. In the subsequent developments we used the method proposed in Section 3.1.2 to reduce the computational effort and allow a straightforward implementation. In this case, the prediction of stator flux and rotor current at instant $k+2$ can be obtained by shifting one sample step of equations (4.51) and (4.52) as:

$$x(k+2) = A_d x(k+1) + B_d u(k+1), \tag{4.55}$$

The stator active and reactive powers at instant $k+2$ can be calculated as follows:

$$P_s^p(k+2) = -\frac{3}{2}\psi_{ds}^p(k+2)\frac{L_m}{L_s}\omega_s i_{qr}^p(k+2), \tag{4.56}$$
$$Q_s^p(k+2) = \frac{3}{2}\frac{\omega_s\psi_{ds}^p(k+2)}{L_s}\left(\psi_{ds}^p(k+2) - L_m i_{dr}^p(k+2)\right).$$

The prediction of stator voltage at time $k+1$ can be estimated by given equation:

$$u_{\alpha s}(k+1) = u_{\alpha s}(k)\cos(\omega_s T_{sp}) - u_{\beta s}(k)\sin(\omega_s T_{sp}), \tag{4.57}$$
$$u_{\beta s}(k+1) = u_{\alpha s}(k)sin(\omega_s T_{sp}) + u_{\beta s}(k)cos(\omega_s T_{sp}).$$

Similarly, the stator voltage transformation from $\alpha\beta$ reference to dq reference frame is given by:

$$u_{ds}(k+1) = u_{\alpha s}(k+1)\cos(\theta_s) + u_{\beta s}(k+1)\sin(\theta_s), \tag{4.58}$$
$$u_{qs}(k+1) = u_{\beta s}(k+1)\cos(\theta_s) - u_{\alpha s}(k+1)\sin(\theta_s).$$

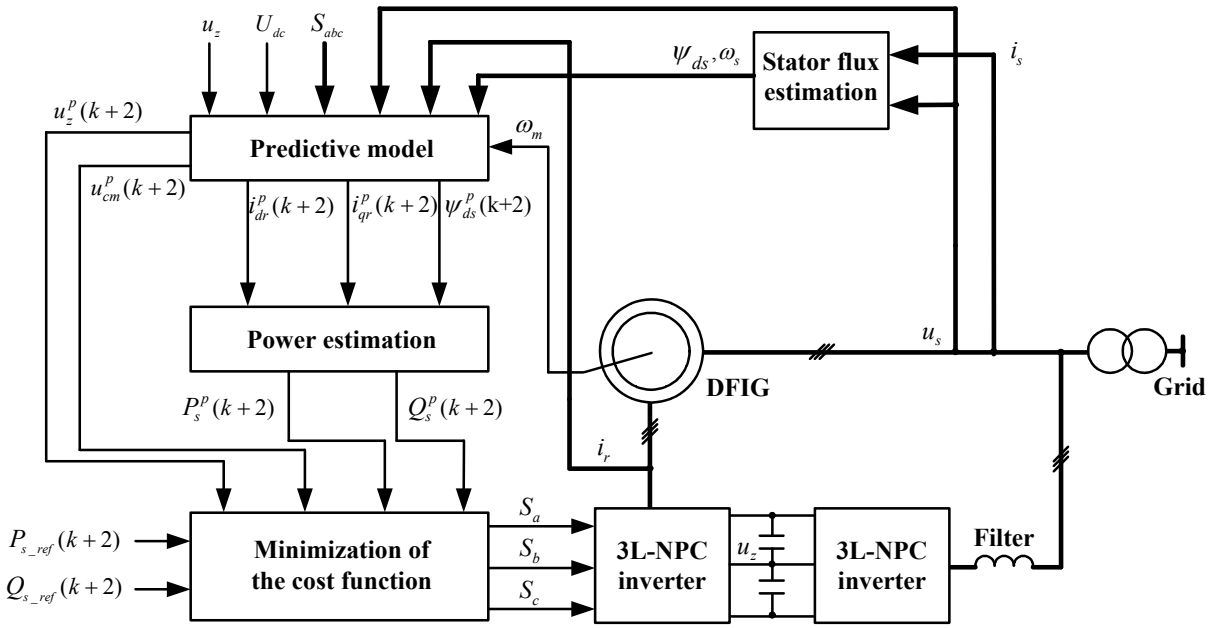

Figure 4.8: Block diagram of proposed control scheme for DFIG connected to 3L-NPC inverter.

Finally, the overall block diagram of the proposed control scheme is shown in Fig. 4.8. The goal of the predictive control is to minimize the cost function presented in (4.50). In each sample time, the predictive algorithm evaluates for every possible switching states and then selects the one that achieves the minimum value for applying in the next sampling instant. In short, the algorithm can be summarized in the following steps:

- Step 1: *Measurements:* $i_s(k)$, $i_r(k)$, $u_s(k)$, $u_z(k)$, ω_m and U_{dc}.
- Step 2: *Read the reference values:* $P_s^*(k)$ and $Q_s^*(k)$.
- Step 3: *Estimate:* Stator flux estimation $\psi_{ds}(k)$ by using (4.43).
- Step 4: *Predict the control variable at time k+1:* Stator flux $\psi_{ds}^p(k+1)$, rotor current $i_{dr}^p(k+1)$, $i_{qr}^p(k+1)$, neutral-point voltage $u_z^p(k+1)$ for 27 switching states based on (4.51), (4.52) and (4.53) respectively, then estimate the stator power $P_s^p(k+1)$, $Q_s^p(k+1)$ and n_c by using (4.54) and (3.16).
- Step 5: *Predict with corresponding switching transitions:* Stator flux $\psi_{ds}^p(k+2)$, rotor current $i_{dr}^p(k+2)$, $i_{qr}^p(k+2)$, neutral-point voltage $u_z^p(k+2)$ from (4.55), (4.53) and CMV $u_{cm}^p(k+2)$ from (4.49), then estimate the stator power $P_s^p(k+2)$ and $Q_s^p(k+2)$ based on (4.54).
- Step 6: *Evaluate:* cost function g_{rsc} by using equation (4.50) .

- Step 7: *Optimize:* Select the optimal value and apply to the inverter. Return to Step 1.

4.4 Simulation results

To test the performance of the proposed control scheme, simulation was performed with the Matlab/Simulink software and the algorithm is programmed using SFunction Builder Block. The implementation via such a block is selected to allow easy experimental implementation. The model of the DFIG was implemented in Simulink according to a stator coordinate for simplicity and prioritizing the simulation speed. The DFIG is rated at 2 MW and its parameters are listed in Table 4.1.

Table 4.1: DFIG parameters.

Parameter	Value	Description
P_{rated}	2 [MW]	Rated stator three phase active power
$U_{s-rated}$	690 [V]	Line to line nominal stator voltage
$U_{r-rated}$	2070 [V]	Line to line nominal rotor voltage
$I_{s-rated}$	1760 [A]	Each phase nominal stator current
$n_{s-rated}$	1500 [rpm]	Synchronous speed
p	2	The number pairs of poles
R_s	2.6 [mΩ]	Stator resistance
R_r	2.9 [mΩ]	Rotor resistance
$L_{\sigma s}$	87 [μH]	Stator leakage inductance
$L_{\sigma r}$	87 [μH]	Rotor leakage inductance
L_m	2.5 [mH]	Mutual inductance
J	0.314 [kg.m^2]	Moment of inertia
f_s	50 [Hz]	Frequency of the grid
U_{dc}	1200 [V]	DC-link voltage
C_{dc}	16000 [μF]	DC-link capacitor

In order to evaluate the dynamic performance, a comparison between MPDPC and deadbeat power control [77] with space vector modulation which used converter redundant switching states to balance DC-link capacitor voltages [25] (DPC-SVM) is established under different modes of speed and the same parameters in Table 4.1. The SVM implemented for the deadbeat controller has a sampling frequency $f_{svm} = 3$ kHz. For the MPDPC, a sampling frequency $f_{sp} = 20$ kHz is considered. This value has been selected to obtain an average switching frequency $f_{sw} = 1.5$ kHz similar to the DPC-SVM.

Given the global objective which is to control the power factor (PF), the reactive power reference is considered to be given by:

$$Q_{s\_ref} = P_{s\_ref}\frac{\sqrt{1-PF^2}}{PF}. \tag{4.59}$$

The DFIG was assumed to be functioning in speed control, i.e., the rotor speed is set externally to a constant value, and has slow changes because of the large inertia of the wind turbine. The initial active power and power factor reference were - 2 MW and $PF = 1$ at 0.5 s. The active power reference presents a steps from -2 MW to -1 MW at 1 s, then steps from -1 MW to -1.5 MW at 2 s (Fig. 4.9(a)). While the PF is changed from 1 to 0.9 at 1 s, then is changed from 0.9 to -0.9 at 1.5 s and from -0.9 to 0.9 at 2 s. The PF changes produce reactive power reference using equation (4.59) from 0 Var to -0.484 MVar at 1 s, then is changed from -0.484 MVar to 0.484 MVar at 1.5 s and from 0.484 MVar to -0.727 MVar at 2 s ('-' refers to generating active power and absorbing reactive power) (Fig. 4.9(c)).

As the machine operates at synchronous speed, slip is zero. Consequently, the power of the rotor is approximately zero as illustrated in Fig. 4.9(b). Figs. 4.9(b) and 4.9(d) indicate that the active power is tracking its references with fast dynamics and without affecting the reactive power. The proposed method presents better performance compared to the DPC-SVM. The DPC-SVM has worse results principally because the dynamic of the inverter and especially the influence of the neutral-point voltage variation are not taken into account in the control. As can be seen in Fig. 4.9, the power ripples of DPC-SVM is bigger than the proposed method. In fact, the mean absolute percentage error of stator active and reactive powers of proposed method are only 1.32% and 1.98% better than the results of 8.74% and 13.1% of DPC-SVM method.

The steady state of the stator current for the DPC-SVM controller and the MPDPC are presented in Figs. 4.10(a) and 4.10(c). To analyze THD of the output current, Powergui FFT toolbox has been used. The harmonic spectrum of stator current (i_{sa}) under the steady state condition of -1.5 MW and -0.727 MVar at synchronous speed for DPC-SVM and MPDPC are shown in Figs. 4.10(b) and 4.10(d). It can be seen that the THD value for the stator current for propsed method is much lower than DPC-SVM, from 6.72% to 2.52%. Thus, a THD of the stator current of less than 5% is met well within the limit required by the international standards such as IEC-61727 and IEEE-519. The quantitative comparisons of the two control methods at steady state, including the THD of the stator current is summarized in Table 4.2.

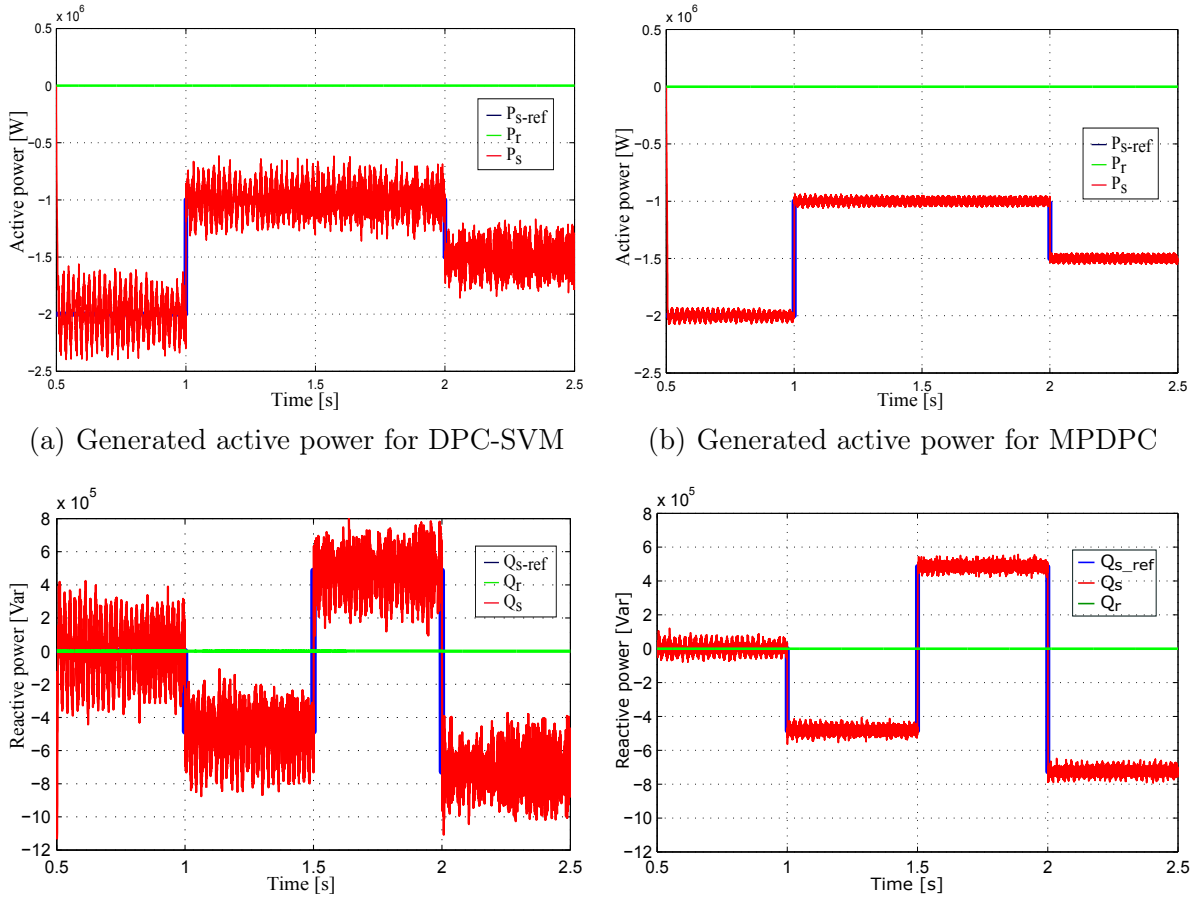

(a) Generated active power for DPC-SVM

(b) Generated active power for MPDPC

(c) Generated reactive power for DPC-SVM

(d) Generated reactive power for MPDPC

Figure 4.9: The dynamic response of active and reactive power with synchronous speed for DPC-SVM and MPDPC.

Table 4.2: Comparison of steady state performance for two controllers.

Method	MAPE of P_s	MAPE of Q_s	THD of i_{sa}
DPC-SVM	8.74%	13.1%	6.72%
Proposed method	1.32%	1.98%	2.52%

One of the main drawback of 3L-NPC structure is balancing voltage of the DC-link capacitor. Fig. 4.11 shows the evolution of the neutral-point voltage u_z under different of power steps. The result indicates that the balance of DC-link capacitor voltage is guaranteed with MAPE of voltage deviation 0.41% in spite of the transition of power references.

The performance of the proposed method is also examined while varying the rotor speed from 1200 to 1800 rpm as shown in Fig. 4.12. The active power reference is changed from -2 MW to -1 MW at 1.5 s and from -1 MW to -1.5 MW at 2 s (Fig.

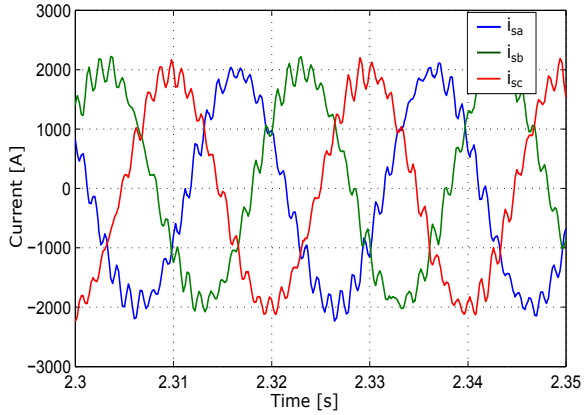

(a) The steady state of the stator current for DPC

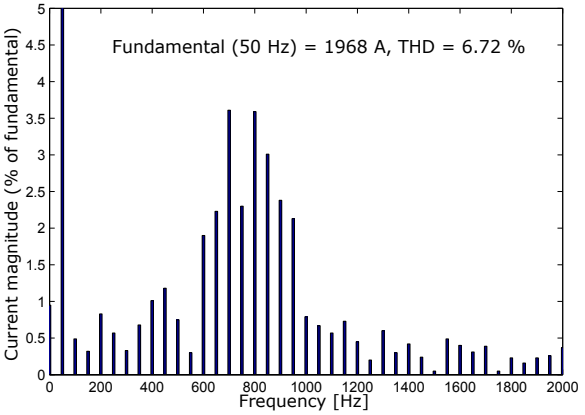

(b) Fast Fourier Transform of the stator current for DPC

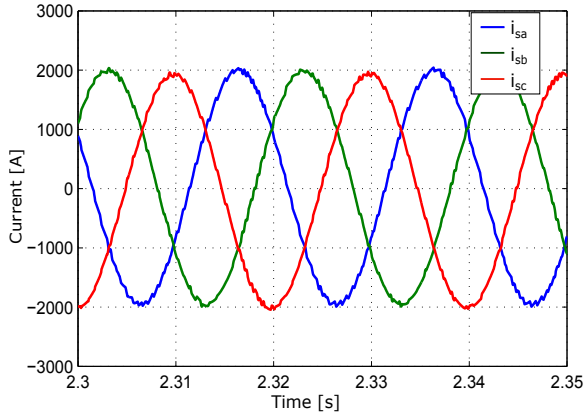

(c) The steady state of the stator current of MPDPC

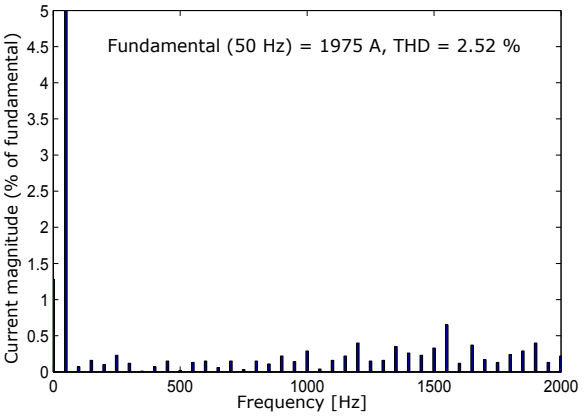

(d) Fast Fourier Transform of the stator current for MPDPC

Figure 4.10: The steady state and FFT of the stator current with synchronous speed for DPC-SVM and MPDPC.

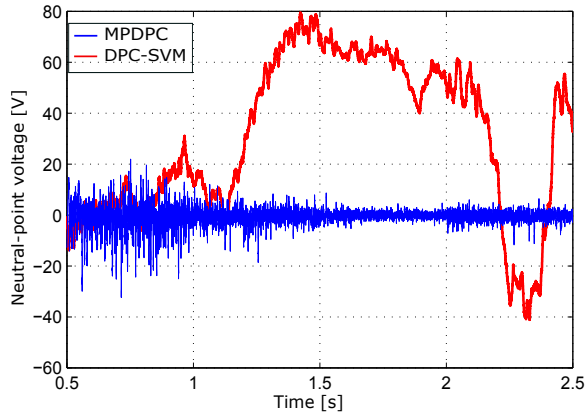

Figure 4.11: Performance of the u_z for two controllers with synchronous speed.

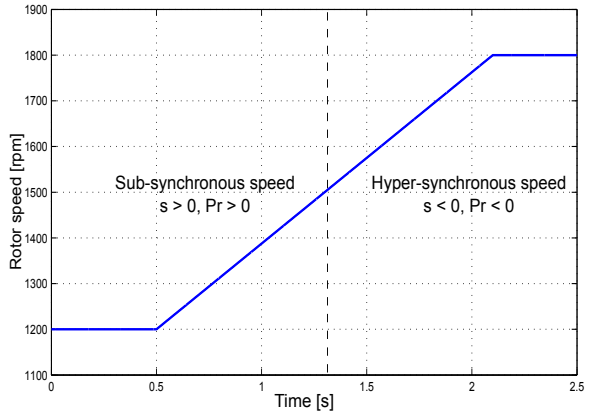

Figure 4.12: Rotor angular speed time response.

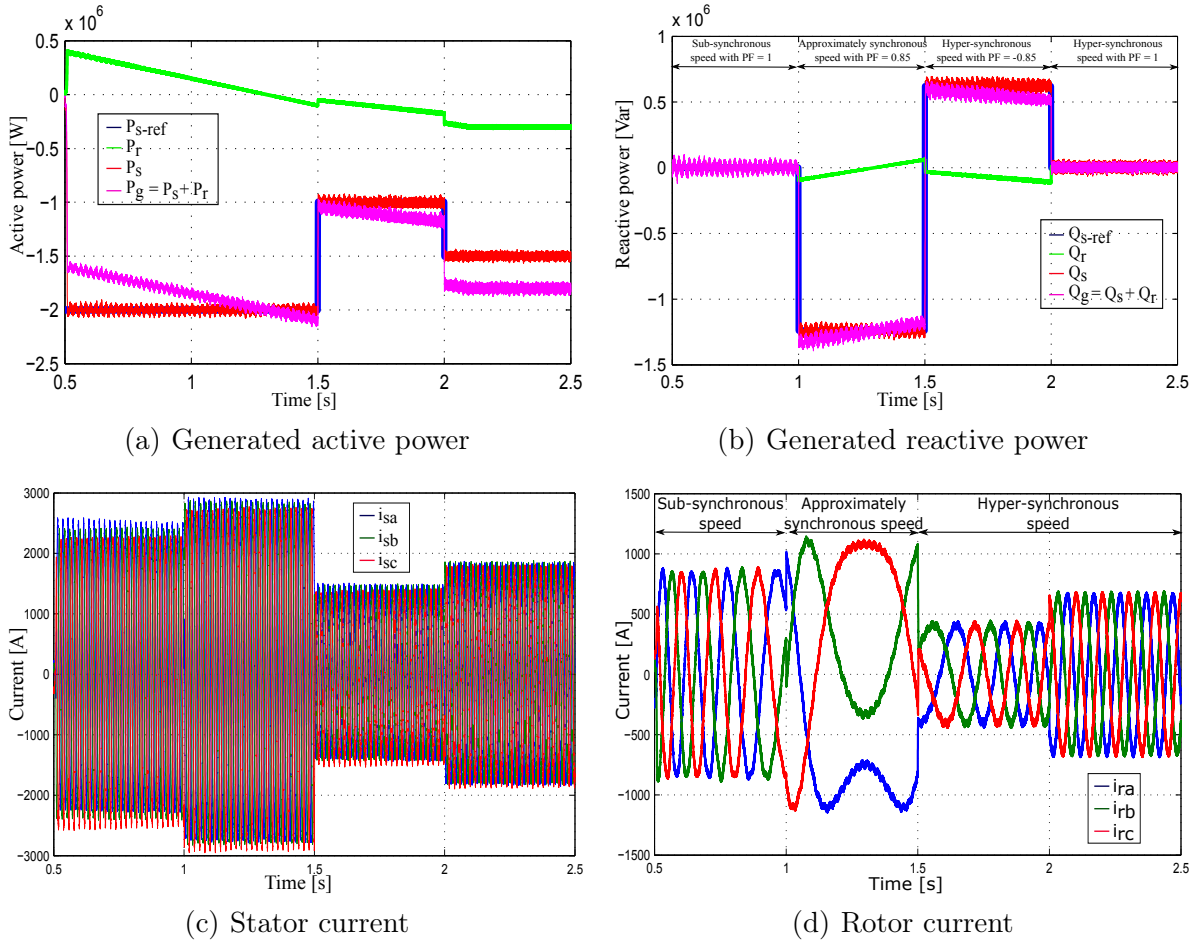

(a) Generated active power

(b) Generated reactive power

(c) Stator current

(d) Rotor current

Figure 4.13: The dynamic response of the power and current with rotor speed variation.

4.13(a)). While the reactive power reference is changed from -1.24 MVar to 0.62 MVar at 1.5 s and from 0.62 MVar to 0 Var at 2 s, corresponding with the change of power factor from 1 to a leading (0.85) or lagging (-0.85). When the rotor speed of the generator is greater than synchronous speed, the slip is negative ($s = -0.2$), thus, the rotor power P_r will be transferred from the generator rotor to the grid through the rotor converters of the DFIG, whereas the RSC operates as a rectifier and the GSC as an inverter. The powers delivered to the grid P_g and Q_g which are the sum of the stator and rotor powers are illustrated in Figs. 4.13(a) and 4.13(b). On the contrary, the slip is positive ($s = 0.2$) with sub-synchronous speed. This positive slip means that the rotor power P_r will be positive and will be received from the grid through the converters in which the RSC operates as an inverter and the GSC as a rectifier (Fig. 4.13).

On the other hand, a high common mode voltage can cause overvoltage stress in the

winding insulation of the electrical machine fed by power converter, producing deterioration and reducing the lifetime of the machine. Fig. 4.14 shows the common mode voltage is reduced by changing the weighting factor value λ_{cm} from 0 to 250 while maintaining an acceptable quality of current and power.

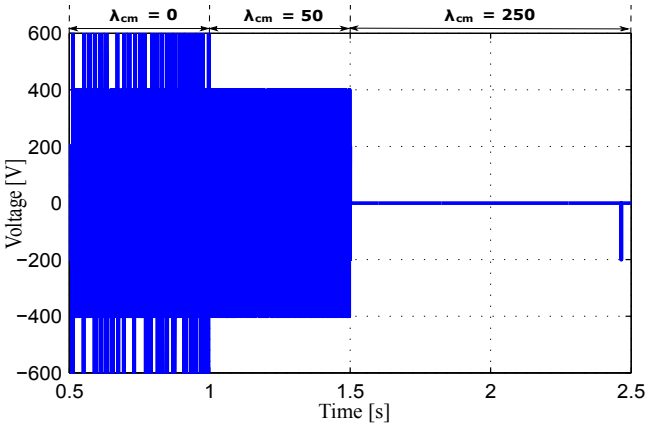

Figure 4.14: Performance of common-mode voltage.

Moreover, the machine parameters such as stator, rotor resistances, and inductance depend on the operating point and the temperature, affecting the accuracy of the controller. To confirm the robustness of the proposed method against variations of DFIG parameters, the values of the stator and rotor resistances R_s and R_r have been varied up to 50%, while the values of inductances L_s, L_r and L_m have been reduced to 50%. The machine operates at synchronous speed. The results shown in Fig. 4.15 demonstrate that the active and reactive powers are continuously tracking their references with slight

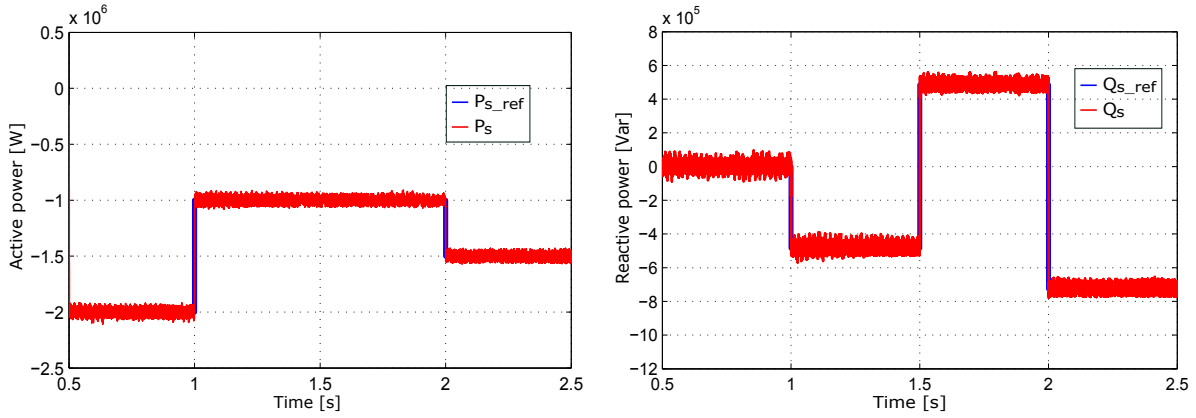

(a) The dynamic response of active power (b) The dynamic response of reactive power

Figure 4.15: Response of step tests for active and reactive powers with variation of DFIG parameters.

increase of the power ripples and THD of stator current. Thus, it is possible to indicate that the proposed control strategy is robust and can operate under the parameter variations.

4.5 Conclusions

In this chapter, a new direct power control method for DFIG system has been proposed in a direct manner to control the active and reactive powers. The DFIG and inverter discrete-time models are used to predict the behavior of the stator flux, rotor currents, neutral-point voltage and common-mode voltage. Using this information, the best switching state that minimizes a predefined cost function is selected and applied in the next sampling instant. Compared to DPC-SVM, the proposed method provides a fast transient response and better steady state performance. In addition, the peak of common-mode voltage can be reduced by adding a corresponding term in the cost function. The simulation results confirm the effectiveness and the robustness of the control scheme under the power, speed and parameters variation.

Chapter 5

Model Predictive Power Control based on Lyapunov function for 3L-NPC back-to-back converter

Finite control set model predictive control (FCS-MPC) has been discussed in the previous chapters and its principles can be widely applied to power converters and electrical machines thanks to its benefits such as simple implementation, easy taken into account additional constraint and delay compensation. In spite of the good performance, the FCS-MPC has some drawbacks to be addressed, one of them being the stability issue. A remarkable tool to solve this problem is Lyapunov stability theory. In [89, 90], a *practical stability* of FCS-MPC is presented to design a suitable cost function with one-step horizon by finding terminal weighting matrix based on the linear quadratic regulator (LQR) problem. Another approach is proposed in [91], based on imposing model predictive direct torque control (MPDTC) which ensures the stability within a certain norm bound. In [92], [93] a Lyapunov function based on an FCS model is proposed for reduce the execution time of the algorithm to control the current of three-phase two-level voltage source converter. A control scheme for Permanent Magnet Synchronous Machine (PMSM) which uses a control Lyapunov function (CLF) constraint to guarantee closed loop stability is presented [94, 95].

In this present work, in order to ensure the stability of the closed loop, we revisit the methodology employed in the previous chapters for the model predictive direct power control scheme by incorporation stability related information derived from a control Lyapunov function before the loop optimization. Therefore, aside the reinforcement of the

stability, the amount of calculation required for the proposed method is reduced compared with the conventional FCS-MPC, supporting the feasibility of the real time implementation. To validate the effectiveness of this proposal, two cases are presented. The first one is the control of the 3L-NPC inverter connected the grid and the second one is the 3L-NPC connected to the rotor of the DFIG. Moreover, by means of suitable weighting factor, the proposed method can provide a flexible approach to reduce certain common-mode voltage levels and keep the switching frequency device below 1 kHz. Simulation results are presented to confirm the efficiency of the proposed control system.

5.1 Improved Predictive Direct Power Control based on Lyapunov function for Grid connected 3L-NPC Inverter

5.1.1 Model predictive direct power control based on Lyapunov function

The dynamics model based on virtual flux orientation which is presented in Section 3.1.1 can be used for modeling the system. Hence, the continuous-time dynamic model is rewritten in the $\alpha\beta$ reference frame as:

$$\frac{di_{g\alpha}}{dt} = \frac{1}{L_f}\Big(\frac{U_{dc}}{6}(2S_a - S_b - S_c) + \omega\psi_{g\beta} - R_f i_{g\alpha}\Big), \tag{5.1}$$

$$\frac{di_{g\beta}}{dt} = \frac{1}{L_f}\Big(\frac{U_{dc}}{2\sqrt{3}}(S_b - S_c) - \omega\psi_{g\alpha} - R_f i_{g\beta}\Big),$$

$$\frac{d\psi_{g\alpha}}{dt} = -\omega\psi_{g\beta},$$

$$\frac{d\psi_{g\beta}}{dt} = \omega\psi_{g\alpha},$$

$$\frac{du_z}{dt} = \frac{1}{4C}\Big((2|\,S_a| - |\,S_b| - |\,S_c|)i_{g\alpha} + \sqrt{3}(|\,S_b|) - |\,S_c|)i_{g\beta}\Big).$$

Considering the system to be oriented with virtual grid flux (Fig. 3.5), the components of grid voltage become as:

$$u_{gd} = \psi_{gq} = 0;\ u_{gq} = \hat{U}_g \approx \omega\psi_{gd}, \tag{5.2}$$

where $\hat{U}_g$ is the magnitude of the grid voltage.

The active and reactive powers flow to the grid can be expressed in dq reference frame based on the equation (5.2) as [29]:

$$\begin{aligned} P_g &= \frac{3}{2}\left(u_{gd}i_{gd} + u_{gq}i_{gq}\right) = \frac{3}{2}\omega\psi_{gd}i_{gq} = \frac{3}{2}\hat{U}_g i_{gq}, \\ Q_g &= \frac{3}{2}\left(u_{gq}i_{gd} - u_{gd}i_{gq}\right) = \frac{3}{2}\omega\psi_{gd}i_{gd} = \frac{3}{2}\hat{U}_g i_{gd}. \end{aligned} \tag{5.3}$$

Furthermore, the dynamics of grid current in dq reference frame is also derived from the equations (3.31) and (5.2):

$$\begin{aligned} \frac{di_{gd}}{dt} &= -\frac{R_f}{L_f}i_{gd} + \frac{1}{L_f}u_{inv\_d} + \omega i_{gq}, \\ \frac{di_{gq}}{dt} &= -\frac{R_f}{L_f}i_{gq} + \frac{1}{L_f}u_{inv\_q} - \frac{1}{L_f}\hat{U}_g - \omega i_{gd}. \end{aligned} \tag{5.4}$$

The grid current in dq reference frame can be obtained through a transformation from the stationary to a synchronous rotating frame using the following equation:

$$\begin{aligned} i_{gd} &= i_{g\alpha}\cos\theta + i_{g\beta}\sin\theta, \\ i_{gq} &= i_{g\beta}\cos\theta - i_{g\alpha}\sin\theta, \end{aligned} \tag{5.5}$$

where θ denotes the angular position of rotating frame with respect to stationary frame. It can be obtained by the phase locked loop (PLL).

Defining the state errors of the grid current $\widetilde{i}_{gd}$, $\widetilde{i}_{qq}$:

$$\begin{aligned} \widetilde{i}_{gd} &= i_{gd} - i^*_{gd}, \\ \widetilde{i}_{gq} &= i_{gq} - i^*_{gq}, \end{aligned} \tag{5.6}$$

where the grid current references are calculated according to equation (5.3):

$$\begin{aligned} i_{gd}^{*} &= \frac{2Q_g^{*}}{3\hat{U}_g}, \\ i_{gq}^{*} &= \frac{2P_g^{*}}{3\hat{U}_g}. \end{aligned} \tag{5.7}$$

and substituting into the system dynamics given by equation (5.4), we have the dynamics of the errors for the grid current as:

$$\begin{aligned} \frac{d\widetilde{i}_{gd}}{dt} &= -\frac{R_f}{L_f} i_{gd} + \frac{1}{L_f} u_{inv\_d} + \omega i_{gq} - \frac{di_{gd}^{*}}{dt}, \\ \frac{d\widetilde{i}_{gq}}{dt} &= -\frac{R_f}{L_f} i_{gq} + \frac{1}{L_f} u_{inv\_q} - \frac{1}{L_f}\hat{U}_g - \omega i_{gd} - \frac{di_{gq}^{*}}{dt}. \end{aligned} \tag{5.8}$$

Since the frequency of the grid ($f = 50$ Hz) is smaller than sampling frequency ($f_s = 20$ kHz), we can consider:

$$\frac{di_{gd}^{*}}{dt} = 0; \ \frac{di_{gq}^{*}}{dt} = 0. \tag{5.9}$$

According to equation (5.3), the active and reactive powers can be controlled via the grid current components i_{gd} and i_{gq}. Therefore, we can use a control Lyapunov candidate function to ensure that the active and reactive powers are maintained according to the active power reference P_g^{*} and reactive power reference Q_g^{*} as:

$$V\left(\widetilde{i}_{gd}, \widetilde{i}_{gq}\right) = \frac{1}{2} K_d \widetilde{i}_{gd}^{2} + \frac{1}{2} K_q \widetilde{i}_{gq}^{2}, \tag{5.10}$$

with derivative

$$\dot{V}\left(\widetilde{i}_{gd}, \widetilde{i}_{gq}\right) = K_d \widetilde{i}_{gd} \frac{d\widetilde{i}_{gd}}{dt} + K_q \widetilde{i}_{gq} \frac{d\widetilde{i}_{gq}}{dt}, \tag{5.11}$$

where K_d and K_q are the positive gains.

In order to reduce the computational cost, we impose a pruning method for the choices inside the feasible finite set of controls based on the decrease of the Lyapunov function as illustrated in Fig. 5.1. At each switching instant only switching policies corresponding to a negative $\dot{V}$ will be considered as admissible for in the evaluation of the MPC cost function.

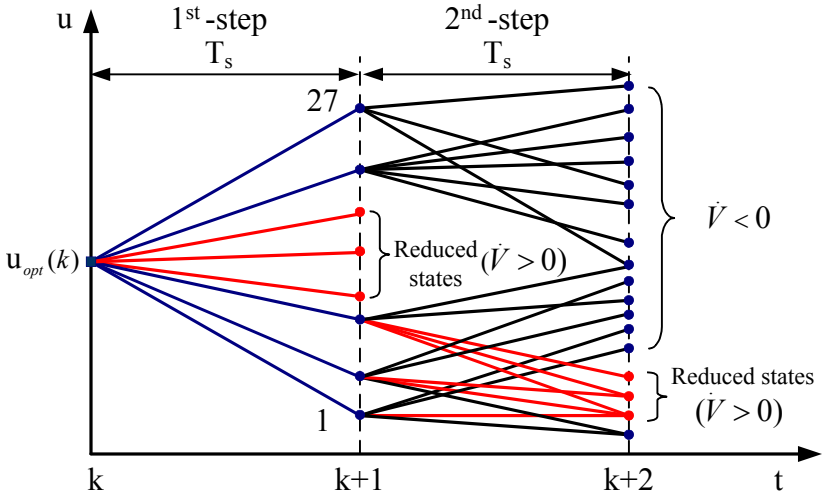

Figure 5.1: The improved FCS-MPC algorithm with reduced candidate sequences.

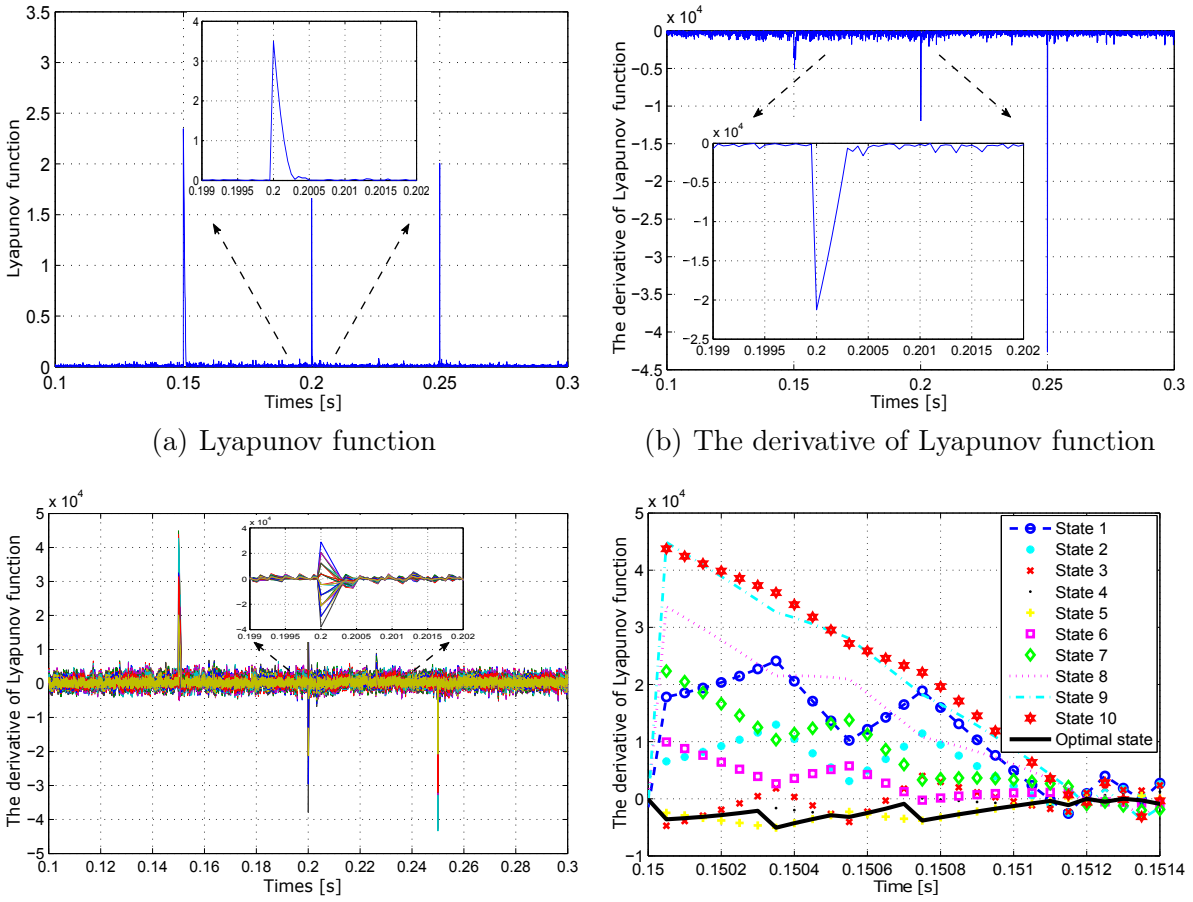

(a) Lyapunov function

(b) The derivative of Lyapunov function

(c) The prediction derivative of Lyapunov function for all switching states

(d) Switching sequence selection based on predicted stability and cost function minimization

Figure 5.2: The dynamic responses for the Lyapunov function and its derivative.

In order to illustrate the behaviour and the choices made along the real time control let us consider a simulation scenario around a set-point. Figs. 5.2(a) and 5.2(b) show the Lyapunov function and its derivative which guarantee the stability of the system as long as $\dot{V}$ is negative at each moment in time. Fig. 5.2(c) demonstrates the effect of each switching state, and then considering states that pass a stability test ($\dot{V} < 0$) in order to be selected for the loop optimization. With the aim to clarify this process, the detail of the selection with 10 switching states can be illustrated in Fig. 5.2(d). For example, at the time $t = 0.1502$ s, there are 3 switching configurations (state 3, 4 and 5) which satisfy the stability condition. Next, the optimal state is selected by minimizing the cost function among these feasible alternatives. Consequently, the state 4 is determined at this time as optimal.

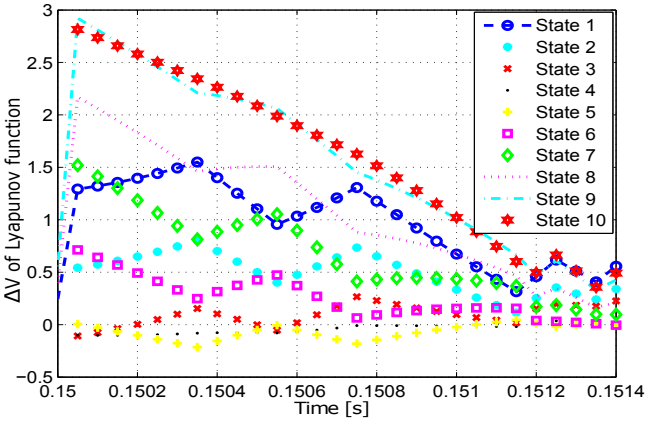

Figure 5.3: ΔV of Lyapunov function.

Nevertheless, due to discrete set control voltage, there is a different selection based on Lyapunov candidate function $\dot{V}$ and $\Delta V = V(k+1) - V(k)$ and the MPC based selection. Referring to Fig. 5.3, consider time $t = 0.1506$ s, only state 5 has $\Delta V < 0$, on the contrary, 3 switching states (state 3, 4 and 5) have $\dot{V} < 0$ (Fig. 5.2(d)). Thus, in fact the approximation of derivative Lyapunov function ΔV is worse than using $\dot{V}$ to select the switching decreasing Lyapunov function. Based on this basic principle of selection, the optimal control sequence $u_{opt} = [S_a \; S_b \; S_c]^T$ is the one which minimizes the cost function:

$$u_{opt} = \arg\left\{ \min_{u_k \in \{-1,0,1\}^3, u_{k+1} \in \{-1,0,1\}^3} g_{grid}\left(u_k, u_{k+1}\right) \right\}. \tag{5.12}$$

$$\text{subject to} \quad \dot{V}(k) < 0$$

$$\dot{V}(k+1) < 0$$

Is worth to be mentioned that the selection is not redundant with the cost function minimization. Thus, considering the constraints in the optimization problem leads to lost of performance (from the point of view of the optimization cost function). This is the price to be paid to guarantee a Lyapunov decrease all by optimizing the cost function.

The feasibility of the constraints in the optimization (5.12) is equivalent to the validation of a Lyapunov function definition. Conversely, the feasibility domain of the problem 5.12 represents the validity domain of the Lyapunov function. From this point of view, it should be mentioned that the decrease of the Lyapunov function cannot be guaranteed in the neighbourhood of the origin due to the quatification of the control signal. A measure of the neighborhood of the origin is analysed in Section 5.2, in order to provide a Input-to-State Stability type of argument for the overall control scheme. Finally, the flowchart of overall control technique for the model predictive power control (MPPC) based on Lyapunov function is illustrated in Fig. 5.4.

5.1.2 Illustration of selection criteria in simulation

Simulations were carried out using MATLAB/Simulink and SimPowerSystems toolbox to test the effectiveness of the proposed control strategy. The parameters of the system used for simulation studies is given in Table 3.1. The sampling time T_s set to 50 μs which is appropriate for the average device switching frequency $f_{sw} = 2.5$ kHz.

In order to validate the bidirectional power flow ability under a unity power factor operation, the active power reference P_{g_ref} changes from 15 kW to - 15 kW at $t = 0.155$ s, corresponding with the change of power factor from 1 to -1. Fig. 5.5 shows that the controller provides fast tracking response and good dynamic performance during the transient. The grid voltage is in phase with the current in a rectifying mode and out of phase with the current in an inverting mode. The phase shift variation between the grid voltage and current is depicted in Fig. 5.6.

With the aim to study better the efficiency of the proposed method, the results obtained from conventional FCS-MPC [96] with the same conditions are also presented. Then, to fully confirm the over range of operation of the proposed scheme with different power factor, a second dynamic test is performed. The reference values of active and reactive powers are set at 5 kW and -2 kVar, corresponding to negative power factor ($PF = -0.93$). At $t = 0.15$ s, the reference of active power is changed to 8 kW, leading the power factor reaching about -0.97. Then at $t = 0.2$ s, the reactive power reference

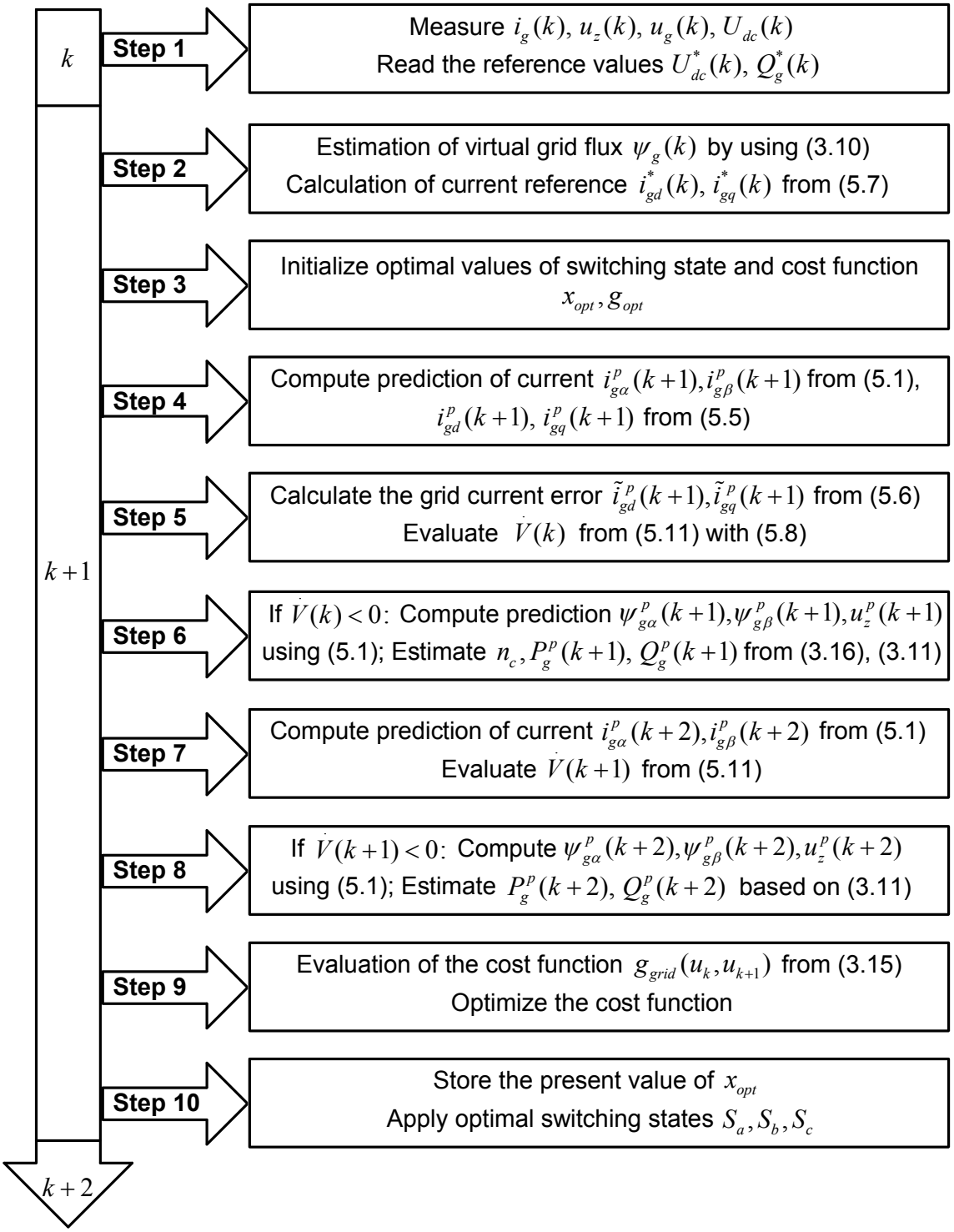

Figure 5.4: Execution flow diagram of the proposed control method.

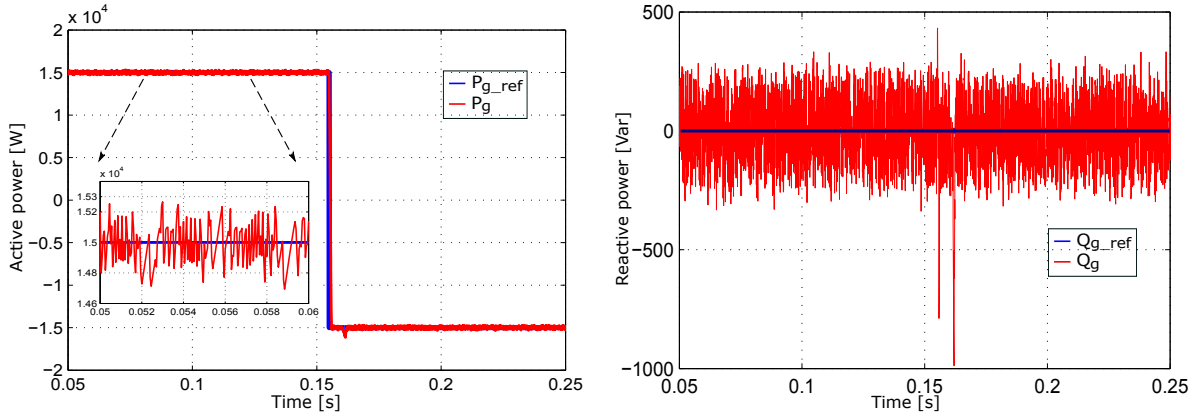

(a) Active power (b) Reactive power

Figure 5.5: The transient power responses for a step in the active power reference from 15 to -15 kW at $t = 0.155$ s.

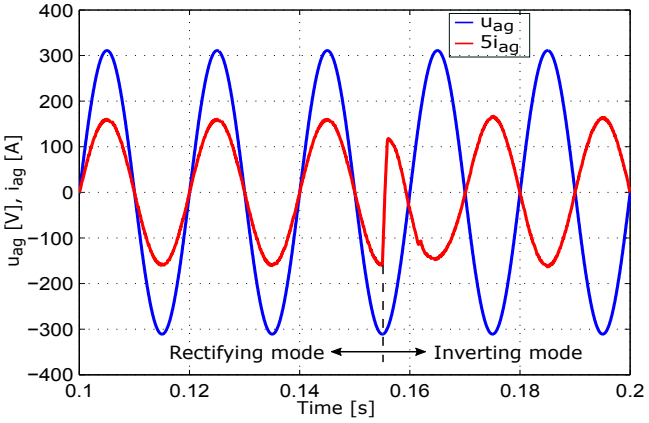

Figure 5.6: Steady state grid voltage and current waveforms.

Q_{g_ref} is changed to 2 kVar, forcing the operation to lagging power factor. Finally, a step change in the active power reference from 8 kW to 5 kW is applied at $t = 0.25$ s, leading to a redution of the power factor from 0.97 to 0.93. The results shown in Fig. 5.7 indicate that the active and reactive powers can track their reference values and reach their steady state conditions with fast dynamic response. The mean absolute percentage error of active and reactive powers for conventional FCS-MPC are 1.95% and 5.57%, whereas, for the proposed method they are 2.15%, and 6.84%, respectively.

The total harmonic distortion (THD) can be used to evaluate the steady state performance. The current spectrum of grid current for conventional FCS-MPC and the proposed method are depicted in Figs. 5.8(b) and 5.8(d). The THD of grid current using conventional method is 3.57%, while the THD for the proposed method is 3.71%, which is still below the accepted limit of the IEEE 519 standard. It is clear that the proposed method has the same steady state of grid current than conventional method

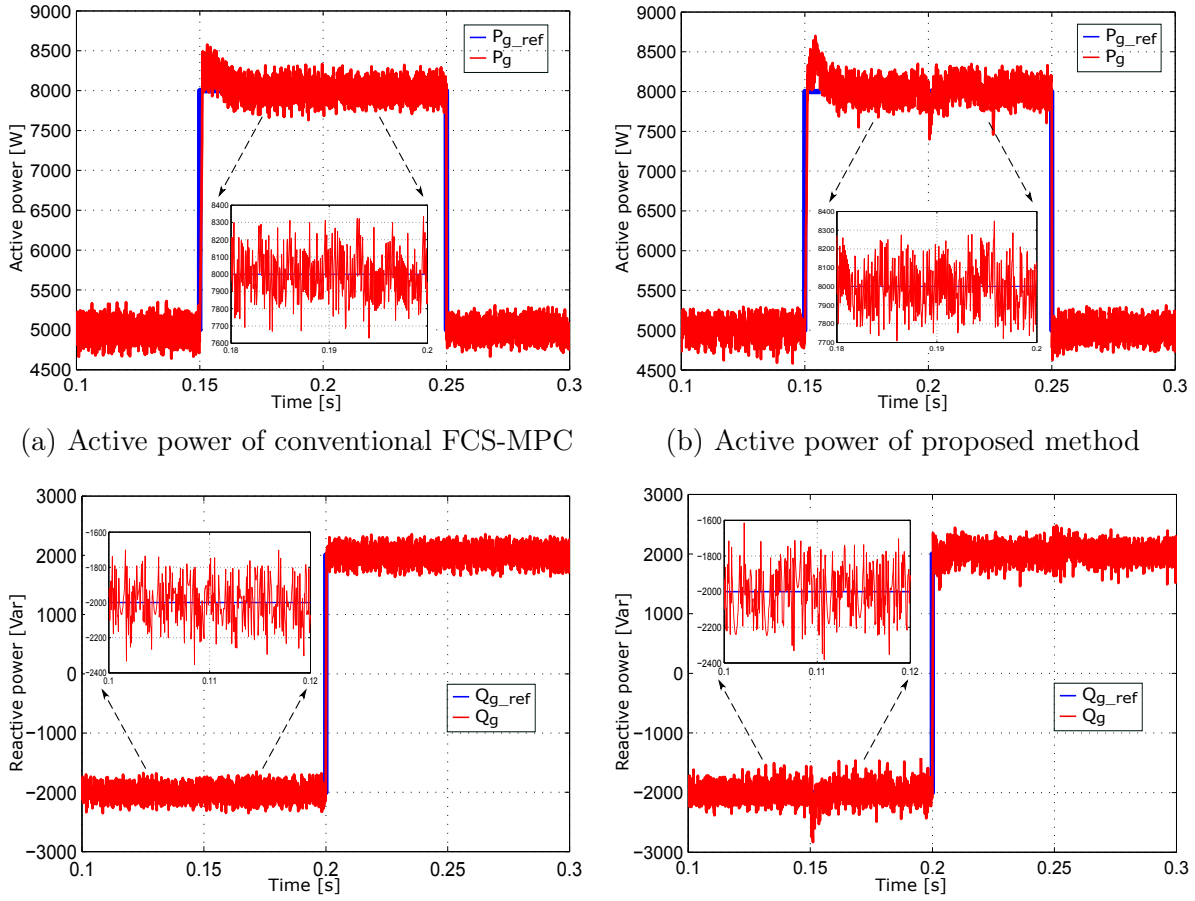

(a) Active power of conventional FCS-MPC

(b) Active power of proposed method

(c) Reactive power of conventional FCS-MPC

(d) Reactive power of proposed method

Figure 5.7: The dynamic response of active and reactive powers for conventional FCS-MPC and proposed method.

as shown in Figs. 5.8(a) and 5.8(c). The simulation results illustrate that the MAPE of power and THD of the current for the proposed method increase slightly compared with conventional FCS-MPC. However, in practice, the average combinations calculated of the proposed method are 61 depending on the measured states and power references. Thus, the proposed control method reduces the average amount of calculations needed by about 91% compared with the conventional method. Indeed, the average computation time required of the conventional FCS-MPC is about 92 μs, while the proposed method needs only 35 μs in a 3.3 GHz, i5-6600 CPU, permitting a real time implementation with extended horizons. Consequently, it is possible to indicate that the proposed MPPC based on Lyapunov function technique shows the same output performances but on the basis of a reduced computational time, in comparison with the conventional FCS-MPC scheme.

The major drawback of 3L-NPC inverter is the balance of DC-link capacitor voltages.

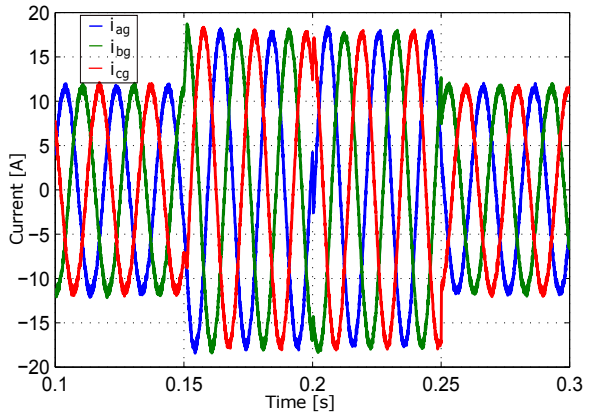

(a) The current transient response of conventional method

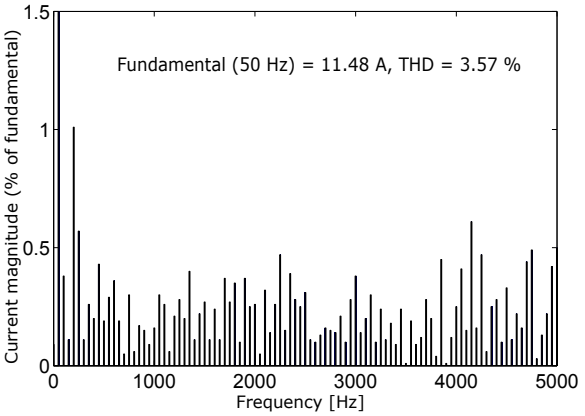

(b) FFT of the grid current for conventional method

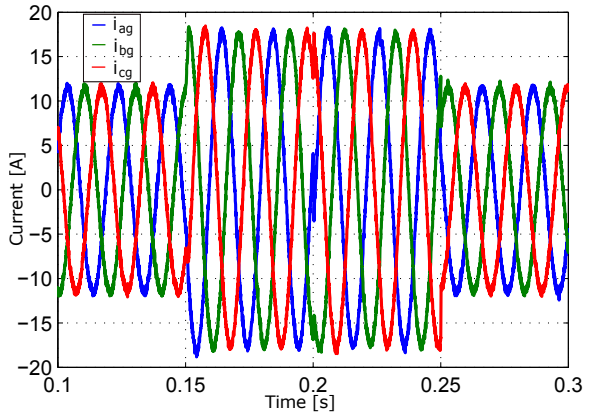

(c) The current transient response of proposed method

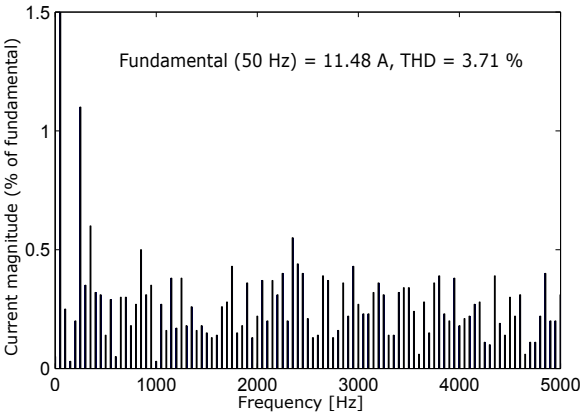

(d) FFT of the grid current for proposed method

Figure 5.8: The dynamic response and FFT of the grid current for conventional method and proposed method.

In order to test the behavior of the system under DC load variation, a resistance load R_{load} varies from 72 Ω to 45 Ω at $t = 0.15$ s and from 45 Ω to 72 Ω at $t = 0.25$ s. As shown in Fig. 5.9, although there is a small overshoot at transition steps but the DC-link voltage is maintained at its reference value with good voltage balance between DC-link capacitor.

To validate the ability of the proposed method against parameter variations, we have considered a variation of parameters which the values of the inductance L_f has been varied up to 40%, while the value of resistance R_f has been increased to 50% of its real value. The test condition is the same as that in Fig. 5.7. Fig. 5.10 presents the results of the conventional and proposed method with parameter variations. It is obviously that both the active and reactive powers can track theirs reference values with small increase of the power ripples, but still remains an acceptable THD of grid current.

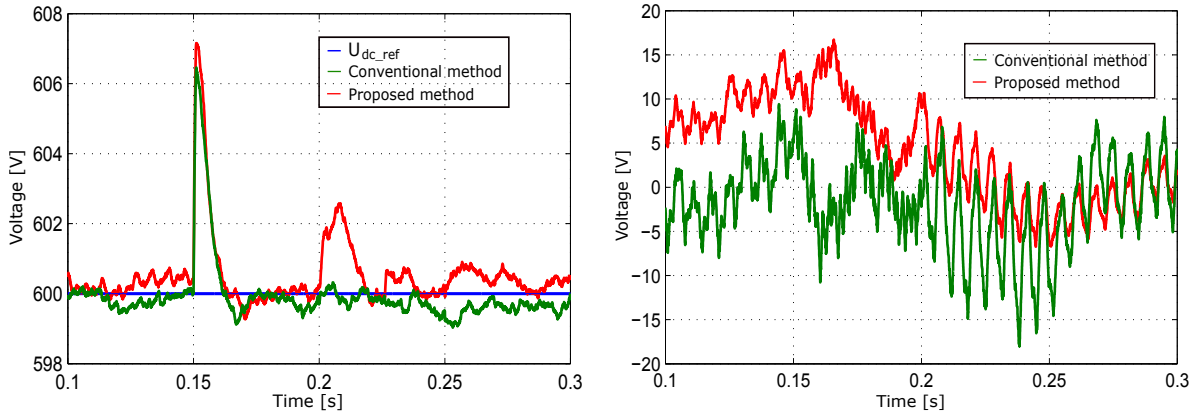

(a) The DC-link voltage response (b) Performance of the neutral-point voltage

Figure 5.9: The DC-link voltage and neutral-point voltage responses for the conventional and proposed method.

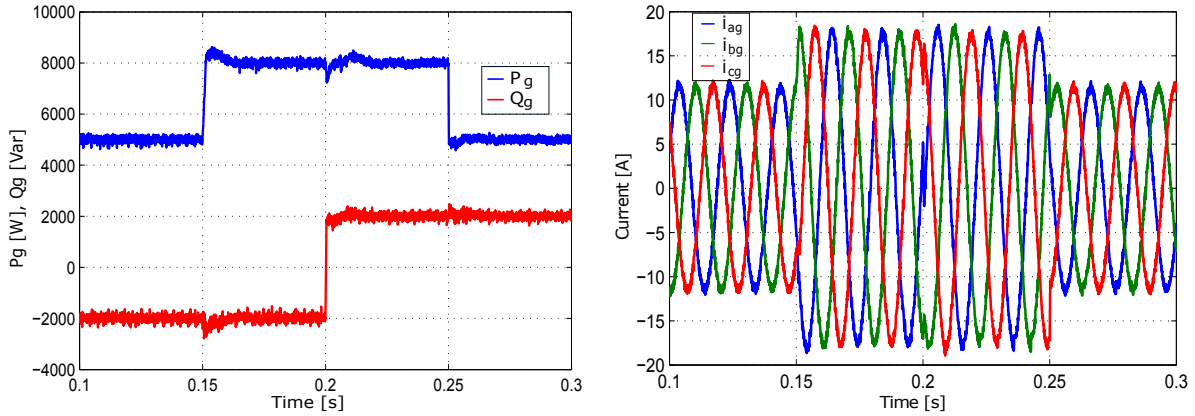

(a) Dynamic response of active and reactive powers for the proposed method (b) Grid current waveform for the proposed method

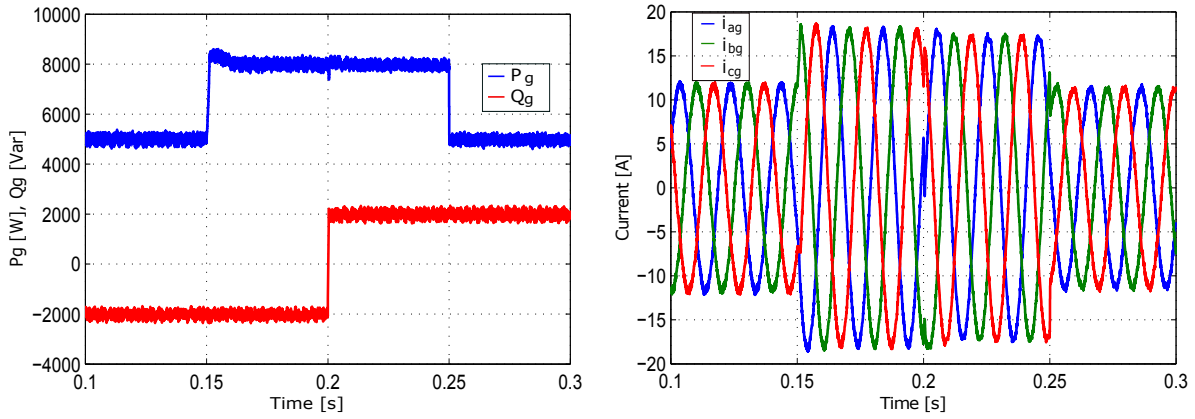

(c) Dynamic response of active and reactive powers for the conventional method (d) Grid current waveform for the conventional method

Figure 5.10: Transient response simulation results with parameter variations for the conventional and proposed method.

5.2 Model Predictive Direct Power Control Based on Lyapunov Function for DFIG Fed by a 3L-NPC Inverter

5.2.1 Proposed model predictive direct power control based on Lyapunov function

Since the system is oriented with stator flux ($u_{ds} = \psi_{qs} = 0$, $u_{qs} = \hat{U}_g \approx \omega_s \psi_{ds}$), the rotor current of DFIG can be simplified as:

$$\begin{aligned} \frac{di_{dr}}{dt} &= \frac{L_m \hat{U}_g}{\omega_s L_s T_s \sigma L_r} - \frac{R_\sigma}{\sigma L_r} i_{dr} + \omega_r i_{qr} + \frac{1}{\sigma L_r} u_{dr}, \\ \frac{di_{qr}}{dt} &= \frac{\omega_m L_m \hat{U}_g}{\omega_s L_s \sigma L_r} - \frac{R_\sigma}{\sigma L_r} i_{qr} - \omega_r i_{dr} - \frac{L_m}{\sigma L_s L_r} u_{qs} + \frac{1}{\sigma L_r} u_{qr}, \end{aligned} \tag{5.13}$$

where $\hat{U}_g$ is the magnitude of the grid voltage which can be assumed constant and obtained by using the phase locked loop.

To obtain the discrete-time of the rotor current, an Euler approximation can be used:

$$\begin{aligned} i^p_{dr}(k+1) &= \frac{L_m \hat{U}_g T_{sp}}{\omega_s L_s T_s \sigma L_r} + \left(1 - \frac{R_\sigma T_{sp}}{\sigma L_r}\right) i_{dr}(k) + T_{sp} \omega_r i_{qr}(k) + \frac{T_{sp}}{\sigma L_r} u_{dr}(k), \\ i^p_{qr}(k+1) &= \frac{\omega_m L_m \hat{U}_g T_{sp}}{\omega_s L_s \sigma L_r} + \left(1 - \frac{R_\sigma T_{sp}}{\sigma L_r}\right) i_{qr}(k) - \omega_r T_{sp} i_{dr}(k) - \frac{L_m T_{sp}}{\sigma L_s L_r} u_{qs}(k) + \frac{T_{sp}}{\sigma L_r} u_{qr}(k), \\ i^p_{dr}(k+2) &= \frac{L_m \hat{U}_g T_{sp}}{\omega_s L_s T_s \sigma L_r} + \left(1 - \frac{R_\sigma T_{sp}}{\sigma L_r}\right) i^p_{dr}(k+1) + T_{sp} \omega_r i^p_{qr}(k+1) + \frac{T_{sp}}{\sigma L_r} u^p_{dr}(k+1), \\ i^p_{qr}(k+2) &= \frac{\omega_m L_m \hat{U}_g T_{sp}}{\omega_s L_s \sigma L_r} + \left(1 - \frac{R_\sigma T_{sp}}{\sigma L_r}\right) i^p_{qr}(k+1) - \omega_r T_{sp} i^p_{dr}(k+1) - \frac{L_m T_{sp}}{\sigma L_s L_r} u_{qs}(k+1) \\ &\quad + \frac{T_{sp}}{\sigma L_r} u^p_{qr}(k+1), \end{aligned} \tag{5.14}$$

where T_{sp} is the sampling time.

The neutral-point voltage at instant $k+1$ and $k+2$ can be accomplished by using equation (4.53) which is presented in Section 4.2.2.

The stator power can be expressed based on equations (4.41) and (4.42) as:

$$\begin{aligned} P_s &= -\frac{3}{2}\psi_{ds}\frac{L_m}{L_s}\omega_s i_{qr} = -\frac{3}{2}\hat{U}_g\frac{L_m}{L_s}i_{qr}, \\ Q_s &= \frac{3}{2}\hat{U}_g\left(\frac{\psi_{ds}}{L_s} - \frac{L_m}{L_s}i_{dr}\right) = \frac{3}{2}\hat{U}_g\left(\frac{\hat{U}_g}{\omega_s L_s} - \frac{L_m}{L_s}i_{dr}\right). \end{aligned} \tag{5.15}$$

Since the grid voltage amplitude does not vary under normal operating conditions, from equation (5.15), it follows that the stator power is proportional with rotor current. Thus, this principle can be used to control the stator active and reactive powers by means of the rotor current components. In this case, the rotor currents will be used as state variable, while the stator powers and rotor voltage are considered as the output and control input. The state error of the rotor current can be defined by following equation:

$$\begin{aligned} \widetilde{i}_{dr} &= i_{dr} - i^*_{dr}, \\ \widetilde{i}_{qr} &= i_{qr} - i^*_{qr}, \end{aligned} \tag{5.16}$$

where the reference values of rotor current are achieved from the equation (5.15):

$$\begin{aligned} i^*_{dr} &= -\frac{2Q^*_s L_s}{3\hat{U}_g L_m} + \frac{\hat{U}_g}{\omega_s L_m}, \\ i^*_{qr} &= -\frac{2P^*_s L_s}{3\hat{U}_g L_m}. \end{aligned} \tag{5.17}$$

Replacing the rotor currents i_{dr}, i_{qr} in equation (5.13) by their errors $\widetilde{i}_{dr}$, $\widetilde{i}_{qr}$ which are defined in equation (5.16), one obtains the error dynamic system of the rotor current as:

$$\begin{aligned} \frac{d\widetilde{i}_{dr}}{dt} &= \frac{L_m\hat{U}_g}{\omega_s L_s T_s \sigma L_r} - \frac{R_\sigma}{\sigma L_r}i_{dr} + \omega_r i_{qr} + \frac{1}{\sigma L_r}u_{dr} - \frac{di^*_{dr}}{dt}, \\ \frac{d\widetilde{i}_{qr}}{dt} &= \frac{\omega_m L_m\hat{U}_g}{\omega_s L_s \sigma L_r} - \frac{R_\sigma}{\sigma L_r}i_{qr} - \omega_r i_{dr} - \frac{L_m}{\sigma L_s L_r}u_{qs} + \frac{1}{\sigma L_r}u_{qr} - \frac{di^*_{qr}}{dt}, \end{aligned} \tag{5.18}$$

with assuming $\frac{di^*_{dr}}{dt} = 0$; $\frac{di^*_{qr}}{dt} = 0$ due to higher sampling rate.

In order to guarantee the stability, a Lyapunov candidate function can be used to ensure that the active and reactive powers are maintained according to the active power

reference P_s^* and desired power factor (PF) as:

$$V\left(\widetilde{i}_{dr},\widetilde{i}_{qr}\right)=\frac{1}{2}K_d\widetilde{i}_{dr}^2+\frac{1}{2}K_q\widetilde{i}_{qr}^2, \tag{5.19}$$

with

$$\Delta V=V\left(\widetilde{i}_{dr}^p(k+1),\widetilde{i}_{qr}^p(k+1)\right)-V\left(\widetilde{i}_{dr}(k),\widetilde{i}_{qr}(k)\right), \tag{5.20}$$

where K_d and K_q are the positive gains.

To reduce the computational burden when two-step horizon is considered, we impose a pruning method based on the decrease of the Lyapunov function described above. With the aim to ensure the stability of the closed loop, at each switching instant only control voltages assuring $\Delta V<0$ have to be considered in the evaluation of the MPC cost function. As shown in Fig. 5.11, ones a switching state is determined to satisfy the stability condition ($\Delta V<0$), then this feasible alternative is selected for the loop optimization. Nevertheless, due to model uncertainties and the structure of the discrete set control voltages, the candidate Lyapunov function (5.19) does not converge to zero in general, its decrease being feasible only outside a reagion containing the origin. Thus, the closed-loop system is converging to a set centered in zero at best. In this section, we can characterize the stability of the system using an attractivity such as Input to State Stability (ISS) [97–99] during the optimization problem, two cases are considered: the first one correspond to $V(k)>\varepsilon_v$ and the second one $V(k)<\varepsilon_v$. If $V(k)>\varepsilon_v$ only switches obtaining $\Delta V<0$ are considered and if $V(k)<\varepsilon_v$ only switches assuring $V(k+1)<\varepsilon_v$ are considered (Fig. 5.12). Hence, ε_v can be used as a stabilizing constraint which guarantees feasibility and stability for the optimization problem. The detail of the selection and influence of this parameter will present in next section. Moreover, to avoid a high jump in phase voltage and reduce the number of commutations, only combination of inputs having a difference of one switch in the inverter are considered. Consequently, referring to equation (4.50), we can obtain the optimal control sequence by given equation:

$$\begin{aligned} u_{opt}=\arg\left\{\min_{u_k\in\{-1,0,1\}^3,u_{k+1}\in\{-1,0,1\}^3} g_{rsc}\left(u_k,u_{k+1}\right)\right\}. \\ \text{subject to}\quad \left((\mathrm{V(k)}>\varepsilon_\mathrm{v})\,\&\,(\Delta\mathrm{V}<0)\right)\vee\left((\mathrm{V(k)}<\varepsilon_\mathrm{v})\,\&\,(\mathrm{V(k+1)}<\varepsilon_\mathrm{v})\right) \\ \|u_k-u_{k+1}\|<1 \end{aligned} \tag{5.21}$$

Finally, a block diagram of the whole control strategy is shown in Fig. 5.13. The aim of the proposed model predictive control based on Lyapunov function can be achieved by using algorithm 3.

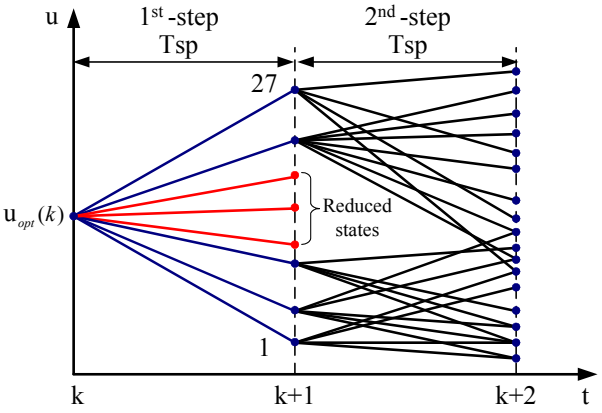

Figure 5.11: The improved FCS-MPC algorithm.

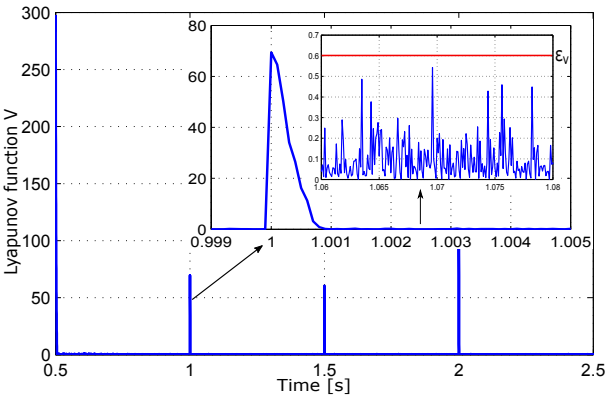

Figure 5.12: Lyapunov function V and its bound.

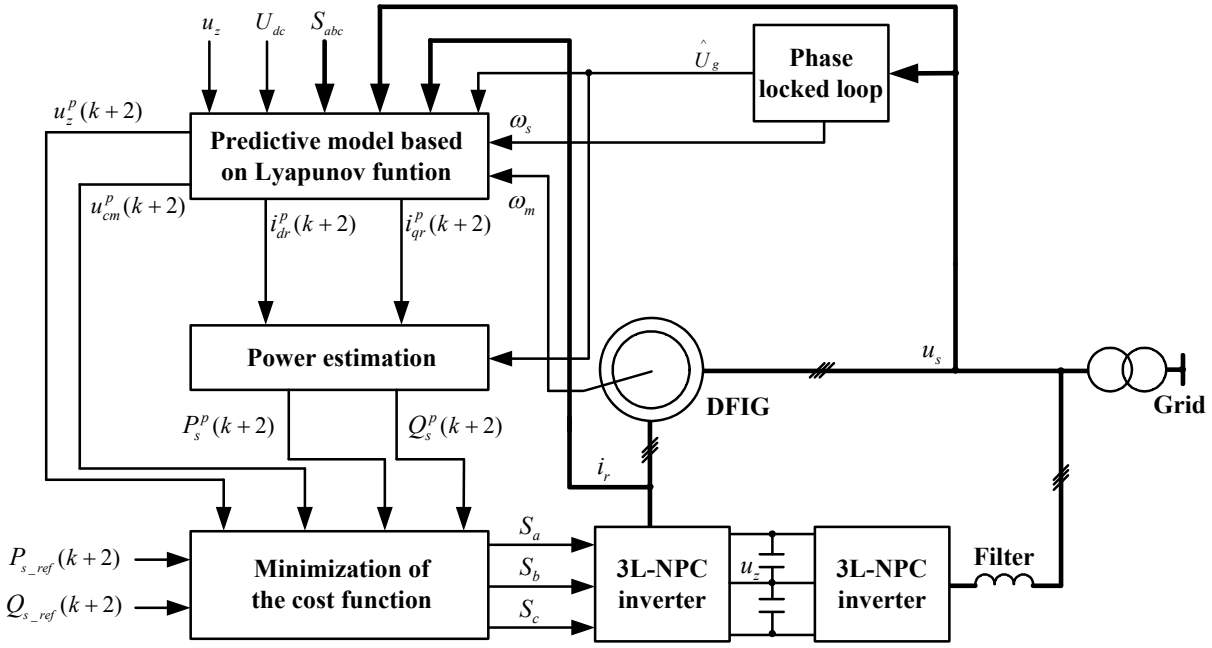

Figure 5.13: Block diagram of proposed control technique based on the Lyapunov function.

5.2.2 Simulation results

Simulations of the proposed control strategy for a DFIG connected 3L-NPC inverter were performed by using the Matlab/Simulink. The power control strategy has adopted sampling frequency $f_{sp} = 10$ kHz which creates the equivalent switching frequency $f_{sw} = 1$ kHz. The DFIG parameters are shown in Table 4.1. The weighting factors of the cost function in (4.50) are $\lambda_{dc} = 8000$, $\lambda_n = 13000$ and $\lambda_{cm} = 350$.

Algorithm 3: Algorithm of model predictive direct power control based on Lyapunov function

Measure $i_r(k)$, $u_z(k)$, $u_s(k)$, $\omega_m(k)$ and $U_{dc}(k)$;
Read the reference values $P_s^*(k)$ and $Q_s^*(k)$;
Calculate the rotor current reference $i_{dr}^*(k)$, $i_{qr}^*(k)$ by using equation (5.17) ;
Extrapolation of references $P_s^*(k+2)$, $Q_s^*(k+2)$ and $u_{qs}(k+1)$;
`/*` x_{opt}, g_{opt} `are the optimal values of the switching states and cost function */`
Initialize optimal values of the switching state x_{opt} and cost function g_{opt} ;
for $i = 1$ *to* 27 **do**
  Compute predictions: $u_{dr}^p(k+1)$, $u_{qr}^p(k+1)$ from (4.45) and (4.46), $i_{dr}^p(k+1)$ and $i_{qr}^p(k+1)$ from (5.14) ;
  Calculate the rotor current error: $\widetilde{i}_{dr}^p(k+1)$ and $\widetilde{i}_{qr}^p(k+1)$ by using equation (5.16) ;
  Evaluate the candidate Lyapunov function: $V(k+1)$, $V(k)$, ΔV based on (5.19) and (5.21) ;
  if $((V(k) > \varepsilon_v)\,\&\,(\Delta V < 0)) \vee ((V(k) < \varepsilon_v)\,\&\,(V(k+1) < \varepsilon_v))$ **then**
    Prediction of neutral point voltage: $u_z^p(k+1)$ by using (4.53) ;
    Estimate the values: n_c from (3.16), $P_s^p(k+1)$ and $Q_s^p(k+1)$ from (5.15) ;
    Predict corresponding switching transitions ;
    `/* m = length(switching transitions corresponding) */`
    for $j = 1$ *to* m **do**
      Predict next state of variables: $u_{dr}^p(k+2)$, $u_{qr}^p(k+2)$ based on (4.45) and (4.46), $i_{dr}^p(k+2)$, $i_{qr}^p(k+2)$ based on (5.14) and $u_{cm}^p(k+2)$ from (4.49) ;
      Estimation of power: $P_s^p(k+2)$ and $Q_s^p(k+2)$ by using (5.15) ;
      Compute the cost function g_{rsc} from (4.50);
      if $g_{rsc} < g_{opt}$ **then**
        $g_{opt} = g_{rsc}$; $x_{opt} = i$;
Store the present value of x_{opt} and apply optimal switching states: S_a, S_b, S_c;

In order to show the efficiency of the proposed control system, various active and reactive power steps with synchronous speed (1500 rpm) were carried out with long simulation times (20 s). As shown in Figs. 5.14(a) and 5.14(b), the proposed control strategy can achieve the fast dynamic response and good tracking reference of the active and reactive powers. To illustrate the performance clearly, zoom of simulation results from 0.5 s to 2.5 s with the detail are presented in Figs. 5.14(c) and 5.14(d). The rotor speed is assumed to be synchronous. At $t = 0.5$ s, the initial active power reference is set at -2 MW, while the reactive power reference is set to 0 Var to work unity power factor ($PF = 1$). The active power commanding steps from -2 MW to -1 MW at 1 s, and then steps from -1 MW to -1.5 MW at 2 s as illustrated in Fig. 5.14(c). While the PF required changes from 1 to 0.9 at 1 s, then changes from 0.9 to -0.9 at 1.5 s and from -0.9 to 0.9 at

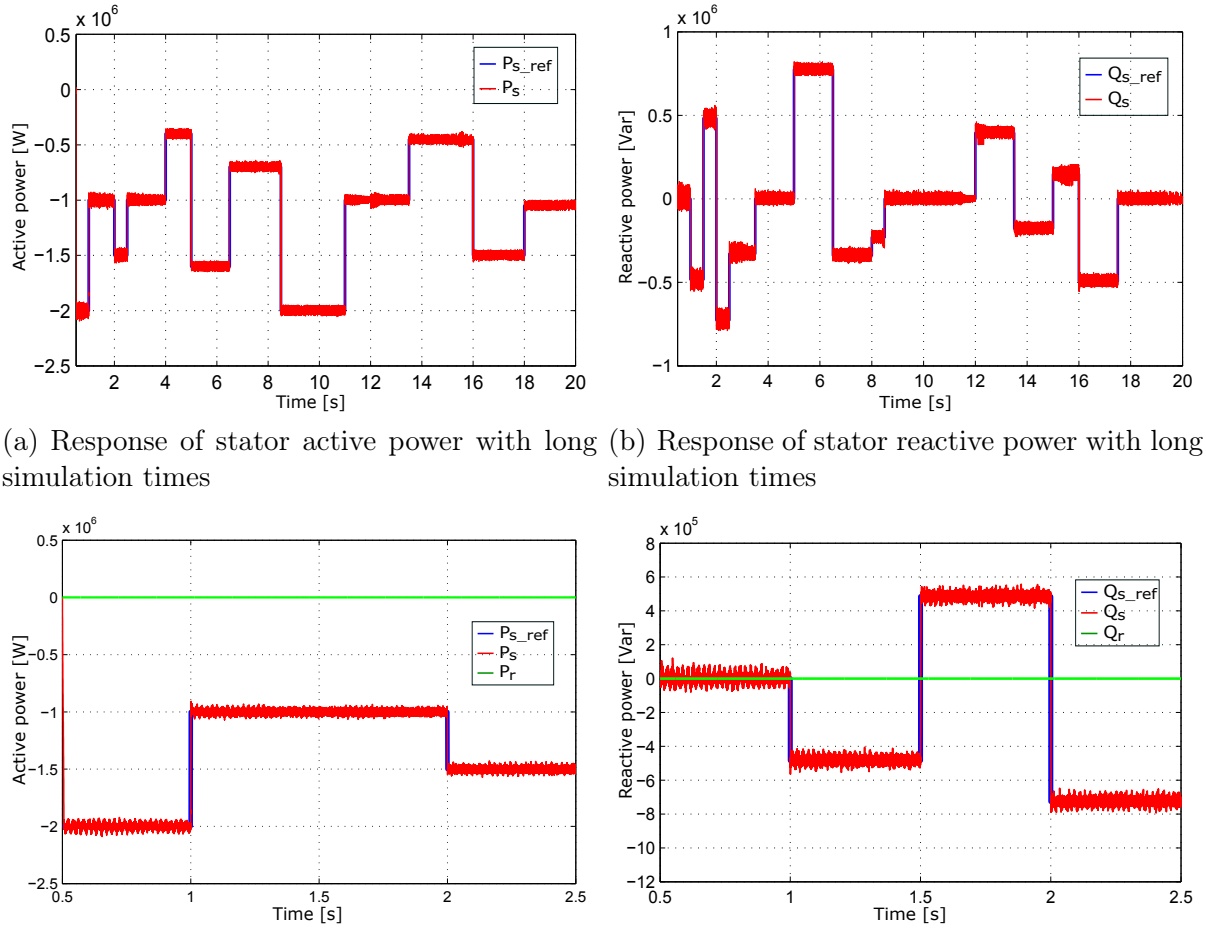

(a) Response of stator active power with long simulation times

(b) Response of stator reactive power with long simulation times

(c) Generated active power

(d) Generated reactive power

Figure 5.14: Response of active and reactive power with synchronous speed under power reference variations.

2 s. Thus, the corresponding reactive power steps from 0 Var to -0.484 MVar at 1 s, then steps from -0.484 MVar to 0.484 MVar at 1.5 s and from 0.484 MVar to -0.727 MVar at 2 s. There are small steady state error in the powers, where the mean absolute percentage error of active and reactive powers are 1.4%, and 1.98%.

Fig. 5.15 shows the steady state and its harmonic spectrum of stator current with synchronous speed. The THD of stator current (i_{sa}) is 3.14% lower than 5% limit required by the IEEE 519 standard. Moreover, the average number of calculations needed of the proposed algorithm are 46 in practice. As a result, the computations required are reduced about 93% compared with conventional FCS-MPC. In fact, the average computation time of the proposed method is 35 μs with respect to the conventional FCS-MPC (125 μs) in a 3.3 GHz, i5-6600 CPU, allowing the implementation of a real time operating system.

The performance of the proposed control method is also investigated with variable

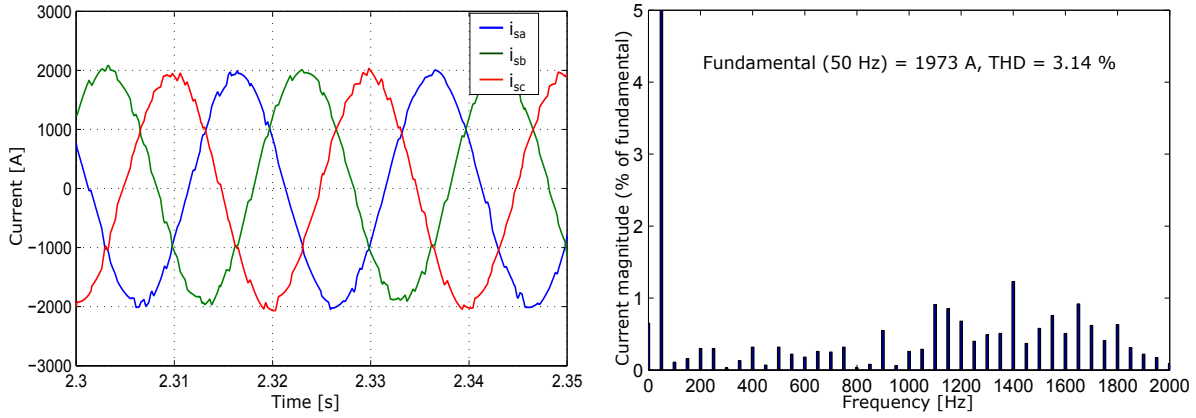

(a) Steady state of stator current

(b) Stator current harmonic spectra

Figure 5.15: The steady state and harmonic spectrum of stator current with synchronous speed.

rotor speed from 1200 to 1800 rpm as shown in Fig. 5.16(c). The system starts at 0.5 s with stator active power reference of -2 MW and unity power factor ($Q_s^* = 0$). The stator active power reference presents a step from -2 MW to -1 MW at 1.5 s and then steps from -1 MW to -1.5 MW at 2 s (Fig. 5.16(a)). The stator reactive power reference is stepped from -1.24 MVar to 0.62 MVar at 1.5 s and then to 0 Var at 2 s as depicted in Fig. 5.16(b), corresponding to leading power factor operation ($PF = 0.85$) at 1 s, lagging power factor operation ($PF = -0.85$) at 1.5 s and unity power factor operation ($PF = 1$) at 2 s. Fig. 5.16 illustrates the waveforms of the generated active power, reactive power, stator current and rotor current. It is shown that the decoupled control of the stator active and reactive powers is achieved under sub-synchronous and hyper-synchronous operation. It is important to highlight that the controller accurately tracks the commanding value under the condition of variable rotor speed and steps of power references, validating the tracking capability of the proposed method. In addition, the results were performed with using the stability condition $\dot{V}\left(\widetilde{i}_{dr}, \widetilde{i}_{qr}\right) < 0$ instead of $\Delta V < 0$. The quality of the system is deteriorated because the THD of the stator current is increased to 5.59% which exceeds the 5% limit required by the IEEE 519 standards. Thus, the proposed method uses the stability condition $\Delta V < 0$ to achieve high performance. To verify the feasibility of the controller, a comparison of different method is also presented in Table 5.1.

The selection of values for the weighting factor need to be chosen carefully to achieve a satisfactory control, but the guidelines proposed in [42] can be used. A high value of λ_{dc} will control the voltage unbalance accurately but with higher power tracking errors and THD of the stator current. To maintain an acceptable performance, the weighting factor λ_{dc} can be selected so that the drift in capacitor voltages is set within about 3%

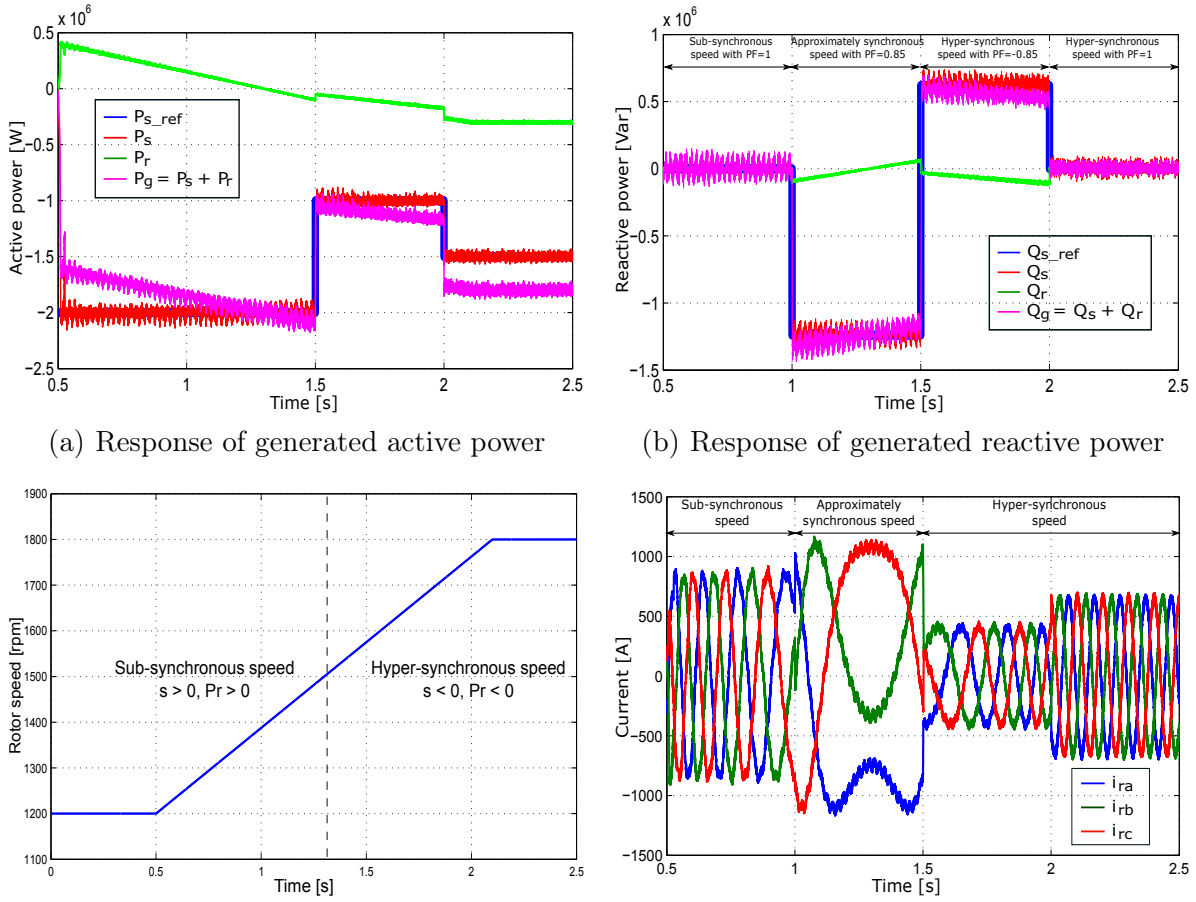

(a) Response of generated active power

(b) Response of generated reactive power

(c) Rotor angular speed time response

(d) Rotor current

Figure 5.16: Tracking behavior of the proposed control technique with variable rotor speed and different power step.

Table 5.1: Comparison of dynamic performance for different control methods at $t = 1.6$ s.

Method	MAPE of P_s	MAPE of Q_s	THD of i_{sa}	Computation time
Conventional FCS-MPC	1.24%	1.76%	4.75%	125 μs
Proposed method using $\dot{V} < 0$	1.26%	1.83%	5.59%	35 μs
Proposed method using $\Delta V < 0$	1.25%	1.81%	4.86%	35 μs

of nominal DC-link voltage. For megawatt applications, the device switching frequency should be set below 1 kHz to allow the reduction of power losses [61]. For system with a finite number of control actions, it is simply to determine the best value of weighting factor by evaluating the specific performance of the system. For the DFIG based wind conversion system, the THD is considered as a key to evaluating the performance. To perform the investigation, an exhaustive search is carried out based on simulation. As

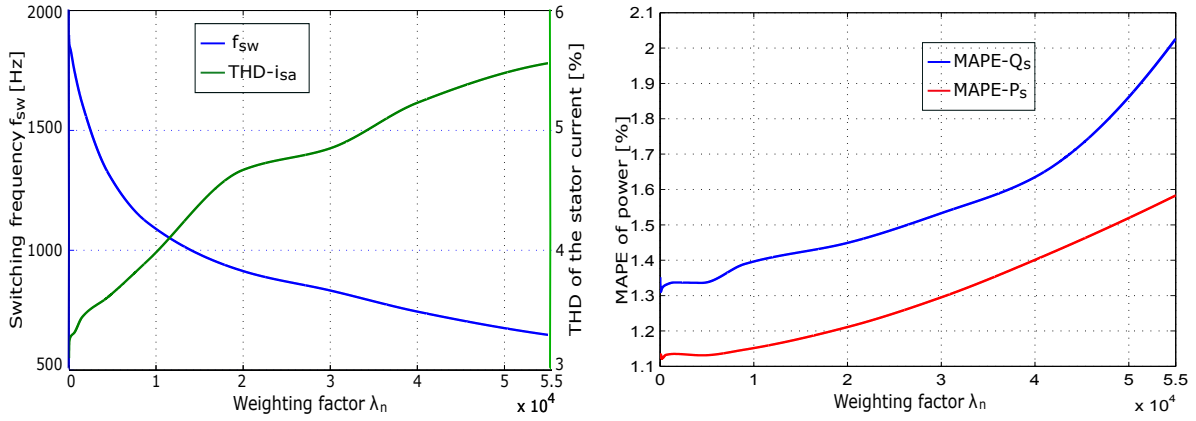

Figure 5.17: Weighting factor influence on: (a) The THD of the stator current and average switching frequency. (b) The power errors.

the weighting factor λ_n increases from 0 to 55000, the f_{sw} reduces from 1898 to 647 Hz with a slight increase in power errors (Fig. 5.17(b)) and the THD of the stator current from 3.1% to 5.56% (Fig. 5.17(a)). As a result, the weighting factor λ_n is set at 13000 to ensure the low THD of the stator current and the switching frequency device of 1 kHz.

In addition, a high common-mode voltage can cause shaft voltage, leakage current leads to premature failure of the machine bearings. As shown in Fig. 5.18, the CMV is reduced by increasing the weighting factor value λ_{cm} from 0 to 100 at $t = 1$ s and then to 350 at $t = 1.5$ s. It is seen that the peak value of CMV is reduced to 66.67% from $U_{dc}/2$ to $U_{dc}/6$ by setting λ_{cm} at 350. However, the THD of stator current, power tracking error and drift in capacitor voltage increase due to the additional weighting term λ_{cm}. For this reason, the weighting factors λ_{dc}, λ_n and λ_{cm} can be chosen at value 8000, 13000 and 350 to achieve an acceptable quality of current, capacitor voltage balancing, reduction of switching frequency and CMV.

In this study, the parameter ε_v can be considered as a tuning parameter which can be selected by making a compromise between the total harmonic distortion of the stator current, power ripples and the average amount of calculations required. If ε_v is chosen at zero, the Lyapunov function assures the convergence of the system. However, the THD of the stator current and power errors increase, then the quality of the system is deteriorated. In this case, the THD of the current is 5.57% and MAPE of active and reactive powers are 1.91%, and 2.5%, respectively. On the contrary, increasing ε_v leads to a better performance but increase computational burden. Fig. 5.19 demonstrates the

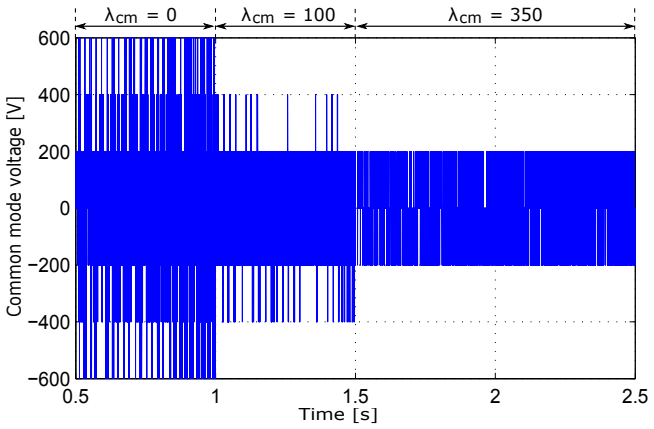

Figure 5.18: Performance of the common-mode voltage with the variation of λ_{cm}.

influence of selecting ε_v on the system performance. For instance, ε_v is chosen at 0.6 to achieve satisfactory performance and computational burden.

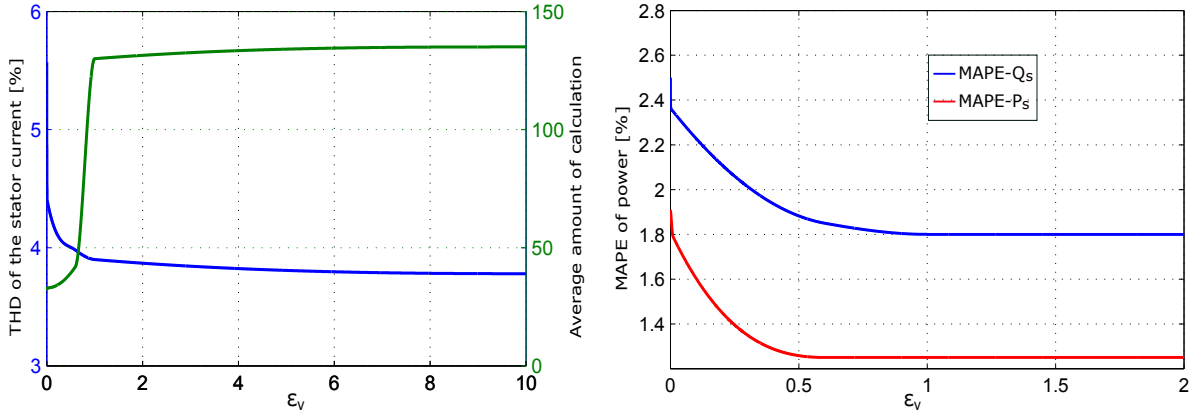

Figure 5.19: Parameter ε_v influence on: (a) The THD of the stator current and average amout of calculations. (b) The power ripples.

5.3 Conclusions

In this chapter, a new model predictive direct power control method based on Lyapunov function has been proposed to control directly the active and reactive powers for DFIG based wind energy conversion system. Firstly, the mathematical model of the system is established, and then the appropriate cost function is defined to track the active and reactive powers, maintain their balanced capacitor voltages, reduce the switching

frequency and common-mode voltage. Secondly, a Lyapunov function based on a predictive model is proposed where candidate inputs satisfy the stability conditions before they are used in the loop optimization. The resulting controller guarantees the stability of the system with the direct Lyapunov stability which is impossible with conventional FCS-MPC. In addition, the proposed method can reduce the computational effort compared with the conventional FCS-MPC method, allowing the real time implementation of two-step horizon. Finally, in order to verify the performance of control scheme, there is a comparison between the conventional FCS-MPC and the proposed method under different operating modes. Simulation results are provided to confirm and validate the efficiency of the proposed control strategy. In addition, to improve the efficiency of power conversion, the device switching frequency maintains below 1 kHz that is not achievable with the classical control methods where higher switching frequency is necessary to obtain similar results. Consequently, the proposed method is suitable to control the DFIG based wind turbine for megawatt range wind power applications.

Chapter 6

Model Predictive Power Control with Dead-time Compensation for 3L-NPC back-to-back converter

In inverter control, it is necessary to insert a dead-time in gating signals to avoid the short circuit across the inverter DC voltage source. In general, when the converter is modeled, it is assumed that the control signals and the semiconductor devices are ideal. This causes an error between the desired value and actual achieved value. Thus, the dead-time effect will distort the output voltage and current, leading to increase the total harmonic distortion (THD) of the current. Moreover, the turn-on/off time is inevitable in practical device, resulting commonly in voltage distortion. To solve this problem, several techniques have been proposed. In most case, compensation techniques are based on an average value theory and the lost voltage due to dead-time effect is added to the voltage reference [100–102]. Another method is presented in [103, 104] which used a pulse based compensation strategy to realize to each pulse obtained with a Pulse Width Modulation (PWM) technique. In [105–107], a compensated voltage based on a feedforward method is fed to the reference voltage in order to generate a modified voltage. Further, some solutions have been suggested to compensate the dead-time effect by using disturbance observer [108, 109] and hysteresis band [110]. Recently, the dead-time compensation schemes based on model predictive control are widely used due to its benefits [111–114].

This chapter presents a new compensation strategy of model predictive control for 3L-NPC converter in order to address the dead-time effect of the switching devices. It is shown that by taking into account the dead-time in the model, it is possible to compensate

its effects. In this study, we will focus on the modelling of errors caused by dead-time and swiching-time delays induced by the physical switching mechanism. With this approach, the model to predict the inverter output voltage and neutral-point voltage takes into account the dead-time and turn on/off time taken by the converter to compensate its effects. In order to verify the feasibility and effectiveness of the proposed compensation algorithm, simulation will be carried out by using Matlab/Simulink and SimPowerSytem toolbox.

6.1 Compensation of errors due to dead-time and switching-time delays

In the real implementation of the 3L-NPC inverter, considering a dead-time in the modeling is necessary to prevent the simultaneous conduction of two switching devices in each leg of the inverter. The dead-time causes output current waveform distortion, current ripple and increases the THD, especially with high switching frequency [92, 111, 112]. In practice, the switch takes turn-on time and turn-off time to reach the steady state. This time also influences the output voltage and neutral-point current. The voltage vector during the dead-time and switching-time delays is determined according to the state between previous switching state and present switching state and the sign of the phase current. The commutation process from state [O] to state [P] is illustrated in Fig. 6.2(a). For example, in switching state [O], switches S_{11} and S'_{12} are turned "ONJ. If $i_{ag} > 0$, the clamping diode D_{Z11} is turned "ONJ. For ideal case without dead-time, the switch S'_{12} is turned "OFF"and S_{12} is turned "ONJ simultaneously, so that the output voltage changes from zero to $U_{dc}/2$ at the same time. If the dead-time t_d and turn-on time t_{on} are considered, the real gate signals and output voltage approximation are shown in Fig. 6.1(a). S_{12} switches from "OFF"to "ONJ after the dead-time and the path of i_{ag} remains unchanged. After S_{12} is "ONJ, it requires a turn-on time for the switch to be fully turned "ONJ and conduct current. Thus, the output actual voltage is clamped at zero. So the load current is commutated from D_{Z11} to S_{12} and the output voltage switches to $U_{dc}/2$ after the dead-time and turn-on time (Fig. 6.2(a)). Hence, the real output voltage is reduced by $t_d + t_{on}$ and shown with the rectangular pattern in Fig. 6.1(a). For the switching transition from [P] to [O] with $i_{ag} > 0$, S_{12} is turned "OFF"and S'_{12} is turned "ONJ after the dead-time. Because of the turn-off time t_{off}, S_{12} is continuously conducted, leading to the output voltage remains $U_{dc}/2$. Then, the real output voltage switches to zero after

the turn-off time. This means that the switching state [P] is extended by t_{off}. In brief, the influence of dead-time and turn-on/off time on output voltage can be illustrated in Figs. 6.1 and 6.2. Therefore, neglecting a saturation voltage of IGBT and a forward voltage of the freewheeling diode, the real output voltage of one phase u_{xZ_real} applied during a sampling period T_s can be expressed as follows:

(i) $(S_x(k-1)=0)\,\&\,(S_x(k)=1)$,

(ii) $(S_x(k-1)=-1)\,\&\,(S_x(k)=0)$,

(iii) $(S_x(k-1)=1)\,\&\,(S_x(k)=0)$,

(iv) $(S_x(k-1)=0)\,\&\,(S_x(k)=-1)$,

(v) $((sign(i_{xg})>0)\,\&$**(i)**$)\vee((sign(i_{xg})<0)\,\&$**(iv)**$)$,

(vi) $((sign(i_{xg})>0)\,\&$**(iii)**$)\vee((sign(i_{xg})<0)\,\&$**(ii)**$)$,

(vii) $((sign(i_{xg})<0)\,\&$**(i)**$)\vee((sign(i_{xg})>0)\,\&$**(iv)**$)$,

(viii) $((sign(i_{xg})<0)\,\&$**(iii)**$)\vee((sign(i_{xg})>0)\,\&$**(ii)**$)$,

$$u_{xZ\_real}(k)=\begin{cases}\dfrac{T_s-t_d-t_{on}}{T_s}u_{xZ}(k), & \text{if condition (v) is satisfied,}\\ \dfrac{t_{off}}{T_s}u_{xZ}(k-1), & \text{if condition (vi) is satisfied,}\\ \dfrac{T_s-t_{off}}{T_s}u_{xZ}(k), & \text{if condition (vii) is satisfied,}\\ \dfrac{t_d+t_{on}}{T_s}u_{xZ}(k-1), & \text{if condition (viii) is satisfied,}\\ u_{xZ}(k) & \text{otherwise,}\end{cases} \tag{6.1}$$

where u_{xZ}, i_{xg} are the inverter output voltage and grid current of one phase $x=a,b,c$.

Furthermore, the dead-time can also affect the neutral-point voltage because of the different neutral-point current as shown in Fig. 6.2 [115]. In order to clarify this effect, the switching commutation from [O] to [N] with $i_{ag}<0$ is taken as an example (Fig. 6.2(d)). $S_{12}^{'}$ and S_{11} are turned "ONJ, and the current is conducted by $S_{12}^{'}$ and clamping diode D_{Z12}. During the dead-time interval t_d, $S_{12}^{'}$ is state "ONJ then the current continuously remains, leads to $i_{dc1a}=i_{ag}$. The commutation is complete after $S_{11}^{'}$ is fully turned

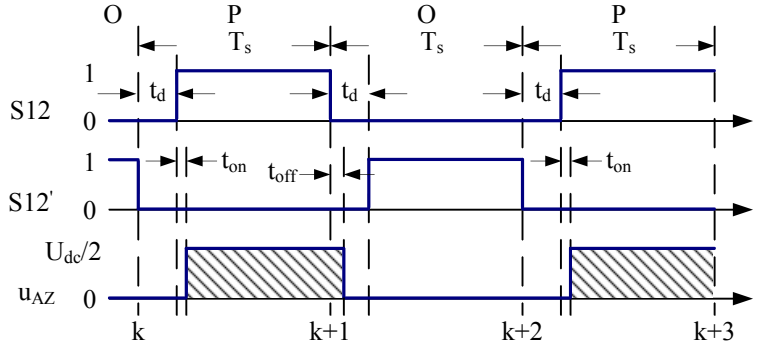

(a) Dead-time effect of switching states O and P with $i_{ag} > 0$

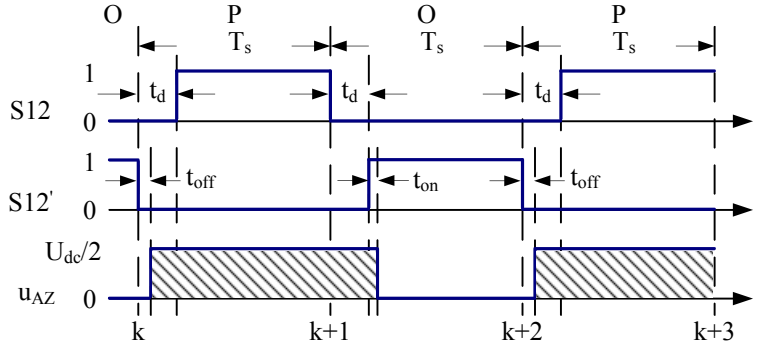

(b) Dead-time effect of switching states O and P with $i_{ag} < 0$

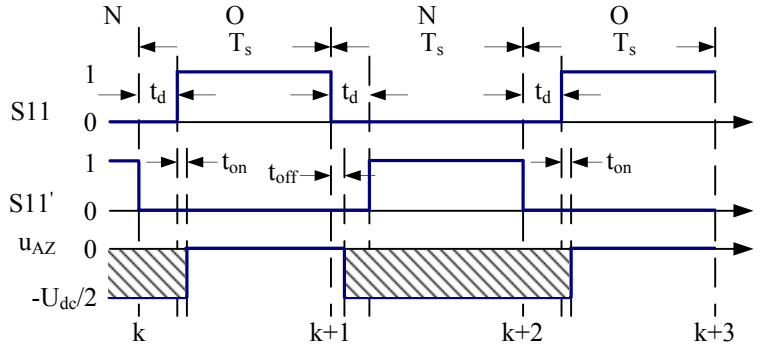

(c) Dead-time effect of switching states N and O with $i_{ag} > 0$

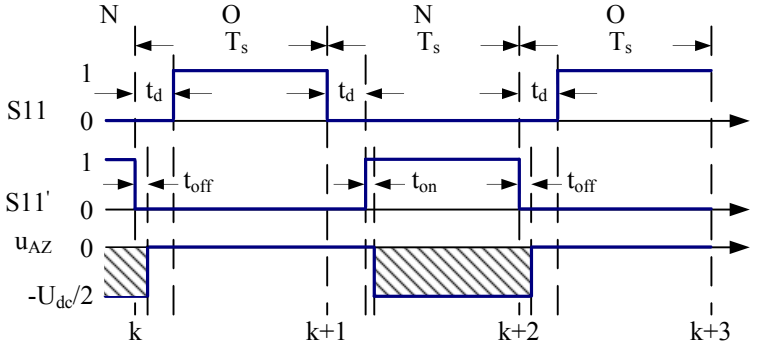

(d) Dead-time effect of switching states N and O with $i_{ag} < 0$

Figure 6.1: The effect of dead-time and turn-on/off time on inverter output voltage.

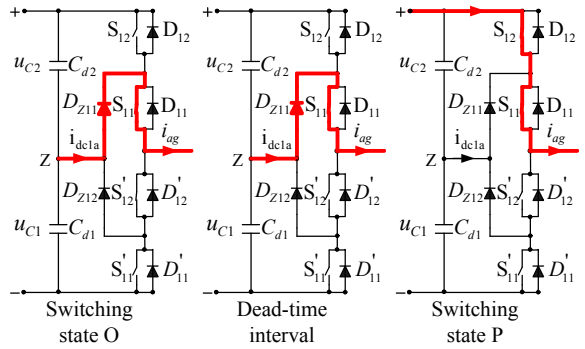

(a) Commutation from switching state O to P with $i_{ag} > 0$

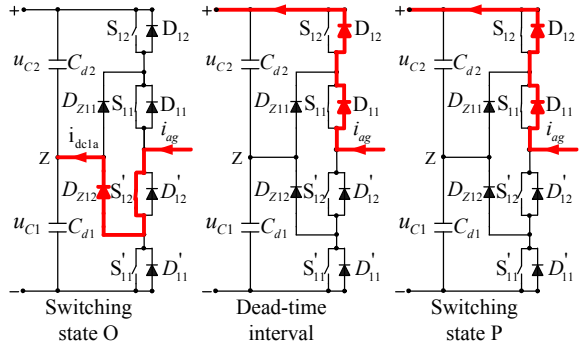

(b) Commutation from switching state O to P with $i_{ag} < 0$

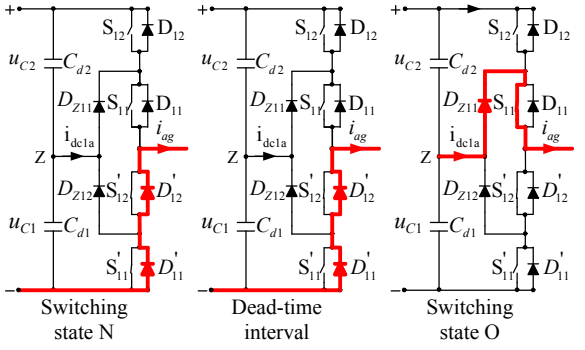

(c) Commutation from switching state N to O with $i_{ag} > 0$

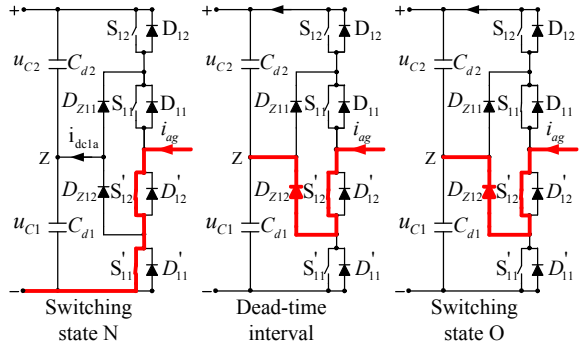

(d) Commutation from switching state N to O with $i_{ag} < 0$

Figure 6.2: Commutation during the dead-time.

"ONJ with turn-on time t_{on}. Hence, the neutral-point current i_{dc1a} is conducted within $t_d + t_{on}$ time. Considering the dead-time and switching-time delays, the corresponding neutral-point current of one phase can be summarized as:

$$i_{dc1x} = \begin{cases} \dfrac{t_d + t_{on}}{T_s} i_{xg}, & \text{if condition } \textbf{(v)} \text{ is satisfied,} \\ \dfrac{T_s - t_{off}}{T_s} i_{xg}, & \text{if condition } \textbf{(vi)} \text{ is satisfied,} \\ \dfrac{t_{off}}{T_s} i_{xg}, & \text{if condition } \textbf{(vii)} \text{ is satisfied,} \\ \dfrac{T_s - t_d - t_{on}}{T_s} i_{xg}, & \text{if condition } \textbf{(viii)} \text{ is satisfied,} \\ (1 - |S_x|) i_{xg}, & \text{otherwise,} \end{cases} \tag{6.2}$$

where i_{dc1x} is the neutral-point current of one phase $x = a, b, c$.

The summary of commutation process taking into account the dead-time effect presented in Table 6.1.

Table 6.1: Commutation during a transition of 3L-NPC inverter considering the dead-time effect.

Transition	Positive load current		Negative load current	
	Conducted switches	State	Conducted switches	State
From [O] to [P]	S_{11}, D_{Z11}	O	S'_{12}, D_{Z12}	O
	S_{11}, D_{Z11}	$t_d + t_{on}$	S'_{12}, D_{Z12}	t_{off}
	S_{11}, S_{12}	P	S_{11}, D_{12}	P
From [P] to [O]	S_{11}, S_{12}	P	D_{11}, D_{12}	P
	S_{11}, S_{12}	t_{off}	D_{11}, D_{12}	$t_d + t_{on}$
	S_{11}, D_{Z11}	O	S'_{12}, D_{Z12}	O
From [N] to [O]	D'_{11}, D'_{12}	N	S'_{11}, S'_{12}	N
	D'_{11}, D'_{12}	$t_d + t_{on}$	S'_{11}, S'_{12}	t_{off}
	S_{11}, D_{Z11}	O	S'_{12}, D_{Z12}	O
From [O] to [N]	S_{11}, D_{Z11}	O	S'_{12}, D_{Z12}	O
	S_{11}, D_{Z11}	t_{off}	S'_{12}, D_{Z12}	$t_d + t_{on}$
	D'_{11}, D'_{12}	N	S'_{11}, S'_{12}	N

By using the equation (3.3), the neutral-point voltage for compensate the dead-time can be rewritten:

$$\frac{du_{z\text{-}real}}{dt} = -\frac{1}{2C} i_{dc1\text{-}real} = -\frac{1}{2C} \left(i_{dc1a} + i_{dc1b} + i_{dc1c} \right), \tag{6.3}$$

with i_{dc1a}, i_{dc1b}, i_{dc1c} given by equation (6.2).

The real inverter output voltage considering the dead-time effect is calculated in terms of phase to neutral voltages:

$$u_{inv\_real} = \frac{2}{3} \left(u_{AZ\_real} + a u_{BZ\_real} + a^2 u_{CZ\_real} \right), \tag{6.4}$$

where the real phase to neutral voltage u_{AZ_real}, u_{BZ_real}, u_{CZ_real} are obtained from equation (6.1).

6.2 Application of model predictive control with dead-time compensation to grid connected 3L-NPC inverter

According to equation (3.8), the grid current is represented in discrete-time by using the first-order forward Euler approximation as follows:

$$i^p_{g\alpha}(k+1) = \Big(1 - \frac{R_f T_s}{L_f}\Big) i_{g\alpha}(k) + \frac{T_s}{L_f}\omega\psi_{g\beta\_real}(k) + \frac{T_s}{L_f}u_{inv\alpha\_real}(k), \tag{6.5}$$
$$i^p_{g\beta}(k+1) = \Big(1 - \frac{R_f T_s}{L_f}\Big) i_{g\beta}(k) - \frac{T_s}{L_f}\omega\psi_{g\alpha\_real}(k) + \frac{T_s}{L_f}u_{inv\beta\_real}(k),$$

where the real inverter output voltage with dead-time compensation in $\alpha\beta$ frame $u_{inv\alpha\_real}(k)$, $u_{inv\beta\_real}(k)$ are calculated by using equation (6.4) and $\alpha\beta$ transformation; the virtual grid fluxes $\psi_{g\alpha\_real}(k)$, $\psi_{g\beta\_real}(k)$ are estimated from the equation (3.10).

The discrete-time of neutral-point voltage can be obtained from equation (6.3) as:

$$u^p_{z\_real}(k+1) = u_{z\_real}(k) - \frac{T_s}{2C}\Big(i_{dc1a}(k) + i_{dc1b}(k) + i_{dc1c}(k)\Big),$$
$$u^p_{z\_real}(k+2) = u^p_{z\_real}(k+1) - \frac{T_s}{2C}\Big(i^p_{dc1a}(k+1) + i^p_{dc1b}(k+1) + i^p_{dc1c}(k+1)\Big), \tag{6.6}$$

where the neutral-point currents $i_{dc1x}(k)$ and $i^p_{dc1x}(k+1)$ are estimated by using equation (6.2).

The same direct power control based on Lyapunov function presented in Section 5.1.1 is considered here, but taking into account the dead-time effect in the simulations. A comparison between the results obtained without and with compensation of dead-time is presented.

Several simulations have been done using MATLAB/Simulink and the SimPowerSystems toolbox in order to validate the proposed compensation scheme. The simulation configurations are under exactly the same as the Section 3.1.4. The converter is constructed by using twelve IGBT modules PM50RSA060 from Powerex with the parameters as denoted in Table 6.2.

The active and reactive powers exchanged with the grid are shown in Fig. 6.3. The results indicate that the proposed control is able to track the power reference with fast

Table 6.2: Parameters of IGBT.

Parameter	Value	Description
t_d	5 [μs]	Dead-time
t_{on}	0.95 [μs]	Turn-on time
t_{off}	2.5 [μs]	Turn-off time
V_f	2.6 [V]	Saturation voltage of IGBT
V_{fd}	1.7 [V]	Forward voltage of diode

dynamic response. Fig. 6.4(a) illustrates the grid phase current along with the corresponding grid voltage under the same power reference variation. The grid current is proportional to the active and reactive powers as depicted in Fig. 6.4(b).

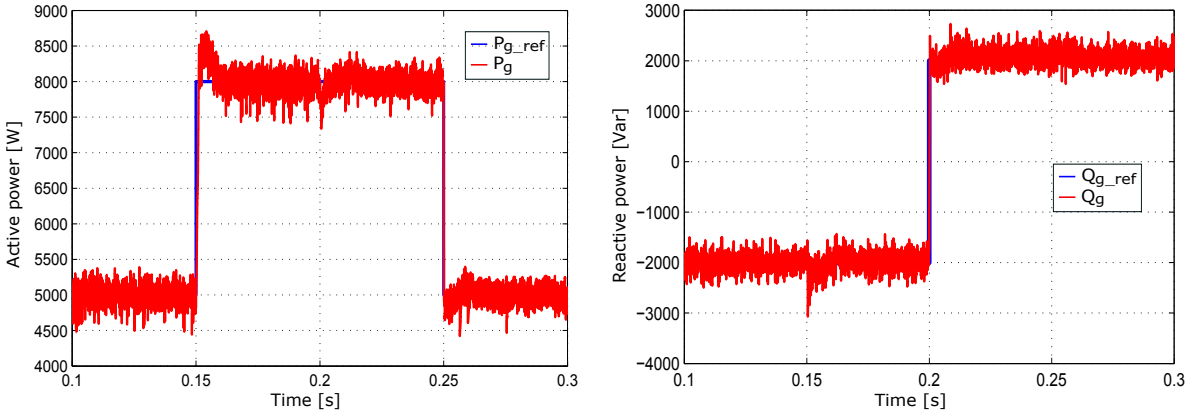

(a) Active power (b) Reactive power

Figure 6.3: Transient operation of active and reactive powers.

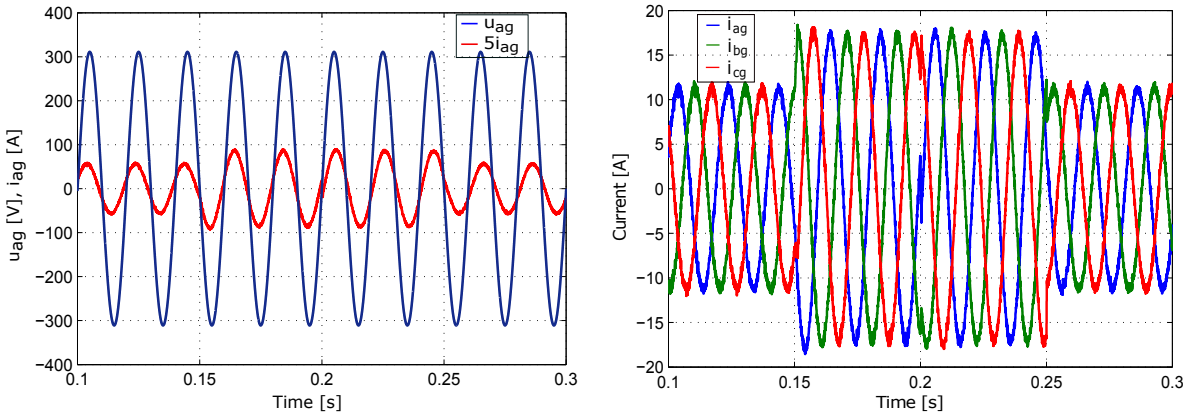

(a) Phase current and voltage (b) Three-phase grid current response

Figure 6.4: Transient response of grid currents.

For further verification of the dead-time compensation method, the spectrum of the grid current is analyzed and compared for the uncompensated and compensated case in Figs. 6.5(a) and 6.5(b). For the uncompensated case in Fig. 6.5(a), the amplitude of the order harmonics are larger, which is caused by the dead-time effect. The THD for the uncompensated grid current is around 4.6%. But for the compensated current, the order harmonic components have been reduced as illustrated in Fig. 6.5(b). Comparing the grid current spectrum in Fig. 6.5(a) and Fig. 6.5(b), the proposed compensation method has better performance. Moreover, with the dead-time compensation, the mean absolute percentage error has been reduced from 2.31% to 2.29% for active power and from 8.03% to 7.65% for reactive power, respectively. Also the THD for the grid current is reduced from 4.6% to 4%. In reality, the dead-time and switching-time delays are influenced by various factors like propagation delay or device nonlinearity. So, the compensation can not totally eliminate the dead-time effect. However, it is possible to indicate that the proposed method can achieve a good compensation performance with a lower THD of the current.

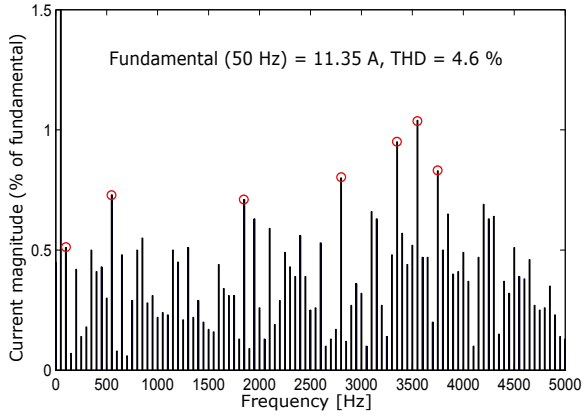

(a) Current spectrum without compensation

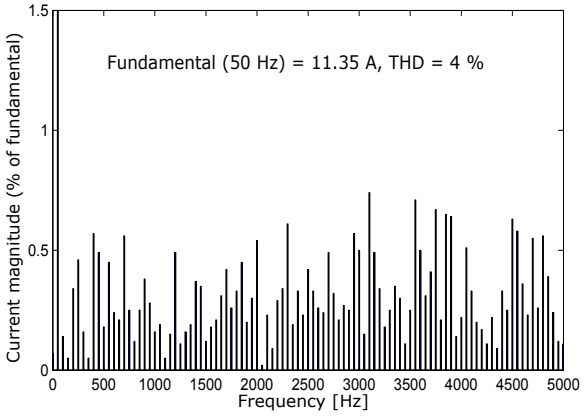

(b) Current spectrum with compensation

Figure 6.5: Grid current spectrum with and without dead-time compensation.

6.3 Application of model predictive control with dead-time compensation to DFIG connected 3L-NPC inverter

Considering the dead-time effect, the real inverter voltage in dq reference frame can be achieved from equation (4.46):

$$u^{dq}_{r\_real} = K u^{DQ}_{inv\_real} e^{-j\theta_r}, \tag{6.7}$$

where $u^{DQ}_{inv\_real}$ is the real inverter voltage in DQ frame given by equation (6.4).

On the other hand, the effects of dead time on common-mode voltage can be expressed as follows:

$$u_{cm\_real} = \frac{u_{AZ\_real} + u_{BZ\_real} + u_{CZ\_real}}{3}. \tag{6.8}$$

By using the modified inverter voltage, neutral-point voltage and common-mode voltage in equations (6.7), (6.3) and (6.8) to impose on the dynamic model of DFIG in equation (4.37), we can predict the rotor current, stator flux and power taking into account the dead-time effect at switching state. Therefore, the proposed dead-time compensation is accomplished by using the control method presented in Section 4.3.

A simulation was set up in MATLAB/Simulink and the SimPowerSystems toolbox in order to investigate the proposed dead-time compensation algorithm. The sampling time is 100 μs to maintain a significant lower average switching frequency of 1 kHz. The parameters of DFIG and IGBT used in this work are reported in Tables 4.1 and 6.2. The weighting factors λ_{dc}, λ_n and λ_{cm} was set to 50, 20000 and 200.

In order to observe the dynamics response of the DFIG, various active and reactive power steps with rotor speed varying from 1200 to 1800 rpm during the period 0.5-2.1 s (Fig. 4.12) were carried out. Figs. 6.6(a) and 6.6(b) show the results step of active and reactive powers. The reference of active power presents a step from -2 MW to -1 MW at 1.5 s and then returns to -1.5 MW at 2 s. While the power factor is changed from 1 to 0.85 at 1.5 s, from 0.85 to -0.85 at 1.5 s and from -0.85 to 1 at 2 s. From this simulation result one can see that the proposed controller can reach the reference values with fast dynamic response, and is robust to speed variations. The transient response of stator and rotor currents are illustrated in Figs. 6.6(c) and 6.6(d).

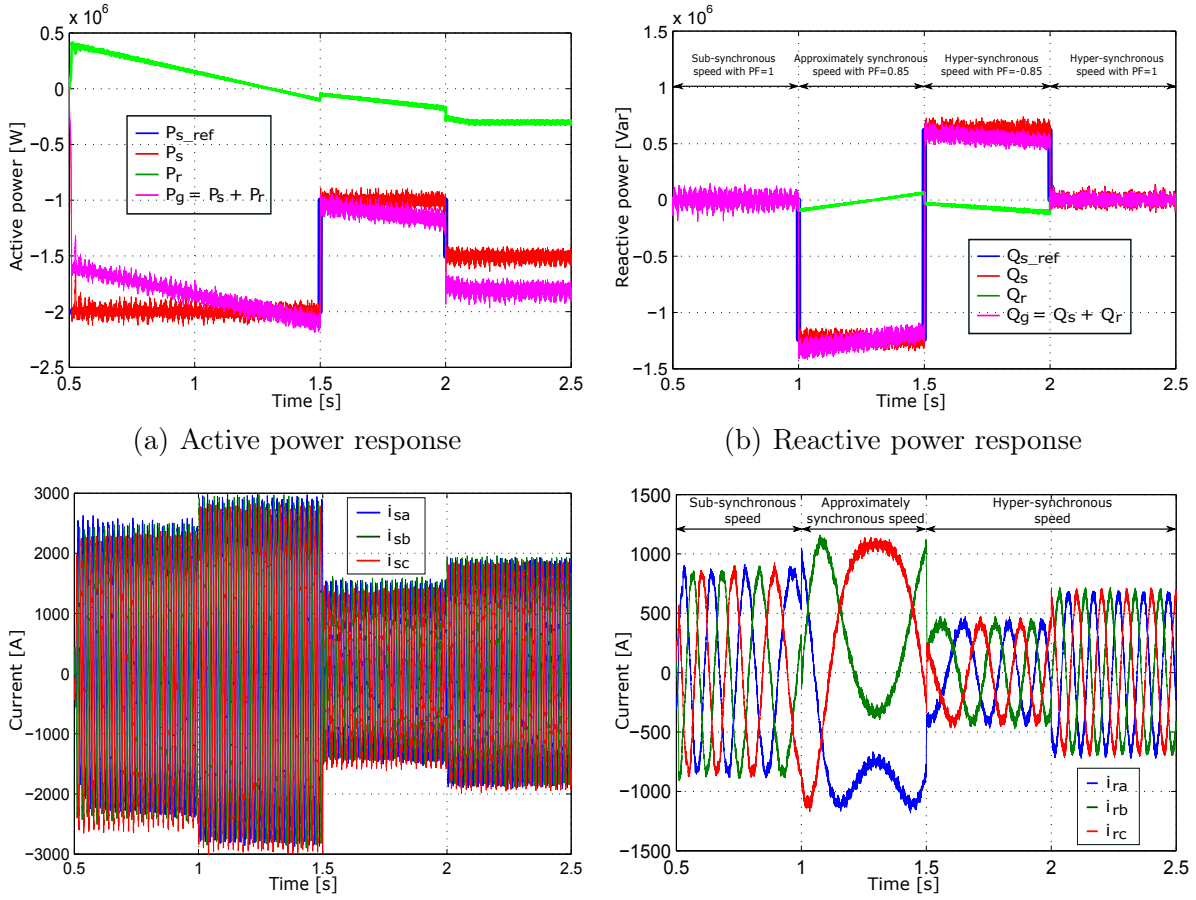

(a) Active power response

(b) Reactive power response

(c) Three-phase stator current

(d) Three-phase rotor current

Figure 6.6: Transient performance of proposed method under rotor speed variations and various power steps.

With the aim to evaluate the steady state performance, the harmonic spectra of the stator current for the uncompensated and compensated case are analyzed and compared in Fig. 6.7, which is drawn by the Powergui toolbox using Fast Fourier Transform (FFT) algorithm. Fig. 6.7(a) shows that the amplitude of the order harmonic is larger for uncompensated case due to dead-time effect. Thus, the distortion of the current is increased and the THD of stator current was as high as 4.3%. By taking into account the impact of dead-time in the model, the order harmonic components of proposed compensation method have been largely reduced, especially the 21^{th}, 22^{th} and 23^{th} order harmonic as depicted in Fig. 6.7(b). The THD of the stator current is also reduced from 4.3 % to 3.03 % which is under the 5% limit required by the IEEE 519 standards. To clarify the efficiency of the present method, the comparison for several power references and rotor speeds is summarized in Table 6.3. Moreover, the mean absolute percentage error is reduced from 2.25% to 1.68% for active power and from 2.22% to 1.65% for reactive power, respectively.

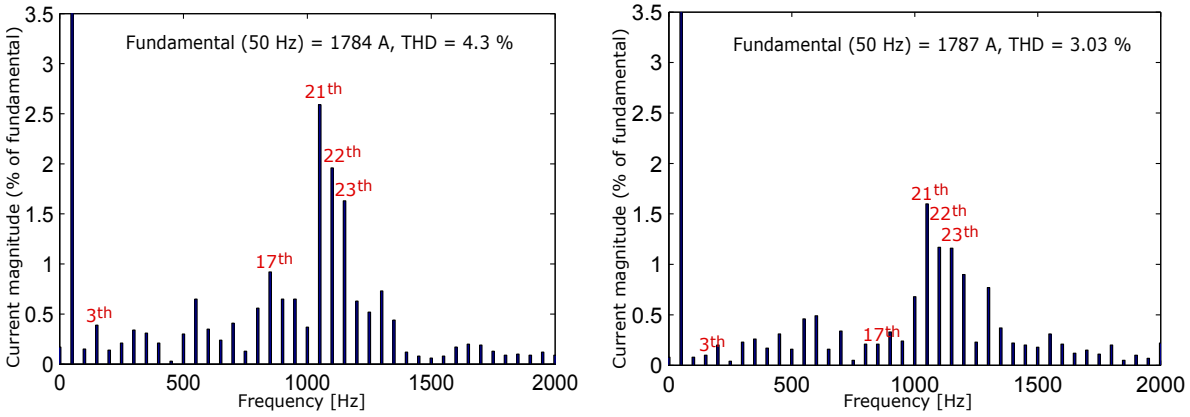

(a) Without compensation (b) With compensation

Figure 6.7: Stator current spectrum with and without compensation.

Table 6.3: Comparison of THD.

P_{s_ref} (MW)	Q_{s_ref} (MVar)	ω_r (rpm)	THD without compensation (%)	THD with compensation (%)
-2	0	1313	2.97	2.57
-2	-0.62	1463	2.48	2.06
-1	0.62	1688	4.3	3.03
-1.5	0	1800	3.8	3.25

6.4 Conclusions

This chapter has analyzed the influence of the dead-time and switching-time delays in the model predictive control and proposed a novel compensation method to improve the current distortion. In this method, the average inverter output voltage and neutral-point voltage in a sampling time have been derived from the theoretical analysis of the inverter during dead-time effect. The proposed compensation method is quite simple so that the algorithm can be easily implemented directly into the controller while maintaining an acceptable quality of the current and power. The effectiveness of the proposed method was demonstrated through simulation for two control schemes: grid connected inverter and DFIG connected inverter. It can be concluded that the proposed method has a better performance compared to the uncompensated method.

Chapter 7

Conclusions

In recent years, wind turbine technology shows a trend towards the research and development of the large wind turbine into both generator and power converter configuration. The topology of variable wind speed using doubly fed induction generator (DFIG) is one of the highest wind turbine market with power in the range in 1.5-6 MW. Moreover, the three-level neutral-point clamped (3L-NPC) inverter structure is considered a good solution for high power due to its advantages: reduction of the total harmonic distortion (THD) and the common-mode voltage, and increasing the power level of inverter thanks to a decreased voltage applied to each component. In this thesis, we have investigated different model-based strategies and developed finite control set model predictive control (FCS-MPC) with two-step prediction for two converters within a DFIG system: rotor side converter and grid side converter. We have demonstrated that this predictive control can achieve better control performance in terms of power quality and dynamic response compared to conventional method with space vector modulation. The main drawbacks of FCS-MPC are the computational burden. The computational burden has been reduced considering only switches that assures few commutations or a decreasing of a Lyapunov function. This allows a real time implementation for predictive horizons of two steps. The stability has been assured considering only switching combinations assuring the decreasing of a Lyapunov function, assuring in this way the stability of the closed loop. Finally the dead-effect has been studied. The last chapter presents a method to compensate the dead time effects in voltage and currents, improving the steady state performance.

7.1 Summary of Contributions

The major contributions and conclusions of this thesis are summarized as follows:

1. A development of finite control set model predictive control is presented to control 3L-NPC inverter

In this dissertation, an FCS-MPC strategy was employed to track the current while maintaining voltage balance of DC-link capacitor and reducing the switching frequency for 3L-NPC inverter. The principle of the proposed control scheme is to use the dicrete-time model to predict the behavior of the load current and DC-link capacitor voltages for all possible configurations of voltage vectors. Two-step horizon is proposed to compensate the issue associated with implementation of digital control. In order to reduce the amount of calculation, the same voltage vector is considered instead of different vectors. The predictive control method gives better performance compared to linear current controller with space vector modulation. Furthermore, the simulation results for FCS-MPC with one prediction step and two proposed prediction steps are presented and compared.

2. Two advanced control schemes based on FCS-MPC are proposed to control grid connected 3L-NPC inverter

An FCS-MPC formulation for grid connected 3L-NPC inverter was presented in this thesis. The computational cost is mitigated by considering two control approaches. In the first control strategy, to limit the possible switching transitions, only combination of inputs having a difference of one switch in the inverter is considered. The grid active and reactive powers can be controlled based on the predicted values of virtual flux and grid current. In the second one, the key novelty of the proposed method relates to the approach to design a cost function. The cost function that includes the error between the possible inverter output voltage and its references, DC-link capacitor voltage balancing and reduction of switching frequency, will be used. The reference voltage vector is obtained by using the inverse procedure of the model current prediction. Then the modified cost function is introduced by the equivalent transformation. Our proposal does not require any additional control loop and modulation block, leads to benefits in implementation simplicity.

3. An FCS-MPC strategy is proposed for DFIG connected 3L-NPC inverter

The control of active and reactive powers of DFIG are accomplished by optimizing the predefined cost function which include the power errors, the additional constraint of neutral-point voltage, switching frequency and common-mode voltage. In order to verify the performance of control scheme, there is a comparison between deadbeat power control with space vector modulation and proposed method under the same condition of power step and rotor speed. Furthermore, this controller can reduce the common-mode voltage and is able to achieve the robustness with parameter variations.

4. Stability of FCS-MPC strategy is addressed for 3L-NPC back-to-back converter

In order to include stability criteria in the switching policy, we propose a novel selection scheme for the control action. This incorporates a restriction of the viable switching configurations derived from a control Lyapunov function prior to the effective cost optimization. The average computational time of the proposed method is greatly reduced compared with the conventional FCS-MPC, allowing hardware implementation of the algorithm. Moreover, the influence and the selection of weighting factor are also analyzed and presented in this thesis. By keeping the switching frequency of 1 kHz, it is suitable to control the DFIG based wind turbine for megawatt range applications.

5. Model predictive power control with dead-time compensation for 3L-NPC back-to-back converter is introduced

The dead-time effect of power converter when governed by FCS-MPC is analyzed. Then, by taking into account the dead-time and switching-time delays in the prediction model, their effects can be compensated. This methodology is applied to two control schemes: grid connected converter and DFIG connected converter. In order to validate the effectiveness of the proposed compensation method, a comparison with uncompensated method is presented and analyzed.

6. Simulation studies are performed to verify the system operations

In order to confirm the feasibility and effectiveness of the proposed control strategy, all simulation studies were carried out in Matlab/Simulink and SimPowerSystems toolbox. The predictive control algorithms are programmed using SFunction Builder Block for easy real time implementation. The simulation times have been revised on a large time-scale in order to show the efficiency independent with the transitories.

7.2 Future work

The future research works can be suggested as follows:

1. Complete control systems of DFIG based wind turbines with 3L-NPC back-to-back converter

To clarify the performance of DFIG based wind turbines, an investigation of overall control system considering wind speed controller deserves a particular attention for the integration of different sub-systems and the analysis of the global performances.

2. FCS-MPC with fixed switching frequency for 3L-NPC inverter

The variable switching frequency operation with the FCS-MPC method leads to a wide harmonic spectrum of the current, deacreasing the performance of the system. Thus, by keeping the switching frequency constant, we can maintain the advantages of the classical FCS-MPC while improving the steady state performance.

3. FCS-MPC for DFIG based wind turbines under unbalanced network conditions

A development of FCS-MPC for DFIG based wind turbines under unbalanced grid voltage can rerpesent an interesting research subject in order to eliminate the unbalanced problem.

4. Experimental results of the proposed method

To provide convincing evidence for the proposed control strategy, experimental test should be carried out and this is representing the main objective in order to bring the current line of research towards a wide acceptance and to validate/adjust the assumptions made along the design procedure as presented in the present manuscript.

Appendix A

The three-phase magnitude of the ideal system can be expressed as:

$$
\begin{aligned}
x_a &= \hat{X}\sin(\omega t + \varphi), \\
x_b &= \hat{X}\sin(\omega t + \varphi - \frac{2\pi}{3}), \\
x_c &= \hat{X}\sin(\omega t + \varphi + \frac{2\pi}{3}),
\end{aligned}
\tag{A.1}
$$

where $\hat{X}$, ω, φ are the amplitude, angular frequency and phase shift of the space vetor.

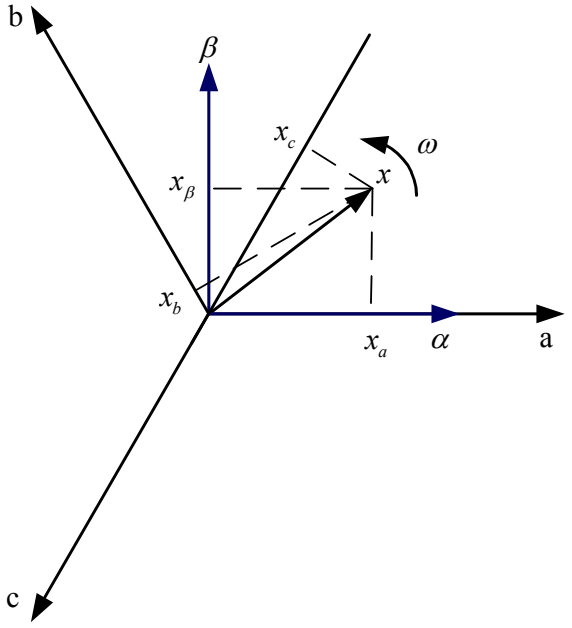

Figure A.1: Space vector presentation in three-phase (abc) and stationary reference frame ($\alpha\beta$).

The space vector can be represented in term of three-phase as (Fig. A.1):

$$
x = \frac{2}{3}(x_a + a x_b + a^2 x_c),
\tag{A.2}
$$

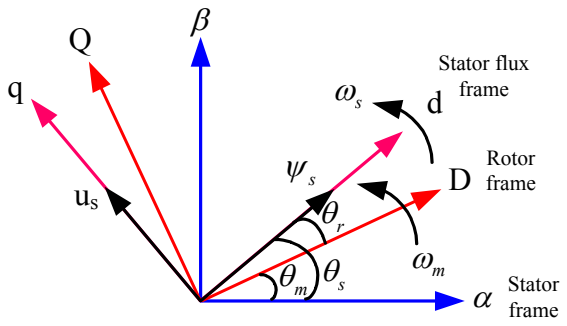

Figure A.2: Space vector representation in different reference frames.

with $a = e^{j2\pi/3} = -\frac{1}{2} + j\frac{\sqrt{3}}{2}$.

The constant 2/3 of expression (A.2) is chosen to scale the space vector according to the peak amplitude of the three-phase magnitude.

The space vector defined by (A.2) can be expressed in the stationary reference frame $(\alpha\beta)$ as:

$$x = x_\alpha + jx_\beta. \tag{A.3}$$

Thus, the $\alpha\beta$ components of the space vector can be calculated from the *abc* magnitude as follows:

$$\begin{aligned} x_\alpha &= \mathrm{Re}\{x\} = \frac{2}{3}\left(x_a - \frac{1}{2}x_b - \frac{1}{2}x_c\right), \\ x_\beta &= \mathrm{Im}\{x\} = \frac{1}{\sqrt{3}}\left(x_b - x_c\right). \end{aligned} \tag{A.4}$$

Therefore, the space vector in the stationary reference frame can be rewritten in matrix form by using Clarke transformation as:

$$\begin{bmatrix} x_\alpha \\ x_\beta \end{bmatrix} = \frac{2}{3}\begin{bmatrix} 1 & -\frac{1}{2} & -\frac{1}{2} \\ 0 & \frac{\sqrt{3}}{2} & -\frac{\sqrt{3}}{2} \end{bmatrix}\begin{bmatrix} x_a \\ x_b \\ x_c \end{bmatrix}. \tag{A.5}$$

Besides the stationary reference frame attached to the stator, the space vector equations can be formulated in a general reference frame which rotates at the synchronous speed ω_s as shown in Fig. A.2. In the same way, the space vector can be expressed in the synchronous reference frame (dq) as follows:

$$x^{dq} = x_d + jx_q. \tag{A.6}$$

Moreover, the space vector can be formulated in the rotor reference frame (DQ) aligned with the rotor which rotates at the electric angular speed ω_m:

$$x^{DQ} = x_D + jx_Q. \tag{A.7}$$

For referencing space vector into different reference frames, the rotational transformation (Park transformation) is used. For example, the transformation from $\alpha\beta$ coordiantes to DQ coordinates is done by:

$$x^{DQ} = \begin{bmatrix} x_D \\ x_Q \end{bmatrix} = \begin{bmatrix} \cos\theta_m & \sin\theta_m \\ -\sin\theta_m & \cos\theta_m \end{bmatrix} \begin{bmatrix} x_\alpha \\ x_\beta \end{bmatrix}, \tag{A.8}$$

where θ_m is the electric angular position of the shaft.

Similarly, to transform from $\alpha\beta$ reference frame to dq reference frame, the following expression is used:

$$x^{dq} = \begin{bmatrix} x_d \\ x_q \end{bmatrix} = \begin{bmatrix} \cos\theta_s & \sin\theta_s \\ -\sin\theta_s & \cos\theta_s \end{bmatrix} \begin{bmatrix} x_\alpha \\ x_\beta \end{bmatrix}, \tag{A.9}$$

where θ_s is stator flux angle in the stationary reference frame.

Finally, the relationship between DQ reference frame and dq reference frame is:

$$x^{dq} = x^{DQ} e^{-j\theta_r}. \tag{A.10}$$

Bibliography

[1] Global wind power statistics 2015. Technical report, Global wind energy council, 2015.

[2] Renewables global status report 2016. Technical report, Renewable Energy Policy Network for the 21st Century (REN21), 2016.

[3] Global wind energy outlook 2014. Technical report, Global wind energy council, 2014.

[4] Ke Ma, Lucian Tutelea, Ion Boldea, Dan M. Ionel, and Frede Blaabjerg. Power Electronic Drives, Controls, and Electric Generators for Large Wind Turbines-An Overview. *Electric Power Components and Systems*, 43(12):1406–1421, 2015.

[5] Frede Blaabjerg, Marco Liserre, and Ke Ma. Power Electronics Converters for Wind Turbine Systems. *IEEE Transaction on Industrial Electronics*, 48(2):708–719, Mar 2012.

[6] Roberto Cardenas, Ruben Pena, Salvador Alepuz, and Greg Asher. Overview of Control Systems for the Operation of DFIGs in Wind Energy Applications. *IEEE Transaction on Industrial Electronics*, 60(7):2776–2798, July 2013.

[7] Zhe Chen, Josep M. Guerrero, and Frede Blaabjerg. A review of the State of the Art of Power Electronics for Wind Turbines. *IEEE Transactions on Power Electronics*, 24(8):1859–1875, Aug 2006.

[8] Marco Liserre, Roberto Cardenas, Marta Molinas, and Jose Rodriguez. Overview of Multi-MW Wind Turbines and Wind Parks. *IEEE Transaction on Industrial Electronics*, 58(4):1081–1095, Apr 2011.

[9] Gonzalo Abad, Jesus Lopez, Miguel A. Rodriguez, Luis Marroyo, and Grzegorz Iwanski. *Doubly fed induction machine-Modelling and control for wind energy generation*. John Wiley, 2011.

[10] Jose Rodreguez, Jih-Sheng Lai, and Fang Zheng Peng. Multilevel inverters: A Survey of Topologies, Controls, and Applications. *IEEE Transaction on Industrial Electronics*, 49(4):724–738, Aug 2002.

[11] Salvador Alepuz, Sergio Busquets-Monge, Josep Bordonau, Javier Gago, David Gonzalez, and Josep Balcells. Interfacing Renewable Energy Sources to the Utility Grid Using a Three-Level Inverter. *IEEE Transaction on Industrial Electronics*, 53 (5):1504–1511, Oct 2009.

[12] Samir Kouro, Mariusz Malinowski, K. Gopakumar, Josep Pou, Leopoldo G. Franquelo, Bin Wu, Jose Rodriguez, Marcelo A. Perez, and Jose I. Leon. Recent Advances and Industrial Applications of Multilevel Converters. *IEEE Transaction on Industrial Electronics*, 57(8):2553–2579, Aug 2010.

[13] R. C. Portillo, M. M. Prats, J. I. Leon, J. A. Sanchez, J. M. Carrasco, E. Galvan, and L. G. Franquelo. Modeling Strategy for Back-to-Back Three-Level Converters Applied to High-Power Wind Turbines. *IEEE Transactions on Industry Electronics*, 53(5):1483–1491, Oct 2006.

[14] Lie Xu and Phillip Cartwright. Direct Active and Reactive Power Control of DFIG for Wind Energy Generation. *IEEE Transactions on Energy Conversion*, 21(3): 750–758, Sept 2006.

[15] S. Muller, M. Deicke, and R. W. De Doncker. Doubly fed induction generator systems for wind turbines. *IEEE Industry Applications magazine*, 8(3):26–33, May 2002.

[16] Jose Rodriguez and Patricio Cortes. *Predictive Control of Power Converters and Electrical Drives*. John Wiley, 2012.

[17] Venkata Yaramasu and Bin Wu. *Model Predictive Control of Wind Energy Conversion Systems*. IEEE Press Series on Power Engineering. John Wiley, 2016.

[18] S. Vazquez, J. Rodriguez, M. Rivera, L. G. Franquelo, and M. Norambuena. Model Predictive Control for Power Converters and Drives: Advances and Trends. *IEEE Transactions on Industrial Electronics*, PP(99):1–1, 2016.

[19] Bogdan M. Wilamowski and J. David Irwin. *Power electronics and motor drives*. Taylor and Francis Group, 2011.

[20] M. P. Kazmierkowski and L. Malesani. Current control techniques for three-phase voltage-source PWM converters: a survey. *IEEE Transactions on Industrial Electronics*, 45(5):691–703, Oct 1998.

[21] B. Wu, Y. Lang, N. Zargari, and S. Kouro. *Power Conversion and Control of Wind Energy Systems*. IEEE Press Series on Power Engineering. John Wiley & Sons, 2011.

[22] R. Teodorescu, M. Liserre, and P. Rodriguez. *Grid Converters for Photovoltaic and Wind Power Systems*. Wiley-IEEE Press, 2011.

[23] M. Weinhold. A new control scheme for optimal operation of a three phase voltage DC link PWM converter. In *Proc. PCIM*, pages 371–383, 1991.

[24] B. Hopfensperger, D. J. Atkinson, and R. A. Lakin. Stator flux oriented control of a doubly fed induction machine with and without position encoder. In *Proceeding of IEEE Power Electronics Application*, volume 147, pages 241–250, 2000.

[25] B. Wu. *High-power converters and AC drives*. Wiley-IEEE Press. John Wiley & Sons, 2006.

[26] J. Pou, J. Zaragoza, S. Ceballos, M. Saeedifard, and D. Boroyevich. A Carrier-Based PWM Strategy With Zero-Sequence Voltage Injection for a Three-Level Neutral-Point-C lamped Converter. *IEEE Transactions on Power Electronics*, 27(2):642–651, Feb 2012.

[27] Jiabing Hu and Xiaoming Yuan. VSC-based direct torque and reactive power control of doubly fed induction generator. *Journal Renewable Energy*, 40:13–23, April 2012.

[28] C. A. Martins, X. Roboam, T. A. Meynard, and A. S. Carvalho. Switching frequency imposition and ripple reduction in DTC drives by using a multilevel converter. *IEEE Transactions on Power Electronics*, 17(2):286–297, Mar 2002.

[29] Mariusz Malinowski, Marian P. Kazmierkowski, Steffan Hansen, Frede Blaabjerg, and G. D. Marques. Virtual-Flux-Based Direct Power Control of Three-Phase PWM Rectifiers. *IEEE Transaction on Industrial Applications*, 37(4):1019–1027, /August 2001.

[30] J. Hu and Z. Q. Zhu. Investigation on Switching Patterns of Direct Power Control Strategies for Grid-Connected DC-AC Converters Based on Power Variation Rates. *IEEE Transactions on Power Electronics*, 26(12):3582–3598, Dec 2011.

[31] Mohammad Verij Kazemi, Ahmad Sadeghi Yazdankhah, and Hossein Madadi Kojabadi. Direct power control of DFIG based on discrete space vector modulation. *Journal Renewable Energy*, 35:1033–1042, 2010.

[32] M. Malinowski, M. Jasinski, and M. P. Kazmierkowski. Simple direct power control of three-phase PWM rectifier using space-vector modulation (DPC-SVM). *IEEE Transactions on Industrial Electronics*, 51(2):447–454, Apr 2004.

[33] Fadia Sebaaly, Hani Vahed, Hadi Y. Kanaan, Nazih Moubayed, and Kamal Al Haddad. Design and Implementation of Space Vector Modulation-Based Sliding Mode Control for Grid-Connected 3L-NPC Inverter. *IEEE Transaction On Industrial Electronics*, 63(12):7854–7863, December 2016.

[34] J. Hu, L. Shang, Y. He, and Z. Q. Zhu. Direct Active and Reactive Power Regulation of Grid-Connected DC/AC Converters Using Sliding Mode Control Approach. *IEEE Transactions on Power Electronics*, 26(1):210–222, January 2011.

[35] J. Hu, H. Nian, B. Hu, Y. He, and Z. Q. Zhu. Direct Active and Reactive Power Regulation of DFIG Using Sliding-Mode Control Approach. *IEEE Transactions on Energy Conversion*, 25(4):1028–1039, December 2010.

[36] Jianzhong Zhang and Shuai Xu. Application of Fuzzy Logic Control for Grid-Connected Wind Energy Conversion System. In Elmer P. Dadios, editor, *Fuzzy Logic - Tool for Getting Accurate Solutions*, chapter 3, pages 50–77. InTech, 2015.

[37] K. Belmokhtar, M. L. Doumbia, and K. Agbossou. Modelling and fuzzy logic control of DFIG based Wind Energy Conversion Systems. In *2012 IEEE International Symposium on Industrial Electronics*, pages 1888–1893, May 2012.

[38] Teresa Orłowska-Kowalska, Frede Blaabjerg, and Jose Rodriguez. *Advanced and Intelligent Control in Power Electronics and Drives*. Studies in Computational Intelligence. Springer, 2014.

[39] S. Li, M. Fairbank, C. Johnson, D. C. Wunsch, E. Alonso, and J. L. Proao. Artificial Neural Networks for Control of a Grid-Connected Rectifier/Inverter Under Disturbance, Dynamic and Power Converter Switching Conditions. *IEEE Transactions on Neural Networks and Learning Systems*, 25(4):738–750, Apr 2014.

[40] Baohua Dong, S. Asgarpoor, and Wei Qiao. ANN-based adaptive PI control for wind turbine with doubly fed induction generator. In *2011 North American Power Symposium*, pages 1–6, Aug 2011.

[41] S. Mohagheghi, G. K. Venayagamoorthy, and R. G. Harley. Optimal Neuro-Fuzzy External Controller for a STATCOM in the 12-Bus Benchmark Power System. *IEEE Transactions on Power Delivery*, 22(4):2548–2558, Oct 2007.

[42] P. Cortes, M. P. Kazmierkowski, R. M. Kennel, D. E. Quevedo, and J. Rodriguez. Predictive Control in Power Electronics and Drives. *IEEE Transactions on Industrial Electronics*, 55(12):4312–4324, Dec 2008.

[43] J. Hu and Z. Q. Zhu. Improved Voltage-Vector Sequences on Dead-Beat Predictive Direct Power Control of Reversible Three-Phase Grid-Connected Voltage-Source Converters. *IEEE Transactions on Power Electronics*, 28(1):254–267, Jan 2013.

[44] S. Kouro, P. Cortes, R. Vargas, U. Ammann, and J. Rodriguez. Model Predictive Control - A Simple and Powerful Method to Control Power Converters. *IEEE Transactions on Industrial Electronics*, 56(6):1826–1838, June 2009.

[45] S. Vazquez, C. Montero, C. Bordons, and L. G. Franquelo. Model predictive control of a VSI with long prediction horizon. In *2011 IEEE International Symposium on Industrial Electronics*, pages 1805–1810, 2011.

[46] Tobias Geyer and Daniel E. Quevedo. Multistep Finite Control Set Model Predictive Control for Power Electronics. *IEEE Transactions on Power Electronics*, 29(12): 6836–6846, Dec 2014.

[47] Alfeu J. Sguarezi Filho and Ernesto Ruppert Filho. Model-Based Predictive Control Applied to the Doubly-Fed Induction Generator Direct Power Control. *IEEE Transactions on Sustainable Energy*, 3(3):398–406, July 2012.

[48] Arne Linder and Ralph Kennel. Model predictive control for electrical drives. In *Proceeding of IEEE Power Electronics*, pages 1793–1799, Brazil, 2005.

[49] Marcos G. Judewicz, Sergio Alejandro Gonzalez, Noelia I. Echeverria, Jonatan Roberto Fischer, and Daniel O. Carrica. Generalized Predictive Current Control (GPCC) for Grid-Tie Three-Phase Inverters. *IEEE Transaction On Industrial Electronics*, 63(7):4475–4484, 2016.

[50] Sebastien Mariethoz and Manfred Morari. Explicit Model-Predictive Control of a PWM Inverter With an LCL Filter. *IEEE Transactions on Power Electronics*, 56 (2):389–399, Feb 2009.

[51] A. G. Beccuti, M. Kvasnica, G. Papafotiou, and M. Morari. A Decentralized Explicit Predictive Control Paradigm for Parallelized DC-DC Circuits. *IEEE Transactions on Control Systems Technology*, 21(1):136–148, January 2013.

[52] Jose Rodriguez, Marian P. Kazmierkowski, Jose R. Espinoza, Pericle Zanchetta, Haitham Abu-Rub, Hector A. Young, and Christian A. Rojas. State of the Art of Finite Control Set Model Predictive Control in Power Electronics. *IEEE Transaction on Industrial Informatics*, 9(2):1003–1016, May 2013.

[53] B. Q. V. Ngo, P. R. Ayerbe, and S. Olaru. Model Predictive Control with Two-step horizon for Three-level Neutral-Point Clamped Inverter. In *Proceeding of 20th International Conference on Process Control*, pages 215–220, Slovakia, 2015.

[54] Dawei Zhi, LieXu, and Barry W. Williams. Model-Based Predictive Direct Power Control of Doubly Fed Induction Generators. *IEEE Transactions on Power Electronics*, 25(2):341–351, Feb 2010.

[55] Sergio Vazquez, Jianxing Liu, Huijun Gao, and Leopoldo G. Franquelo. Second Order Sliding Mode Control for Three-Level NPC Converters Via Extended State Observer. In *Proceeding of 41st Annual Conference of the IEEE Industrial Electronics-IECON*, pages 5118–5123, 2015.

[56] Sergio Vazquez, Ricardo P. Aguilera, Pablo Acuna, Josep Pou, Jose I. Leon, Leopoldo G. Franquelo, and Vassilios G. Agelidis. Model Predictive Control for Single-Phase NPC Converters Based on Optimal Switching Sequences. *IEEE Transaction On Industrial Electronics*, 63(12):7533–7541, December 2016.

[57] S. Vazquez, A. Marquez, R. Aguilera, D. E. Quevedo, J. I. Leon, and L. G. Franquelo. Predictive direct power control for grid connected power converters with DC-link voltage dynamic reference design. In *2015 IEEE International Conference on Industrial Technology (ICIT)*, pages 2327–2332, Mar 2015.

[58] A. Bouafia, J. P. Gaubert, and F. Krim. Predictive Direct Power Control of Three-Phase Pulsewidth Modulation (PWM) Rectifier Using Space-Vector Modulation (SVM). *IEEE Transactions on Power Electronics*, 25(1):228–236, Jan 2010.

[59] L. Tarisciotti, P. Zanchetta, A. Watson, S. Bifaretti, and J. C. Clare. Modulated Model Predictive Control for a Seven-Level Cascaded H-Bridge Back-to-Back Converter. *IEEE Transactions on Industrial Electronics*, 61(10):5375–5383, Oct 2014.

[60] L. Tarisciotti, P. Zanchetta, A. Watson, J. C. Clare, M. Degano, and S. Bifaretti. Modulated Model Predictive Control for a Three-Phase Active Rectifier. *IEEE Transactions on Industry Applications*, 51(2):1610–1620, Mar 2015.

[61] M. Rivera, M. Perez, V. Yaramasu, B. Wu, L. Tarisciotti, P. Zanchetta, and P. Wheeler. Modulated model predictive control (M2PC) with fixed switching frequency for an NPC converter. In *2015 IEEE 5th International Conference on Power Engineering, Energy and Electrical Drives (POWERENG)*, pages 623–628, May 2015.

[62] J. Rubinic, V. Yaramasu, B. Wu, and N. Zargari. Model predictive control of neutral-point clamped inverter with harmonic spectrum shaping. In *2015 IEEE Energy Conversion Congress and Exposition (ECCE)*, pages 717–722, Sept 2015.

[63] N. Hoffmann, M. Andresen, F. W. Fuchs, L. Asiminoaei, and P. B. Thøgersen. Variable sampling time finite control-set model predictive current control for voltage source inverters. In *2012 IEEE Energy Conversion Congress and Exposition (ECCE)*, pages 2215–2222, Sept 2012.

[64] R. P. Aguilera, P. Lezana, and D. E. Quevedo. Switched Model Predictive Control for Improved Transient and Steady-State Performance. *IEEE Transactions on Industrial Informatics*, 11(4):968–977, Aug 2015.

[65] P. Stolze, P. Karamanakos, M. Tomlinson, R. Kennel, T. Mouton, and S. Manias. Heuristic variable switching point predictive current control for the three-level neutral point clamped inverter. In *2013 IEEE International Symposium on Sensorless Control for Electrical Drives and Predictive Control of Electrical Drives and Power Electronics (SLED/PRECEDE)*, pages 1–8, Oct 2013.

[66] P. Stolze, P. Karamanakos, R. Kennel, S. Manias, and T. Mouton. Variable switching point predictive torque control for the three-level neutral point clamped inverter. In *2013 15th European Conference on Power Electronics and Applications (EPE)*, pages 1–10, Sept 2013.

[67] Peter Stolze, Petros Karamanakos, Ralph Kennel, Stefanos Manias, and Christian Endisch. Effective variable switching point predictive current control for ac low-voltage drives. *International Journal of Control*, 88(7):1366–1378, 2015.

[68] V. Yaramasu, B. Wu, P. C. Sen, S. Kouro, and M. Narimani. High-power wind energy conversion systems: State-of-the-art and emerging technologies. *Proceedings of the IEEE*, 103(5):740–788, May 2015.

[69] P. Cortes, J. Rodriguez, S. Vazquez, and L. G. Franquelo. Predictive control of a three-phase UPS inverter using two steps prediction horizon. In *2010 IEEE International Conference on Industrial Technology*, pages 1283–1288, Mar 2010.

[70] O. Kukrer. Discrete-time current control of voltage-fed three-phase PWM inverters. *IEEE Transactions on Power Electronics*, 11(2):260–269, Mar 1996.

[71] Marian P. Kazmierkowski, R. Krishnan, and Frede Blaabjerg. *Control in Power Electronics*. Academic Press Series in Engineering. Elsevier Science, 2012.

[72] M. Castilla, J. Miret, A. Camacho, J. Matas, and L. G. de Vicuna. Reduction of Current Harmonic Distortion in Three-Phase Grid-Connected Photovoltaic Inverters via Resonant Current Control. *IEEE Transactions on Industrial Electronics*, 60 (4):1464–1472, April 2013.

[73] Niklas Panten, Nils Hoffmann, and Friedrich Wilhelm Fuchs. Finite Control Set Model Predictive Current Control for Grid-Connected Voltage-Source Converters With LCL Filters: A Study Based on Different State Feedbacks. *IEEE Transactions on Power Electronics*, 31(7):5189–5200, July 2016.

[74] Dae Keun Choi and Kyo Beum Lee. Dynamic Performance Improvement of AC/DC Converter Using Model Predictive Direct Power Control With Finite Control Set. *IEEE Transaction On Industrial Electronics*, 62(2):757–767, February 2015.

[75] S. Vazquez, J. I. Leon, L. G. Franquelo, J. Rodriguez, H. A. Young, A. Marquez, and P. Zanchetta. Model Predictive Control: A Review of Its Applications in Power Electronics. *IEEE Industrial Electronics Magazine*, 8(1):16–31, March 2014.

[76] Changliang Xia, Tao Liu, Tingna Shi, and Zhanfeng Song. A Simplified Finite-Control-Set Model-Predictive Control for Power Converters. *IEEE Transactions on Industrial Informatics*, 10(2):991–1022, May 2014.

[77] A. J. Sguarezi Filho and E. Ruppert. A Deadbeat Active and Reactive Power Control for Doubly Fed Induction Generator. *Electric Power Components and Systems*, 38(5):592–602, 2010.

[78] J. W. Kimball and M. Zawodniok. Reducing Common-Mode Voltage in Three-Phase Sine-Triangle PWM With Interleaved Carriers. *IEEE Transactions on Power Electronics*, 26(8):2229–2236, Aug 2011.

[79] S. Lakshminarayanan, G. Mondal, P. N. Tekwani, K. K. Mohapatra, and K. Gopakumar. Twelve-Sided Polygonal Voltage Space Vector Based Multilevel Inverter for an Induction Motor Drive With Common-Mode Voltage Elimination. *IEEE Transactions on Industrial Electronics*, 54(5):2761–2768, Oct 2007.

[80] V. Yaramasu, B. Wu, M. Rivera, M. Narimani, S. Kouro, and J. Rodriguez. Generalised approach for predictive control with common-mode voltage mitigation in multilevel diode-clamped converters. *IET Power Electronics*, 8(8):1440–1450, 2015.

[81] S. Kwak and S. k. Mun. Model Predictive Control Methods to Reduce Common-Mode Voltage for Three-Phase Voltage Source Inverters. *IEEE Transactions on Power Electronics*, 30(9):5019–5035, Sept 2015.

[82] S. Kwak and S. Mun. Common-mode voltage mitigation with a predictive control method considering dead time effects of three-phase voltage source inverters. *IET Power Electronics*, 8(9):1690–1700, 2015.

[83] Lie Xu, Dawei Zhi, and Barry W. Williams. Predictive Current Control of Doubly Fed Induction Generators. *IEEE Transaction on Industrial Electronics*, 56(10): 4143–4153, Oct 2009.

[84] J. Sayritupac, E. Albanez, J. Rengifo, J. M. Aller, and J. Restrepo. Predictive control strategy for DFIG wind turbines with maximum power point tracking using multilevel converters. In *Proc. Power Electronics and Power Quality Applications PEPQA*, pages 1–6, Bogota, 2015.

[85] Jiefeng Hu, Jianguo Zhu, Yongchang Zhang, Glenn Platt, Qishuang Ma, and David G. Dorrell. Predictive Direct Virtual Torque and Power Control of Doubly Fed Induction Generators for Fast and Smooth Grid Synchronization and Flexible Power Regulation. *IEEE Transactions on Power Electronics*, 28(7):3182–3194, July 2013.

[86] Xiangjie Liu and Xiaobing Kong. Model-Based Predictive Control Applied to the Doubly-Fed Induction Generator Direct Power Control. *IEEE Transactions on Automation science and Engineering*, 11(4):1046–1055, July 2014.

[87] B. Q. V. Ngo, P. Rodriguez-Ayerbe, and S. Olaru. Model Predictive Direct Power Control for Doubly fed induction generator based wind turbines with Three-level Neutral-Point Clamped inverter. In *42nd Annual Conference on IEEE Industrial Electronics Society*, pages 3476–3481, Oct 2016.

[88] Dan Sun and Xiaohe Wang. Low-Complexity Model Predictive Direct Power Control for DFIG Under Both Balanced and Unbalanced Grid Conditions. *IEEE Transactions on Industrial Electronics*, 63(8):5186–5196, August 2016.

[89] R. P. Aguilera and D. E. Quevedo. On stability and performance of finite control set MPC for power converters. In *2011 Workshop on Predictive Control of Electrical Drives and Power Electronics*, pages 55–62, Oct 2011.

[90] R. P. Aguilera and D. E. Quevedo. Predictive Control of Power Converters: Designs With Guaranteed Performance. *IEEE Transactions on Industrial Informatics*, 11 (1):53–63, Feb 2015.

[91] T. Geyer, R. P. Aguilera, and D. E. Quevedo. On the stability and robustness of model predictive direct current control. In *2013 IEEE International Conference on Industrial Technology (ICIT)*, pages 374–379, Feb 2013.

[92] Sangshin Kwak, Sung Jin Yoo, and Juncheol Park. Finite control set predictive control based on Lyapunov function for three-phase voltage source inverters. *IET Power Electronics*, 7(11):2726–2732, November 2014.

[93] M. Parvez Akter, Saad Mekhilef, Nadia Mei Lin Tan, and Hirofumi Akagi. Modified Model Predictive Control of a Bidirectional AC-DC Converter Based on Lyapunov Function for Energy Storage Systems. *IEEE Transaction On Industrial Electronics*, 63(2):704–715, February 2016.

[94] Matthias Preindl. Robust Control Invariant Sets and Lyapunov-Based MPC for IPM Synchronous Motor Drives. *IEEE Transaction On Industrial Electronics*, 63 (6):3925–3933, June 2016.

[95] T. Barisa, S. Iles, D. Sumina, and J. Matusko. Flexible Lyapunov Function based Model Predictive Direct Current Control of Permanent Magnet Synchronous Generator. In *2016 IEEE International Power Electronics and Motion Control Conference (PEMC)*, pages 98–103, Sept 2016.

[96] Venkata Yaramasu and Bin Wu. Model Predictive Decoupled Active and Reactive Power Control for High-Power Grid-Connected Four-Level Diode-Clamped Inverters. *IEEE Transaction on Industrial Electronics*, 61(7):3407–3416, July 2014.

[97] Jung-Su Kim, Tae-Woong Yoon, Ali Jadbabaie, and Claudio De Persis. Input-to-state stable finite horizon MPC for neutrally stable linear discrete-time systems with input constraints. *Systems and Control Letters*, 55:293–303, April 2006.

[98] L. Magni, D. M. Raimondo, and R. Scattolini. Regional Input-to-State Stability for Nonlinear Model Predictive Control. *IEEE Transactions on Automatic Control*, 51(9):1548–1553, September 2006.

[99] Andrei A. Agrachev, A. Stephen Morse, Eduardo D. Sontag, Hector J. Sussmann, and Vadim I. Utkin. *Nonlinear and Optimal Control Theory*. Springer, 2004.

[100] S. H. Hwang and J. M. Kim. Dead Time Compensation Method for Voltage-Fed PWM Inverter. *IEEE Transactions on Energy Conversion*, 25(1):1–10, March 2010.

[101] N. Urasaki, T. Senjyu, K. Uezato, and T. Funabashi. An adaptive dead-time compensation strategy for voltage source inverter fed motor drives. *IEEE Transactions on Power Electronics*, 20(5):1150–1160, Sept 2005.

[102] A. Mora, J. Juliet, A. Santander, and P. Lezana. Dead-Time and Semiconductor Voltage Drop Compensation for Cascaded H-Bridge Converters. *IEEE Transactions on Industrial Electronics*, 63(12):7833–7842, Dec 2016.

[103] D. H. Lee and J. W. Ahn. A Simple and Direct Dead-Time Effect Compensation Scheme in PWM-VSI. *IEEE Transactions on Industry Applications*, 50(5):3017–3025, Sept 2014.

[104] D. Leggate and R. J. Kerkman. Pulse-based dead-time compensator for PWM voltage inverters. *IEEE Transactions on Industrial Electronics*, 44(2):191–197, Apr 1997.

[105] Hengbing Zhao, Q. M. J. Wu, and A. Kawamura. An accurate approach of nonlinearity compensation for VSI inverter output voltage. *IEEE Transactions on Power Electronics*, 19(4):1029–1035, July 2004.

[106] A. Cichowski and J. Nieznanski. Self-tuning dead-time compensation method for voltage-source inverters. *IEEE Power Electronics Letters*, 3(2):72–75, June 2005. ISSN 1540-7985.

[107] Jong-Woo Choi and Seung-Ki Sul. Inverter output voltage synthesis using novel dead time compensation. *IEEE Transactions on Power Electronics*, 11(2):221–227, Mar 1996.

[108] Hyun-Soo Kim, Hyung-Tae Moon, and Myung-Joong Youn. On-line dead-time compensation method using disturbance observer. *IEEE Transactions on Power Electronics*, 18(6):1336–1345, Nov 2003.

[109] K. J. Lee, B. G. Park, R. Y. Kim, and D. S. Hyun. Robust Predictive Current Controller Based on a Disturbance Estimator in a Three-Phase Grid-Connected Inverter. *IEEE Transactions on Power Electronics*, 27(1):276–283, Jan 2012.

[110] C. Attaianese, V. Nardi, and G. Tomasso. A novel SVM strategy for VSI dead-time-effect reduction. *IEEE Transactions on Industry Applications*, 41(6):1667–1674, Nov 2005.

[111] Akihiro Irnura, Tornoya Takahashi, Masarni Fujitsuna, Tadanao Zanma, and Shinji Doki. Dead-Time Compensation in Model Predictive Instantaneous-current Control. In *38th Annual Conference of IEEE Industrial Electronics Society (IECON 2012)*, pages 5037–5042, 2012.

[112] A. Kuznietsov, S. Wolf, and T. Happek. Model predictive control of a voltage source inverter with compensation of deadtime effects. In *2015 IEEE International Conference on Industrial Technology (ICIT)*, pages 2532–2536, 2015.

[113] C. Townsend, G. Mirzaeva, and G. Goodwin. Dead-Time Compensation for Model Predictive Control of Power Inverters. *IEEE Transactions on Power Electronics*, PP(99):1–1, 2016.

[114] M. Yang, K. Yang, G. Li, C. Yi, and D. Xu. A Novel Dead-Time Compensation Method for Direct Predictive Control. In *2015 Fifth International Conference on Instrumentation and Measurement, Computer, Communication and Control (IMCCC)*, pages 273–277, Sept 2015.

[115] M. Sprenger, T. Barth, R. Alvarez, M. Tannhaeuser, and S. Bernet. Experimental verification of direct dead-time Control and DC-link neutral-point balancing of a three level neutral-point-clamped (3L-NPC) VSC. In *Proc. IEEE Energy Conversion Congress and Exposition*, pages 409–413, 2013.

université PARIS-SACLAY

ÉCOLE DOCTORALE
Sciences et technologies de l'information et de la communication (STIC)

Titre: Algorithmes de conception de lois de commande prédictives pour les systèmes de production d'énergie

Mots clefs: Commande prédictive, Convertisseur à trois niveaux et clampé par le neutre, Générateur asynchrone à double alimentation, Controle par les fonctions de Lyapunov, Compensation du temps mort

Résumé: Cette thèse vise à élaborer de nouvelles stratégies de commande basées sur la commande prédictive pour le système de génération d'énergie éolienne. La topologie des systèmes de production éolienne basées sur le Générateur Asynchrone à Double Alimentation (GADA) qui convient à des plateformes de génération dans la gamme de puissance de 1.5 à 6 MW est abordée. Du point de vue technologique, le convertisseur à trois niveaux et clampé par le neutre (3L-NPC) est considéré comme une bonne solution pour une puissance élevée en raison de ses avantages: capacité à réduire la distorsion harmonique de la tension de sortie et du courant, et augmentation de la capacité du convertisseur grâce à une tension réduite appliquée à chaque semi-conducteur de puissance.

Une description détaillée de la commande prédictive à ensemble de commande fini (FCS-MPC) avec un horizon de prédiction de deux pas est présentée pour deux boucles de régulation: celle liée au convertisseur connecté au réseau et celle du convertisseur connecté au GADA. Le principe de la commande repose sur l'utilisation d'un modèle de prédiction permettant de prédire le comportement du système pour chaque état de commutation du convertisseur. La minimisation d'une fonction de coût appropriée prédéfinie permet d'obtenir la commutation optimale à appliquer au convertisseur.

La thèse étudie premièrement les problèmes liées à la compensation du temps de calcul de la commande et au choix et aux pondérations de la fonction de coût. Ensuite, le problème de stabilité de la commande FCS-MPC est abordé en considérant une fonction de Lyapunov dans la minimisation de la fonction de coût. Finalement, une étude sur la compensation des effets des temps morts du convertisseur est présentée.

Title: Control design algorithms for Model-Based Predictive Power Control. Application for Wind Energy

Keywords: Doubly fed induction generator (DFIG), Three-level Neutral-Point Clamped Converter (3L-NPC), Finite control set model predictive control (FCS-MPC), Direct power control (DPC), Model predictive direct power control (MPDPC), Control Lyapunov function (CLF), Dead-time compensation, Two-step horizon, Computational burden.

Abstract: This thesis aims to elaborate new control strategies based on Model Predictive control for wind energy generation system. We addressed the topology of doubly fed induction generator (DFIG) based wind generation systems which is suitable for generation platform power in the range in 1.5-6 MW. Furthermore, from the technological point of view, the three-level neutral-point clamped (3L-NPC) inverter configuration is considered a good solution for high power due to its advantages: capability to reduce the harmonic distortion of the output voltage and current, and increase the capacity of the converter thanks to a decreased voltage applied to each power semiconductor.

In this thesis, we presented a detailed description of finite control set model predictive control (FCS-MPC) with two-step horizon for two control schemes: grid and DFIG connected 3L-NPC inverter. The principle of the proposed control scheme is to use system model to predict the behaviour of the system for every switching states of the inverter. Then, the optimal switching state that minimizes an appropriate predefined cost function is selected and applied directly to the inverter.

The study of issues such as delay compensation, computational burden and selection of weighting factor are also addressed in this thesis. In addition, the stability problem of FCS-MPC is solved by considering the control Lyapunov function in the design procedure. The latter study is focused on the compensation of dead-time effect of power converter.

Université Paris-Saclay
Espace Technologique / Immeuble Discovery
Route de l'Orme aux Merisiers RD 128 / 91190 Saint-Aubin, France